LUT
Lappeenranta
University of Technology

Jussi Saari

IMPROVING THE EFFECTIVENESS AND PROFITABILITY OF THERMAL CONVERSION OF BIOMASS

Thesis for the degree of Doctor of Science (Technology) to be presented with due permission for public examination and criticism in the Auditorium of the Student Union House at Lappeenranta University of Technology, Lappeenranta, Finland on the 8th of December, 2017, at noon.

Acta Universitatis
Lappeenrantaensis 777

Supervisors Professor Esa Vakkilainen
LUT School of Energy Systems
Lappeenranta University of Technology
Finland

Docent Juha Kaikko
LUT School of Energy Systems
Lappeenranta University of Technology
Finland

Professor Vitaly Sergeev
Department of Energy Technology
Peter the Great St. Petersburg Polytechnic University
Russia

Reviewers Professor Risto Lahdelma
Department of Mechanical Engineering
Aalto University
Finland

Professor Rikard Gebart
Department of Engineering Sciences and Mathematics
Luleå University of Technology
Sweden

Opponents Professor Risto Lahdelma
Department of Mechanical Engineering
Aalto University
Finland

Professor Tobias Richards
Department of Resource Recovery and Building Technology
University of Borås
Sweden

ISBN 978-952-335-176-9
ISBN 978-952-335-177-6 (PDF)
ISSN-L 1456-4491
ISSN 1456-4491

Lappeenrannan teknillinen yliopisto
Yliopistopaino 2017

Abstract

Jussi Saari
Improving the effectiveness and profitability of thermal conversion of biomass
Lappeenranta 2017
167 pages
Acta Universitatis Lappeenrantaensis 777
Diss. Lappeenranta University of Technology
ISBN 978-952-335-176-9, ISBN 978-952-335-177-6 (PDF), ISSN-L 1456-4491,
ISSN 1456-4491

Sustainably produced and efficiently used biomass has many advantages as an energy source. It provides an opportunity for reducing greenhouse gas emissions by replacing fossil fuels, and is typically also a local energy source. When used for combined heat and power (CHP) production, biomass can provide a dependable source of renewable energy at high efficiency. There are also drawbacks for CHP production and the use of biomass as a fuel, however. Untreated wood is an unstable fuel of uneven quality and low energy density, which limits its potential for fossil fuel replacement. In the current economic environment of relatively low and volatile electricity prices, CHP plants are also a risky investment at best.

This work investigates the possibilities of improving the profitability and effectiveness of small-scale Nordic wood-fired CHP plants through two different approaches. Integration with mild thermochemical conversion processes is studied to find the best integration concepts, and to learn whether such an integrated plant would be superior in its economic and technical performance to stand-alone CHP and biomass conversion plants. Process simulation software was used to investigate the operation and technical performance of the different plants. It was found that while there is little potential to improve energy efficiency, integration can still improve the profitability of the plant. This is achieved mainly through reductions in investment costs, and by increasing the annual operating time of the CHP plant through the introduction of an additional heat consumer that enables the plant to run when the district heat load alone would be less than the plant minimum load.

The second focus of the study is improving the profitability by component design optimization, namely the condenser of a pure CHP plant. Condenser heat transfer and mechanical sizing models were developed in MATLAB environment, and optimization was carried out at different electricity prices. Metaheuristic optimization algorithms were used for the optimization. It was found that while the profitability of the plant depends heavily on the price of electricity, the optimal performance required of the condenser, as well as its design, are affected only slightly by the electricity price at moderate to high price levels. The optimization did not consider the possibility of varying the plant operating strategies, which limits the practical applicability of the results at low electricity price scenarios.

In an effort to reduce the computation time required for the condenser optimization, a novel way of combining two existing metaheuristic optimization methods was shown to perform better than the other tested algorithms, including either of the two on which the new hybrid method was based on. Further testing with other problems is needed to determine if this hybridization is a generally well-performing algorithm, or is merely particularly well suited for the condenser optimization on which it was implemented in this thesis.

Some topics for future research are identified. The economic and operational analysis of the process integration studies was performed only on a small CHP plant, integrated with a comparatively large-scale biomass conversion plant. A larger CHP plant would offer more options for both heat sinks and heat sources as well as operational flexibility, and could yield different results. The optimization of the condenser could be more flexible, allowing varying the plant operation. This could produce more valuable and realistic results on optimal condenser sizing for low electricity price scenarios.

Keywords: CHP, torrefaction, hydrothermal carbonization, integration, condenser, shell-and-tube heat exchanger, optimization, differential evolution, cuckoo search

Acknowledgements

The work presented in this thesis was carried out in the Laboratory of Sustainable Energy Systems of LUT School of Energy Systems in Lappeenranta, Finland, between February 2010 and August 2016.

Firstly, I would like to express my gratitude to my supervisors, Professor Esa Vakkilainen, Docent Juha Kaikko, and Professor Vitaly Sergeev for the guidance and support that they provided.

I humbly thank both reviewers, professors Risto Lahdelma and Rikard Gebart, whose comments and suggestions improved the quality of this thesis. Professor Lahdelma also agreed to act as the opponent together with professor Tobias Richards: I wish to express my gratitude to both opponents.

I am also grateful to my friends and colleagues who co-operated with the publications of the thesis: first and foremost Ekaterina Sermyagina who provided valuable contribution to most of the publications that are part of the thesis, to Mariana Carvalho and Svetlana Afanasyeva who also participated in some of the publications, and Manuel Garcia Pérez who assisted in finishing the final calculations of the work.

I also wish to thank the University of Minas Gerais and there especially Professor Marcelo Cardoso for making my visit possible and assisting in countless ways with both work and practical matters.

Finally, I would like to express my gratitude to many other colleagues and friends for providing valuable discussions both on and off the topic of the thesis. The list of people includes but is not limited to, Kari Luostarinen, Katja Kuparinen, Jaakko Ylätalo, Jarno Parkkinen, Petteri Peltola, Markku Nikku, Marcio Neto, Victoria Palacin Silva, Victoria Karaseva, and Mai Anh Ngo.

Jussi Saari
November 2017
Lappeenranta, Finland

Contents

Abstract

Acknowledgements

Contents

List of publications **11**

Nomenclature **15**

1 Introduction **21**
1.1 Why bio-CHP and biofuels as the focus? 21
1.2 Objectives 23
1.3 Methods 24
1.4 Outline of the thesis 26

2 CHP plant and multi-period model **29**
2.1 Multi-period model 29
2.2 Boiler 31
2.3 Steam cycle 33
2.3.1 Turbine 33
2.3.2 Condenser 34

3 Low-temperature biomass thermochemical conversion **37**
3.1 Background 37
3.2 Torrefaction model 38
3.2.1 Plant configuration 39
3.2.2 Torrefaction products 40
3.2.3 Heat consumption of the torrefaction reactor 43
3.2.4 Stoker boiler 47
3.3 Hydrothermal carbonization model 49
3.3.1 Plant configuration 49
3.3.2 Slurry pressurization and feed heating 50
3.3.3 HTC reactor 51
3.3.4 Product slurry treatment and heat recovery 53
3.3.5 Stoker boiler 54

4 Integration of biomass conversion with a CHP plant **57**
4.1 Background 57
4.2 Integration of torrefaction with the CHP plant 59
4.2.1 Technical performance comparison of different integration options 59

4.2.2 Operational analysis 62
4.2.3 Annual production and consumption 65
4.3 Integration of hydrothermal carbonization with the CHP plant 69
4.3.1 Considered integration cases 69
4.3.2 Performance comparison at design point and minimum load 72
4.3.3 Evaluation of initial technical comparison 76
4.3.4 Effect of carbonization temperature on plant performance 76
4.3.5 Operational analysis 78
4.3.6 Annual production and consumption 82

5 Economic analysis **87**
5.1 Cost assumptions and scenarios 87
5.2 Profitability evaluation of integration concepts 88
5.3 Comparison of the studied cases 90
5.3.1 Investment costs 90
5.3.2 Profitability comparison 90
5.3.3 Sensitivity analysis 95

6 Condenser model **97**
6.1 Background 97
6.2 Large vacuum condenser 98
6.2.1 Calculation procedure 100
6.2.2 Local heat transfer and pressure drop calculation 101
6.2.3 Average-U models: 0-D and HEI standards 103
6.2.4 Validation at base load conditions 104
6.3 Back pressure condenser 109
6.3.1 Fixed parameters and assumptions 110
6.3.2 Heat transfer model 110

7 Condenser optimization **115**
7.1 Background 115
7.1.1 Heat exchanger cost 116
7.1.2 Optimization methods and algorithms 116
7.2 Objective function 118
7.2.1 Effect of condenser on plant performance 119
7.2.2 Condenser cost model 121
7.2.3 Objective function evaluation 122
7.3 Optimization algorithms 125
7.3.1 Differential evolution 125
7.3.2 Cuckoo search 127
7.3.3 Genetic Algorithm 134
7.4 Results 135
7.4.1 Extraction steam DHC mass minimization 135
7.4.2 Back pressure DHC optimization 135
7.5 Improving the optimization speed 138

7.5.1 Evaluation of algorithm performance and control parameter settings 140

8 Conclusions **147**
8.1 Main findings of the study 147
8.2 Future research needs 150

References **153**

Publications

List of publications

This thesis is based on the following papers, which are referred to in the text with Roman numerals I-VII. The rights have been granted by publishers to include the papers in the thesis.

I. Saari, J., Kaikko, J., Vakkilainen, E., and Savolainen, S. (2014). Comparison of power plant steam condenser heat transfer models for on-line condition monitoring. *Applied Thermal Engineering*, 62(1), 37-47.

II. Saari, J., Afanasyeva, S., Vakkilainen, E., and Kaikko, J. (2014). Heat transfer model and optimization of a shell-and-tube district heat condenser. In: Zevenhoven, R., ed., *Proceedings of the 27th International Conference on Efficiency, Cost, Optimization, Simulation and Environmental Impact of Energy Systems (ECOS)*, 1920-1934. Turku, Finland.

III. Sermyagina, E., Saari, J., Zakeri, B., Vakkilainen, E., and Kaikko, J. (2015). Effect of heat integration method and torrefaction temperature on the performance of an integrated CHP-torrefaction plant. *Applied Energy*, 149(1). 24-34.

IV. Saari, J., Kuparinen, K., Sermyagina, E., Vakkilainen, E., Kaikko, J. and Sergeev, V. The effect of integration method and carbonization temperature on the performance of an integrated hydrothermal carbonization and CHP plant. Submitted to *BioResources*, 2017.

V. Saari, J., Sermyagina, E., Vakkilainen, E., Kaikko, J. and Sergeev, V. (2016). Integration of hydrothermal carbonization and a CHP plant: Part 2 – operational and economic analysis. *Energy*, 113, 574-585.

VI. Saari, J., Machado, M.d.O.C., Sermyagina E., Kaikko, J., and Vakkilainen, E. (2016). Optimization of a Shell-and-Tube District Heat Condenser for a Small Back Pressure CHP Plant. In: Meyer, Josua, ed., *Proceedings of the 12th International Conference on Heat Transfer, Fluid Mechanics and Thermodynamics (HEFAT)*, 270-277. Malaga, Spain.

VII. Sermyagina, E., Saari, J., Vakkilainen, E., and Kaikko, J. (2016). Integration of torrefaction and a CHP plant: operational and economic analysis. *Applied Energy*, 183, 88-99.

Author's contribution

The candidate was the principal investigator in Publications I-II and IV-VI. In Publication I, Mr Savolainen contributed with his practical experience in plant operation and maintenance issues. In Publication II, Mrs Afanasyeva assisted with composing the text, and in performing the optimization algorithm control parameter sensitivity analysis.

In Publication III, Mrs Sermyagina was the principal investigator performing the final plant simulations, composing the paper, and analysing the results. The candidate developed the torrefaction and boiler component models for the plant, co-operated in the

development of the plant integration model, and composed the parts of the article text related to these topics.

In Publication IV, Mrs Kuparinen assisted with composing the paper, and Mrs Sermyagina contributed to the modelling of the hydrothermal carbonization process. In Publication V, Mrs Sermyagina performed the plant investment cost analysis, and assisted with composing the text.

In Publication VI, Mrs Machado and Mrs Sermyagina assisted in composing the text. In publication VII, Mrs Sermyagina was the principal investigator; the candidate's contribution was the CHP plant part-load model and the framework for the economic analysis, and assisting with the operational analysis of the CHP plant.

In all the publications Prof. Vakkilainen and Docent Kaikko participated actively as supervisors. Prof. Sergeev participated as supervisor in Publications IV and V.

Related publications not included in this thesis

Hamaguchi M., Saari, J., and Vakkilainen E. (2013). Bio-oil and biochar as additional revenue streams in South American Kraft pulp mills. *BioResources*, 8(3), 3399-3413.

Saari, J., Zakri, B., Sermyagina, E., and Vakkilainen, E. (2013). Integration of Torrefaction Reactor with Steam Power Plant. *8th international Black Liquor Colloquium - Black liquor and Biomass to Bioenergy and Biofuels*. Belo Horizonte, Brazil.

Sermyagina, E., Saari, J., Kaikko, J., and Vakkilainen, E. (2015). Hydrothermal carbonization of coniferous biomass: Effect of process parameters on mass and energy yields. *Journal of Analytical and Applied Pyrolysis*, 113, 551-556.

Sermyagina, E., Saari, J., Kaikko, J., and Vakkilainen, E. (2015). Pre-treatment of Coniferous Biomass via Hydrothermal Carbonization and Torrefaction: Mass and Energy Yields. *International Bioenergy Conference and Exhibition*

Sermyagina, E., Nikku, M., Saari, J., Kaikko, J., and Vakkilainen, E. (2015). Design of multifunctional bench-scale device for thermochemical processes. *IEA Bioenergy Conference 2015*.

Saari, J., García Pérez M., Vakkilainen, E., and Kaikko, J. Impact of problem formulation and control parameter settings on shell-and-tube heat exchanger optimization with different metaheuristics. Submitted to *Energy Conversion and Management*, 2017

Other publications during the thesis research

Afanasyeva, S., Saari, J., Kukkonen, S., Partanen, J., and Partanen, O. (2013). Optimization of wind farm design taking into account uncertainty in input parameters. *Annual Conference of European Wind Energy Association (EWEA)*.

Afanasyeva, S., Saari, J., Kalkofen, M., Partanen, J., and Pyrhönen, O. (2014). Technical, economic and uncertainty modelling of a wind farm project. *27th International Conference on Efficiency, Cost, Optimization, Simulation and Environmental Impact of Energy Systems (ECOS 2014)*.

Afanasyeva, S., Saari, J., Kalkofen, M., Partanen, J., and Pyrhönen, O. (2016). Technical, economic and uncertainty modelling of a wind farm project. *Energy Conversion and Management*, 107, Special Issue on Efficiency, Cost, Optimisation, Simulation and Environmental Impact of Energy Systems (ECOS)-2014, 22-33

Afanasyeva, S., Karppanen J., Saari, J., Partanen, J., and Pyrhönen, O. (2016). Integrated Approach for the Design of Wind Farm Infrastructure. In: *IEEE PES Innovative Smart Grid Technologies Conference Europe (ISGT-Europe)*. 1-6. October 9-12, 2016, Ljubljana, Slovenia.

Afanasyeva, S., Saari, J., Partanen, J., and Pyrhönen, O. Cuckoo Search for wind farm optimization with auxiliary infrastructure. Submitted to *Wind Energy*, 2016.

Nomenclature

Latin alphabet

a	annuity factor	–
a,b,c,d	constants in experimental correlations	–
A	area	m^2
c	specific price of energy product	€/MWh
c_p	specific heat, constant pressure process	kJ/(kgK)
c_v	coefficient of variance	–
C	cost	€
C_f	coefficient of friction	–
CBM	module cost	€
CF	crossover fraction	–
CR	crossover rate	–
d_o	heat exchanger tube outside diameter	m
D	1. diameter	m
	2. number of decision variables in optimization problem	–
E	1. energy yield	–
	2. energy	J
f	friction factor	–
F	1. correction factor for HEI standards heat transfer correlation	–
	2. weight factor in differential evolution	–
g	acceleration due to gravity	m/s^2
G	1. conductance	W/K
	2. mass velocity	$kg/(m\ s^2)$
	3. generation in population-based optimization	–
h	1. height	m
	2. specific enthalpy	kJ/kg
	3. heat transfer coefficient	$W/(m^2K)$
h_{fg}	latent heat of evaporation	kJ/kg
h_{fs}	latent heat of melting	kJ/kg
i	interest rate	–
i,j,k	indexes	–
k	thermal conductivity	W/(mK)
K	1. turbine constant	m^2
	2. absolute surface roughness	m
	3. loss coefficient	–
	4. recombination factor	
L	length	m
LHV	lower heating value	MJ/kg
m	mass	kg
M	mass yield	–
MC	fuel moisture, fractional wet basis: m_{H2O}/m_{total}	–

MS	mutation scale parameter	–
n	plant economic operating time	a
n	vector of normal-distributed random numbers	
N	number	–
NP	population size (number of parents/particles)	–
NPV	net present value	€
NTU	number of transfer units	–
p	1. pressure	Pa
	2. probability	–
p	vector of normal-distributed random numbers	–
P	1. power	W
	2. operating period	–
	3. tube pitch	–
PBP	payback period	a
PEC	purchased equipment cost	€
q	vector of normal-distributed random variables	
Q	energy (heat or fuel)	J
r	random variable	–
R	1. ratio	–
	2. thermal resistance	K/W
R”	thermal resistance	m^2K/W
s	step size vector	–
t	time	h
T	temperature	K, °C
TCI	total capital investment	€
TTD	terminal temperature difference	°C
U	overall heat transfer coefficient	$W/(m^2K)$
u	trial vector in differential evolution or cuckoo search	
v	specific volume	m^3/kg
v	noise vector in differential evolution	
V	volume	m^3
w	velocity	m/s
x	steam quality	–
x	solution vector	

Greek alphabet

α	scaling factor	-
β	Lévy exponent	-
γ	uniform-distributed random number	-
Γ	Gamma function	
Δ	change, difference	
ε	1. heat exchanger effectiveness	-
	2. uniform-distributed random number	-
η	efficiency	-

ϕ	specific heat consumption	W/(kg s)
Φ	thermal power	W
λ	air ratio	-
μ	1. turbine intake ratio	-
	2. dynamic viscosity	Pa s
	3. mean value	
ρ	density	kg/m^3
σ	standard deviation	-

Dimensionless numbers

Nu	Nusselt number
Pr	Prandtl number
Re	Reynolds number
$\tilde{Re}$	two-phase Reynolds number in condensing flow

Subscripts

90 °	perpendicular turn at the shell-side nozzle of a heat exchanger
a	air
amb	ambient
ann	annulus
aux	auxiliary
b	boiler
bc	biochar
bd	blowdown
bed	BFB boiler bubbling bed
bf	baffle plate
c	cold
ch	channel
cl	clean
C	carbon
d	1. dry matter
	2. decision variable in a candidate solution vector
db	dry basis
D	design point
DHC	district heat condenser
E	elite
eff	effective
el	electricity
evap	evaporation
f	1. fuel
	2. flange
feed	feedstock (torrefaction or HTC)

FOB	free, on board
FT	flash tank
furn	furnace
FW	feedwater
g	gas
gen	generator
gr	gravity
h	hot
hc	hydrochar
i	1. inside
	2. index
in	inlet, flow into
ini	initial
ip	impingement plate
j	index
L	liquid
lm	logarithmic mean
loss	loss
LS	live steam
man	manufacturing
mat	material
max	maximum
MCR	maximum continuous rating
min	minimum
nzl	nozzle
o	outside
OD	off-design
opt	optimum
OTL	outer tube limit
out	outlet, out from
p	1. constant pressure
	2. purchased
pr	processing
pump	pump or pumps
r0, r1, r2	candidate solution vectors chosen randomly from a population
rad	radiation
react	reaction
ret	district heating water returning to the CHP or heat plant
s	1. isentropic
	2. sold
sat	saturated state
SG	steam generator
sh	1. shear
	2. shell

SH	superheater
SP	slurry pump
spec	specific
stack	stack
tb	tube
tf	thermal, fouling
torr	torrefaction
tot	total
ts	tubesheet
T	transverse
ub	unburnt
U	U-turn, in tubes of U-tube heat exchanger
V	vapour
w	tube wall
W	water
WB	water-to-biomass

Abbreviations

0-D	zero dimensional (one-point mean)
2-D	two dimensional
BA	bat algorithm
BFB	bubbling fluidized bed
CBM	cost, basic module
CFD	computational fluid dynamics
CHP	combined heat and power
CS	cuckoo search
COA	cuckoo optimization algorithm
CPU	central processing unit
DE	differential evolution
DH	district heat
DHC	district heat condenser
EA	evolutionary algorithm
ES	evolution strategy
FA	firefly algorithm
FOB	free on board
GA	genetic algorithm
GHG	greenhouse gas
HEI	heat exchanger institute
HHV	higher heating value
HP	high pressure
HRX	heat recovery heat exchanger
HS	harmony search
HTC	hydrothermal carbonization
IPPC	Intergovernmental Panel on Climate Change

IRR	internal rate of return
LHV	lower heating value
LP	low pressure
LPPH	low pressure feedwater preheater
MCR	maximum continuous rating
NFE	number of function evaluations
NP	number of parents
NPV	net present value
NTU	number of transfer units
O&M	operation and maintenance
OTL	outer tube limit
PBP	payback period
PEC	purchased equipment cost
PSO	particle swarm optimization
SA	simulated annealing
SCAH	steam coil air heater
SG	steam generator
SH	superheater
TCI	total capital investment
TEMA	Tubular Exchanger Manufacturers Association
TTD	terminal temperature difference

1 Introduction

This thesis investigates the possibilities of improving the profitability of small-scale bio-fired combined heat and power (CHP) plants considering the uncertainties of today's economic environment in the energy sector. The problem is approached from two directions: process integration of the CHP plant and a thermochemical biomass treatment process, and component-level design optimization.

1.1 Why bio-CHP and biofuels as the focus?

During the last decades, climate change as a result of anthropogenic greenhouse gas (GHG) emissions has received increasing attention. Most GHG emissions originate from various thermal energy conversion processes. The International Panel on Climate Change (IPCC) has identified bioenergy to have significant potential to mitigate GHG emissions, provided that the resources are used sustainably, and the energy systems for using the resources are efficient. (IPCC, 2011)

In addition to climate change concerns, there are also other demands on energy systems. Security of supply, affordable price, creating jobs and stimulating local economy are characteristics often considered desirable for the energy systems providing heat and electricity. Depending on the implementation, bioenergy can help address also some of these issues.

The process of converting biomass from a primary energy source into a final energy service such as electricity supply, heating or mechanical work, involves typically multiple steps. The main processes applicable for bioenergy are summarized in Figure 1.1 (IPCC, 2011). In Finland and other Nordic countries, most of the biomass used originates from forests. The large-diameter stemwood from final harvests is mainly used by the forest industry for pulp, paper and mechanical wood products, but much of the logging residues, stumps, and small-diameter stemwood from forest thinning, as well as various solid and liquid industrial waste streams end up as being used for bioenergy. Together with significant small-scale domestic use of firewood, these combine to a total of 26 % of the national energy use, making wood-based fuels the single largest fraction of total energy consumption in Finland. (Official Statistics of Finland, 2016) Wood-based biomass is mainly combusted for supplying the heat and power needs of industry in combined heat and power (CHP) plants, and for district heating both in heat-only plants and in CHP production.

CHP production using local wood biomass sources is a strategy that combines a renewable energy source with high energy efficiency, supply security, and local origin. Compared to separate production of heat and power from a similar primary energy source, co-generation in a CHP plant improves energy efficiency by as much as 25 to 30 percent. In Nordic countries CHP production is used for the purposes of district heating (DH). As DH consumption varies significantly with seasonal temperature variation, so does the

electricity production of the CHP producing district heat. From the point of view of national electricity supply, this can be seen as another advantage of bio-CHP compared to other carbon-neutral energy sources; while wind and solar production are by nature intermittent and volatile, and nuclear depends on long periods of stable base-load operation to cover the investment, power produced by CHP naturally peaks in winter when the heat load is high as well.

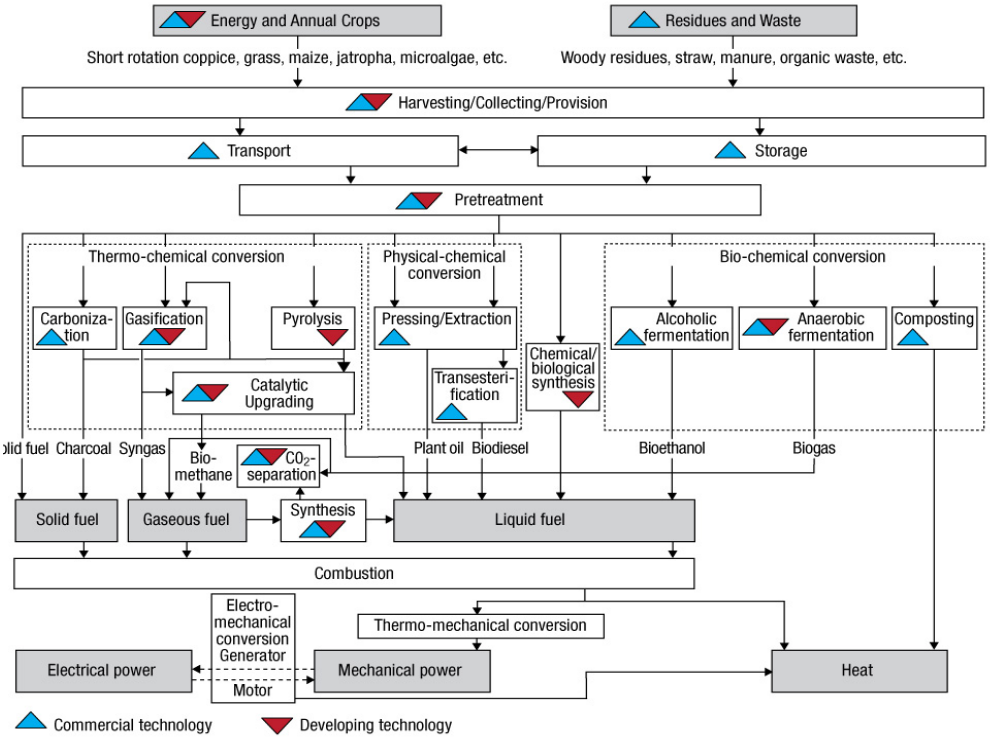

Figure 1.1: Bioenergy conversion paths from primary energy to energy service. (IPCC, 2011)

In Finland, a clear majority of district heat production takes place in CHP plants, which are typically back pressure steam cycles utilizing low-cost solid biomass or fossil fuel. In Figure 1.1, this corresponds to some of the simplest and shortest processes possible: pretreatment usually consists only of chipping the wood before combustion as solid fuel, to produce energy services in the form of heat and, through thermo-mechanical and electro-mechanical conversions, electrical power.

Although biomass-fired CHP production has several clear advantages, there are also drawbacks. While having the period of maximum power production during high demand is a clear advantage from the point of view of the power system, for an investor CHP production is advantageous in comparison to heat-only boilers only if the price of electricity is sufficient to justify the additional investment. Currently the electricity markets in Northern Europe are at a period of change, where uncertainty over renewable

power subsidies, emission trading, and the future of nuclear power create serious doubts about the future price of electricity. As a result, investment in CHP production has become increasingly uncertain, and optimal plant design more difficult.

Some of the characteristics of untreated wood biomass also pose limits to its use. In storage, wood tends to collect moisture and degrade. It has low energy density per volume and mass, which means that the distance between harvesting and combustion cannot be long, or the logistics will become uneconomical, and the GHG emissions will increase as well. Finally, untreated wood poses limitations on combustion technology: for example, the existing pulverized coal boilers cannot typically fire large amounts of untreated wood.

Torrefaction and hydrothermal carbonization are technologies for improving the quality of solid biomass. In Figure 1.1, they fall under the category of thermochemical conversion and therein, carbonization. Compared to untreated wood, the resulting biochars have higher energy density, hydrophobic behaviour in the presence of moisture, and in both chip and pellet form they are brittle enough for co-firing with fossil coal in pulverized coal boilers. From GHG emission mitigation point of view, such conversion technologies can assist in replacing fossil fuel use with bioenergy.

1.2 Objectives

The goal of this thesis was to investigate Nordic CHP plant design and optimization from different aspects for the purpose of identifying ways to improve profitability and energy effectiveness in today's uncertain environment. There are two separate focus areas; process integration of thermochemical biomass conversion and Scandinavian CHP plant, and condenser design and optimization. The following research questions were posed:

Q1 How are CHP plant operation and economics affected by integration with a biomass conversion process other than combustion?

Q2 What are the best ways of integrating biomass conversion processes with co-generation plants?

Q3 Can integration with a biomass conversion process serve as a buffer against uncertain electricity prices in Nordic co-generation plants?

Q4 What biochar price levels are required for mild pyrolysis of wood biomass to be profitable?

Q5 How is the optimal district heat condenser design affected by varying equipment and electricity costs?

Q6 What lessons can be learned from the practical solving process of these problems?

1.3 Methods

In broad terms, the goal of the study was to find the best integrated CHP and thermochemical conversion plant configurations and condenser designs, and find the significant conclusions from the results. Optimization is defined as the search of the best possible solution to a problem. In mathematical terms this often means searching for an extreme value (maximum or minimum) of an objective function. Within an energy system, different levels of design and optimization can be defined. Frangopoulos (2002) identifies three levels of energy system optimization for a given scope:

A) Synthesis optimization: selecting the set of components and their connections
B) Design optimization: selecting the component specifications and process fluids
C) Operation optimization: finding the best way to operate a defined system at specified conditions.

Among the levels of optimization, synthesis optimization is particularly challenging. Traditionally it is a step where optimization methods in the mathematical meaning of the word have been little used for a number of reasons. First, combining a robust model to an efficient search algorithm to allow for thorough and efficient search of optimal configuration is extremely challenging, and second, it is often difficult to define "best" in a clear, unambiguous way that would yield itself to an automated mathematical optimization process. As a result, synthesis optimization still largely depends on engineers' knowledge, experience and creativity to design a system that is suitable and reasonably well performing for the intended purposes, and which can then be improved and optimized in the design optimization process.

The usefulness of an automated process that could find an optimal system configuration is clear, and indeed such techniques have been developed and used successfully for certain specific energy system synthesis optimization problems. In practice, such methods are still difficult to implement, are often restrictive, and lack robustness.

Within this thesis, research questions Q1 to Q4 can be considered to be part of the synthesis optimization of an integrated CHP – thermochemical conversion plant and analysing the results of the process, while question Q5 concerns the design optimization of a single component, the district heat condenser. The CHP plant considered in both the integration and condenser optimization studies was a small backpressure plant with nominal rating of 8 MW power and 20 MW district heat at full load. Seven scientific publications analysing different technical and economic aspects of the topics were drafted during the research. Figure 1.2 summarizes the contents of these publications, how they relate to different aspects of the research, and the main contributions of the earlier publications to the following ones.

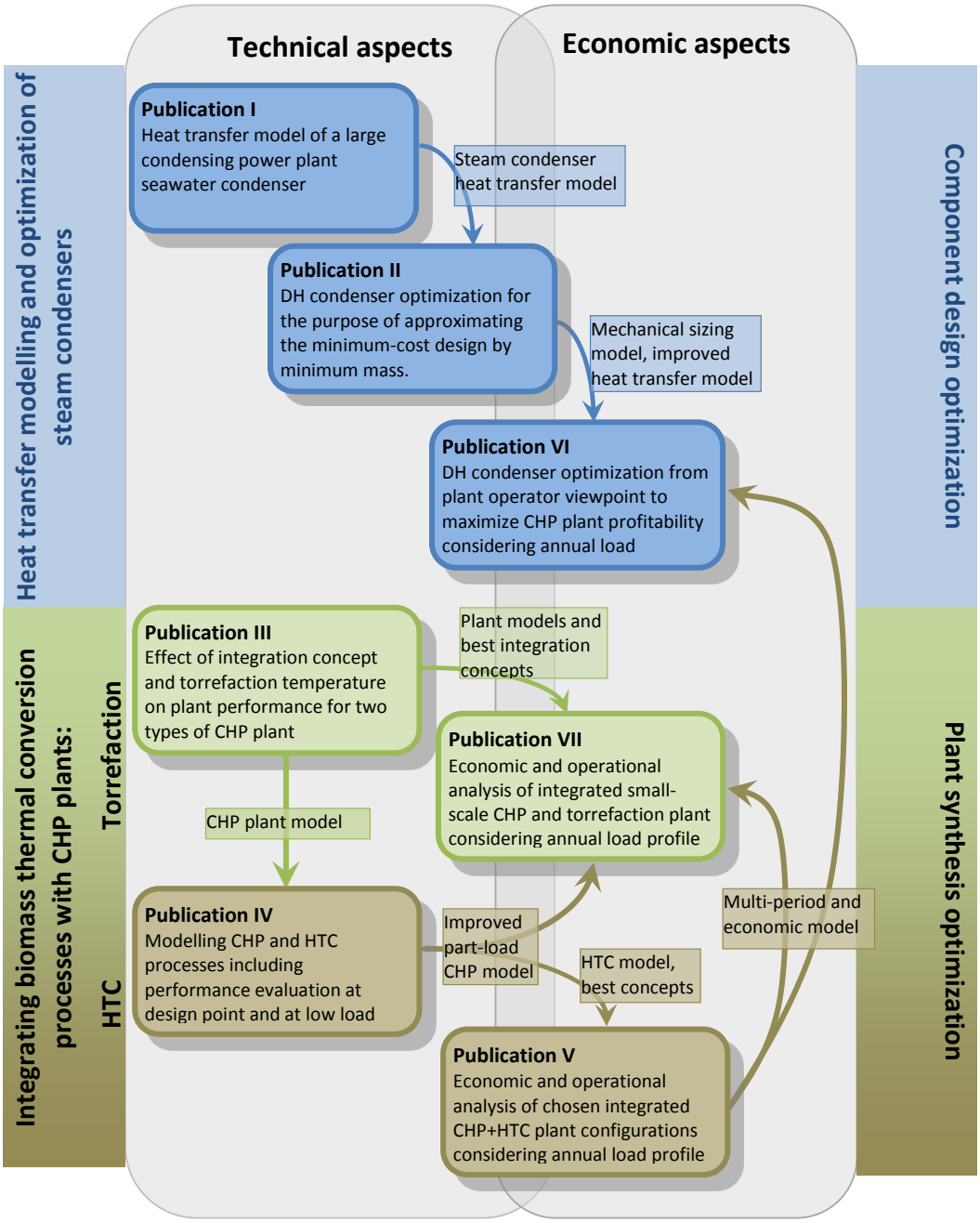

Figure 1.2: An overview of the appended papers.

The first step of the process of analysing the systems and components and finding the best plant configurations or components designs was modelling the systems. **Publication I** presented the heat transfer model of a large seawater-cooled vacuum condenser and the validation of the model against measured plant data. **Publication II** and **Publication VI** adapted the model for district heat condenser optimization, as well as implemented the heat exchanger mechanical sizing algorithm and cost model. All heat exchanger modelling was performed in MATLAB environment.

The CHP plant model was developed with a commercial process simulation software IPSEpro. The initial model, together with the torrefaction process model, was published in **Publication III**, where an initial technical analysis of promising integration concepts and evaluation of suitable process values was performed. The torrefaction model was based on published data on the torrefaction of various Nordic forest biomasses at different process conditions. A simple mathematical model was developed and used to create the necessary component modules for use in the process simulation software.

In **Publication IV**, the CHP plant model and particularly the part-load modelling were developed further, and the HTC process model and the required component modules were implemented. The modelling of the thermochemical process of hydrothermal carbonization was based on experimental results published earlier in Sermyagina *et al.* (2015).

After the initial steps for finding the best plant synthesis for process integration were taken in **Publication III** and **Publication IV**, the final economic plant synthesis optimization was performed in **Publication V** (HTC) and **Publication VII** (torrefaction) in order to answer research questions Q1 to Q4. In the scope of this work, an automated plant synthesis optimization system for integrated CHP – biomass treatment processes was considered infeasible, and not attempted. A discretized multi-period model was developed to account for annual variations of load and operating conditions, and the results were analysed to find the economically most profitable configurations. Sensitivity analysis was performed for answering research question Q3.

Publication VI aimed at answering the research question Q5. The results from a multi-period model first used in **Publication V** were combined, with minor adaptations, with the heat transfer model developed earlier to obtain a mathematical representation of the economic profitability of the plant as a function of condenser configuration. This model was then used in combination with a metaheuristic optimization algorithm.

1.4 Outline of the thesis

Chapter 2 presents a description of the backpressure CHP plant considered in this thesis. The design-point and part-load modelling of the main boiler and steam cycle components is described, as well as the constraints likely to limit the plant operation at minimum and maximum load, or when another process is integrated to the plant. The annual district heat

load profile, and the multi-period approximation of the plant annual operation is also presented in this chapter.

Chapter 3 presents the thermochemical biomass conversion modelling. The mathematical models of the drying, heating, conversion and cooling processes, as well as the mass and energy yields as functions of operating parameters are described. Configurations of the stand-alone carbonization plants and the relevant component models are also covered in this chapter.

The technical studies of integration of both thermochemical conversion processes to the CHP plant are described in Chapter 4. For both processes, the results of the initial technical analysis at one or a small number of operating points are presented. The impact of carbonization temperature is also evaluated. On the basis of the initial technical studies, the most promising cases are selected for more detailed study. These cases are analysed in more detail by using the multi-period model described in Chapter 2. The results are used to obtain data on how each of the integrated plant configurations affect the CHP plant operation, and to find the total annual fuel and feedstock consumptions, and the amounts of heat, power and biochar produced. Chapter 5 presents the economic analysis of those cases that were chosen for detailed operational and annual net production and consumption analysis in Chapter 4.

Chapter 6 presents the condenser heat transfer modelling. After starting with the initial heat transfer model of the large condensing power plant sea water condenser, the validation and analysis of the necessary level of modelling detail, the chapter continues to describe how this model was adapted for a district heat condenser model to be used in optimization, which is then described in Chapter 7. The mechanical sizing and cost model of the condenser is described, followed by the optimization algorithms used, and the implementation of the objective function and the optimization.

Finally, chapter 8 summarizes the main findings of the thesis. The answers found to the research questions are presented here. In some cases also some significant limitations imposed by the assumptions applied in the work were found, and these are also explained. The thesis concludes with a description of some of the main issues still requiring further work.

2 CHP plant and multi-period model

A small modular biomass-fired backpressure plant with a 29 MW thermal output bubbling fluidized bed (BFB) boiler based on the one described by Komulainen (2012) is considered in this study. At design point conditions the plant has a net output of 20 MW district heat and 8 MW electricity. The turbine has a partial admission regulating stage and separate high-pressure (HP) and low-pressure (LP) parts with an extraction at the HP exhaust, controlled by the LP turbine inlet valve. The design point extraction pressure is 8.5 bar. There is a single backpressure DH condenser.

The schematic diagram of the CHP plant is shown in Figure 2.1; the design point operating parameters and ambient conditions are summarized in Table 2.1. IPSEpro process simulation software has been used to model the CHP process. The model was developed initially for Publication III and later improved for Publication IV. This chapter describes the final model of Publication IV, which was also used in publications V, VI and VII to obtain the main results of the thesis.

To consider the annual variation of the DH load, ambient conditions and fuel properties, a multi-period model was implemented. Off-design models of the main components were developed to evaluate the performance of the plant at varying loads and ambient conditions. The multi-period model is presented in chapter 2.1, followed by a description of the design-point and off-design modelling of the boiler in chapter 2.2, and the steam cycle in chapter 2.3.

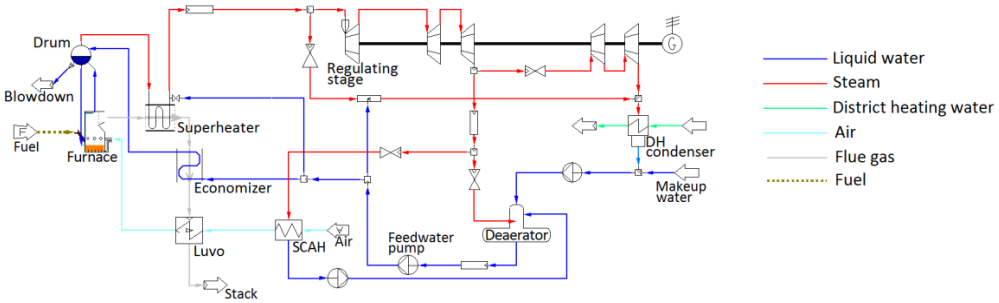

Figure 2.1: Schematic diagram of the CHP plant model.

2.1 Multi-period model

A district heat load duration curve was approximated by a peak load of 35 MW, 20 MW heat load at 1800 hours, linear reduction to 2.6 MW at 7890 hours, and finally steady 2.6 MW load for the remaining summer hours. This was represented by two full-load periods, P1 and P2, followed by a steadily reducing DH load at 4 MW intervals (P3 to P6) until the summer period, which was split to a low-load P7 and minimum-load P8.

The moisture of the wood chips was assumed to increase towards winter. The temperature of the boiler fuel and HTC feedstock was set at the average ambient temperature of each

period. The combustion air temperature, taken from the boiler room, was assumed to be 20 °C higher than the ambient temperature. The ambient temperatures were based on 30-year monthly average temperatures gathered by the Finnish Meteorological Institute (Finnish Meteorological Institute, 2015) for Jyväskylä, a city in central Finland. The DH water output and return temperatures were based on ambient temperature according to Koskelainen *et al.* (2006). The data for fuel properties and temperature levels for each period are listed in Table 2.2; load curve approximation and multiperiod approximation of heat and power production are plotted on Figure 2.2.

Table 2.1: Main characteristics of the CHP plant at the design point.

Category	Parameter	Quantity
Fuel and ambient conditions	Wet-basis fuel moisture *MC*	50%
	Fuel LHV, moist fuel / dry matter	8.53 / 19.5 MJ/kg
	Ambient temperature	0 °C
Boiler	Fuel input (LHV)	32.6 MW
	Net thermal power	28.9 MW
	Live steam parameters	92 bar / 505 °C
	Boiler efficiency η_b	87.7 %
Turbine	Inlet steam parameters	90 bar / 500 °C
	Regulating stage isentropic efficiency $\eta_{s,R}$	0.70 *
	HP turbine isentropic efficiency $\eta_{s,HP}$	0.887
	LP turbine isentropic efficiency $\eta_{s,LP}$	0.833
	Extraction pressure	8.6 bar
Condenser	Back pressure	0.80 bar
	DH water output/return temperature	90/50 °C
Deaerator	Pressure	5.6 bar
Generator	Gross electric power	8.66 MW
CHP plant parameters	Net electric power	8.00 MW
	District heat (DH) power	20.00 MW
	Electrical efficiency η_{el}	24.0 %
	Total CHP efficiency η_{tot}	86.0 %

* Valves wide open

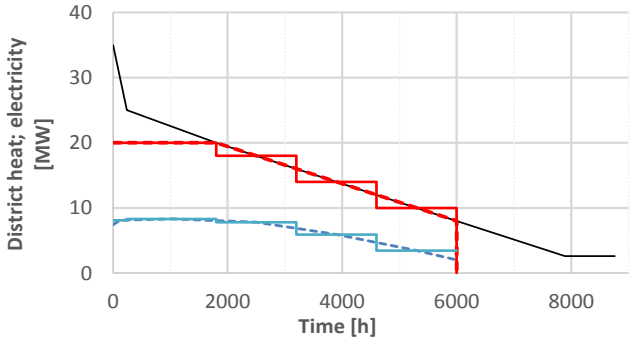

Figure 2.2: Annual district heat load variation (black) and production of district heat (red) and electricity (blue) in the CHP plant.

Table 2.2: Summary of the load points and their durations during a year in multi-period approximation of annual plant operation.

Parameter	**P0**	**P1**	**P2**	**P3**	**P4**	**P5**	**P6**	**P7**	**P8**
Time									
period duration [h]	0	240	1560	1400	1400	1400	1400	490	870
cumulative at end [h]	0	240	1800	3200	4600	6000	7400	7890	8760
Load and production									
mean heat load [MW]	35	30	22.5	18	14	10	6	4	2.6
CHP heat output [MW]	20	20	20	18	14	10	6	0	0
Temperatures									
ambient [°C]	-20	-10	-5	0	5	10	12	15	15
makeup water [°C]	5	5	5	5	10	10	10	10	10
DH water out [°C]	105	90	85	80	75	75	75	75	75
DH water return [°C]	60	50	50	50	45	45	45	45	45
Fuel									
moisture [$m_{H2O}/m_{dry+H2O}$]	0.55	0.55	0.55	0.50	0.50	0.45	0.45	0.40	0.40
temperature [°C]	-20	-10	-5	0	5	10	12	15	15
LHV [MJ/kg]	7.43	7.43	7.43	8.53	8.53	9.62	9.62	10.72	10.72

2.2 **Boiler**

The boiler model consists of furnace, superheater and economizer components, and an IPSEpro standard library heat exchanger representing the air preheater (luvo). A steam coil air heater (SCAH) is available as well.

The furnace module determines all boiler losses except the stack loss. The losses at the design point are stack loss Φ_{stack} = 2.5 MW (T_{stack} = 150 °C); radiation loss Φ_{rad} = 0.1 MW; blowdown loss at 1% of feedwater flow Φ_{bd} = 0.1 MW; ash heat loss Φ_{ash} = 0.02 MW; unburnt loss Φ_{ub} = 0.2 MW; and other losses 1% of fuel power, Φ_{other} = 0.3 MW. These yield a design-point boiler efficiency of η_b = 0.88, defined as

$$\eta_b = \frac{\dot{m}_{LS} h_{LS} - \dot{m}_{FW} h_{FW}}{\dot{m}_f \left(h_f + LHV_f\right) + \dot{m}_a h_a} \tag{2.1}$$

where subscripts LS, FW, f and a refer to live steam, feedwater, fuel and air.

The radiation and conduction losses $\Phi_{loss,rad}$ [kW] were assumed constant, and estimated from net output at maximum continuous rating $\Phi_{b,MCR}$ (European Committee for Standardisation, 2003),

$$\Phi_{rad} = 0.0315\ \Phi_{b,MCR}{}^{0.7}. \tag{2.2}$$

Ash losses Φ_{ash} consist of the sensible heat lost with ash removal as bottom ash at bed temperature T_{bed}, and fly ash from the filters at stack temperature T_{stack} :

$$\Phi_{\text{ash}} = \dot{m}_{\text{ash,tot}} c_{\text{p,ash}} \left[R_{\text{ash,b}} \left(T_{\text{bed}} - 0°\text{C} \right) + \left(1 - R_{\text{ash,b}} \right) \left(T_{\text{stack}} - 0°\text{C} \right) \right] , \tag{2.3}$$

where $\dot{m}_{\text{ash,tot}}$ is the total ash flow rate including unburnt carbon, $R_{\text{ash,b}}$ is the fraction of ash removal that is taken as bottom ash, estimated at $R_{\text{ash,b}}$ = 0.75, and $c_{\text{p,ash}}$ is the ash specific heat, $c_{\text{p,ash}}$ = 1.1 kJ/kgK. The unburnt carbon fraction in ash increases with reducing boiler load and bed temperature. The unburnt loss Φ_{ub} is obtained from

$$\Phi_{\text{ub}} = R_{\text{ash,C}} \, \dot{m}_{\text{ash,tot}} \, LHV_{\text{C}} , \tag{2.4}$$

where $R_{\text{ash,C}}$ is the mass fraction of carbon in removed ash and LHV_{C} the lower heating value of carbon, LHV_{C} = 32 MJ/kg. $R_{\text{ash,C}}$ is assumed to increase linearly as a function of bed temperature from 0.25 at design point to 0.50 at minimum load, T_{bed} = 700 °C.

Blowdown loss Φ_{bd} is obtained by assuming that 1% of feedwater flow is removed at saturated liquid state at drum pressure at all loads. Finally, other unaccounted losses are assumed to amount to one percent of fuel LHV input.

Combustion in the furnace at the design point takes place with an excess air ratio of λ_{D} = 1.2, increasing to λ_{min} = 1.35 at minimum load. The bed temperature is assumed to be T_{bed} = 900 °C at the design point, and 700 °C at minimum load.

The design-point performance of heat transfer surfaces is summarized in Table 2.3 below. At part load, the heat transfer surface operating parameters change. The furnace is modelled as isothermal, with steam generator thermal power Φ_{SG} varying relative to fourth power of the furnace temperature T_{furn} [K],

$$\Phi_{\text{SG,OD}} = \Phi_{\text{SG,D}} \frac{T_{\text{fum,OD}}{}^4}{T_{\text{fum,D}}{}^4} , \tag{2.5}$$

where subscripts D and OD refer to design and off-design values.

Table 2.3: BFB boiler heat transfer surfaces.

Surface	Steam generator	Superheater	Economizer	Luvo	SCAH
Conductance *G*	n/a	28.5 kW/K	30 kW/K	32 kW/K	1.9 kW/K
Flue gas $T_{\text{in}}/T_{\text{out}}$	-/905 °C	905/560 °C	560/290 °C	290/150 °C	n/a
Cold fluid $T_{\text{in}}/T_{\text{out}}$	310/310 °C	310/590 °C	157/285 °C	35/235 °C	n/a

The convection-dominated surfaces (superheater, economizer and luvo) are modelled as counterflow heat exchangers. Radiation effects are assumed to be minor and not considered. The heat transfer rates Φ [kW] are obtained from

$$\Phi = G\,\Delta T_{\mathrm{lm}}\,, \tag{2.6}$$

where G [kW/K] is the product of the heat transfer area A [m^2] and overall heat transfer coefficient U [kW/m^{2}K].

Off-design conductances are found by assuming small fouling and wall resistances, and small transport property changes. The convection heat transfer coefficient is proportional to 0.8:th power of mass flux in the tube and, approximately, also outside of it in high Reynolds number cross flow across tube banks according to correlations by Dittus and Bölter (1930) as referred by Winterton (1998) and Zukauskas (1987) as referred by Incropera and DeWitt (2002). As the water, steam and air flow rates also change roughly in proportion to the flue gas flow rate change, the off-design conductance G_{OD} is approximated by

$$G_{\mathrm{OD}} = G_{\mathrm{D}}\left(\frac{\dot{m}_{\mathrm{FG,OD}}}{\dot{m}_{\mathrm{FG,D}}}\right)^{0.8}. \tag{2.7}$$

2.3 Steam cycle

2.3.1 Turbine

Isentropic efficiency η_{s} = 0.88 is assumed for the turbine modules at the optimum flow rate. The efficiency change due to flow rate change is modelled as a function of mass flow relative to the optimum flow with polynomial fits based on Tveit *et al*. (2005) for the regulating stage, Equation (2.8), and Jüdes *et al*. (2009) for the working stages, Equation (2.9) (see Figure 2.3). Optimum efficiency is assumed at 10 kg/s in the HP turbine and regulating stage, and 9 kg/s for the LP turbine. The swallowing capacity of the turbine is typically slightly higher than the design point flow.

$$\eta_{\mathrm{s}} = -2.4\left(\frac{\dot{m}_{\mathrm{OD}}}{\dot{m}_{\mathrm{D}}}\right)^2 + 4.2\frac{\dot{m}_{\mathrm{OD}}}{\dot{m}_{\mathrm{D}}} - 1.1, \tag{2.8}$$

$$\frac{\eta_{\mathrm{s}}}{\eta_{\mathrm{s,opt}}} = -1.0176\left(\frac{\dot{m}}{\dot{m}_{\mathrm{opt}}}\right)^4 + 2.4443\left(\frac{\dot{m}}{\dot{m}_{\mathrm{opt}}}\right)^3 - 2.1812\left(\frac{\dot{m}}{\dot{m}_{\mathrm{opt}}}\right)^2 + 1.0535\left(\frac{\dot{m}}{\dot{m}_{\mathrm{opt}}}\right) + 0.701 \tag{2.9}$$

Moisture droplets in the steam reduces turbine efficiency; a reduction of 0.8 % to 1.2 % of efficiency per every 1 % average stage moisture content has been reported (Sanders, 2004). In the presence of moisture the final isentropic efficiency of a multi-stage turbine component is estimated from the dry efficiency η_{s} obtained from Equation (2.9) by

$$\eta_{\mathrm{s,x\text{-}corr}} = \eta_{\mathrm{s}} - \frac{1 - x_{\mathrm{o}}}{2}. \tag{2.10}$$

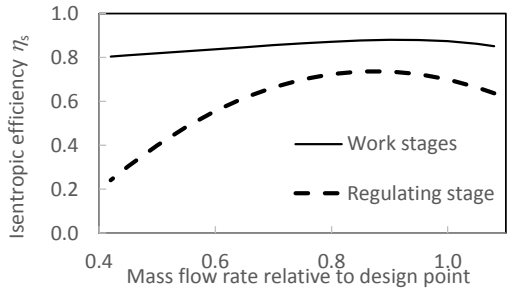

Figure 2.3: Isentropic efficiency of turbines as a function of mass flow rate.

The changing mass flow rate changes also pressures; these are bound by the ellipse law (Traupel, 1966), simplified here by assuming a constant intake ratio μ and $n \approx 1$ for steam, and combining the design-point values to a turbine constant K [m^2]:

$$\frac{\dot{m}_{OD}}{\dot{m}_D} = \frac{\mu_{OD}}{\mu_D} \frac{p_{in,OD}}{p_{in,D}} \sqrt{\frac{(pv)_{in,D}}{(pv)_{in,OD}}} \sqrt{\frac{1-\left(p_{out,OD} / p_{in,OD}\right)^{\frac{n+1}{n}}}{1-\left(p_{out,D} / p_{in,D}\right)^{\frac{n+1}{n}}}} \tag{2.11}$$

$$\Rightarrow \dot{m}_{OD} = K \frac{\sqrt{p_{in,OD}^{\ 2} - p_{out,OD}^{\ 2}}}{\sqrt{(pv)_{in,OD}}}$$

2.3.2 Condenser

District heat is produced in a single-stage shell-and-tube condenser. In thermal conversion integration studies, where the condenser design was fixed and not subject to optimization, a condenser with 400 m^2 effective heat transfer area was assumed. Design-point parameters were set at a district heat output of Φ_{DH} = 20 MW, and DH water output/return temperatures of 90/50 °C. The overall heat transfer coefficient was assumed $U_{DHC,D}$ = 3400 W/m^{2}K and steam-side Δp_h = 0.02 bar. These yield a terminal temperature difference TTD = 3.5 °C and steam pressure p_h = 0.80 bar.

The condenser module in the CHP plant model was designed to estimate off-design performance by using the ε-NTU method. The heat transfer coefficient $U_{DHC,OD}$ was approximated from steam pressure p_h, district heating water mass flow rate $\dot{m}_c$ [kg/s], and mean temperature and T_c [°C].

At the design point, the thermal resistances are assumed to split at a ratio of 35 % tube inside convection, 25 % tube outside condensation and 40 % conduction, where conduction includes both the tube wall resistance and the fouling resistances. At part load, the convection and condensation resistances will change. The resistance changes are estimated by using a correlation presented by Eagle and Ferguson (1930) as referred by

Sinnott (2005) for convection, and on an adaptation from a graph in Holmström (1982) for condensation. Combined, this results in Equation (2.12) for the off-design heat transfer coefficient $U_{\mathrm{DHC,OD}}$:

$$U_{\mathrm{DHC,OD}} = U_{\mathrm{DHC,D}} \cdot \left[0.35 \left(\frac{\dot{m}_{\mathrm{c,D}}}{\dot{m}_{\mathrm{c}}} \right)^{0.8} \left(\frac{T_{\mathrm{c,D}}}{T_{\mathrm{c}}} \right)^{0.5} + 0.25 \left(\frac{p_{\mathrm{h,D}}}{p_{\mathrm{h}}} \right)^{0.064} + 0.4 \right]^{-1} \tag{2.12}$$

The steam-side pressure drop is assumed to change proportionally to the dynamic pressure $½\rho w^2$:

$$\Delta p_{\mathrm{h,OD}} = \Delta p_{\mathrm{h,D}} \frac{v_{\mathrm{h,D}}}{v_{\mathrm{h,OD}}} \left(\frac{\dot{m}_{\mathrm{h,OD}} v_{\mathrm{h,OD}}}{\dot{m}_{\mathrm{h,D}} v_{\mathrm{h,D}}} \right)^2 . \tag{2.13}$$

3 Low-temperature biomass thermochemical conversion

This chapter describes the two biomass thermochemical conversion processes, torrefaction and hydrothermal carbonization (HTC). The focus is on the description of the thermochemical processes themselves and their modelling for the purpose of plant and integration modelling. The necessary component models and also the modelling of the stand-alone torrefaction and HTC plants are described. Integration modelling is described in chapter 4.

3.1 Background

Torrefaction and hydrothermal carbonization (HTC) are both mild thermochemical processes taking place at relatively low temperatures. The biochar products, torrefied biochar and hydrochar, have higher carbon content and heating value than the feedstock. The oxygen content is reduced. Compared to untreated biomass, both biochars are hydrophobic, brittle, and easier to store due to their higher energy densities and reduced tendency to decay. The significant difference between the processes is that in torrefaction the reactions take place at approximately atmospheric pressure in an inert gas, while in HTC the feedstock is in a pressurized water slurry, typically at saturated state.

Both processes consist of a number of simultaneous and consecutive chemical reactions (Bergman *et al*., 2005; Kruse *et al*., 2013). Detailed modelling of these was considered to be beyond the scope of this work; rather the goal was to develop a relatively simple model that could be implemented as part of a component model in a process simulation software to provide a reasonable estimate of mass and energy yields for the purpose of plant-level modelling and economic analysis.

The main components of wood are three polymeric structures: hemicellulose, cellulose and lignin, of which hemicellulose is affected most by both torrefaction and HTC. The reactions taking place in the two processes have similarities, but the presence of water in HTC results in some important differences in the decomposition, and the behaviour of the products as well (Funke & Ziegler, 2010; Libra *et al*., 2011; Bach & Skreiberg, 2016). Most importantly, the wood components, particularly hemicellulose and cellulose, become significantly less stable in the presence of hot liquid water. This makes it possible to use clearly lower temperature ranges in HTC.

In dry torrefaction the temperature levels are typically in the range of 200…300 ºC. Bergman *et al*. (2005) report that under 250 °C only hemicellulose undergoes limited devolatilization, while cellulose and lignin are practically unaffected; at higher temperatures, the decomposition of hemicellulose becomes extensive, and to a lesser extent also lignin and cellulose are affected. This is supported by the thermogravimetric analysis by Chen & Kuo (2010). In HTC the presence of water means that the decomposition of hemicellulose begins already at 180 °C (Yan *et al*., 2009). According to Bobleter (1994) as referred by Bach and Skreiberg (2016), also the decomposition of

cellulose begins already at 200 °C, and becomes extensive at 250 °C. Only lignin remains relatively stable up to 250 °C (Li *et al*., 2007). As a result, in HTC, temperatures of 180…260 °C are sufficient to achieve significant carbonization.

As the reactions of the two processes are somewhat similar, so are the reaction products, but their behaviours differ due to the presence of water in HTC. Dry torrefaction produces a gas-phase mixture consisting of significant fractions of water vapour and carbon dioxide, some carbon monoxide, and various organic compounds of mostly low to moderate heating value. Hydrogen and methane are present only in trace amounts. The organic compounds include organic acids, furfurals and phenols (Prins *et al*., 2006b). Similar products are reported for hydrothermal carbonization by Hoekman *et al*. (2011) and (2013), but as the process takes place in liquid water, the organic compounds remain dissolved in the water phase rather than being removed with the reactor off-gas.

The water in hydrothermal carbonization dissolves not only the water-soluble light organic products: it has been reported that also much of the inorganic elements are dissolved and removed from the solid product, reducing the amount of alkalis and chlorine, as well as other inorganic compounds in biomass (Reza *et al*., 2013). In dry torrefaction these remain mostly in the solid biochar, where their mass fractions increase due to the decomposition and removal of some of the organic polymeric components.

Alkalis and chlorine cause erosion, corrosion and slagging in boilers, which limits the fraction of fossil coal that torrefied biochar can replace in pulverized coal boilers (Koppejan *et al.*, 2012; Kludze *et al.*, 2013). The mechanical properties of hydrochar pellets have also been found to be superior to dry-torrefied pellets in being more hydrophobic and resistant to breaking up when immersed in water, mechanically more durable, and having a higher energy density. (Kambo & Dutta, 2014)

In addition to the treatment of wood chips, which is the topic of this thesis, both processes lend themselves to the conversion of non-woody biomasses as well. Dry torrefaction of herbaceous plants and various agricultural residues has been proposed in several studies (Bridgeman *et al.*, 2008; Deng *et al.*, 2009; Patel *et al.*, 2011). Similarly the hydrothermal carbonization of various biomass residues such as weed plants (Gao *et al.*, 2013), corn husk (Minaret & Dutta, 2016), and bark (Gao *et al.*, 2016) have been investigated. An advantage of hydrothermal carbonization in terms of possible feedstocks is the ability to use biological waste streams having very high moisture contents, such as municipal or industrial sludges (Ramke *et al.*, 2009; Alatalo *et al.*, 2013): the moisture content is no disadvantage in a process where the feed is mixed with water to form a slurry in any case. Within the scope of this work, only the carbonization of Nordic forest wood is considered.

3.2 Torrefaction model

A model to predict the product yields and energy inputs and outputs was first developed on the basis of existing, published experimental data. This was then implemented in IPSEpro simulation software. IPSEpro includes a Module Development Kit (MDK) for

creating new component models, and was thus considered particularly suitable for modelling a process requiring a number of special modules not available in typical process simulation software packages.

3.2.1 Plant configuration

The torrefaction equipment considered consists of three parts: a dryer, a torrefaction reactor, and a cooler for the solid product. When torrefaction is operated as a stand-alone process, an additional boiler is used for heat supply, where also the gas-phase torrefaction product is combusted. In Publication III, which focused on the pure thermodynamic performance of different plant and integration configurations, the boiler type and its fuel were not considered, and the torrefaction temperature varied from 200 °C to 300 °C. In Publication VII, focusing on the economics and operation of integrated torrefaction and CHP plants, a 250 °C torrefaction temperature was considered. For the stand-alone plant it was assumed that a small grate-fired boiler supplying superheated steam for indirect torrefaction reactor heating would be utilized. Steam was selected over flue gas for being a safer option and less of a fire hazard in operation than the considerably hotter flue gases.

Figure 3.1 shows a schematic diagram of the IPSEpro model of the stand-alone process model with the chip-fired stoker boiler. The separate combustor for the torrefaction gas is used for modelling convenience, not reflecting the actual plant configuration where the gas could be simply fed to the boiler furnace for combustion.

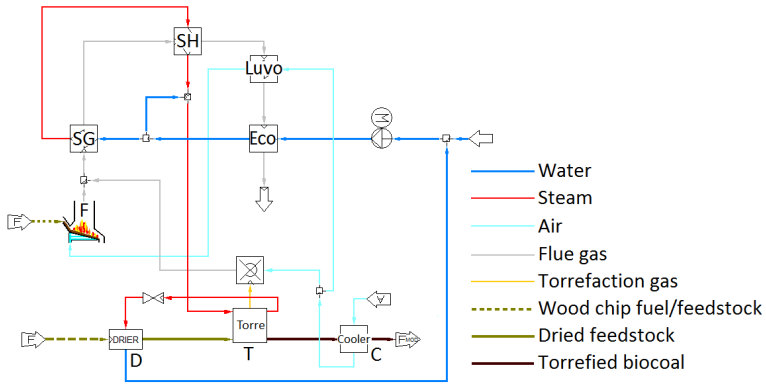

Figure 3.1: Torrefaction process with a wood-fired stoker boiler for heat supply. Components: D dryer, T torrefaction reactor, C solid product cooler, F furnace, SG steam generator, SH superheater, Luvo air preheater, Eco economizer.

Before torrefaction, the feedstock is typically dried to a moisture content of approximately 10% (Bergman, *et al.*, 2005; Kohl *et al.*, 2013). The dryer consumes most of the heat required by the torrefaction process. The dryer type is not specified in the model, but a belt dryer would permit flexibility in selecting the heat source and allow the use of fairly low-temperature sources (Arpiainen & Wilen, 2013). A specific heat consumption of 1.2

kWh/$kg_{H2Oevap}$, considered to represent a typical or conservative estimate for belt dryer heat consumption (Arpiainen & Wilen, 2013; Fagernäs *et al.*, 2010), is assumed. Heat can be supplied for the dryer by flue gas, hot water, or low-pressure steam.

From the dried biomass storage, the biomass feed is assumed to enter the torrefaction reactor at a temperature of 60 °C and moisture of 10%. Indirect heating of the reactor is assumed. The gas-phase products are sent to incineration in the boiler, while the solid product is cooled. The cooler is assumed to be an indirect cooler. The heat is recovered to the furnace combustion air, with 80 °C solid product outlet temperature assumed.

3.2.2 Torrefaction products

Of the three main components of wood, mainly hemicellulose is affected by torrefaction. Above 250 °C, the decomposition of hemicellulose becomes extensive, and also lignin and cellulose start to be affected (Bergman & Kiel, 2005). Mass loss increases with time, but based on experiments with willow, beech and spruce, the rate of mass loss slows down considerably after the first 20 to 30 minutes (Prins *et al.*, 2006a; Repellin *et al.*, 2010).

The torrefaction model used in this study is based on the assumption that the sum of the available energy of feedstock dry matter and the heat of reaction is divided between the available heats of the gaseous and solid products:

$$\dot{m}_{\mathrm{d}}\left(LHV_{\mathrm{d}} + h_{\mathrm{react}}\right) = \dot{m}_{\mathrm{g}} LHV_{\mathrm{g}} + \dot{m}_{\mathrm{bc}} LHV_{\mathrm{bc}}\,, \tag{3.1}$$

where h_{react} [kJ/kg] is the heat of reaction; $\dot{m}_{\mathrm{d}}$, $\dot{m}_{\mathrm{g}}$ and $\dot{m}_{\mathrm{bc}}$ [kg/s] are the mass flow rates of the feedstock dry matter, torrefaction gas and torrefied biochar, and LHV_{d}, LHV_{g} and LHV_{bc} [MJ/kg] are the respective lower heating values.

The solid product mass yield, torrefaction gas heating value, and heat of reaction have been estimated on the basis of published experimental results. The heating value of the solid product is then solved using Equation (3.1). This approach is used because the heating value of the gas, being roughly an order of magnitude less than that of the solid product, would otherwise be subject to potentially very large relative errors from comparatively uncertain solid product LHV estimates.

The available data on the parameters of interest – mass yield, gaseous product heating value, and solid product heating value – suffers from being somewhat limited, as well as dispersed among references using different assumptions, measurement approaches, and experimental parameters. All publicly available data is also from laboratory-scale equipment.

Although varying feedstock quality would affect the reaction kinetics in case of industrial-scale operation, the effect of particle size and shape and impurities is less than the effects of temperature and residence time (Medic *et al.*, 2012). While larger particles react slower, with sufficient reaction time these differences in behaviour become less

pronounced (Basu *et al.*, 2014; Medic *et al.*, 2012). For this reason, and in the absence of public data from industrial-scale equipment, the model used in this work for solid-product mass and energy yields is based on two references, Pach *et al.* (2002) and Phanphanich & Mani (2011), both reporting laboratory-scale results for typical Nordic forest biomasses.

The mass yield M [-], or the ratio of dry solid product to feedstock dry fraction, was determined from

$$M = \frac{\dot{m}_{\mathrm{bc}}}{\dot{m}_{\mathrm{d}}} = 1 - a\left(T_{\mathrm{torr}} - T_{\mathrm{ini}}\right)^{\mathrm{b}}, \tag{3.2}$$

where constants a = 4.47·10^{-4}, b = 1.46 and temperature T_{ini} = 190 °C are obtained by minimizing the residual sums of squares. The resulting curve and the initial data on which it was based are shown in Figure 3.2.

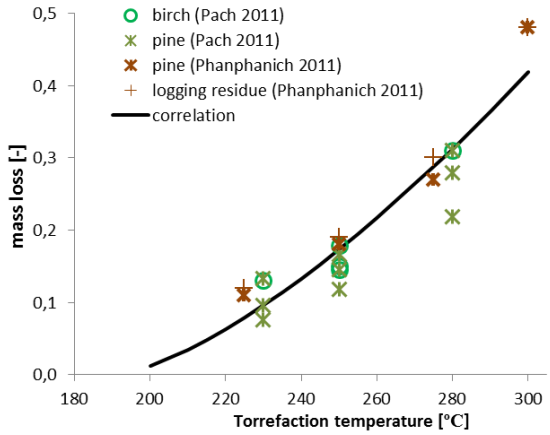

Figure 3.2: Mass loss as a function of torrefaction temperature. The correlation curve represents (1-M), where M is the mass loss obtained from Equation (3.2).

A difference in the torrefaction time – 30 minutes in Phanphanich and Mani (2011) and 1 to 3 hours in (Pach *et al.*, 2002) – appears to have little effect. This can be explained by the significant slowing of the mass loss rate after the first 20–30 minutes. Logging residues appear slightly more reactive than wood, possibly due to the higher ash content and thus an increased presence of catalytic components. Overall, the correlation appears to approximate the mass yield of Scandinavian forest biomasses adequately at residence times of over 30 minutes and varying temperatures.

Experimental results for the gas-phase torrefaction products are even more sparse. The model developed here is based on the results for gaseous products from willow and larch torrefaction (Prins *et al.*, 2006b; Prins, 2005). In the absence of better data, these results

are used despite two significant problems. Firstly, the mass balances were not closed in either reference; the unknown fate of the missing mass leaves a significant uncertainty for the comparatively small mass fraction in the gas phase. Secondly, the results consider only true gas-phase components, but in industrial equipment also some solids and tar are likely to be transported out of the reactor as dust and droplets with the gas stream. In the absence of more accurate information, these results had to be used nonetheless, yielding the following correlation for the gaseous product lower heating value LHV_g:

$$LHV_g = 2.00 + 5.28 \cdot 10^{-5} \cdot (T_{torr} - 190\ °C)^{2.49} \quad (3.3)$$

The correlation curve is plotted together with the data from Prins (2005) and Prins *et al.* (2006b) in Figure 3.3. Due to the limitations in the material library of the IPSEpro software, this gas flow was simulated as such a mixture of carbon dioxide and methane that yields the correct lower heating value.

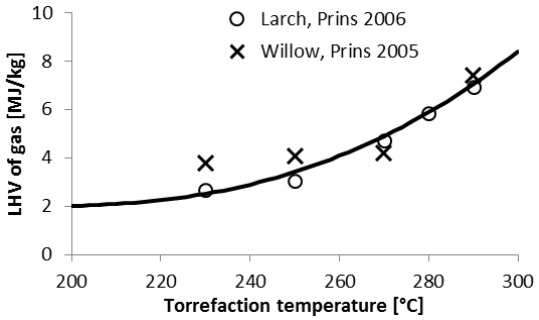

Figure 3.3: Lower heating value of torrefaction gas as a function of torrefaction temperature. Experimental data from Prins *et al.* (2006b) and Prins (2005); the correlation curve represents Equation (3.3).

The reaction enthalpy h_{react} of the torrefaction process is subject to significant uncertainty as well, and published experimental and model-based results are somewhat scattered. Ohliger *et al.* (2013) measured the heat of reaction in 10 % moisture beech torrefaction, with the results varying from 0…+150 kJ/kg endothermic to -150…0 kJ/kg exothermic, while van der Stelt (2011) reports a range from 1.5 MJ/kg endothermic to -1.2 MJ/kg exothermic. According to both of the above, the more exothermic reactions coincided mostly with the highest mass losses. Experimental co-torrefaction of hemicellulose, cellulose and lignin for 60 minutes by Chen & Kuo (2011) indicated an opposite behaviour: increasingly endothermic reactions at increasing torrefaction severity. Other published figures include -170 kJ/kg exothermic for unspecified wood biomass at a temperature of 250 °C (Peduzzi *et al.*, 2014), and -360 kJ/kg for poplar wood at unspecified temperature (Basu *et al.*, 2014).

Although there appears a tendency for torrefaction to exhibit a slightly exothermic heat of reaction more often than not, the data were considered too dispersed and contradictory

to serve as a basis for a model that could predict the change of h_{react} as a function of temperature. A constant exothermic value of -500 kJ/kg$_{feed,dry}$, considered a conservative estimate for determining the solid product energy yield, was thus used.

With the equations and assumptions presented above for the mass yield, the heat of reaction and the gas-phase heating value, the solid product heating value can then be solved from Equation (3.1). The relative change of solid matter dry fraction LHV_{bc}/LHV_{feed} and energy yield E [-], defined as

$$E = \frac{LHV_{bc} m_{bc,d}}{LHV_{feed} m_{feed,d}} \tag{3.4}$$

are plotted as a function of torrefaction temperature together with experimental data from Pach *et al.* (2002) and Phanphanich and Mani (2011) in Figure 3.4. Despite the weaknesses of the data on which some elements of the model is based, the results indicate a reasonably good performance approximately matching the relatively scattered data. The minor overprediction of the mass yield and the underprediction of the increase of the dry solid matter heating value at high temperatures balance each other out for a relatively close match of energy yield. In the area of interest later for the economic analysis, 250 °C, the performance of the model appears to be good, notwithstanding the possible errors in the data due to the reasons described above.

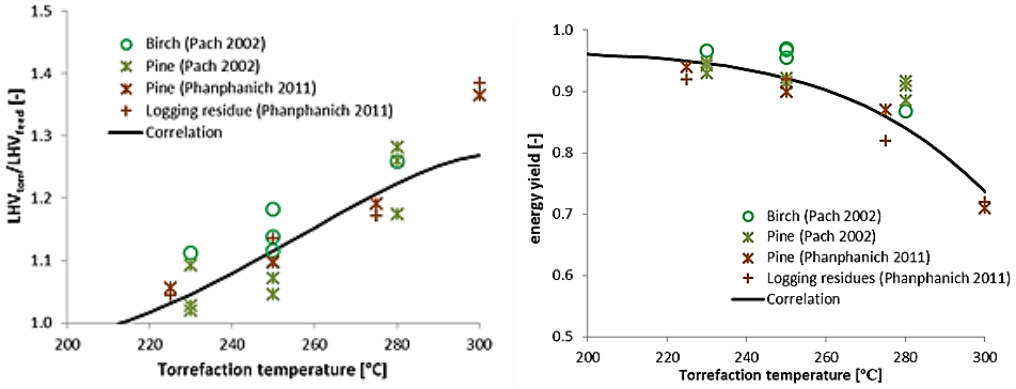

Figure 3.4: Model-based change of solid matter dry fraction LHV_{bc}/LHV_{feed} and energy yield E compared to experimental results in Pach *et al.* (2002) and Phanphanich and Mani (2011).

3.2.3 Heat consumption of the torrefaction reactor

The dried feedstock is torrefied by heating it to a specified reaction temperature and maintaining the temperature for a sufficiently long period, typically 30…60 minutes. Indirect heating of the biomass is assumed in this study, allowing the use of any flow at a sufficient temperature for heat supply. Although torrefaction requires a higher

temperature than drying, the heat consumption of the torrefaction reactor is clearly less than that of the dryer.

As industrial torrefaction reactors are not yet common equipment with known typical heat consumption rates, a model-based approximation had to be used. Accurate modelling of the heat consumption in torrefaction is challenging for several reasons, in particular because of variations in the specific heat of the wood, and uncertainties related to the heat of reaction during torrefaction, as well as the magnitude of heat losses from the reactor. The heat losses, impossible to estimate in detail without considering the design of the reactor, are assumed to be 10% of the reactor net heat consumption.

The model used in this study assumes that the moisture content remains constant up to 100 °C, at which point all moisture is evaporated. The net heat consumption Φ_{torr} [kW] in the torrefaction reactor can be considered to consist of five separate parts: 1) the sensible heat of moist wood temperature change, $\Phi_{<100°\text{C}}$ [kW]; 2) the latent heat of remaining water evaporation, Φ_{evap} [kW]; 3) the sensible heat of dry wood and water vapour, $\Phi_{100°\text{C-Torr}}$ [kW]; 4) the heat of reaction in torrefaction, Φ_{react} [kW], and 5) heat losses, Φ_{loss} [kW]. The sensible heats are obtained from equations (3.5) to (3.8):

$$\Phi_{<100°\text{C}} = \dot{m}_{\text{feed}} \bar{c}_{\text{p},<100°\text{C}} \left(100°\text{C} - T_{\text{feed,in}}\right), \tag{3.5}$$

$$\Phi_{100°\text{C–Torr}} = \dot{m}_{\text{feed}} \left(T_{\text{torr}} - 100°\text{C}\right)\left[\left(1 - MC_{\text{feed}}\right)\bar{c}_{\text{p},d} + MC_{\text{feed}}\bar{c}_{\text{p,vapour}}\right] \tag{3.6}$$

where MC_{feed} is the fractional wet-basis moisture content of the feedstock.

The specific heat of wood has a strong dependence on temperature (Thunman *et al.*, 2001), but shows little (Dupont *et al.*, 2014) or no dependence (Goss & Miller, 1992) on the wood species. Moisture also affects the specific heat. As a result of some of the moisture being not free liquid in the cells but bound to the fibres, the net specific heat of moist wood is greater than the weighted sum of dry and water components (Goss & Miller, 1992). Decomposition of wood begins at approximately 150 °C, affecting the specific heat (Ohliger *et al.*, 2013).

The specific heat of moist wood $\bar{c}_{\text{p},<100°\text{C}}$ [kJ/kgK] was estimated from a correlation by TenWolde *et al.* (1988) as cited in Ragland *et al.* (1991)

$$\bar{c}_{\text{p},<100°\text{C}} = \frac{\bar{c}_{\text{p,d},<100°\text{C}} + 4.19MC_{\text{db}}}{1 + MC_{\text{db}}} + MC_{\text{db}}\left(0.02355\bar{T} - 1.32MC_{\text{db}} - 6.191\right) \tag{3.7}$$

where MC_{db} [-] is the fractional dry basis moisture content and $\bar{T}$ [K] is the average temperature. The dry wood specific heat $\bar{c}_{\text{p,d},<100°\text{C}}$ [kJ/kgK] is obtained from

$$\bar{c}_{\mathrm{p,d,<100°C}} = 0.1031 + 0.003867\bar{T} \,. \tag{3.8}$$

The correlation in Equation (3.8) is valid for dry wood up to 147 °C, from which point onwards wood decomposition begins (Ohliger *et al.*, 2013). A number of other correlations for wood c_p also exist, such as those presented by Skaar (1988), Koch (1969), Gupta *et al.* (2003), and Harada *et al.* (1998). Some studies extend to higher temperatures, the one by Harada *et al.* (1998) to as high as 260 °C. The Harada correlation, however, differs significantly from the others. At the temperature of 147 °C all correlations are within 0.25 kJ/kgK, but when extrapolated to torrefaction temperatures, the range expands to almost 0.57 kJ/kgK at 300 °C. Also using the much lower c_p of char or an average of char and wood c_p's has been suggested (Ohliger *et al.*, 2013). Given the relatively short duration of the heating phase, in this study the properties are assumed to be much closer to those of wood than char. In the absence of a reliable and accurate model, Equation (3.8), yielding the lowest c_p of the compared correlations, with the exception of that of (Harada *et al.*, 1998), is used also in the range of 147°C < T < 300°C, with the knowledge that considerable errors may thus be introduced.

The heat required for the evaporation of the last moisture from the wood is calculated from

$$\Phi_{\mathrm{evap}} = \dot{m}_{\mathrm{feed}} MC_{\mathrm{feed}} h_{\mathrm{fg}} \tag{3.9}$$

where a value of of h_{fg} = 2260 kJ/kg, corresponding to the latent heat of evaporation of free water at 100 °C, is assumed, ignoring the effect of bound moisture. The error thus introduced is assumed to be small and most likely of opposite direction compared to the error caused by the extrapolation of dry wood c_p. The specific heat of water vapour is assumed to be 1.95 kJ/kgK.

Although the bulk of published data indicates somewhat exothermic heat of reaction, which is also assumed for determining the solid product heating value, the data is still varied and sometimes contradictory. To avoid an overly optimistic estimate of the heating benefit from the exothermicity of the reactions, h_{react} is thus assumed to be zero when determining the heating requirement.

Figure 3.5 shows the total heat consumption of the torrefaction reactor at three different temperatures and 10% moisture feedstock at a temperature of 60 °C. The heat consumption of drying the chips from 50% to 10% in the dryer is also indicated for comparison. It is evident from the figure that water evaporation accounts for the vast majority of the energy demand in torrefaction, most of it in the dryer.

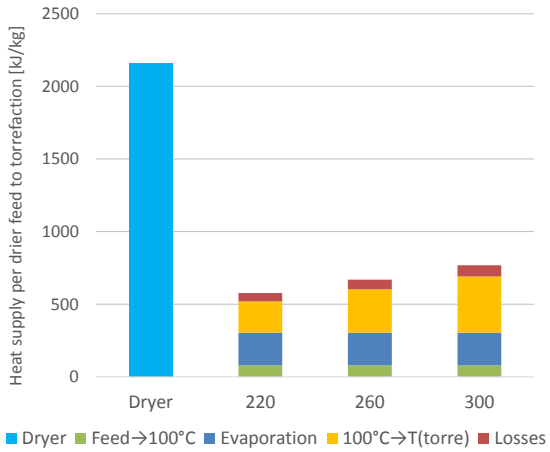

Figure 3.5: Heat consumption of dryer and torrefier at three torrefaction temperatures [°C].

The heat consumption and energy recovery available from the torrefaction process (not including the heating value of the solid product) are shown in Figure 3.6. While at low temperatures the process is a clear net consumer of energy, as torrefaction severity increases, the gas stream volume and heating value increase rapidly, reaching the process heat need at 300 °C. The sensible heat recovered from the process remains negligible in comparison.

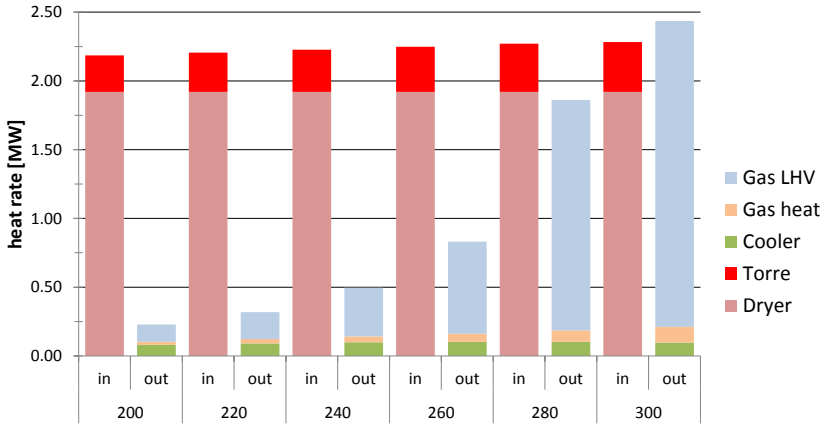

Figure 3.6: Energy consumption in dryer and torrefaction reactor (red) and energy recovery from the process (blue, yellow and green) in the torrefaction of 1 kg/s feedstock flow rate (50% wet basis moisture).

The power consumption of the torrefaction equipment is relatively small in comparison to the heat demand. In this work the power consumption of the torrefaction process is

assumed to be 200 kJ/kg$_{H2O,evap}$ in the dryer, 50 kJ/kg$_{solid,in}$ in the torrefier, and 200 kJ/kg$_{feed}$ for the total sum of power consumption of the other components. The torrefaction power consumption is defined in relation to the dried, 10% moisture feed entering the reactor, and the consumption of other components in relation to wet feedstock entering the dryer.

3.2.4 **Stoker boiler**

In a stand-alone torrefaction plant the heat required by the process is provided by a small separate boiler. In Publication III, which focused on the pure thermodynamic performance of different plant and integration configurations, the boiler type and its fuel were not considered. In Publication VII it was assumed that a small stoker boiler supplying 450 °C superheated steam would be used for indirect heating of a torrefaction reactor operating at 250 °C. Stoker boilers have the advantage of cheaper investment costs particularly in small units, as well as lower power consumption. Heating the reactor cools the steam to approximately 200 °C. The still superheated steam is sent to the feedstock dryer, where it de-superheats and condenses. The condensate is then pumped back to the boiler economizer.

The main boiler fuel is the same wood chips as used for torrefaction. The torrefaction gas is also combusted in the boiler furnace. From the results presented in Figure 3.6 it can be seen that at the torrefaction temperature of 250 °C considered in the economic and operational analysis, the gas still remains a minor part of the required boiler fuel input. The IPSEpro boiler model, as shown in Figure 3.1, includes a separate gas combustor. This exists only for modelling convenience; a separate physical combustor would not be needed in actual equipment, and the gas could be simply combusted in the boiler furnace.

For the production of 5 tons per hour of torrefied biochar at 250 °C temperature, the required design-point thermal output at 0 °C ambient temperature and feedstock moisture content of MC = 50 % is 7.6 MW. As the feedstock temperature and moisture varies, the heat demand of the torrefaction process, and particularly that of the dryer, varies significantly. The maximum torrefaction heat demand of 9.9 MW occurs at the load point P0 (Table 2.2; feedstock MC = 55 %, ambient temperature T_{amb} = -20 °C). At the summer load points of P7 and P8, this is reduced to just little over half as much at 5.1 MW (feedstock MC = 40 %, T_{amb} = +15 °C).

A grate-fired furnace model was created with the IPSEpro Module Development Kit (MDK) software; other parts of the system were modelled with standard IPSEpro library components. Similarly to the BFB furnace module, all boiler losses but the stack loss are determined by the stoker furnace module. Losses at the design point are stack loss Φ_{stack} = 936 kW; radiation loss Φ_{rad} = 101 kW; ash heat loss Φ_{ash} = 7 kW; unburnt loss Φ_{ub} = 308 kW; and other losses Φ_{other} = 68 kW.

The losses listed above yield a design-point boiler efficiency of η_b = 0.82 as defined in Equation (2.1), somewhat lower than in the BFB boiler. The efficiency is reduced

primarily due to higher stack loss. At design point conditions the flue gas stack temperature at full load is 160 °C. To ensure reasonably complete combustion, also a somewhat greater amount of excess air is usually required in a stoker boiler, lowering the adiabatic flame temperature and thus increasing the stack loss for any given flue gas stack temperature.

The radiation and conduction loss Φ_{rad} is obtained similarly to the BFB boiler with Equation (2.2), assuming a maximum continuous rating of Φ_{MCR} = 10.0 MW. Otherwise, the modelling of losses and their variation at different loads is slightly simplified from the BFB model described in chapter 2.1. Ash loss is estimated by assuming an average temperature of 500 °C for removed ash. The unburnt loss is estimated by assuming the fraction of fuel LHV input lost as unburnt increasing linearly with moisture,

$$\Phi_{\mathrm{ub}} = (0.1MC - 0.005)\dot{m}_{\mathrm{f}} LHV_{\mathrm{f}}\,, \tag{3.10}$$

yielding losses in line with those of modern stoker boilers. (U.S. Environmental Protection Agency, 2007).

Unlike in the BFB boiler, there is no SCAH to maintain the stack temperature. Load can be reduced down to slightly below 50 per cent thermal power before the flue gas stack temperature reduces to 135 °C. This was considered the lowest temperature at which there is not yet risk of condensation and corrosion at the economizer surfaces. This constraint is approached, but not breached, during full rate production in summer conditions.

The boiler heat transfer surfaces are arranged so that in the flue gas flow direction the economizer is the last surface. There is no steam air preheater, so sufficient air temperature to allow efficient combustion of sometimes relatively high-moisture biomass in a grate furnace is ensured by placing the air preheater immediately after the superheater.

Heat transfer at the boiler is calculated by using Equation (2.6), with conductances determined by Equation (2.7) and the design-point conductances. The design-point conductances and fluid temperatures of the heat transfer surfaces are listed in Table 3.1 below.

The power consumption of the boiler equipment is estimated at 36 kW at the design point, varying from 17 kW summer conditions (P7 and P8) to 59 kW at winter (P0).

Table 3.1: BFB boiler heat transfer surfaces.

Surface	**Steam generator**	**Superheater**	**Luvo**	**Economizer**
Conductance *G*	6.0 kW/K	7.8 kW/K	3.7 kW/K	32 kW/K
Flue gas $T_{\mathrm{in}}/T_{\mathrm{out}}$	1350/690 °C	690/440 °C	440/340 °C	330/160 °C
Cold fluid $T_{\mathrm{in}}/T_{\mathrm{out}}$	155/185 °C	185/450 °C *	105/305 °C	45/155 °C

* without feedwater injection 515 °C

3.3 Hydrothermal carbonization model

Compared to torrefaction, a more severe carbonization can be achieved at slightly lower temperatures by hydrothermal carbonization. Since the process takes place in saturated liquid water, the feedstock does not need to be dried; the solid product separated from the slurry does need drying, however.

Estimating the HTC product yields as a function of process parameters is based on an earlier experimental study with Nordic forest chips (Sermyagina *et al.*, 2015). In Publication IV, the effects of different HTC temperatures were studied; Publication V assumed a temperature of 220 °C. A residence time of 3 hours, and 1:6 ratio of dry matter to water were assumed in both.

3.3.1 Plant configuration

As a drawback in comparison to dry torrefaction, the HTC process is more complex, as heating and pressurizing the feedstock, and depressurizing of and heat recovery from the product slurry are typically performed in several stages. Because a significant amount of water is heated to a high temperature, an efficient heat recovery scheme is vital for an economically feasible HTC process. In the stand-alone HTC plant the heat recovery is largely performed by a recuperative scheme where steam from gradually depressurized saturated product slurry is used for heating the feed slurry steam. Some of the hot water is typically recirculated to the feed after the solid product has been separated from it, and either hot water or steam can be used as the dryer heat source. Heat integration with a CHP plant allows also other options to recover heat from the product slurry; these concepts are described in chapter 4 below.

The final heating of the HTC reactor requires external heat input; in this study, direct heating by steam injection is considered. Approximately 30 bar, 350 °C steam is supplied either by a separate chip-fired stoker boiler, or in the integrated schemes the CHP plant BFB boiler live steam is throttled and feedwater-injected to a suitable state. The dryer may operate entirely on heat recovered from the product slurry, or may need additional heat.

Two types of stand-alone HTC process are considered. The process in Figure 3.7a is broadly similar to that presented by Erlach *et al.* (2011), utilizing multi-stage depressurization and feed slurry heating for maximum energy efficiency. A simplified variant has also been created with two-stage depressurization and a simple waste heat recovery scheme (Figure 3.7b), where the dryer heat is supplied entirely from low-pressure (LP) flash vapour. In both processes, a small wood-fired boiler supplies 30 bar steam for the reactor.

The simpler scheme requires more steam for the final heating of the reactor, but the overall heat requirements are within 0.3 percent of each other. As the investment cost of

the simpler process is obviously clearly less, only this stand-alone case has been used in further calculations.

Due to the limitations of the IPSEpro software, the slurry is treated as separate water and dry streams in the model, requiring new models also for pumps and heat exchangers. The component models are described in the following.

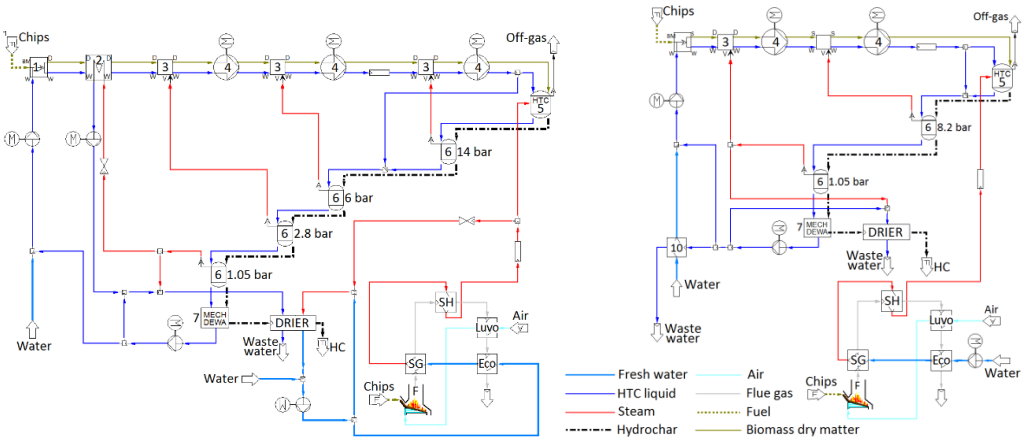

(a) (b)

Figure 3.7: Stand-alone HTC plants with stoker boilers supplying heat. a) A plant similar to that presented in (Erlach *et al.*, 2011), and b) a simplified plant used in this study. Components: 1 feeder, 2 slurry heater, 3 vapour injection, 4 slurry pump, 5 reactor, 6 flash tank, 7 dewatering, F furnace, SG steam generator, SH superheater, Luvo air preheater, Eco economizer.

3.3.2 Slurry pressurization and feed heating

The chips are assumed to be fed to the water in a so-called Kamyr feeder where a cruciform rotor alternates every 90° rotation cycle between chip insertion and high-pressure water injection and flush (Rautalin & Wilén, 1992). The water and dry matter exit the module as separate streams at the same temperature, found from the energy balance. Equation (3.11a) is used if $T_{\mathrm{feed}} \geq 0$°C, Equation (3.11b) with the heat of melting h_{fs} otherwise.

$$\dot{m}_{\mathrm{feed}}(1-MC)c_{\mathrm{p,d}}(T_{\mathrm{out}}-T_{\mathrm{feed}})+\dot{m}_{\mathrm{feed}}MC\,c_{\mathrm{p,W}}(T_{\mathrm{out}}-T_{\mathrm{feed}}) = \dot{m}_{\mathrm{W,in}}c_{\mathrm{p,W}}(T_{\mathrm{W,in}}-T_{\mathrm{out}}) \tag{3.11a}$$

$$\dot{m}_{\mathrm{feed}}(1-MC)c_{\mathrm{p,d}}(T_{\mathrm{out}}-T_{\mathrm{feed}})+\dot{m}_{\mathrm{feed}}\,MC\left[c_{\mathrm{p,W}}(T_{\mathrm{out}}-0\text{°C})+h_{\mathrm{fs}}+c_{\mathrm{p,W,ice}}(0\text{°C}-T_{\mathrm{feed}})\right] = \dot{m}_{\mathrm{W,in}}\,c_{\mathrm{p,W}}(T_{\mathrm{W,in}}-T_{\mathrm{out}}) \tag{3.11b}$$

Subscript d refers to the dry matter and W refers to water, $\dot{m}_{\text{feed}}$ is the total mass flow rate of wet feedstock, and Equation (3.8) is used to determine the dry biomass specific heat $c_{\text{p,d}}$.

Most process concepts require further pressurizing of the slurry in slurry pumps. A piston pump was considered more reliable than a centrifugal one; vendors claim that pumping slurries of up to a 30-60 % dry matter content is feasible (Erlach, 2014). A slurry pump efficiency of $\eta_{\text{SP}} = 0.3$ is assumed based on Erlach (2014), and the slurry enthalpy rise in a pump is found from

$$\Delta h_{\text{SP}} = \frac{1}{\dot{m}_{\text{d}} + \dot{m}_{\text{W}}} \frac{\dot{V}\Delta p}{\eta_{\text{SP}}}. \tag{3.12}$$

The volumetric flow rate assumes wood having the same density as water. Unless very wet, wood is slightly less dense, but as the densities are close and the slurry consists mostly of water, this is considered sufficiently accurate. The outlet temperature is found by setting the enthalpy rise Δh_{SP} of Equation (3.12) to equal the mass-weighted average of the dry matter and water fractions, both having the same outlet and inlet temperatures T_{out} and T_{in} :

$$\Delta h_{\text{SP}} = \frac{\dot{m}_{\text{W}}}{\dot{m}_{\text{d}} + \dot{m}_{\text{W}}} \left[h_{\text{W}}\left(T_{\text{out}}, p_{\text{out}}\right) - h_{\text{W}}\left(T_{\text{in}}, p_{\text{in}}\right) \right] + \frac{\dot{m}_{\text{d}}}{\dot{m}_{\text{d}} + \dot{m}_{\text{W}}} \left[c_{\text{p,d}}\left(T_{\text{out}} - T_{\text{in}}\right) \right] \tag{3.13}$$

Before the reactor, the slurry is pre-heated in most process concepts with flash vapour either by direct injection or in an indirect heat exchanger. The heat exchanger model uses the effectiveness-NTU method. The indirect heater hot-side outlet enthalpy is defined by saturated temperature at outlet pressure. The slurry outlet temperatures are found from the energy balances, Equation (3.14) for injection and Equation (3.15) for the indirect heater:

$$T_{\text{c,out}} = T_{\text{c,in}} + \frac{\dot{m}_{\text{V}}\left(h_{\text{V,in}} - h_{\text{V,out}}\right) - \dot{m}_{\text{W}}\left(h_{\text{W,out}} - h_{\text{W,in}}\right)}{\dot{m}_{\text{d}}\bar{c}_{\text{p,d}}} \tag{3.14}$$

$$T_{\text{c,out}} = T_{\text{c,in}} + \frac{\dot{m}_{\text{h}}\left(h_{\text{h,in}} - h_{\text{h,out}}\right)}{\dot{m}_{\text{d}}\bar{c}_{\text{p,d}} + \dot{m}_{\text{W}}\bar{c}_{\text{p,W}}}. \tag{3.15}$$

3.3.3 **HTC reactor**

As data from industrial-scale HTC reactors is not yet available, modelling the performance of one is subject to significant uncertainties. The uncertainties arise particularly from the dry matter specific heat, reaction enthalpy, and heat losses both with the off-gas and by conduction and radiation from the reactor vessel. The reactor is directly

heated by steam or hot water to bring the slurry to saturated state at the desired temperature. The mass and energy yields *M* and *E* are obtained from correlations based on laboratory-scale experiments (Sermyagina *et al.*, 2015):

$$M = \frac{\dot{m}_{\mathrm{hc,d}}}{\dot{m}_{\mathrm{feed,d}}} = 1 - 0.04079 \cdot \left(T - 150°\mathrm{C}\right)^{0.337} \cdot t^{0.2142} \cdot r_{\mathrm{WB}}{}^{0.3055} \tag{3.16}$$

$$E = \frac{\dot{m}_{\mathrm{hc,d}} HHV_{\mathrm{hc,d}}}{\dot{m}_{\mathrm{feed,d}} HHV_{\mathrm{feed,d}}} = 1 - 0.05632 \cdot \left(T - 150°\mathrm{C}\right)^{0.062} \cdot t^{0.2846} \cdot r_{\mathrm{WB}}{}^{0.4405}. \tag{3.17}$$

where T is the temperature [°C], t the residence time [h], r_{WB} the mass ratio of water to biomass dry fraction [-], and HHV the higher (gross) heating value [MJ/kg]. Subscript hc refers to the product hydrochar, and feed to the feedstock. For conversion between LHV and HHV, feedstock is assumed to have a hydrogen content of 6 mass percent (Alakangas, 2000; Erlach, 2014), reducing slightly in hydrochar (Bach, *et al.*, 2015; Hoekman, *et al.*, 2013) to an estimated 5.5 percent.

The correlations of equations (3.16) and (3.17) are based on experiments made with relatively low ratios of 6 to 8 parts (mass) of water to biomass dry matter (Sermyagina *et al.* 2015). While some results of HTC experiments with different feedstocks using several times higher ratios of water to dry matter, it was estimated that for an economically feasible process the relative amount of water should be kept fairly low to avoid excessively large and expensive equipment. This was conclusion was later supported by the study by Vallejos *et al.* (2017).

Some information on HTC heat of reaction is available in the literature. It is often estimated to be slightly exothermic, depending on the feedstock and reaction severity (Erlach & Tsatsaronis, 2010; Funke & Ziegler, 2011; Libra *et al.*, 2011; Ramke *et al.*, 2009; Yan, Hastings *et al.*, 2010). Yan *et al.* (2010) concluded that the heat of reaction is "very close to zero". Due to the high uncertainty yet small magnitude compared to water heating, the heat of reaction is neglected here.

By neglecting the formation enthalpies of the solid, liquid and gaseous HTC products as small and uncertain terms, the energy balance can be simplified and written in terms of bringing all of the incoming flows to the selected reactor temperature, and in the case of incoming vapour, condensing to the saturated liquid state. This can come from either a small boiler in a stand-alone plant, or when integrated to the CHP plant, live steam throttled and sprayed to the desired pressure and temperature; in either case, approximately 30 bar and 350 °C steam values were used in this work. Solving the energy balance for the heating mass flow rate $\dot{m}_{\mathrm{h}}$ yields

$$\dot{m}_{\mathrm{h}} = \frac{\dot{m}_{\mathrm{d}} c_{\mathrm{p,d}} \left(T_{\mathrm{HTC}} - T_{\mathrm{c,in}}\right) + \dot{m}_{\mathrm{W,in}} \left[h'\left(T_{\mathrm{HTC}}\right) - h_{\mathrm{W}}\left(T_{\mathrm{c,in}}, p_{\mathrm{c,in}}\right)\right] + \Phi_{\mathrm{loss}} + \Phi_{\mathrm{ventloss}}}{h_{\mathrm{h}} - h'\left(T_{\mathrm{HTC}}\right)}, \qquad (3.18)$$

where T_{HTC} is the reactor temperature, subscripts c and h refer to the incoming cold (feedstock slurry) and heating (steam) flows, respectively. Φ_{loss} is the radiation and convection loss from the reactor, and $\Phi_{\mathrm{vent\ loss}}$ the off-gas heat loss. Some steam is lost with the off-gas. The vent loss is estimated by approximating the water in the off-gas as saturated vapour at reactor temperature, and the water mass fraction in the off-gas is $r_{\mathrm{W,vent}} = 1/3$.

The water-to-biomass ratio is the ratio of water from heating flow and the slurry to dry matter, deducting the water lost with the off-gas:

$$r_{\mathrm{WB}} = \frac{\dot{m}_{\mathrm{h}} + \dot{m}_{\mathrm{W,in}} - \dot{m}_{\mathrm{vent}} r_{\mathrm{W,vent}}}{\dot{m}_{\mathrm{d}}} \qquad (3.19)$$

The liquid output contains both water input to the reactor and the liquid reaction products. As the liquid and gas outputs are small compared to the slurry flow, and their use or treatment is beyond the scope of this study, a simple approximation of 2:1 liquid-to-gas ratio is assumed based on Hoekman *et al.* (2011). The liquid is treated as water in the thermal model. Some of the ash possibly dissolving to the liquid is not considered, as the impact on the heat and mass balances would be negligible.

3.3.4 Product slurry treatment and heat recovery

The slurry exits the HTC reactor at a saturated state, and is depressurized in a series of flash tanks where part of the slurry water vaporizes. The vapour mass flow rate is obtained from the energy balance,

$$\dot{m}_{\mathrm{V}} = \frac{\dot{m}_{\mathrm{W1,in}} h_{\mathrm{W1,in}} + \dot{m}_{\mathrm{hc}} c_{\mathrm{p,hc}} \left[T_{\mathrm{hc,in}} - T_{\mathrm{sat}}\left(p_{\mathrm{FT}}\right)\right] + \dot{m}_{\mathrm{W2,in}} h_{\mathrm{W2,in}} - \left(\dot{m}_{\mathrm{W1,in}} + \dot{m}_{\mathrm{W2,in}}\right) h'\left(p_{\mathrm{FT}}\right)}{h''\left(p_{\mathrm{FT}}\right) - h'\left(p_{\mathrm{FT}}\right)}, \qquad (3.20)$$

where p_{FT} is tank pressure, subscript W1 refers to the water in the hydrochar slurry, W2 to the possible additional water input, hc to the hydrochar dry matter, and V to the flash vapour. In the absence of a reliable correlation for hydrochar dry matter, the specific heat $c_{\mathrm{p,hc}}$ is obtained from the correlation for wood, Equation (3.8).

Dewatering power consumption is difficult to estimate, as results of industrial-scale dewatering of wood-based hydrochar are not available. A belt filter or a screw press could dewater anaerobic pulp and paper mill sludge to a 20-30 % dry content with a power consumption of 10-30 kWh/t (Bajpai, 2015). The cell structure of the biomass is largely broken during hydrothermal carbonization, which makes dewatering and drying the hydrochar much easier than doing the same to fresh biomass. In laboratory experiments

dewatering to a moisture content of MC = 30-50 % has been achieved (Ramke *et al.*, 2010). Based on this, it is estimated that MC = 40 % is likely achievable with 30 kWh/t_d power consumption.

Some mass losses are inevitable in dewatering and drying; a total of 1% dry matter mass loss is assumed here. The mass loss of water in dewatering (i.e. water removed from hydrochar, but lost through leaks and evaporation before heat recovery or recirculation) is estimated at 5 % of total water flow entering the dewatering unit.

The heat losses depend on the equipment design, storage, and ambient temperature. The heat loss is likely less for dewatering waste water than for hydrochar, which would have a storage before the dryer. The water and hydrochar temperature drops ΔT_w and ΔT_{hc} are estimated from ambient temperature T_{amb} as $\Delta T_w = 0.1 \cdot (100\ °C - T_{amb})$ and $\Delta T_{hc} = 0.5 \cdot (100\ °C - T_{amb})$.

A belt dryer with a specific heat consumption of ϕ_{spec} = 1.1 kWh/$kg_{H2O\text{-}evap}$ at design point (T_{amb} = 0 °C) and power consumption of 200 kW_{el} / $(kg/s)_{output}$, considered typical for a belt dryer (Arpiainen & Wilen, 2013; Fagernäs *et al.*, 2010), is assumed. The heat of evaporation, 0.678 kWh/$kg_{H2O\text{-}evap}$ is approximately constant, but the energy needed to heat the feedstock and air increases at colder ambient temperatures, as do radiation losses. This part of heat consumption is assumed to vary in direct proportion to temperature difference between the operating temperature, assumed as 70°C, and T_{amb}:

$$\phi_{spec} = 0.678 \frac{\text{kWh}}{\text{kg}_{H_2O,evap}} + \frac{70°C - T_{amb}}{70} \cdot (1.1 - 0.678) \frac{\text{kWh}}{\text{kg}_{H_2O,evap}} \qquad (3.21)$$

3.3.5 **Stoker boiler**

In stand-alone operation, a stoker boiler similar to that of the torrefaction plant was used to supply the necessary heat demand. Two types of stand-alone plant were initially considered, as shown in Figure 3.7. In both cases the HTC reactor would be heated directly by injection of approximately 30 bar, 300…350 °C steam.

In the more complex plant of Figure 3.7a, steam is required also for the thermal dryer. This steam would be produced by throttling the superheated steam to 1 bar and de-superheating it to saturated state by feedwater injection. This case was rejected from further analysis for being a significantly more complex design while offering only a negligible efficiency advantage. The following description thus concerns only the simpler design of Figure 3.7b. In this design the low-pressure flash steam from product slurry depressurization is sufficient for the heat requirement of the thermal dryer, and the boiler thus supplies only the steam needed in the HTC reactor itself.

The boiler design and the modelling of it are largely similar to the stoker boiler of the stand-alone torrefaction plant, described in chapter 3.2.3. Two major differences are clear from comparison of figures 3.1 and 3.7b, however. Firstly, in the indirectly heated torrefaction process, the steam is returned to the boiler cycle as cooled condensate. The HTC process using direct heating does not have a returning condensate flow, necessitating a makeup water flow matching the steam flow rate. Secondly, the off-gas from the HTC reactor has a very low heating value, and the boiler is thus fired entirely with the same wood chips as used for HTC process feedstock.

For the production of 5 tons per hour of hydrochar, the required thermal output at the design point (0 °C ambient temperature and 50 % feedstock wet-basis moisture content) is approximately 5 MW. The heat load varies seasonally, increasing during winter conditions to approximately 6.7 MW at most, and reducing somewhat for the summer. The furnace model, which also determines all boiler losses except for stack loss, is the same as that described in chapter 3.2.3. Losses at the design point are stack loss Φ_{stack} = 652 kW; radiation loss Φ_{rad} = 119 kW; ash heat loss Φ_{ash} = 6 kW; unburnt loss Φ_{ub} = 274 kW; and other losses 1% of fuel power, Φ_{other} = 61 kW.

At design point conditions, the flue gas stack temperature at full load is 160 °C, as in the boiler of the torrefaction plant, resulting in similar design-point boiler efficiency of η_b = 0.82 as defined in Equation (2.1). The radiation and conduction loss Φ_{rad} is obtained from Equation (2.2), assuming a maximum continuous rating of Φ_{MCR} = 7.0 MW. Ash loss is estimated by assuming an average temperature of 500 °C for removed ash. The unburnt loss is estimated with Equation (3.10).

Similarly to the boiler of the torrefaction plant, the constraint of flue gas stack temperature reducing to 135 °C is approached, but not breached, during full rate production of hydrochar in summer conditions.

The heat transfer calculation is based on equations (2.6) and (2.7), and the design-point heat transfer surface parameters listed in Table 3.2 below.

Table 3.2: Boiler heat transfer surfaces of the stoker boiler in the stand-alone HTC plant.

Surface	**Steam generator**	**Superheater**	**Luvo**	**Economizer**
Conductance *G*	5.7 kW/K	2.8 kW/K	3.7 kW/K	2.2 kW/K
Flue gas T_{in}/T_{out}	1360/515 °C	515/410 °C	410/250 °C	250/160 °C
Cold fluid T_{in}/T_{out}	63/237 °C	237/340 °C	20/255 °C	10/63 °C

The power consumption of the boiler equipment is estimated at 37 kW at the design point, varying from 29 kW in summer conditions (P7 and P8) to 56 kW in winter (P0).

4 Integration of biomass conversion with a CHP plant

The integration of dry torrefaction and hydrothermal carbonization was studied by first investigating the technical performance of different integration concepts. In Publication III the integration of torrefaction to two different CHP plants was studied, investigating the impact of torrefaction temperature and the integration scheme on plant performance. Publication IV presented the results of technical evaluation of different integration schemes of HTC process to a small back pressure CHP plant.

The schemes considered most promising on the basis of the results from Publication III and Publication IV were selected for a more detailed operational analysis in Publication V (HTC) and Publication VII (torrefaction). This analysis aimed at finding possible operational bottlenecks at varying loads, and determining the annual fuel and feedstock consumption and heat, power, and biochar production figures.

4.1 Background

Both torrefaction and hydrothermal carbonization processes require significant heat input for drying the feedstock (torrefaction) or hydrochar product (HTC), as well as heating the feedstock to the reaction temperature. Both processes also produce waste heat from cooling the product. This is particularly significant in the HTC process. The torrefaction reactor produces also a fuel gas stream as a side product, which, especially at higher torrefaction temperatures, has a significant heating value.

A biomass-fired combined heat and power (CHP) plant is in many ways an excellent candidate for integration with either carbonization process, as the feedstock logistics and storage and handling facilities already exist, and potential heat sources and sinks for heating and cooling needs are available.

A number of studies of integrated plants combining various biomass conversion processes to CHP or condensing steam power plants have been published. Ethanol production has been studied extensively as a candidate for integration. Starfelt *et al.* (2010) show that integrating ethanol production with a heat and power plant yields a clear improvement of efficiency, with less biomass used for a given amount of district heat, power and ethanol in comparison to stand-alone plants. In a later study, the economic benefits of integration, attributed mainly to increased power production and extended operating time, are shown (Starfelt *et al.*, 2012). Eriksson and Kjellström (2010) found that using combustible residues to maximize electricity production is the best strategy for maximizing both profitability and GHG emission reductions, although this was based on the assumption of relatively high electricity prices.

Ilic *et al.* (2012) found that the integration of ethanol and biogas production with a CHP plant would be competitive compared to producing only heat, although again the conclusion was based on electricity prices of at least 53…65 €/MWh. Later the integration of biofuel production (biogas and ethanol) with CHP plants producing district heat for a

large city (Stockholm) was found to reduce the cost of biofuel production, although the profitability would depend heavily on energy market conditions (Ilic *et al.*, 2014).

Co-generation of sugar, ethanol and electricity has been shown to improve thermodynamic performance over stand-alone plants through decreasing the exergy destruction (Pellegrini & de Oliveira Junior, 2011). By heat integration of the processes, water and process steam consumption can be reduced (Pina *et al.*, 2015). Fahlen and Ahlgren (2009) found integration of gasification with natural gas combined cycle CHP production economical under some scenarios. Integration of pelletization process (Wahlund *et al.*, 2006) with CHP production has also been shown to yield energy efficiency benefits. Efficiency benefits were shown also in the integration of torrefaction with a large coal-fired CHP plant for the purpose of partial or complete fossil coal replacement in the boiler (Starfelt *et al.*, 2015).

In the context of northern European backpressure CHP plants, the seasonal variation of DH load over the year restricts the annual operating time and power production. Integration with a biomass conversion process has been shown to yield benefits in terms of increased operating time and higher power production during this period. Extending the annual operating time increases the capacity factors and incoming cash flow, thus increasing the value of the investment. This has been found to be the case with ethanol production (Starfelt *et al.*, 2010), pelletization and torrefaction (Kohl *et al.*, 2013), and biomass fast pyrolysis (Kohl *et al.*, 2014).

Only a few studies have investigated the integration of torrefaction or hydrothermal carbonization with a backpressure CHP plant. Kohl *et al.* (2013) and (2015) studied one concept of torrefaction-CHP integration. For hydrothermal carbonization, an integration concept aiming at simplifying the HTC process has been published by Erlach *et al.* (2011). This was later compared to two additional ones (Erlach, 2014): a minimum-change integration where the only change to the stand-alone HTC process was using extraction steam from the CHP plant as a heat source, and one where the simplified process was further improved with a superheated steam dryer for improved efficiency. While these integration studies did not reveal possibilities for significant efficiency improvements, they did show potential for significant reduction in complexity, translating to reduced investment costs and likely improved operability as well.

The purpose of this work is first to investigate the different possible ways that low-temperature thermochemical conversion processes (dry torrefaction and HTC) could be integrated to a backpressure CHP plant. The effect of the different integration schemes and the carbonization temperature on the technical performance plant is investigated. The results of this investigation are presented in this chapter, concluding in the determination of annual biochar, heat and power production and feedstock and boiler fuel consumption figures for the different schemes of integrating torrefaction (chapter 4.2) and HTC (chapter 4.3) with a backpressure CHP plant. The production figures are evaluated by using the multiperiod approximation presented in chapter 2.1.

With all cases at all load points the priorities of the operating strategy are primarily to match the district heat production to the heat load, secondarily to achieve nominal biochar output, and thirdly to maximize the power output. Although maximum power production sometimes results in slightly different operation than maximizing the overall CHP efficiency, the differences are small, and fuel saving from efficiency maximization would be insufficient to compensate for the income loss from reduced net power output within the considered economic scenarios.

4.2 Integration of torrefaction with the CHP plant

4.2.1 Technical performance comparison of different integration options

The heat required for the torrefaction process can be provided by various streams, such as hot water, flue gases from the boiler, or steam. For the dryer, low-pressure extraction or back pressure steam is sufficient, but the torrefaction reactor itself requires a higher temperature heat source, in practice necessitating live steam use.

The torrefaction process generates also energy sources: the torrefaction gas from the reactor can be combusted for heat, and heat can be recovered from biochar cooling as well. In all integrated cases, the torrefaction gas is combusted in the CHP plant boiler; in the stand-alone plant it is combusted in the stoker boiler of the plant. In all cases, the biochar cooler heat is recovered by preheating the boiler combustion air. Six different integration concepts, listed in Table 4.1, were considered in the initial technical investigation.

Case T0 represents the separate operation of the CHP plant and torrefaction unit without integration, and is used as the reference point for comparison. In Case T0, the heat demand of the torrefier and dryer is supplied by flue gases from the combustion of torrefaction gas and additional fuel.

Table 4.1: Heat sources in the torrefaction process. Case T0 is the reference case of stand-alone torrefaction process. In all other cases boiler heat sources refer to the boiler of the CHP plant.

Case	Torrefaction reactor	Feedstock dryer
Case T0	Separate stand-alone boiler	Separate stand-alone boiler
Case T1	Saturated water from the boiler drum	Drum water after torrefaction reactor
Case T2	Saturated water from the boiler drum	CHP boiler flue gases after luvo
Case T3	CHP boiler flue gas after superheater	Boiler flue gas after torrefaction reactor
Case T4	CHP boiler flue gas after superheater	Backpressure steam
Case T5	Boiler live steam	Backpressure steam
Case T6	Boiler live steam	Steam/condensate after the torrefier

The following assumptions were used for all integrated cases in the initial technical investigation:

- heat from the torrefied biomass cooling is used for preheating the combustion air
- torrefaction gas is co-fired in the boiler of the CHP plant together with biomass
- torrefaction heat losses are independent of the heating media used
- CHP plant live steam pressure is fixed at the design level
- constant feedstock mass flow rate of 1 kg/s to the torrefaction process is assumed

The load point considered in the initial performance comparison of the cases of Table 4.1 was that of 60% district heat load, Φ_{DH} = 12 MW. In this initial technical analysis, an earlier, somewhat simpler version of the CHP plant model was used. The turbine off-design model was not implemented, i.e. the isentropic efficiency and the extraction pressure were assumed constant. The boiler heat transfer model was largely similar to the one described in chapter 2.2, but differed in minor details of heat transfer surface conductances and the off-design variation thereof. The description of the model can be found in the appended Paper II.

The operating conditions in the initial analysis also differed slightly from the other papers; the chips used as boiler fuel and torrefaction feedstock were assumed to have a 18.8 MJ/kg$_{dry}$ heating value, and MC = 50% moisture content (wet basis). 15 °C ambient temperature and 90/45 °C district heating water output/return temperatures were assumed.

The performances of the integrated plants were considered at different torrefaction temperatures ranging from 200 °C to 300 °C. As the plants were operated so as to produce a constant 12 MW DH output, the parameters considered in the comparison were the boiler solid fuel input $\dot{m}_f$, net electricity output P_{el}, and LHV-basis trigeneration efficiency η_{LHV}, defined as

$$\eta_{LHV} = \frac{\left(P_{gen} - \sum P_{pump} - \sum P_{aux}\right) + \Phi_{DH} + \dot{m}_{bc} LHV_{bc}}{\left(\dot{m}_f + \dot{m}_{feed}\right) LHV_f}, \tag{4.1}$$

where $\dot{m}_f$, and $\dot{m}_{feed}$ are the mass flow rates of the wood chips used as fuel and torrefaction feedstock, $\dot{m}_{bc}$ the production rate of torrefied biochar, LHV_f and LHV_{bc} the lower heating values of untreated wood chips and torrefied biochar, respectively, P_{gen} is the net generator output, P_{pump} the power consumption of the steam cycle pumps, and P_{aux} the auxiliary power consumption, including transformer losses.

Figure 4.1 shows the variation of trigeneration efficiency and boiler solid fuel consumption as a function of the torrefaction temperature. It can be seen that in all integrated cases, the boiler solid fuel input and the trigeneration efficiency of the plant reduce as the torrefaction temperature increases. This is a result of a reducing torrefaction energy yield and increasing gaseous product mass flow rate and heating value. As more and more of the torrefaction feedstock ends up being fed into the boiler furnace of the

CHP plant, where the gas is combusted and its energy converted to heat and power at the efficiency of the CHP plant instead of remaining as solid product LHV, the total trigeneration efficiency of the integrated plant is reduced. At the same time, the solid fuel input to the boiler is reduced, as the torrefaction gas replaces an increasing fraction of the solid fuel.

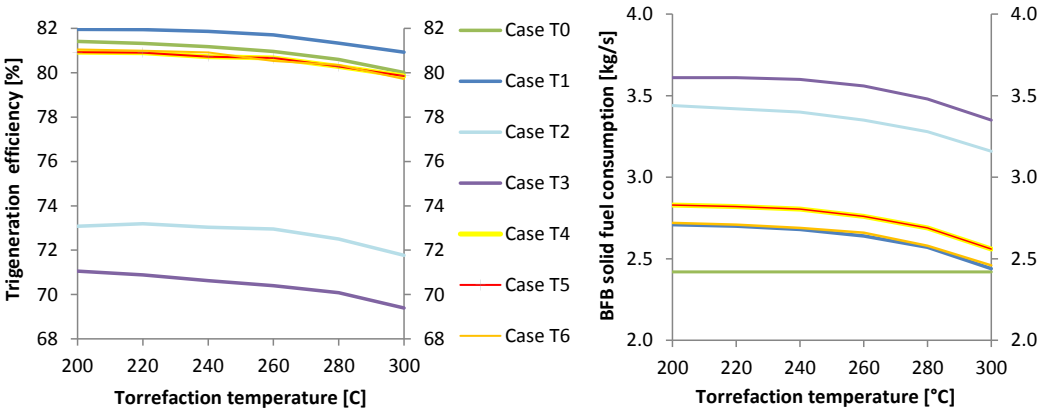

Figure 4.1: Integrated torrefaction and backpressure CHP plants at 60 % (12 MW) DH load and varying torrefaction temperatures: a) trigeneration efficiency and b) solid fuel consumption of the CHP plant boiler.

Another clear conclusion from the results is the clearly inferior efficiency and higher solid fuel input of Case T2 and Case T3. These are the cases where boiler flue gases are used as heat source for the dryer. As the drying is the main heat consumer of the torrefaction process, the operation of the boiler is significantly affected.

In Case T2, flue gas for the dryer heat supply is taken after the luvo. In order to maintain both the boiler combustion air temperature and the flue gas temperature in the dryer sufficiently high, some of the air must be bypassed past the luvo and heated in the steam coil air heater (SCAH) instead. Still, even with a very large SCAH, the boiler output needs to be increased over what the DH load would otherwise require, which in turn requires measures to be taken to prevent boiling in the economizer. Here the problem was solved by means of an auxiliary cooler for the district heating water to allow a larger water and steam flow through the CHP process. The net result is slightly increased power production, but increased complexity and cost, and reduced efficiency due to the auxiliary cooler. Future electricity prices were considered unlikely to be sufficiently high to justify such a concept, and Case T2 was thus rejected from further study.

Case T3 uses flue gas taken from the boiler between the superheater and the economizer, and also suffers from similar issues caused by the torrefaction plant heat demand exceeding what is readily available from the boiler back pass at 12 MW DH load. Again,

a very large SCAH must be used, and still also the boiler load increased to maintain sufficient combustion air heating. This again leads to the need of an auxiliary cooler for DH water, and complexity, cost and efficiency penalties that are unlikely to be offset by the somewhat increased power production. The Case T3 was thus rejected from further study on the same grounds as T2.

The remaining cases were relatively close to each other in performance. Case T1 and Case T2 utilize high-pressure saturated water taken from the boiler drum as the heat source for the torrefaction reactor. While in thermodynamic terms particularly Case T1 appears competitive during part load operation, this advantage is lost at full load. This is because operating the torrefaction plant during full heat load is only possible with reduced feedwater flow rate, and maintaining DH production through turbine bypass. With reduced feedwater flow, but the boiler operating at maximum continuous rating, the only way to prevent boiling in the economizer is to bypass much of the flue gas past the economizer, which inevitably results in poor boiler efficiency.

Using an approximately 300 °C heating medium at a very high pressure for indirect heating of the torrefaction reactor would also likely prove to be impractical and expensive at best. Without a clear performance benefit to justify the cost and difficulty, Case T1 was also rejected from further study despite the fact that it offered the best part-load efficiency. Cases T4 and T5 had practically identical performances in terms of efficiency, power generation and boiler fuel use. Between these two, Case T5 was considered preferable on grounds of the potential fire hazard of using over 500 °C flue gases for heating very dry biomass, as well as the likely costly arrangement of Case T4 where most or all of the boiler flue gas flow is diverter after the superheaters to the torrefaction reactor and then back to the economizer.

Cases T5 and T6 were left as the most promising cases. These use boiler live steam for torrefaction, and either the cooled but still superheated steam returning from the torrefier (T5) or the steam cycle back pressure steam (T6) for dryer heating. These two cases, together with the baseline stand-alone plants of Case T0, were thus selected for closer operational and economic analysis.

4.2.2 Operational analysis

For the operational and economic analysis of the integrated plants, torrefaction parameters of 30 minutes residence time and 250 °C temperature are used. At higher temperatures, the trigeneration efficiency of the integrated plant begins to decrease at an increased rate (see Figure 4.1). The selected parameters result in LHV-basis mass and energy yields of M = 0.83 and E = 0.93, and a solid product dry matter heating value LHV_d = 21.8 MJ/Kg.

Figure 4.2 depicts the changes of significant CHP plant operating parameters of the selected cases as functions of cumulative time in the heat load duration curve. Sub-figure (a) shows the variation of the BFB boiler fuel power (LHV input) and DH output. The

boiler fuel power is shown both as total fuel including the torrefaction gas, and the solid fuel only. The boiler fuel input is similar at full load for all cases; there is a slight reduction in terms of solid fuel, and increase in terms of total fuel load for the integrated cases, but the difference is small. At part loads the boiler fuel input of the integrated cases is significantly increased. Since the minimum load of the plant is limited by the boiler, the increase of boiler load leads to an increase of annual operating time by more than 1000 hours.

At full district heating load the CHP plant has little capacity to increase the boiler load. The limiting parameter is the maximum flue gas flow rate; the integrated cases operate at or near the maximum flue gas flow rate down to 18 MW DH load, with furnace temperature also approaching but not exceeding the maximum value of 950 °C (Figure 4.2b). At this load point the fuel moisture is assumed to reduce to 50% from the winter-time maximum of 55%, which yields the highest boiler fuel load, thermal output, and furnace temperature. The minimum load is restricted by the 700 °C minimum furnace temperature.

Sub-figure 4.2c shows the condenser pressure together with the district heat load and output temperature. Condenser pressure is not affected significantly by the integration concept, as the variation of steam enthalpy at the turbine exhaust is small enough to yield only a negligible effect.

At 20 MW district heat load, the HTC heat demand is enough that at boiler maximum continuous load, the steam flow to the turbine is significantly reduced. To maintain the 20 MW DH output, a large fraction of steam is directed past the turbine through a reduction valve, desuperheated to saturated state with feedwater spraying, and routed to the DH condenser. The steam flow to the turbine is reduced to approximately 2 kg/s as a result (Figure 4.2d). At the peak load point P0, the turbine is bypassed entirely due to the very small steam flow rate. As the flow rate to the turbine is reduced at full load, the HP turbine exhaust pressure and deaerator pressure also reduce in all cases (Figure 4.2e).

The drum and feedwater pressures are shown in Figure 4.2f. In the integrated cases the drum pressure peaks at a higher value than in the stand-alone CHP plant, but remains below the maximum limit.

As load and thus flue gas flow rate are reduced, the boiler heat transfer coefficients are also reduced, but relatively less than the gas flow rate. This results in decreasing flue gas temperatures in the boiler. Full steam superheat can be maintained to load point P4 (14 MW DH load) in the stand-alone Case T0, or to P5 (10 MW DH) in the integrated cases, by reducing spraying in the superheater. A plot of turbine inlet steam temperatures is shown in Figure 4.2d.

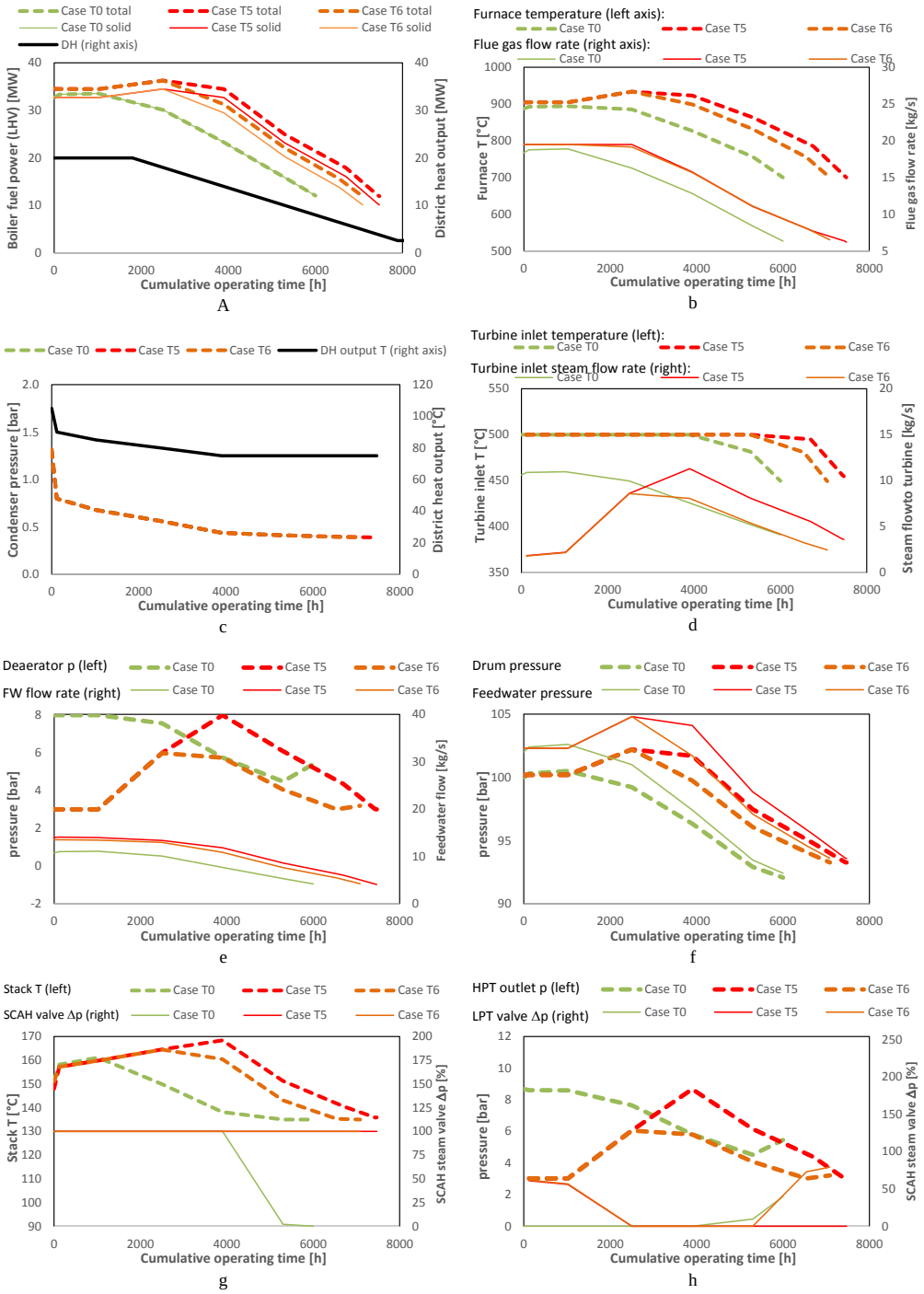

Figure 4.2: Plant operating parameters as functions of cumulative time in the heat load duration curve.

At the low loads the steam temperature at the turbine inlet is inevitably reduced in all cases. Full live steam superheat can be maintained to the lowest part load in Case T5, where the turbine inlet steam temperature is still almost at the design-point value at 6 MW DH load. This is a result of the increased boiler load at any given DH load with Case T5. As the dryer heat source is back pressure steam, this steam is expanded through the turbine for power production, requiring higher boiler output as well; this load increase is also the reason for Case T5 having the longest annual operating time.

At full and nearly full DH load, the flue gas stack temperatures are somewhat elevated from the design point value, reducing the plant efficiency slightly. With the integrated cases the SCAH is not needed to prevent the stack temperature from reducing below the minimum value of 135 °C even at minimum-load conditions. The stack temperatures and the SCAH steam valve Δp are plotted in Figure 4.2g.

Figure 4.2h shows the HP turbine outlet pressure, and the LP turbine valve pressure drop. The reduced turbine flow rate at maximum DH output requires throttling of the steam flow with of the LPT valve to maintain deaerator pressure.

With the stand-alone Case T0 and the integrated Case T6, some throttling of the flow to the LPT becomes necessary also as the minimum load conditions are approached. In case of the stand-alone Case T0, this is due to the need to maintain a sufficiently high pressure of the steam at the SCAH to keep the stack temperature above the minimum value. With Case T6, the reason is the need to maintain the HPT exhaust pressure above the deaerator pressure. With Case T5 the LPT valve is not needed: providing enough backpressure steam for the torrefaction plant feedstock dryer maintains also high enough steam flow through the turbine to keep the HPT exhaust pressure sufficient for both the deaerator and the SCAH.

4.2.3 Annual production and consumption

The annual output and consumption rates of the energy products was obtained with the multi-period approximation of annual production figures. The discretized variation of boiler fuel consumption (including the stoker boiler in Case T0) and DH and the net power output are plotted in Figure 4.3, together with the DH heat demand curve. The torrefied biochar output remains constant at 32.0 MW_{LHV} throughout the torrefaction plant operating period: 8000 hours in Case T0, and the same as the operating time of the CHP plant in the integrated cases. The torrefaction feedstock use rate increases from 27.8 to 30.0 MW_{LHV} as the wood moisture reduces from winter 55 % to summer 40 %.

The integrated torrefaction plants require heat and power from the CHP plant. At the same time, by increasing the annual operating time it is possible to obtain additional revenues from increased CHP production. With Case T5, the power production during most of the part-load operation is increased as well. The biochar production of the torrefaction unit is 30.3 MW_{LHV} throughout whole the operating period: 8000 hours in Case T0, and equal to the CHP operating hours in the integrated cases.

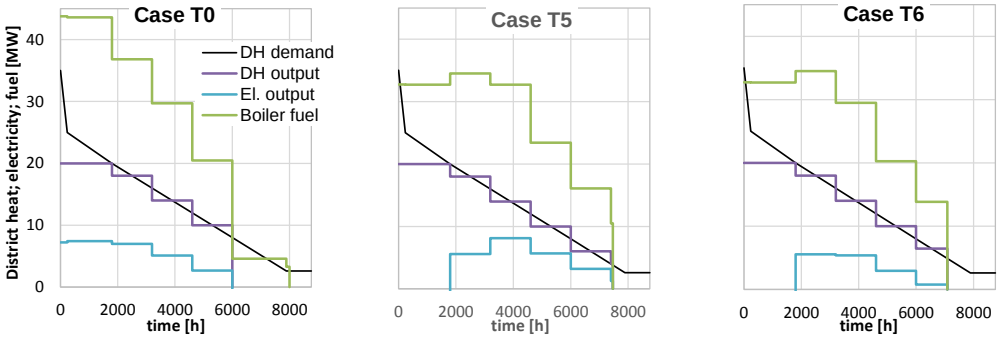

Figure 4.3: Annual production of CHP products (power and heat) together with boiler fuel consumption using the multi-period model, and the DH demand curve. Case T0 includes the boiler fuel used in the separate stoker boiler of the torrefaction plant.

Case T0 with separate stand-alone plants shows clearly higher boiler fuel input during full load, where the stoker boiler power comes in addition to the full load operation of the CHP plant. At part load, the stand-alone Case T0 and integrated Case T6 show similar boiler fuel consumptions until the 6000-hour point, when the CHP plant is shut down in Case T0. The net power production of Case T6 is reduced due to the power consumption of the torrefaction plant equipment. Case T5 shows a different pattern: using back pressure steam from the turbine exhaust to supply heat to the torrefaction feedstock dryer yields a clear increase of power generation from approximately 3000 hours onwards, and thus also requires more boiler fuel input.

At the full-load periods, the integration with torrefaction reduces the net power output of both integrated scenarios to approximately zero; the figures are in fact slightly negative. This is due to the need to bypass most of the boiler steam through the reduction valve to the torrefaction plant dryer and the district heat condenser to maintain both torrefaction and the necessary DH output. While the turbine is not completely bypassed for most of the 20 MW DH load period, the very small remaining power output is exceeded by the combined power consumption of the torrefaction plant and the auxiliary power consumption of the CHP plant.

Table 4.2 summarizes the overall figures of annual net production and consumption of various energy streams. The sold and purchased electricity is separated for the purposes of further economic analysis, since they have different prices.

The trigeneration efficiencies of the plants are evaluated with equations (4.2) and (4.3). The values are calculated in terms of both lower heating value (LHV) and higher heating value (HHV) from the net annual energy production of electricity $E_{el,net}$, district heating Q_{DH} and biochar Q_{bc}, and the input of wood chips as boiler fuel Q_f and torrefaction feedstock Q_{feed}:

$$\eta_{\mathrm{LHV}} = \frac{E_{\mathrm{el,net}} + Q_{\mathrm{DH}} + Q_{\mathrm{bc,LHV}}}{Q_{\mathrm{feed,LHV}} + Q_{\mathrm{f,LHV}}} \tag{4.2}$$

$$\eta_{\mathrm{HHV}} = \frac{E_{\mathrm{el,net}} + Q_{\mathrm{DH}} + Q_{\mathrm{bc,HHV}}}{Q_{\mathrm{feed,HHV}} + Q_{\mathrm{f,HHV}}} \tag{4.3}$$

Table 4.2: Annual energy inputs and outputs of separate CHP and torrefaction plants, co-located plants (Case T0), and the three integration options.

Case:	CHP	Torrefaction	Case T0	Case T5	Case T6
Fuel input					
CHP boiler fuel $Q_{\mathrm{f,BFB}}$ [GWh$_{\mathrm{LHV}}$]	157.3	-	157.3	208.3	191.9
Torre stoker boiler $Q_{\mathrm{f,S}}$ [GWh$_{\mathrm{LHV}}$]	-	51.4	51.4	-	-
Torre feed $Q_{\mathrm{feed,LHV}}$ [GWh$_{\mathrm{LHV}}$]	-	230.6	230.6	212.6	203.3
Total $Q_{\mathrm{chips,HHV}}$ [GWh$_{\mathrm{HHV}}$]	193.6	342.7	536.3	513.5	482.8
Total $Q_{\mathrm{chips,LHV}}$ [GWh$_{\mathrm{LHV}}$]	157.3	282.0	439.2	420.9	395.1
Energy products					
Net electricity $E_{\mathrm{el,net}}$ [GWh]	39.0	-6.6	32.4	30.3	18.9
Sold electricity $E_{\mathrm{el,s}}$ [GWh]	39.0	0	34.0	31.6	20.2
Purchased electricity $E_{\mathrm{el,p}}$ [GWh]	0	6.6	1.6	1.3	1.4
District heat output Q_{DH} [GWh]	94.8	0	94.8	103.2	101.8
Biochar output $Q_{\mathrm{bc,HHV}}$[GWh$_{\mathrm{HHV}}$]	0	255.8	255.8	236.6	226.5
Biochar output $Q_{\mathrm{bc,LHV}}$ [GWh$_{\mathrm{LHV}}$]	0	242.4	242.4	224.2	214.6
Trigeneration efficiency					
η_{LHV} [%]	85.1	83.6	84.1	85.0	84.9
η_{HHV} [%]	69.1	72.7	71.4	72.1	71.9

As can be expected, the total annual fuel consumptions of the integrated cases are clearly higher than in the case of the stand-alone of CHP plant. The biochar output along with electricity and DH generation are higher for Case T5 than T6 due to longer plant operating time. The stand-alone CHP plant has a higher efficiency in LHV terms than the stand-alone torrefaction case, or any of the considered integrates. Since the torrefaction feedstock is not burned, except for the off-gas from the reactor, the loss with latent heat of biomass moisture decreases and the cases including torrefaction have better efficiencies in terms of HHV than the pure CHP plant.

Figure 4.4 shows the distribution of the relative fractions of the annual outgoing energy streams from the studied processes. The blue-green tones represent products; losses are shown in yellow-red tones. The results are again broadly similar for all the studied cases.

Approximately half of all outgoing energy flows is biochar. Due to the extended operating times of the CHP plants in the integrated cases, the share of district heat is slightly increased. The share of electricity is the smallest in Case T6, where the loss of power

output due to integration is not compensated for by the increased steam flow through the turbine at part loads.

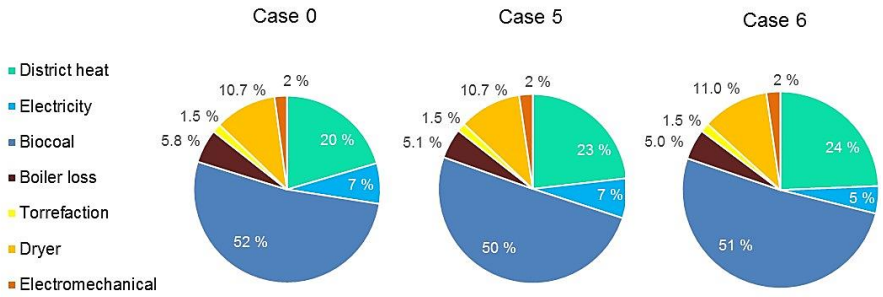

Figure 4.4: Outgoing energy flows as fractions of the annual consumption and production figures of the plant.

Among losses, the dryer and boiler losses are the largest. The fraction of boiler loss is slightly reduced in the integrated cases due to the use of the somewhat more efficient BFB boiler of the CHP plant. The heat consumption of the torrefaction unit itself and the electromechanical losses of the plant are relatively small fractions of the balance. The main variations of the balance among the integrated options are connected to the operation time of the plant during the year. Between the T5 and T6, the effect of increased steam flow through the turbine shows due to the use of backpressure steam for drying show as higher fraction of electricity in the balance.

The variation of the trigeneration efficiencies in terms of LHV and HHV within the operating time is shown in Figure 4.5. It is evident that the efficiencies of the considered integrated schemes are virtually the same, and differ only slightly from the co-located stand-alone plants of Case T0.

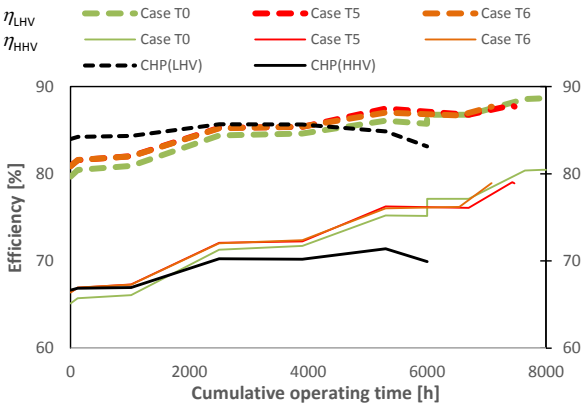

Figure 4.5: Variation of LHV- and HHV-based efficiencies as a function of cumulative operating time for the different cases.

Compared to the pure CHP, the efficiencies of all cases including torrefaction tend to improve towards increasing cumulative operating hours. The reduction of torrefaction process losses is mainly a result of a reducing fuel moisture as well as an increasing ambient temperature combining to reduce the dryer losses, which are the main loss source of the torrefaction process.

4.3 Integration of hydrothermal carbonization with the CHP plant

4.3.1 Considered integration cases

Six different integration concepts are considered, in addition to a separate stand-alone plant (Case H0, Figure 3.7b). Case H1 is close to the stand-alone process but uses steam from the boiler of the CHP plant for heating the HTC reactor. The steam is taken as boiler live steam, throttled to 30 bar pressure and desuperheated by feedwater spraying to a temperature of 350 °C.

Case H2 is based on the scheme in Figure 3.7a. Similarly to Case H1, CHP boiler live steam replaces the stoker boiler as the reactor heat supply. The reduced flow of 1.05 bar LP flash vapour for the dryer is also augmented by backpressure steam from the CHP plant. While the total heat demand of this arrangement is similar to the HTC process of Case H1 and offers little benefit in stand-alone HTC operation, in an integrated plant the CHP plant steam cycle benefits thermodynamically from heat being taken at a lower temperature level in backpressure steam instead of live steam.

In cases H3 to H6 the HTC process differs significantly from the stand-alone one; these integration schemes are shown in Figure 4.6. Case H3 is based on the integration proposed by Erlach *et al.* (2011). Otherwise similar to Case H1, the HP flash vapour is used in the CHP plant LP preheater (LPPH).

In cases H4 to H6 the HTC process is simplified by using feedwater alone or with drum water (H5 and H6) to make the slurry pumps unnecessary: the chips are fed to the already pressurized hot water stream. The drum water is also hot enough for reactor heating. The HP flash tank pressure is set so as to match the LP flash vapour output to dryer heating requirement, and the warm waste water stream is used to heat the combined CHP and HTC makeup water flow, which is significantly increased in these cases due to limited recirculation.

In cases other than H4 to H6, where most of the HTC process water is fresh from the CHP steam cycle, the ratio of recirculated to fresh water in the HTC feed is maintained at 3:1. In Case H4 and Case H5 only the condensate return from CHP plant LPPH is recirculated. In Case H6 some of the depressurized slurry water is recirculated and heated indirectly with the drum water and directly by HP flash vapour injection, but the ratio of recirculation to fresh water remains much less than 3:1.

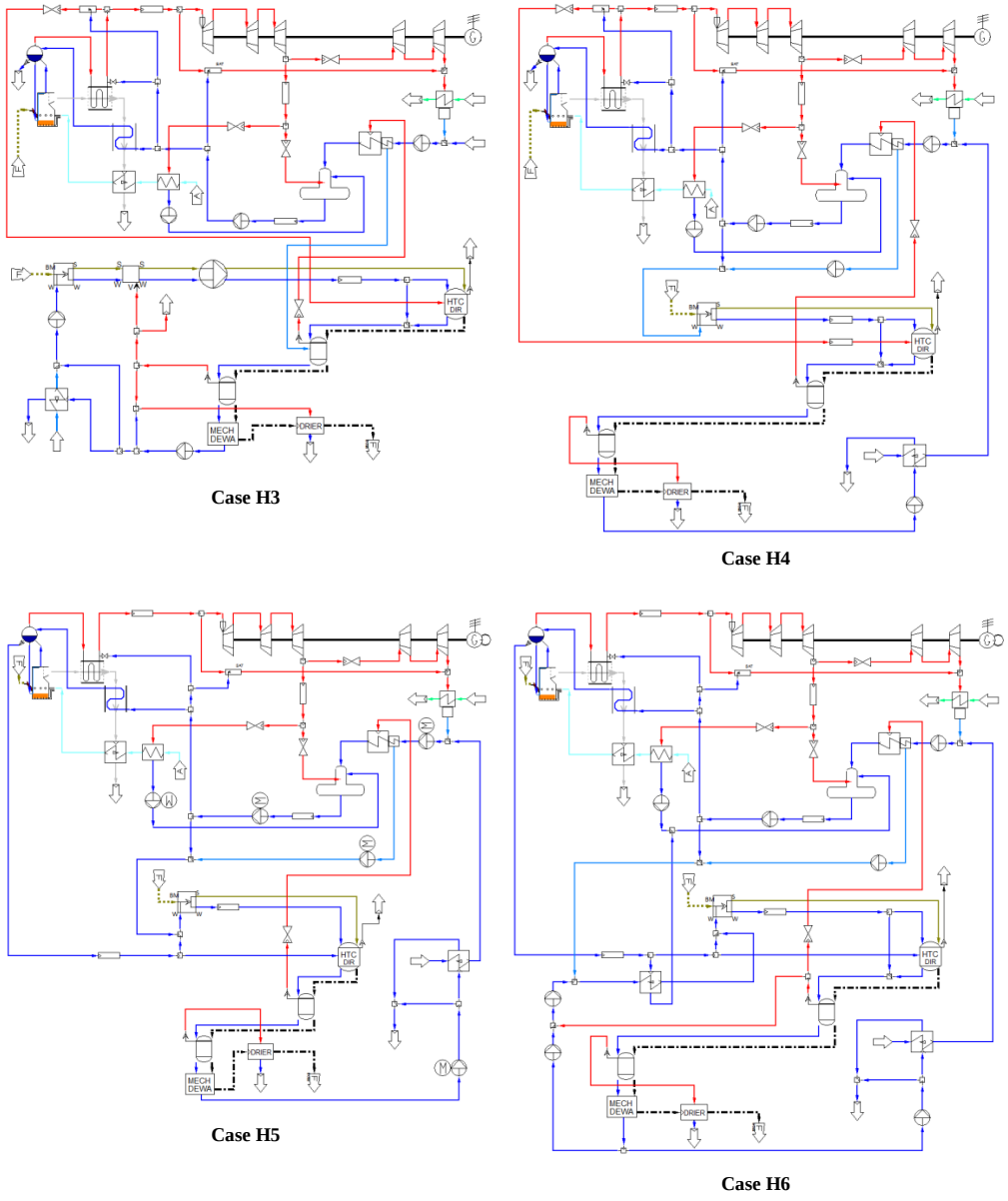

Figure 4.6: Process flow diagrams of integration cases H3 to H6

An effective heating and heat recovery scheme is vital to achieve a reasonable efficiency in the HTC process. The design-point heat rates of heating and heat recovery are listed in Table 4.3. Depending on the case, heat input to the feed to reach the required reactor conditions takes place in different stages: to the water before the chip feeder, to the slurry feed, or directly to the reactor; all but reactor heating are potential sinks for recovering the relatively low-grade heat from the hydrochar slurry.

Table 4.3: Main parameters of feed slurry heating and heat recovery for the integrated cases at the design point.

Case	H1	H2	H3	H4	H5	H6
Water input and heating [MW]:						
Fresh water input	0.05	0.10	0.03	5.37 *	9.84 *	0.70 *
Waste water recirculation	2.57	2.43	3.27	1.09 **	1.06 **	2.47
Waste water heat recovery	0.26	-	0.17	1.87	2.06	1.61
Indirect water heating	-	-	-	-	-	1.52
Slurry heating [MW]:						
Flash vapour (indirect)	-	1.63	-	-	-	-
Flash vapour (direct)	5.83	6.58	1.43	-	-	-
Reactor direct heating	5.11	3.17	8.83	7.86	3.39	8.51
Dryer heat supply [MW]:						
Waste water	0.41	0.78	0.48	-	-	-
flash vapour	2.79	0.40	2.73	3.21	3.21	3.21
Backpressure steam	-	2.03	-	-	-	-
Heat recovery to CHP [MW]:						
Makeup water preheater	-	-	-	1.87	2.06	1.61
LP feed heater	-	-	3.44	4.02	4.05	3.49
Heat transfer area [m^2]:						
Makeup water HRX	20	-	20	60	60	60
HTC water indirect heater	-	-	-	-	-	60
Slurry preheater	-	40	-	-	-	-
LPPH	-	-	58	58	58	69

* From CHP drum and/or feedwater stream
** Condensate from LPPH

In Case H1 and Case H2, where the HTC process is broadly similar to the stand-alone one, heat recovery from the hydrochar product slurry flash vapour to the feed slurry stream is dominant. Case H3 requires more reactor heating, as the CHP process takes a significant fraction of the available flash vapour. In cases H4 to H6 the chips are fed into already fully pressurized and significantly heated water, while the much-increased waste water stream is cooled in a heat exchanger to heat the similarly increased combined CHP and HTC makeup water stream. In Case H4 and Case H6 the slurry is heated mostly in the reactor itself. Case H5, using mostly hot drum water, requires little additional slurry heating after chip insertion.

The heat transfer areas are estimated by assuming the following values of overall heat transfer coefficient: water-to-water 1.0 kW/m^2K, indirect slurry feed heater 2.0 kW/m^2K and CHP plant LPPH 3.0 kW/m^2K. In cases H4 to H6, the fresh water to the HTC process is obtained as fully pressurized and significantly heated from the CHP steam cycle. As this water stream carries significant heat with it, more of the product slurry heat must be recovered to the water streams of both processes by using indirect heat exchangers. While these are additional components that add cost and complexity to the system, the heat transfer areas required remain relatively small, and these additions to the process must be

weighed against the benefit of simplifying the feed slurry heating and pressurization by removing the need for slurry pumps and slurry stream heating.

4.3.2 Performance comparison at design point and minimum load

In the initial analysis residence time, the temperature and ratio of water to dry matter are assumed as 3 h, 220 °C and 6:1 in all cases, resulting in mass and energy yields of $M = 0.626$ and $E = 0.779$. With these parameters, the corresponding hydrochar dry matter heating values are $HHV_{hc,d} = 25.8$ MJ/kg and $LHV_{hc,d} = 24.7$ MJ/kg dry, or at the final MC = 5 % moisture content, $HHV_{hc} = 24.5$ MJ/kg and $LHV_{hc} = 23.3$ MJ/kg. Hydrochar production is constant at 5 t/h in every case.

The design point (fuel MC = 50%, maximum DH production and 0 °C ambient temperature) and low load (MC_f = 45%, 40 % DH load and T_{amb} = 10 °C) energy consumption and power, heat and hydrochar production figures are listed in Tables 4.4 and 4.5. Polygeneration efficiencies are shown both in terms of LHV and HHV, defined as

$$\eta_{LHV} = \frac{P_{el,net} + \Phi_{DH} + \dot{m}_{hc} LHV_{hc}}{\dot{m}_f LHV_f} \tag{4.4}$$

$$\eta_{HHV} = \frac{P_{el,net} + \Phi_{DH} + \dot{m}_{hc} HHV_{hc}}{\dot{m}_f HHV_f} \tag{4.5}$$

where $P_{el,net}$ is the net electrical output remaining after CHP and HTC auxiliary consumptions, and subscript f refers to the wood chip input, both as boiler fuel and HTC feedstock. There are only small efficiency differences between the separate plants, and the six integrates.

At maximum district heat production, the separate plants give slightly better overall efficiency (see Table 4.4). This is because in the integrates the CHP plant must reduce its production, and the overall efficiency of the HTC plant is somewhat less than that of the CHP plant. This is the case despite the slightly better efficiency of the CHP plant BFB boiler compared to the HTC plant's smaller stoker boiler.

The poorest efficiencies are found in Case H4 and Case H5, where little or no HTC process fluid is recirculated. This increases the waste water flow to 10-11 kg/s from the 3-5 kg/s of the other cases. Despite heat recovery cooling of the waste water to 40±5 °C, this inevitably increases heat losses. Case H4, where this is combined with a low CHP cycle output, has the poorest efficiency, but at 79.1 % in LHV terms still only 0.7 percentage points below the 79.8 % net figure of the separate HTC and CHP plants. Case H1 yields a slightly higher power output than the other integrates at 6.0 MW, but still below the 7.4 MW of the separate plants. Also here Case H4 at 5.3 MW comes out as the worst one.

Table 4.4: Energy consumption and heat, power and hydrochar production figures at 100 % DH load and T_{amb} = 0 °C ambient temperature.

Case	H0	H1	H2	H3	H4	H5	H6
Fuel input							
CHP boiler [MW_{LHV}]	32.5	36.7	36.7	36.7	36.7	36.7	36.7
HTC feed [MW_{LHV}]	36.3	36.3	36.3	36.3	36.3	36.3	36.3
HTC stoker boiler [MW_{LHV}]	6.1	-	-	-	-	-	-
Total [MW_{LHV}]	74.9	73.0	73.0	73.0	73.0	73.0	73.0
Total [MW_{HHV}]	91.0	88.7	88.7	88.7	88.7	88.7	88.7
Electricity							
CHP plant P_{gen} [MW]	8.66	7.27	7.17	7.01	6.53	6.86	6.96
CHP self-use P_{aux}+P_{pumps} [MW]	0.66	0.73	0.73	0.73	0.83	0.83	0.82
HTC self-use [MW]	0.61	0.56	0.56	0.54	0.42	0.42	0.45
Net power output [MW]	7.39	5.98	5.87	5.74	5.28	5.61	5.68
District heat output [MW]	20.0	20.0	20.0	20.0	20.0	20.0	20.0
Polygeneration efficiency							
η_{LHV} [%]	0.798	0.800	0.799	0.797	0.791	0.795	0.796
η_{HHV} [%]	0.675	0.677	0.676	0.674	0.669	0.673	0.673

Figures for the minimum-load situation are presented in Table 4.5. Here a different result is seen: in all integrates except Case H5, the CHP plant steam flow rate is increased. The integration thus has the opposite effect on polygeneration efficiency than at full load. The effect is further increased by the increasing load improving also the component efficiencies in the CHP plant. Case H2 yields both the highest electricity production and the best overall efficiency.

The efficiency of Case H3 is reduced slightly because at reduced CHP but full HTC load, the main condensate flow becomes insufficient to act as a heat sink for the heat available from the product slurry steam; a small fraction of the flash vapour has to be vented to the atmosphere. The differences in the efficiencies are still very small, ranging from 75.2 % to 76.5 %. The efficiency of Case H3 could be expected to decrease rapidly at any lower loads, as the vented flash vapour would no longer be small.

Cases H1 and H2 are the two most efficient cases both at 100% and 40% DH load at almost the same efficiency. The separate plants of Case H0 ranks third at both load points, at nearly the same figures as H1 and H2 at full load, but somewhat further behind at 40%. The remaining four configurations rank differently at full and 40% load; Case H3 achieves almost the same efficiency as cases H0, H1 and H2 at full load, but becomes the worst at 40% load. Among the cases using feedwater and drum water, Case H4 performs poorest at both load points. Case H5 and Case H6 are almost identical in terms of efficiency at both loads.

Table 4.5: Energy consumption and heat, power and hydrochar production figures at 40 % DH load and T_{amb} = +10 °C ambient temperature.

Case	H0	H1	H2	H3	H4	H5	H6
Fuel input							
CHP boiler [MW_{LHV}]	12.0	18.2	19.3	18.1	18.2	17.8	18.0
HTC feed [MW_{LHV}]	37.2	37.2	37.2	37.2	37.2	37.2	37.2
HTC stoker boiler [MW_{LHV}]	5.8	-	-	-	-	-	-
Total [MW_{LHV}]	55.0	55.5	56.5	55.3	55.4	55.0	55.2
Total [MW_{HHV}]	65.2	65.7	66.9	65.5	65.6	65.2	65.4
Electricity							
CHP plant P_{gen} [MW]	2.37	3.04	4.06	2.01	2.37	2.30	2.41
CHP self-use P_{aux}+P_{pumps} [MW]	0.41	0.47	0.49	0.48	0.57	0.57	0.56
HTC self-use [MW]	0.59	0.56	0.56	0.54	0.42	0.42	0.44
Net power output [MW]	1.37	2.01	3.01	0.99	1.37	1.31	1.41
District heat output [MW]	8.0	8.0	8.0	8.0	8.0	8.0	8.0
Polygeneration efficiency							
η_{LHV} [%]	0.759	0.765	0.768	0.748	0.754	0.758	0.757
η_{HHV} [%]	0.666	0.670	0.673	0.656	0.661	0.665	0.664

Case H2 appears to be arguably the most energy efficient of the considered options. The difference is small, however, and this is also the most complex integration scheme. In addition to higher investment cost, the operation and control of the plant is likely to prove to be complex. There is a risk that the indirect slurry heater may prove to be prone to clogging and severe fouling. The flows and pressure levels must also be carefully managed, as the pressure gradients from the product slurry to the feed are often small, and the feed slurry comes very close to saturated state and boiling before each pressurization stage.

Figure 4.7 shows selected operating parameters that limit the maximum and minimum loads of the CHP plant for the studied cases. It can be seen that in the maximum-load case (Table 4.7), the power output is limited by the flue gas flow rate in all cases. Case H3 is practically at the limit of turbine capacity as well.

At minimum load, the separate plants are limited to the 8 MW DH load by the furnace temperature, and the SCAH inlet valve is also almost fully open. If the load was reduced even just slightly, the minimum stack temperature could no longer be maintained. In contrast, all of the integrated cases operate at 770-790 °C furnace temperature, and the SCAH steam valves are barely if at all open. All cases are also still some way off from the point where bypassing the turbine entirely should be considered. It is thus clear that integration would allow the CHP plant to be run at DH loads noticeably lower than without integration.

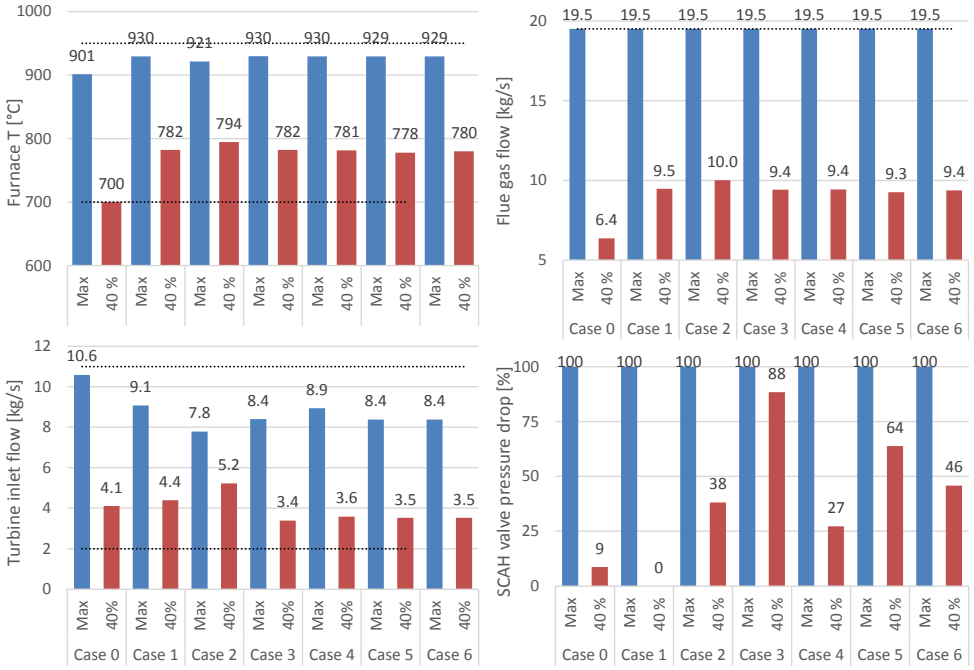

Figure 4.7: CHP process parameters at maximum (blue bars; 0 °C ambient temperature and 50% fuel moisture) and 40% (red; T_{amb} = +10 °C and *MC* = 45 %) DH loads. The dotted black lines represent minimum and/or maximum values for the parameter.

It is evident from the results that the heat integration will not bring significant efficiency benefits compared to having separate HTC and CHP plants. There are two other advantages from the integration, however. Firstly, by integrating the HTC to the CHP plant, the total investment cost will be reduced. Removing the need to have separate boiler plant to supply the heat for the HTC process is the clearest and most obvious advantage, but there are also saving opportunities with biomass storage and handling. Particularly cases H4, H5 and H6 present also clearly simplified processes without slurry heaters or slurry pumps, although the more than doubled waste water flow rate and the resulting increase in waste water handling costs will at least partially offset these savings.

A second advantage is the ability to run the plant at lower part loads; the minimum load of the separate CHP plant is at 8 MW DH load. At the same DH load all integrates still show potential to operate at a clearly lower DH load. This will allow the chip-fired CHP plant to operate into warmer periods of low heat load, thus reducing the period of time when heat must be produced with auxiliary heat-only boilers typically firing clearly more expensive fuels such as light oil, pellets, or natural gas if available.

The disadvantage of integration in all cases is that in the period of full DH load, either the HTC operation must be suspended or reduced, or the CHP plant must reduce either heat or power production.

4.3.3 Evaluation of initial technical comparison

The energy efficiency of HTC and CHP processes cannot be noticeably improved by integrating them. Only two of the studied cases, Case H1 and Case H2, rate better than the separate processes of Case H0, but the difference is small. There are other clear advantages with the integration, however. Integration allows the CHP plant to be run over longer period annually. It reduces the fuel costs by allowing cheaper wood fuel to be used, and the investment costs of an integrate are likely to be smaller than the cost of two separate plants.

Cases H2 and H3 appear somewhat problematic; Case H2 will be the most expensive to invest in without the benefit of a clear efficiency advantage with which to justify the additional cost. The increased electricity production at part load is unlikely to be enough to offset the expense, and there appears to be a higher risk of operational problems. Case H3 is reasonably efficient compared to the other plants at high DH loads, but its efficiency will suffer severely at periods of very low DH load.

Cases H4 and H5 are clearly the simplest, but require waste water treatment plants of more than twice the capacity of the other cases. Between these two cases, Case H5 is both simpler and slightly more efficient than Case H4 which has the poorest overall efficiency of all cases at both 100% and 40% DH load. Case H6 represents effectively an improved Case H5 with reduced water consumption and waste water flow rate, as well as a marginally better efficiency, to offset a slightly more complex process.

On the grounds presented above, cases H2, H3 and H4 are rejected from further study. The following chapters 4.2.4 and 4.2.5 described the effect of HTC temperature on the performance of the remaining cases, and the operational characteristics of these cases.

4.3.4 Effect of carbonization temperature on plant performance

A temperature range of 180…240 °C is considered, the same as the range of the measurements used as the basis for mass and energy yield correlations in Sermyagina *et al*. (2015). Each case has been calculated at 20 °C intervals within this range. The residence time has been maintained at 3 h, and the ratio of water to dry matter at 6:1.

Figure 4.8 shows the variation of net electric power output (sub-figure a) and the fuel consumption of the CHP boiler (sub-figure b) at full and 40% DH load. At full load, a clearly reducing full-load power production can be observed in all of the integrates, which is a natural result of an additional heat consumer requiring steam as the plant is operated at the maximum continuous rating of the boiler while maintaining the DH output. The fuel consumption of the boiler is thus also constant at this maximum limit for all

integrated cases. Additionally, some of the power output is lost for HTC electricity consumption. This is the sole reason for the lower power production of Case H0 compared to the pure CHP plant at both load cases.

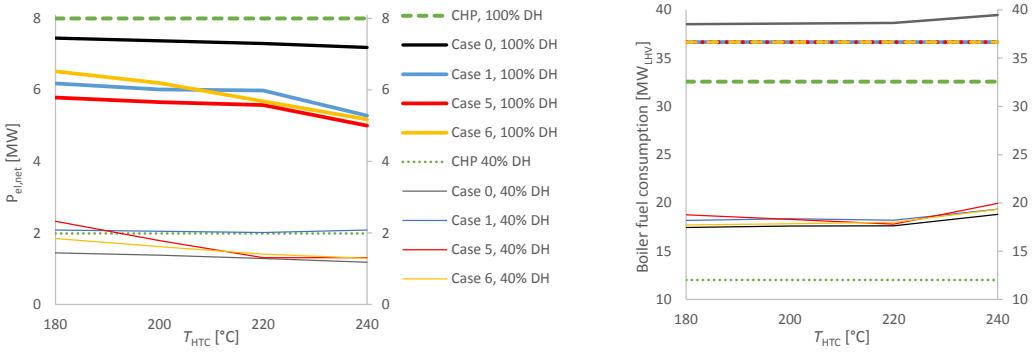

(a) (b)

Figure 4.8: Effect of the HTC temperature on a) net power production and b) boiler fuel consumption.

At 40% load, the pure CHP plant and Case H1 integrate have almost identical power outputs. This is a coincidence of opposing effects compensating for each other. The CHP plant requires some constriction of the LPT control valve to maintain sufficient pressure at the SCAH for the stack temperature to remain above its minimum limit, and the reduced boiler load results also in a significant reduction of the turbine inlet temperature. With Case H1, the boiler load is enough for very little SCAH heat input to suffice, and the live steam temperature also remains almost at the nominal value. The additional power output thus gained is almost exactly matched by the HTC power consumption. Case H0 equals the CHP output minus HTC consumption.

Cases H5 and H6 exhibit different behaviour: as the HTC temperature is reduced, less and less flash vapour is available for the LPPH, and thus an increasing amount of extraction steam is needed for the CHP deaerator. The expansion of this additional steam flow in the HP turbine shows as increased power production. The effect is clearly stronger in Case H5 with a simpler and less efficient heat recovery scheme, in fact enough so that not only the power output but also boiler fuel consumption increases as the HTC temperature is reduced from 220 °C to 180 °C, despite the HTC heat consumption slightly reducing.

When the HTC temperature is increased from 220 °C to 240 °C, the increase in process heat consumption is clearer. The full-load power production goes down at an increasing rate, while the 40% load boiler fuel consumption goes up. This is particularly pronounced with Case 5, where an increasing amount of hot HTC waste water must be bypassed past the heat recovery heat exchanger. This is due to the fact that as the main condensate flow remains relatively small in the CHP water-steam cycle but the heat available as flash

vapour from HTC increases, the main condensate temperature must be kept low enough to maintain the condensate below the saturation temperature.

In Case H1, the relatively simple 2-stage heat recovery scheme reaches its limit of efficient operation at approximately 220 °C. At 240 °C, preventing the feed slurry from approaching within 5 °C of boiling point requires venting some of the HP flash vapour at 40% DH load, and bypassing the waste water HRX at 100% DH load case, which shows as reduced 100% load power output and increased 40% load boiler fuel consumption.

Figure 4.9 shows the impact of HTC temperature on the plant trigeneration efficiencies in terms of LHV and HHV. Here the differences between the cases are relatively small, and all cases – integrated or not – are mostly within one percentage point of each other. The differences between the cases increase somewhat at 40% DH load and 240 °C HTC temperature, where the losses of HTC process in Case 5 increase noticeably more than in the other cases due to the need to bypass the HRX to maintain a low enough water temperature at the LPPH. Case 1 suffers the least due to the fraction of energy products from the CHP process, which has higher efficiency than the HTC, being the greatest. This compensates partially for the increased losses in the HTC process at this temperature.

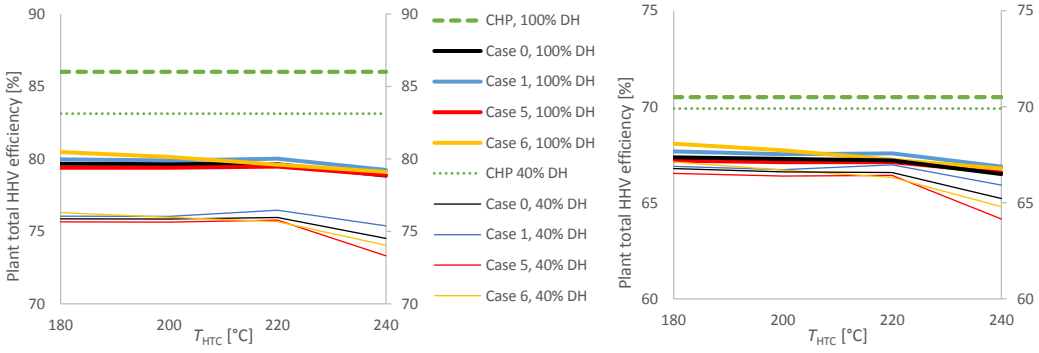

(a) (b)

Figure 4.9: The effect of HTC temperature on trigeneration efficiency based on a) LHV and b) HHV of fuel and hydrochar.

4.3.5 Operational analysis

Based on the results of the temperature analysis, 220 °C carbonization temperature appears to be a limit beyond which the efficiencies of the integrated plants start to become increasingly poor. Based on this, a 3-hour residence time, 220 °C carbonization temperature and 6:1 ratio of water to biomass dry matter is assumed for the operational analysis of the different plant configurations.

As with the integration of torrefaction and HTC plants, the operating strategies are aimed at maximizing the net power output P_{el} and extending the operating period of the CHP plant, but prioritizing heat and hydrochar production when operating at maximum load.

Although particularly with the integrated cases maximizing power production sometimes results in slightly different operation than maximizing the overall CHP efficiency, even at the low electricity price scenarios the fuel cost saving from efficiency maximization is insufficient to compensate for the income loss from reduced net power output.

Figure 4.10 depicts the changes of selected significant plant operating parameters as functions of cumulative time in the heat load duration curve. Sub-figures (a) and (b) show the variation of boiler power fuel power (LHV input) and condenser pressure together with the district heat load and output temperature. The condenser pressure is not affected significantly by the integration concept as the variation of steam enthalpy at the turbine exhaust is small enough to yield only a negligible effect. The boiler fuel input is increased in the integrated cases, however; the increase is slight at full load, but more significant at part loads, and leads to an increase of 1000 to 2000 hours of annual operating time.

At full DH load the stand-alone CHP plant has little capacity to increase the boiler load. The small increase potential is used in the integrated cases at full and nearly full load. The boiler is then limited by the flue gas flow rate (Figure 4.10c). The maximum furnace temperature of 950 °C is approached, but not exceeded, in the integrated cases at 18 MW DH load. At this load point, the fuel moisture is assumed to reduce to 50% from the winter maximum of 55%, which yields the highest boiler fuel load and furnace temperature. Drum pressure does not approach its maximum limit (Figure 4.10g).

At 20 MW DH load, the heat demand from the hydrothermal carbonization plant is high enough that at the boiler maximum continuous load the steam flow to the turbine is significantly reduced; to maintain 20 MW heat output, a large fraction of steam is directed past the turbine through a reduction valve, de-superheated to saturated state with feedwater spraying, and routed to the DH condenser. The steam flow to the turbine is approximately halved as a result (Figure 4.10d). As the flow rate to the turbine is reduced at full load, the HP turbine exhaust pressure and deaerator pressure reduce also in all cases (sub-figures f and h). The flue gas stack temperatures are somewhat elevated from their design point value of 150 °C to 160 °C at maximum boiler load, which reduces the total efficiency of the plant slightly.

As the boiler load and thus flue gas mass flow rate are reduced, the heat transfer coefficients in the convective heat transfer surfaces of the boiler are reduced as well, but relatively less than the gas flow rate reduces. This results in decreasing flue gas temperatures in the boiler. Full steam superheat can be maintained down to load point P4, corresponding to a 14 MW DH load, in the stand-alone Case H0, or to P5 (10 MW district heat load) in Case H1, by reducing the feedwater spraying in the superheater, but at lower loads the turbine inlet temperature will be inevitably reduced in both cases.

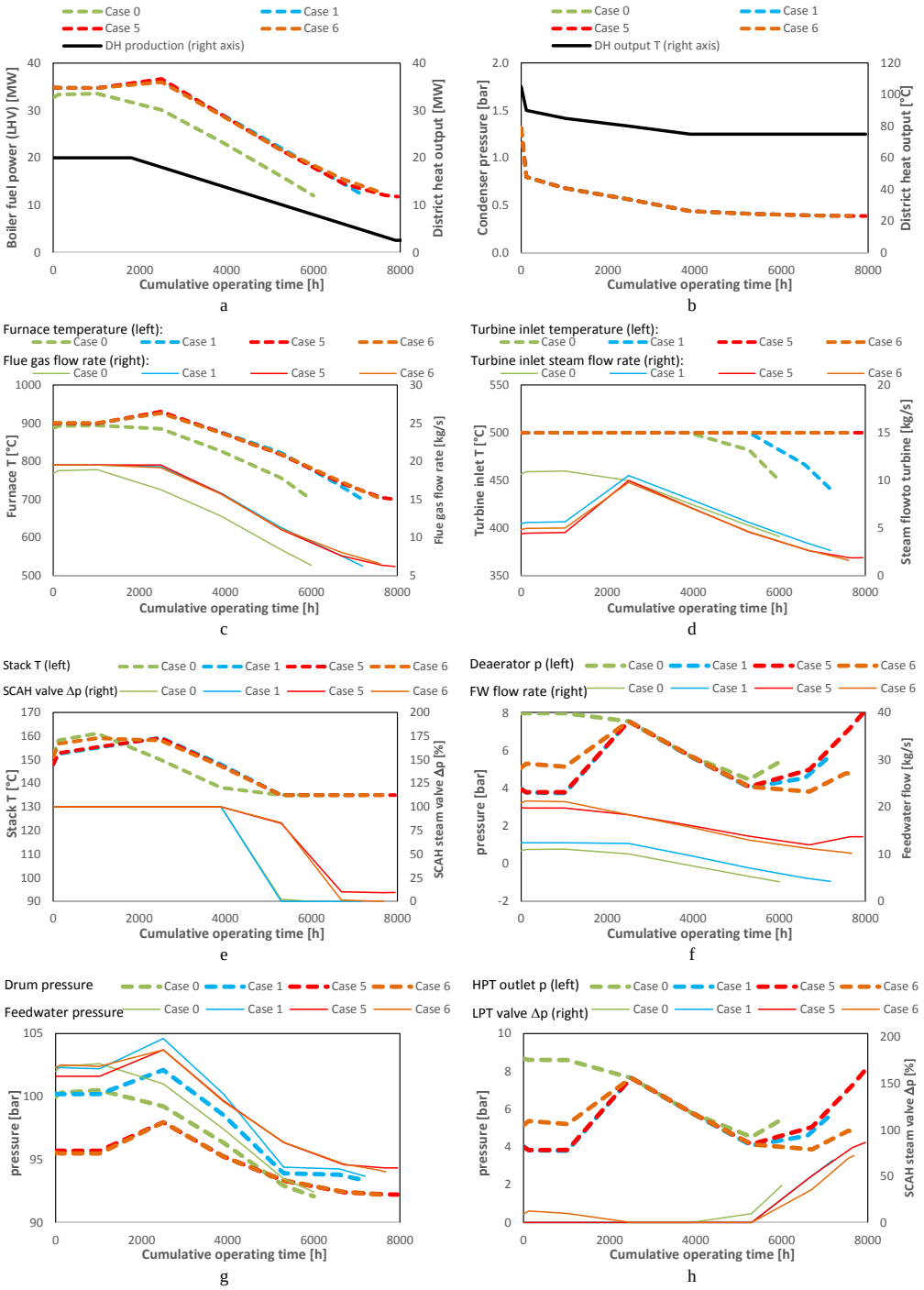

Figure 4.10: Plant operating parameters as functions of cumulative time in the heat load duration curve.

Full live steam superheat can, however, be maintained down to minimum boiler load in both Case H5 and Case H6. In these cases, the HTC heating is taken from the drum as liquid, necessitating a high feedwater flow rate (Figure 4.10f). As the DH load is reduced, but the HTC heat load remains relatively unchanged, the fraction of thermal load extracted from the flue gas in the superheater is reduced relatively more than the total boiler load reduces. As a result, maintaining 500 °C live steam temperature becomes possible in these cases.

At a low enough load, the flue gas temperatures approach the minimum limits of 135 °C stack temperature and 700 °C furnace temperature. The stack temperature is maintained at first by using the SCAH for preheating the air before the luvo from approximately 10 MW DH load downwards. Due to the combination of increasing heating need in the SCAH and reducing pressure levels in the turbine, at load point P6 (8 MW DH) the LPT valve is used to maintain sufficient steam pressure at HPT exhaust to keep the stack temperature at 135 °C. At a slightly lower DH load the same has to be done also with the integrated cases. The minimum operating point of 8 MW heat output (40% DH load) is reached when the furnace temperature reaches 700 °C at 6000 hours of cumulative operating time.

With the integrated cases H5 and H6, an additional restriction at low loads is the reducing main condensate flow as the flow from the DH condenser reduces. The waste heat from HTC flash vapour is recovered to the condensate stream in a low-pressure feed preheater (LPPH), but unlike the condensate flow, the flash vapour flow rate varies little between the different load points. The significant HTC feedwater flow is also part of the main condensate in these cases, increasing the flow, but as the DH power is reduced towards the minimum, boiling would still occur before the deaerator unless measures are taken to prevent this.

Boiling is prevented by a combination of two means. Firstly, increasing deaerator pressure allows a higher condensate temperature. Secondly, by bypassing some of the HTC waste water past the heat recovery heat exchanger (HRX), the condensate entering the LPPH can be made colder, enabling more heat to be absorbed before reaching saturated state.

Increasing the deaerator pressure reduces the power generation slightly, but has little effect on losses or efficiency. The method is limited by the maximum deaerator pressure, and the ability to heat the main condensate stream only to the saturation temperature of the flash vapour, however. Bypassing part of the HTC wastewater past the HRX allows decreasing the DH output further in the CHP process, but at the cost of increased losses and reduced efficiency. As the heat recovery bypass allows a longer period of HTC operation and DH production to smaller loads, it is still economical to do so.

4.3.6 Annual production and consumption

The annual output and consumption rates of energy products are obtained with the multi-period approximation of annual production similarly as with torrefaction. The discretized variation of boiler fuel consumption (including the stoker boiler in Case T0) and DH and net power output are plotted in Figure 4.11, together with the DH heat demand curve. The hydrochar output remains constant at 32.4 MW_{LHV} throughout the HTC operating period: 8000 hours in Case H0, and the same as CHP operating time in the integrated cases. The HTC feedstock rate increases from 35.2 to 38.0 MW_{LHV} as the wood moisture reduces from a winter value of 55 % to a 40 % summer value.

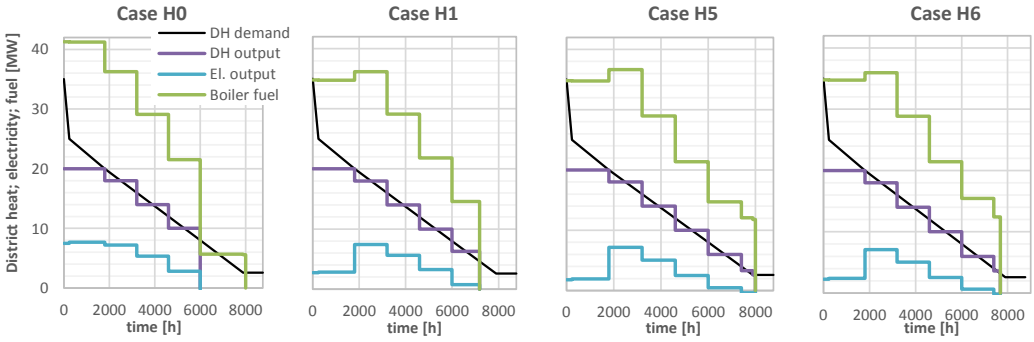

Figure 4.11: Annual production of CHP products (power and heat) together with boiler fuel consumption using the multi-period model, and the DH demand curve. Case H0 includes the boiler fuel used in the separate HTC stoker boiler.

Table 4.6 shows the total annual net production and consumption figures. Electricity is separated to sold and purchased for the purposes of economic analysis, because these have different prices. The total efficiency of the polygeneration plant is also calculated and listed in Table 4.6. These are obtained in terms of both LHV and HHV from the net annual energy production of electricity $E_{el,net}$, district heat Q_{DH} and hydrochar Q_{hc}, and the wood chip input in boiler fuel Q_f and HTC feedstock Q_{feed}:

$$\eta_{LHV} = \frac{E_{el,net} + Q_{DH} + Q_{hc,LHV}}{Q_{feed,LHV} + Q_{f,LHV}} \tag{4.6}$$

$$\eta_{HHV} = \frac{E_{el,net} + Q_{DH} + Q_{hc,HHV}}{Q_{feed,HHV} + Q_{f,HHV}} \tag{4.7}$$

The stand-alone CHP process has a higher efficiency than the stand-alone HTC process in terms of LHV, but as the HTC feedstock is not burnt, the water latent heat loss decreases, resulting in nearly the same HHV efficiencies for both. The differences in efficiencies between the integrated processes are relatively small, with figures mostly between those of the CHP and HTC stand-alone processes, as could be expected.

Case H1 with the more complex HTC heat recovery scheme of the stand-alone process is the most efficient one, in HHV terms more so than either stand-alone process. The good HHV efficiency is explained by extending the operation of the CHP process towards the summer periods, where wood moisture and thus latent heat losses are reduced. The same reason explains why Case H5, the process with the lowest LHV efficiency but also the longest annual operating time, is less behind the other processes in HHV efficiency than in LHV efficiency.

Table 4.6: Annual energy inputs and outputs of separate CHP and HTC plants, co-located separate plants (Case 0), and the three integrated cases.

Case	CHP	HTC	H0	H1	H5	H6
Fuel input						
CHP boiler fuel $Q_{f,BFB,LHV}$ [GWh_{LHV}]	157.3	-	157.3	201.8	212.2	208.4
HTC stoker boiler $Q_{f,S,LHV}$ [GW_{LHV}]	-	49.8	49.8	-	-	-
HTC feed $Q_{HTC,LHV}$ [GWh_{LHV}]	-	292.1	292.1	261.5	292.1	280.0
Total $Q_{chips,HHV}$ [GWh_{HHV}]	193.6	415.7	609.2	565.8	613.8	595.2
Total $Q_{chips,LHV}$ [GWh_{LHV}]	157.3	342.0	499.3	463.3	504.3	488.4
Other energy products						
Net electricity $E_{el,net}$ [GWh]	39.0	-4.85	34.1	28.79	24.53	25.64
Sold electricity $E_{el,s}$ [GWh]	39.0	0	35.3	28.79	24.77	25.69
Purchased electricity $E_{el,p}$ [GWh]	0	4.85	1.22	0	0.23	0.05
District heat output Q_{DH} [GWh]	94.8	0	94.8	102.3	105.1	104.2
Hydrochar output $Q_{hc,HHV}$ [GWh_{HHV}]	0	292.1	292.1	262.4	292.1	280.0
Hydrochar output $Q_{hc,LHV}$ [GWh_{LHV}]	0	259.2	259.2	233.0	259.2	248.8
Trigeneration efficiency						
η_{LHV} [%]	85.1	74.4	77.7	78.6	77.1	77.5
η_{HHV} [%]	69.1	69.1	69.1	69.4	68.7	68.9

The relative fractions of annual outgoing energy flows from the process are shown in Figure 4.12. The blue-green tones represent products, and losses are shown in yellow-red tones. Here, too, the results are broadly similar between the different cases. Among the losses, the largest is the loss of HTC feedstock heating value into liquid and gas fractions, followed by dewatering and drying loss, and boiler loss. The dewatering and drying loss consists only of losses in dewatering and storage, and the difference between the heat consumption of the thermal dryer and the latent heat of the evaporated water. The heat of evaporation in thermal dryer is not considered a loss, as this heat is fully recovered as an increase of the solid product LHV.

While a fairly small fraction of the total, the heat loss with waste water is noticeably larger in Case H5, resulting in this scheme having the poorest overall efficiency. Case H6, which is similar to Case H5, but benefits from a more complex recirculation and heating arrangement to achieve reduced waste water flow rate and losses, has only slightly better

overall efficiency than Case H5 as the waste water loss still remains significantly greater than in Case H1.

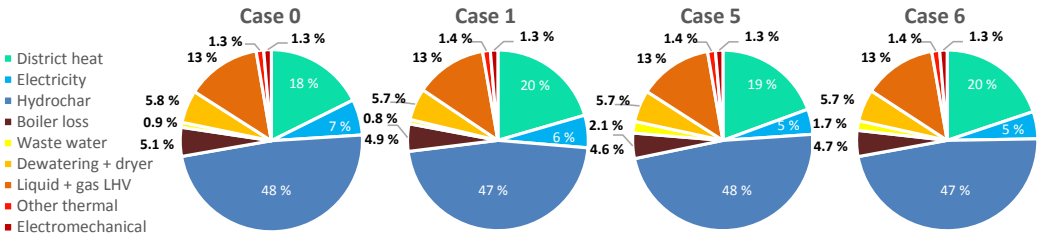

Figure 4.12: Outgoing energy flows from the process in terms of LHV.

The variation of the LHV and HHV efficiencies as a function of cumulative operating time is plotted in Figure 4.13a. The minimum-change integration scheme of Case H1 has the best efficiencies throughout the year, but only by a narrow margin until approximately 6000 hours, or 8 MW DH load. At very low loads the efficiencies of Case H5 and Case H6 reduce faster, and eventually become significantly worse than even the stand-alone HTC plant at 8000 hours.

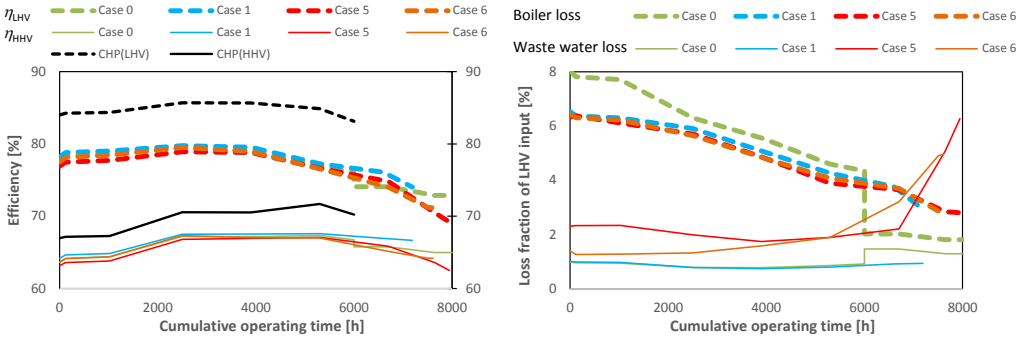

A b

Figure 4.13: Variation of (a) efficiency and (b) main losses (boiler and waste water) as a function of cumulative operating time for the different cases

Although the loss of feedstock LHV to liquid and gas fractions is the single greatest loss component, it remains constant and fixed by the choice of HTC parameters. The second largest component, drying and dewatering losses, varies only relatively little and cannot be significantly affected either by integration method or by plant operation. It is thus the boiler and waste water losses which actually vary the most between the cases and load points; the variation of these losses are shown in Figure 4.13b.

The waste water loss can be seen to increase significantly towards the low-load end of the curve in both Case H5 and Case H6. At high loads the water loss in Case H6 is significantly less than that of Case H5 due to the improved HTC feed heating scheme, but towards the lowest DH loads the Case H6 water loss increases to become even higher than that of Case H5. This is due to the need to bypass the warm waste water stream past the heat recovery heat exchanger in order to maintain the ability of the LPPH to absorb the heat of condensing vapour from the flash tank. The Case H6, with its reduced water flow, needs bypassing already at a higher CHP load, negating part of the efficiency advantage of this arrangement.

In terms of boiler losses, all integrates are broadly similar. The lower efficiency of the stoker boiler shows as a slightly increased boiler losses at CHP part load. The greater combined load of the two boilers makes the stand-alone boiler loss much greater at full CHP load.

5 Economic analysis

One concern for the profitability of any energy sector investment in the current situation is the significant uncertainty over future energy prices, emission trading, subsidies and taxes. Currently without subsidies or significantly increased CO_2 emission cost through taxation or emission trading, biochar produced by either torrefaction or the HTC process is not a competitive alternative to coal. The electricity markets in Northern Europe are also at a period of change, and uncertainty over renewable power subsidies and the future of nuclear power create serious doubts about the price of electricity. This makes the economic evaluation of a pure CHP plant also subject to significant uncertainty. A range of different scenarios are thus considered regarding both biochar and electricity prices.

The multi-period model described in chapter 2.1 is used to obtain the annual production and consumption of energy products as a weighted sum in evaluating the different integrated plant concepts, and in slightly simplified form also in district heat condenser optimization.

In both integration studies with biomass conversion technologies and condenser optimization, the cost of the basic CHP plant and the boiler have been estimated on the basis of data in Kuitunen (2007).

5.1 Cost assumptions and scenarios

Three different electricity price scenarios are considered for the market price of sold electricity. Constant electricity prices throughout the plant operating time are assumed. The electricity prices have been estimated from the scenarios for electricity market price development presented in a report ordered by the Finnish Ministry of Employment and Economy (Pöyry Management Consulting, 2015).

The operating and maintenance (O&M) costs $r_{O\&M}$ represent the ratios of expenses spent annually on operating and maintenance to the total capital investment (TCI) of the same unit. For a small-scale bio-fired CHP plant a value of $r_{O\&M,CHP}$ = 4 % is assumed, based on data from Kuitunen (2007). This is assumed to be unchanged for the CHP plant whether the plant is co-located with an independent biomass conversion process or not, in integration studies, and regardless of the size and cost of the district heat condenser in condenser optimization.

As torrefaction and HTC are new technologies, there is no experience-based data for the operating costs of industrial-scale equipment for these processes. To obtain a conservative estimate and account for possible difficulties of starting industrial-scale operation of a new technology, the O&M cost of the torrefaction unit is estimated slightly higher, at $r_{O\&M,torre}$ = 6 % . In addition to the novelty of the technology, the HTC plant has also the additional challenge of operating with a two-phase slurry. Several components may prove to be prone to fouling, clogging and corrosion, and an even higher O&M fraction of $r_{O\&M,HTC}$ = 8 % is thus assumed to obtain a conservative estimate.

The combined $C_{O\&M}$ for each integrated plant configuration is then obtained by using the mean $r_{O\&M}$ weighted with the fractions of CHP and either the torrefaction or HTC plant cost,

$$C_{O\&M,CHP+torre} = \left(r_{O\&M,CHP} \frac{PEC_{CHP}}{PEC_{CHP+torre}} + r_{O\&M,torre} \frac{PEC_{torre}}{PEC_{CHP+torre}} \right) \cdot TCI \qquad (5.1)$$

and

$$C_{O\&M,CHP+HTC} = \left(r_{O\&M,CHP} \frac{PEC_{CHP}}{PEC_{CHP+HTC}} + r_{O\&M,HTC} \frac{PEC_{HTC}}{PEC_{CHP+HTC}} \right) \cdot TCI \, . \qquad (5.2)$$

The assumed values of cost data when not treated as variables are listed at Table 5.1.

Table 5.1: Energy and O&M cost assumptions used in economic analysis.

Cost item	**value**
Wood chip price c_f	20 €/MWh$_{LHV}$
Price of purchased electricity price $c_{el,p}$	100 €/MWh
Price of sold electricity (high) $c_{el,s}$	77 €/MWh
Price of electricity (medium) $c_{el,s}$	44 €/MWh
Price of electricity (low) $c_{el,s}$	21 €/MWh
District heat price c_{DH}	60 €/MWh
Price of biochar (torrefied pellets or hydrochar) c_{bc}	40 €/MWh$_{LHV}$
Annual O&M cost ratio, CHP plant only $r_{O\&M,CHP}$	4 % of TCI
Annual O&M cost ratio, torrefaction plant $r_{O\&M,torre}$	6 % of TCI
Annual O&M cost ratio, HTC plant $r_{O\&M,HTC}$	8 % of TCI

5.2 Profitability evaluation of integration concepts

The different plant concepts integrating a basic CHP plant with torrefaction or the HTC process are evaluated by using three different evaluation metrics: net present value (NPV), internal rate of return (IRR) and payback period (PBP). While NPV is usually recommended as the best evaluation metric if only one is used (Megginson & Smart, 2008; Sinnott, 2005), and typically all methods give the same accept/reject decision, in case of mutually exclusive projects of different scope, they may sometimes suggest a different ranking of the options; three different metrics are thus used here (Megginson & Smart, 2008).

The NPV of a project is the sum of the total present worth of future cash flows during the economic project life time of n years discounted at an interest rate of i, minus the value of total capital investments TCI:

$$NPV = \frac{(1+i)^n - 1}{i \cdot (1+i)^n}\left[E_{\mathrm{el,s}} c_{\mathrm{el,s}} + Q_{\mathrm{DH}} c_{\mathrm{DH}} + Q_{\mathrm{bc}} c_{\mathrm{bc}} - \left(Q_{\mathrm{f,LHV}} + Q_{\mathrm{feed,LHV}}\right) c_{\mathrm{f}} - E_{\mathrm{el,p}} c_{\mathrm{el,p}} - C_{\mathrm{O\&M}}\right] - TCI \qquad (5.3)$$

where $E_{\mathrm{el,s}}$ and $E_{\mathrm{el,p}}$ are the electricity sold and purchased annually [MWh] and $c_{\mathrm{el,s}}$ and $c_{\mathrm{el,p}}$ the prices thereof [€/MWh], Q_{DH} is the annual district heat production [MWh] and c_{DH} the district heat price [€/MWh], Q_{bc} the annual biochar (torrefied biochar or hydrochar) production [MWh] and c_{bc} the biochar price [€/MWh], $Q_{\mathrm{f,LHV}}$ and $Q_{\mathrm{feed,LHV}}$ the annual wood chip consumptions for boiler fuel and biochar production feedstock and c_{f} the price of wood chips [€/MWh], and $C_{\mathrm{O\&M}}$ is the annual operating and maintenance cost [€]. An economic life time of n = 25 years and an interest rate of i = 0.10 are assumed.

The IRR is found by using Equation (5.3) and solving iteratively such interest i that the NPV becomes zero. The PBP is found similarly by setting the NPV to zero in Equation (5.3), and solving for the number of years n.

The total capital investment (TCI) is the total amount of money needed to purchase and install all the equipment necessary for the plant. The cost data for standard equipment, such as pumps, heat exchangers and tanks has been taken from the literature (Peters *et al.*, 2003; Sinnott, 2005). The cost of specialized HTC process equipment, such as slurry pumps, pellet and filter presses, wood chip dryers and conveyors, is based on vendor information from Erlach (2014). Torrefaction reactor cost has been estimated at near the upper end of the relatively wide range of equipment cost presented in Batidzirai *et al.* (2013). In addition to the cost of purchased equipment (PEC), the TCI includes other direct costs related to the installation of equipment, various indirect costs such as engineering, supervision and start-up related expenses, as well as contractor fees, contingencies and working capital costs. The methodology of determining these costs has been explained in detail in Publication V and Publication VII.

The annual net cash flow rates of the different integrated scenarios are also compared at different interest rates. While an interest rate of i = 0.10 used in Equation (5.3) is considered to represent a level of profit that an investor would probably require for an investment to be considered attractive, funding for the project would likely be available at a clearly cheaper rate. The annual net cash flow rate is thus evaluated also at an interest rate of i = 0.05 to obtain an estimation for whether the plant would reach break-even at expected values of costs. The annual net cash flow rate is obtained from

$$C_{\mathrm{tot}} = E_{\mathrm{el,s}} c_{\mathrm{el,s}} + Q_{\mathrm{DH}}\, c_{\mathrm{DH}} + Q_{\mathrm{bc}} c_{\mathrm{bc}} - \left(Q_{\mathrm{f,LHV}} + Q_{\mathrm{feed,LHV}}\right) c_{\mathrm{f}} - \frac{i \cdot (1+i)^n}{(1+i)^n - 1} TCI - E_{\mathrm{el,p}} c_{\mathrm{el,p}} - C_{\mathrm{O\&M}}, \qquad (5.4)$$

where the multiplier term for *TCI* represents the fraction of the investment that is annually amortized.

5.3 Comparison of the studied cases

5.3.1 Investment costs

The investment costs of the studied cases are summarized in Table 5.2 below. The CBM figure represents the total cost of the bare module (i.e. including costs related to the erection of equipment such as instrumentation, piping, electrical installation, etc.). A more detailed breakdown of the TCI figure can be found in Publication V and Publication VII. Boiler in the PEC breakdown refers to the stoker boiler of the torrefaction and HTC plants when not integrated to the CHP plant, and "Torre" is used as an abbreviation for the torrefaction plant.

Table 5.2: Investment costs of the studied cases. "Torre" refers to the torrefaction plant, and boiler to the separate stoker boiler supplying heat to the non-integrated torrefaction or HTC plants. All costs figures are listed as millions of euros.

	CHP	Torre	HTC	T0	T5	T6	H0	H1	H5	H6
PEC										
Torre	-	3.0	-	3.0	2.7	2.7	-	-	-	-
HTC	-	-	3.7	-	-	-	3.7	3.7	3.2	3.2
Boiler	-	1.8	1.6	1.8	-	-	1.6	-	-	-
CHP	5.8	-	-	5.8	5.8	5.8	5.8	5.8	5.8	5.9
CBM	16.6	12.5	15.3	29.1	23.2	23.2	31.9	27.3	26.0	26.2
TCI	27.1	20.7	25.0	47.7	38.1	38.1	52.0	44.5	42.5	42.7

It can be seen that between the torrefaction and the HTC processes, the simpler, atmospheric-pressure torrefaction results in a slightly cheaper plant than the HTC where much of the process takes place under significant pressure. Integration allows clear cost savings in comparison with the co-located but separate plant. By far the most significant saving is the omission of the separate boiler when heat is provided by the CHP plant. Cost savings are possible also particularly in the HTC process, where cases H5 and H6 are much simpler in comparison to the stand-alone HTC plant and its minimum-change integrated equivalent H1.

The cost of the CHP plant is not affected significantly by the integration. Cases H5 and H6 are both approximately 0.1 M€ more expensive due to the much increased capacity of the feedwater system to provide sufficient pressurized process water to the HTC plant, although due to rounding, only H6 shows a higher PEC figure in the table.

5.3.2 Profitability comparison

The results of the profitability evaluation by the IRR, NPV and PBP methods at varying biochar prices are shown in Figure 5.1 (torrefaction) and Figure 5.2 (HTC). When not used as variables, the costs of Table 5.1 are used, with an interest rate of 10 % and a 25-

year plant economic lifetime. Three scenarios are assumed for the plant TCI and the sold electricity prices. The investment cost scenarios considered are the base scenario of Table 5.2 (thick black lines in the figure), and optimistic (green lines) and pessimistic (red lines) adjusted 25% down and up, respectively, from the baseline scenario. The electricity price scenarios refer to the costs presented in Table 5.1, and are represented by line type: solid (high), dashed (medium) and dotted (low). The black crosses represent the cost of char at which the considered economic parameter reaches the value of a simple CHP plant without an integrated biomass conversion process.

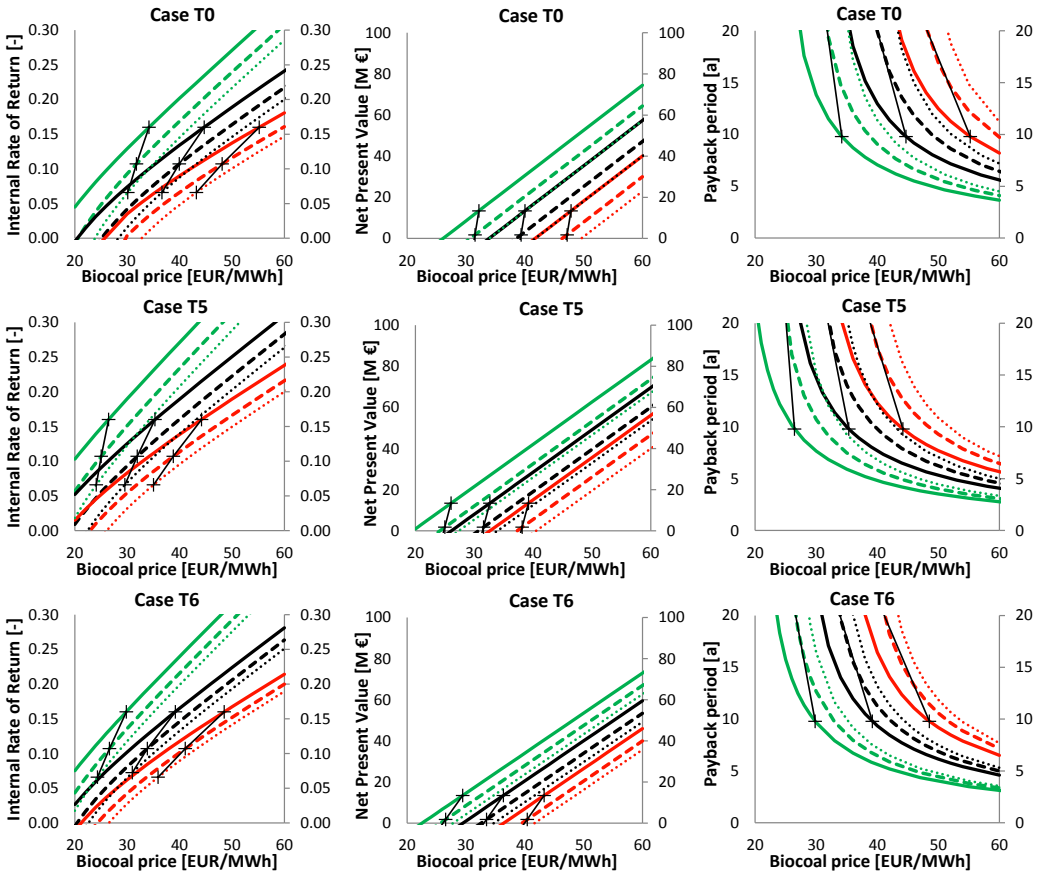

Figure 5.1: Studied cases combining CHP with torrefaction compared in terms of IRR, NPV and PBP. The crosses connected by black lines represent the hydrochar prices required to improve the economic parameter shown in the figure over a stand-alone CHP. The green lines represent optimistic (-25%), red lines pessimistic (+25%) investment cost. Solid lines represent high, dashed lines medium, and dotted lines low electricity price.

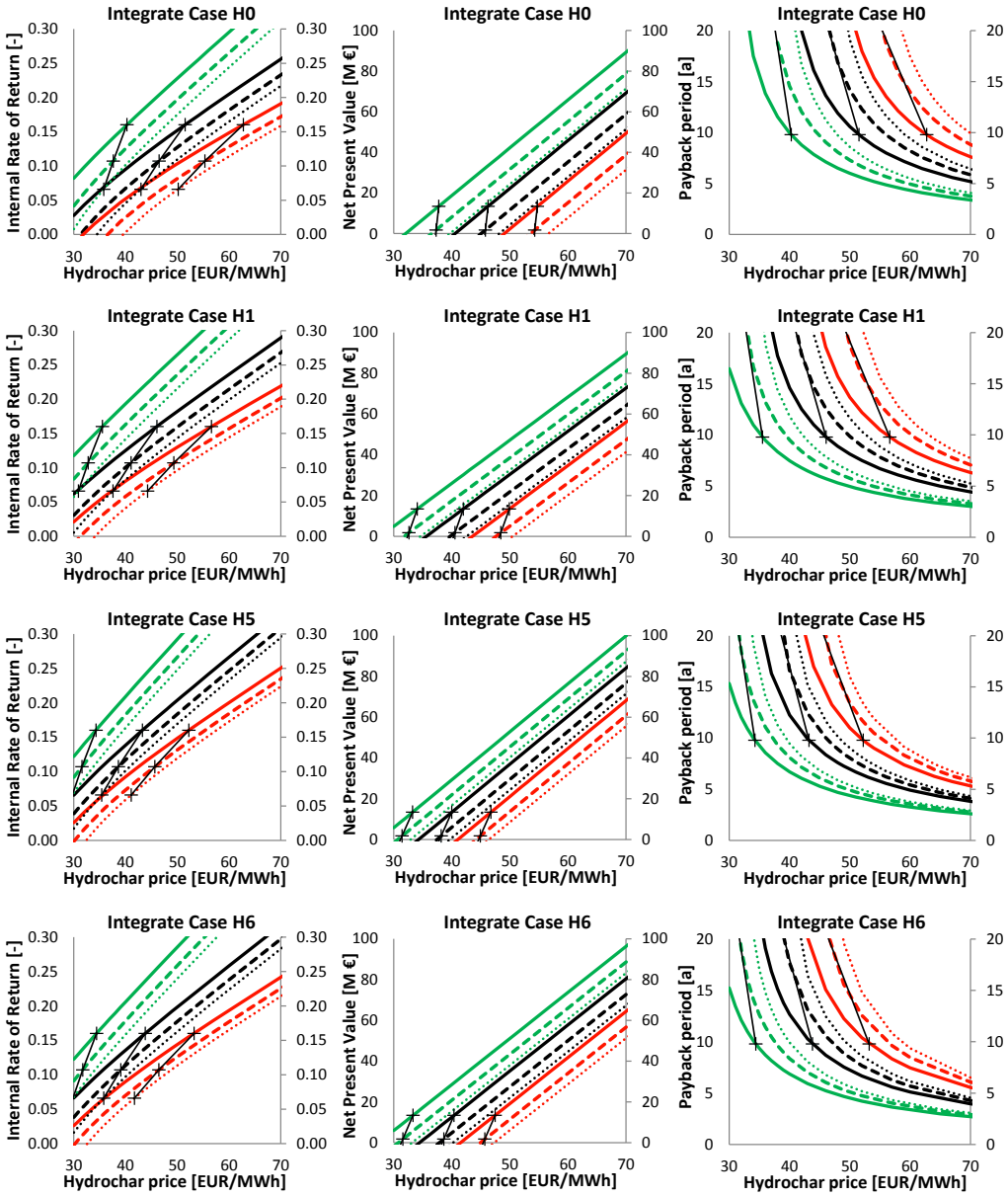

Figure 5.2: Studied cases combining CHP with hydrothermal carbonization compared in terms of IRR, NPV and PBP. The crosses connected by black lines represent the hydrochar prices required to improve the economic parameter shown in the figure over stand-alone CHP. The green lines represent optimistic (-25%), red lines pessimistic (+25%) investment cost. Solid lines represent high, dashed lines medium, and dotted lines low electricity price.

Some general trends are evident from the results shown in Figures 5.1 and 5.2. Firstly, it can be seen that both with torrefaction and HTC, all economic figures of merit are improved by moving from the separate, co-located plants (T0 and H0) to the integrated plants. Another clear conclusion is that due to the lower cost of torrefaction equipment in comparison with HTC, a lower price of char is sufficient to achieve profitability, or an improvement over a stand-alone CHP plant. Among the torrefaction integrates, all three figures of merit show Case T5 to be the economically best scenario. Among the HTC integrates, Case H5 appears to be the best, although Case H6 is only marginally inferior.

Between T5 and H5, is appears that depending on the investment cost and electricity price scenario considered, approximately 5…10 € higher prices are required for hydrochar than for torrefied biochar to raise the economic parameters above the figures of a pure CHP plant. With the baseline investment cost and a medium electricity price scenario, the required price for torrefied biochar is approximately 32 €/MWh, while price of hydrochar should reach 39 €/MWh before the economic performance will show improvement over a pure CHP plant.

The cash flow rates for the considered cases, as well as the three stand-alone processes are shown in Tables 5.3 (torrefaction and CHP) and 5.4 (HTC). The economic parameters of Table 5.1 and unadjusted investment costs of Table 5.2 are used in the evaluation. A medium electricity price scenario is assumed. It can be seen that if an interest rate of 10% is expected for the investment, the CHP plant returns only a marginally profitable net cash flow, while both torrefaction and HTC processes fail to reach break-even. At 5% interest profitability improves, and of the biomass conversion processes the stand-alone torrefaction plant yields a slightly positive net cash flow rate.

Table 5.3: Annual net cash flow rates of stand-alone torrefaction and CHP plants, combined on the same site but not integrated (Case T0) and the integrated cases (T5 and T6).

	Torrefaction	**CHP**	**T0**	**T5**	**T6**
Investment amortization (i = 10 %) [M€]	-2.28	-2.98	-5.26	-4.20	-4.20
Investment amortization (i = 5 %) [M€]	-1.47	-1.84	-3.39	-2.71	-2.71
Operation and maintenance [M€]	-1.65	-1.08	-2.32	-1.75	-1.75
Boiler fuel [M€]	-1.03	-3.15	-4.17	-4.17	-3.84
Torrefaction feedstock [M€]	-4.61	0	-4.61	-4.25	-4.07
Purchased electricity [M€]	-0.66	0	-0.16	-0.13	-0.14
Sold electricity [M€]	0	1.71	1.49	1.39	0.89
Sold district heat [M€]	0	5.69	5.69	6.19	6.11
Sold biochar [M€]	9.69	0	9.69	8.97	8.59
Annual net cash flow (i = 10 %) [M€]	-0.54	0.19	0.35	2.05	1.59
Annual net cash flow (i = 5 %) [M€]	0.27	1.34	2.22	3.54	3.09

Table 5.4: Annual net cash flows of a stand-alone HTC plant, on the same site with CHP (H0), and integrated cases (H1, H5 and H6).

	HTC	**H0**	**H1**	**H5**	**H6**
Investment amortization (i = 10 %) [M€]	-2.75	-5.73	-4.91	-4.68	-4.70
Investment amortization (i = 5 %) [M€]	-2.19	-4.03	-3.36	-3.17	-3.19
Operation and maintenance [M€]	-2.00	-3.08	-2.48	-2.31	-2.33
Boiler fuel [M€]	-1.00	-4.14	-4.04	-4.24	-4.24
HTC feedstock [M€]	-5.84	-5.84	-5.23	-5.84	-5.60
Purchased electricity [M€]	-0.48	-0.12	0	-0.02	-0.005
Sold electricity [M€]	0	1.55	1.27	1.09	1.13
Sold district heat [M€]	0	5.69	6.14	6.31	6.25
Sold hydrochar [M€]	10.37	10.37	9.32	10.37	9.96
Annual net cash flow (i = 10 %) [M€]	-1.70	-1.30	0.07	0.66	0.46
Annual net cash flow (i = 5 %) [M€]	-1.14	0.40	1.62	2.17	1.97

Combining the torrefaction or HTC with the CHP plants (Cases T0 and H0) on the same site naturally increases the magnitude of the figures in all cases compared to a single stand-alone plant. With both of the thermal conversion processes, integration by any of the studied schemes improves the figures clearly over the co-located plants. All integrated schemes share the advantage of reduced investment and O&M costs compared to co-located separate plants, as well as increased district heat output. These advantages outweigh the one drawback shared by most of the integrated schemes, which is the inability to operate the biomass conversion processes for the full 8000 hours assumed for the stand-alone plants.

For torrefaction, the best results are obtained with Case T5. Compared to the other integrate, Case T6, this case has the advantage of higher electricity sales profit. While full-load electricity production is much reduced even in this case (see Figure 4.3), the part-load power output is significantly increased as a result of using backpressure steam for the torrefaction dryer. Together with the increased operating time, this is enough to reach almost the same annual net electricity production as the stand-alone CHP plant.

Among the HTC plants, integration also appears to improve the figures over the stand-alone HTC and/or CHP plants. Unlike the stand-alone HTC plant, all integrates are profitable with the 10% interest rate profit requirement, although Case H1 only marginally so. The cash flow rates obtained with Case H1 compare unfavourably also to the CHP plant, but the other two integrates, Case H5 and the similar but slightly more energy-efficient Case H6 both show an increasing cash flow rate also compared to the CHP plant at 10% interest rate.

Assuming an interest rate of 5 %, all of the integrated HTC cases become more clearly profitable, with a greater net cash flow rate than a pure CHP plant. The cash flow rate of the combined but non-integrated stand-alone plant of Case H0 also rises to a positive figure, although still inferior to the integrates. With either interest rate, the HTC stand-alone process is unprofitable, therefore making Case H0 also inferior to a pure CHP plant.

All integrated cases improve the annual net cash flow in comparison to having two separate processes, and except for Case H1 at the higher interest rate of 10%, also improve the cash flow of the pure CHP plant, with Case H5 providing the highest increase.

5.3.3 Sensitivity analysis

A simple sensitivity analysis was carried out to evaluate the sensitivities of different plant configuration options to variations of different costs and prices. This was performed by varying each chosen parameter up and down by 20%, and plotting the resulting change of investment IRR as a tornado graph. A baseline investment cost and medium sold electricity price scenario are assumed in this graph. The results of the analysis are shown for torrefaction in Figure 5.3, and for HTC in Figure 5.4.

The profitability of the torrefaction and HTC stand-alone plants is clearly very sensitive especially to the price of the wood feedstock, as well as to the investment and O&M costs. The profitability of the CHP plant is much less affected by the price of wood chips, as both conversion efficiency and the prices assumed for the products are better than in the stand-alone HTC plant.

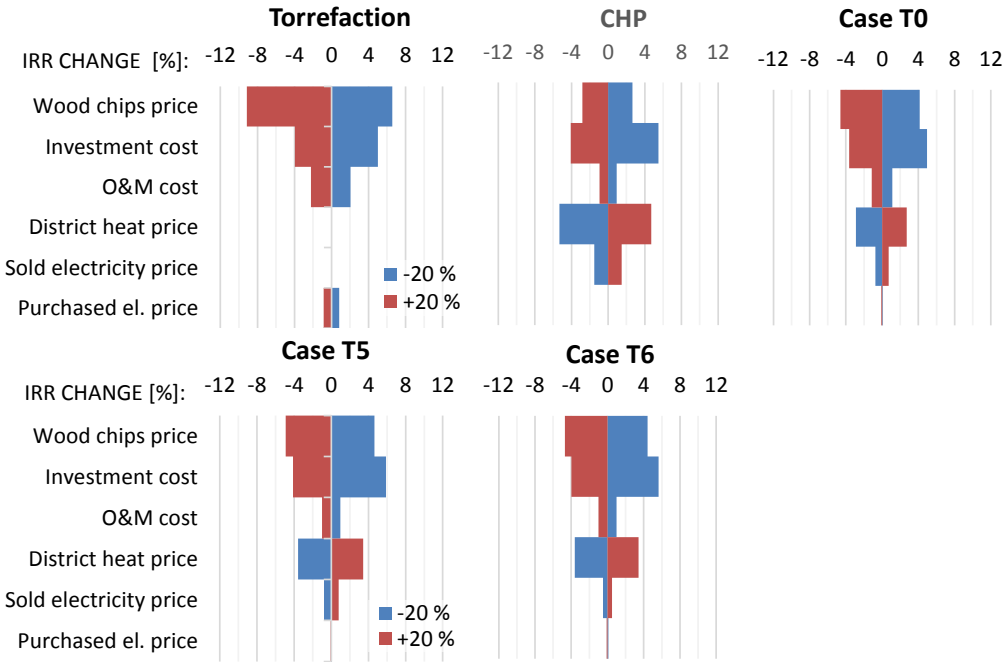

Figure 5.3: Sensitivity analysis of IRR with ±20 % change of parameters for the torrefaction plant, CHP plant, and different co-located and integrated torrefaction-CHP cases. IRR variation is shown in percentage points.

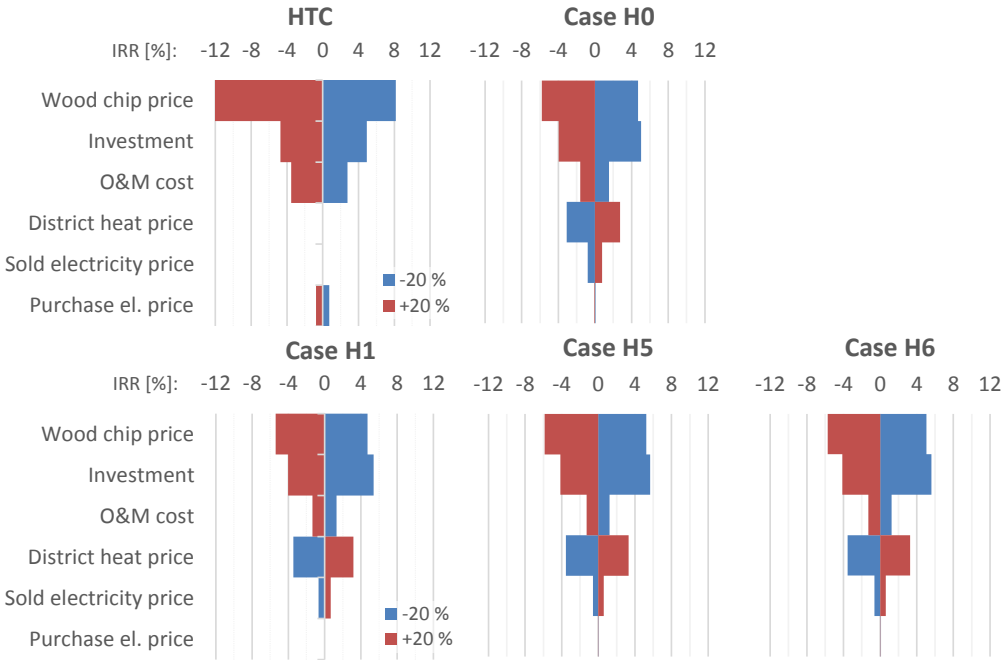

Figure 5.4: Sensitivity analysis of IRR with ±20 % change of parameters for HTC plant configurations. IRR variation is shown in percentage points.

The CHP plant is most sensitive to the price of district heat, which is the main product. Sensitivity to electricity price appears superficially low. Electricity price is likely by far the most volatile of the prices, however; while the 20% variation of parameters can be considered moderately large for most of the parameters, electricity price is subject to several times greater uncertainty.

The sensitivities of the different combined cases are broadly similar to each other. Changes in raw wood or investment cost will yield the biggest changes in profitability, but compared to a stand-alone torrefaction or HTC process, sensitivity to these prices is much reduced. Compared to the CHP, the sensitivity to varying district heat or electricity price is also much reduced in the four cases combining both processes.

6 Condenser model

This section describes the condenser model developed for the purpose of optimization. After a brief review of literature on steam condenser modelling for power plants in chapter 6.1, chapter 6.2 describes the heat transfer model, originally developed for large condensing power plant seawater condensers and presented in Publication I. Model validation is included. Following this, the adaptation of the developed model for a CHP plant back pressure district heat condenser (DHC) is presented in chapter 6.3. The chapter is based on the final model developed and presented in Publication VI, which in turn includes some model improvements and mechanical sizing methodology from Publication II.

6.1 Background

Most shell-and-tube heat exchanger optimization studies are based on rating the heat exchangers by using an average overall heat transfer coefficient U to determine the heat transfer area. This is usually reasonable with single-phase heat exchangers, such as in the studies by Mizutani *et al.* (2003), Muralikrishna & Shenoy (2000); Ponce-Ortega *et al.* (2009); Sanaye & Hajabdollahi (2010); Babu & Munawar (2007); and Costa & Queiroz (2008).

With condensers, local variations are often considered. Accounting for the velocity reduction due to condensation has been done by calculating U at steam inlet and outlet conditions and using their average in Hajabdollahi *et al.* (2011). A finned-tube condenser is modelled by using multiple elements in Sanaye & Dehghandokht (2011). Other heat transfer evaluation methods have also been used in optimization, such as commercial software (Chaudhuri *et al.*, 1997), and computational fluid dynamics (CFD) (Stevanović *et al.*, 2001), both of which consider only single-phase heat exchangers.

While a single-phase liquid-liquid heat exchanger can be modelled adequately with a single average overall heat transfer coefficient, power plant steam condensers are more problematic due to spatial variations in steam pressure, saturation temperature, and condensate inundation. In an attempt to account for these, published power plant steam condenser models have already for several decades involved mostly detailed 2-D and 3-D numerical models. Al-Sanea *et al.* (1983) used first a single-phase 2-D model, and later implemented a two-phase 2-D model (Al-Sanea *et al.*, 1985). A quasi-3-D method used to model power station condensers is reported by Zhang *et al.* (1993). Malin (1997) used a 3-D model to model a marine condenser. Ramon and Gonzalez (2001) developed a 3-D model of a church window -type condenser, and Prieto *et al.* (2003) compared the results of a similar model to HEI correlations and a 2-D simplification of the 3-D model. More recently, Zeng *et al.* (2012) have developed 3-D models of three power plant condenser configurations, and compared the results to HEI correlations. While the 3-D models are likely the most accurate option in the absence of extensive proprietary data available to condenser manufacturers, the difficulties of modelling two-phase flow, phase

change and interaction of the two phases will still produce significant uncertainties in the results.

In Publication I, which considered the development of a condenser component model to be run as part of a plant model in an on-line condition monitoring software, such a condenser model would clearly be impractically complex and time-consuming. A similar problem arises within the topic of this thesis: when the condenser model must be run hundreds or thousands of times by the optimization algorithm, a 3-D CFD model would clearly be impractical.

To find the best compromise solution to the conflicting requirements of a short calculation time and good modelling accuracy, three different types of heat transfer models were implemented, validated and compared: one based on correlations by the Heat Exchanger Institute (HEI), a simple 0-D model with a single average overall heat transfer coefficient U, and a two-dimensional (2-D) simplification of the actual tube bundle geometry.

The 2-D method used in this work differs from that of Prieto *et al.* (2003) mainly in the treatment of condensation heat transfer. In Prieto *et al.* (2003) the vapour phase heat transfer coefficient was determined by using the single-phase equations from Taborek (1983) as the basis, with the phase change and heat and mass transfer modelled according to the film theory by Colburn and Hougen (1934), corrected by Ackermann's factor according to Ackermann (1937). In Publication I, the condensate film heat transfer coefficient was obtained from Nusselt's correlation for single horizontal tube without vapour shear, originally presented in Nusselt (1916), and modified by a shear correction according to Shekriladze & Gomelauri (1966) and Butterworth (1977).

For validation, measured plant data was available only for a large seawater-cooled vacuum condenser plant. Due to the more complex geometry and much higher flow velocities, this was considered to be the more challenging case to model. Thus, while the CHP plant backpressure condenser model had to be implemented and used without validation, it was assumed that a modelling methodology providing adequate accuracy with the vacuum condenser model would be adequate also for the backpressure condenser.

6.2 Large vacuum condenser

The heat transfer model was initially developed for large, approximately 200…250 MW seawater-cooled vacuum condensers. Three different types of condenser tube bundle configurations were studied. Labelled A, B, and C, these are shown in Fig. 6.1, with the simplified 2-D geometries to illustrate the treatment of steam flow in the models. The simplification is based on the assumption of steam entering the tube bank perpendicularly, and estimating the average number of rows j_{max} that the steam would flow across in the bundle. Each tube bundle has two water-side passes, splitting the shown tube bundles to top and bottom passes in case of configuration A, and left- and right-side passes in configurations B and C.

In the 2-D model the steam flow is assumed to be in perfect cross flow across the tubes. The vapour and liquid phases of the wet steam are assumed to have always the same flow direction. In geometries A and C, the number of tubes N_T transverse to the steam flow is estimated to remain relatively constant. Each row thus has N_{TOT} / j_{max} tubes in transverse direction to the steam flow. Geometry B represents a so-called church window type condenser, in which the cross-sectional area for steam flow reduces more clearly towards the centre of each "church window". The tube bank is estimated to narrow steadily until finally $N_{T,jmax} = 0.30N_{T,1}$. The tube arrangement in each condenser is equilateral triangular.

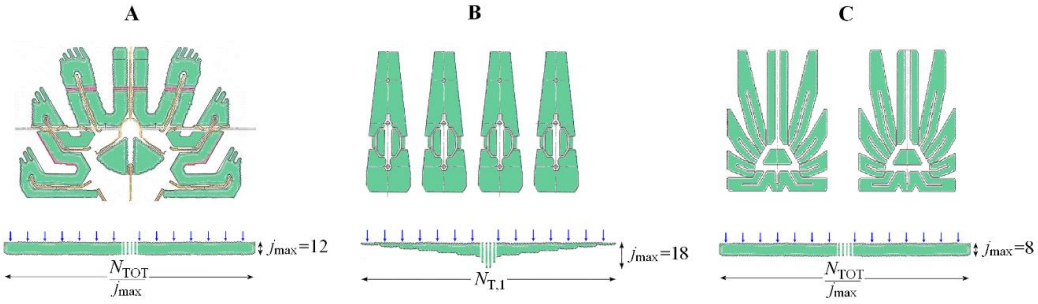

Figure 6.1: Studied tube bundle configurations. The green area in the top figures represents the actual tube bundle configuration viewed in tube axis direction, the lower figures present the 2-D model simplifications.

The main physical characteristics as well as typical operating conditions are described in Table 6.1. The plants operate at base load, with the water flow switched between a lower (winter) and higher (summer) value. Seawater temperature varies from 0 to 20 °C.

Table 6.1: Main specifications and typical base-load operating conditions of the studied condenser types.

Tube bundle geometry	**A**	**B**	**C**
Tube material	SMO steel	Titanium	Titanium
Number tubes per pass [-]	5225	6500	8800
Tube thermal conductivity [W/mK]	14	21	21
Tube outer diameter [mm]	28	24.0	22.0
Tube wall thickness [mm]	0.8	0.5	0.5
Tube pitch [mm]	35.0	32.5	27.5
Tube length [m]	8.89	8.97	9.27
Shell width [m]	6.7	6.7	6.7
Cooling water mass flow rate [kg/s]	4800 or 6200	4500 or 5900	4400 or 5800
Steam mass flow rate [kg/s]	105	105	105
Steam pressure at inlet [	25-60	20-55	20-55

6.2.1 Calculation procedure

The algorithm divides each water-side pass in i_{max} segments in the tube axis direction, and j_{max} rows in the steam flow direction (see Figure 6.2). With data for the incoming water and steam flow rates and states to element (i,j) obtained from the outlet conditions of elements (i-1,j) and (i,j-1), the calculation is performed iteratively for both passes, one segment i at a time, starting with an initial guess of steam mass flow rate into element (i,1), and adjusting this until the vapour-phase flow after (i,j_{max}) becomes zero. The water is assumed to be mixed between the passes. Steam pressure drop before entry to tube bank $\Delta p_{h,in}$ is calculated separately for each segment i,

$$\Delta p_{h,in,i} = ½\rho_{h,V,i}\, w_{h,V,i}^2 \cdot 2 \tag{6.1}$$

where velocity $w_{h,V,i}$ is based on the free flow area in the shell to segment i, with flow area of $L_{tb}B_{sh}$ / ($2i_{max}$).

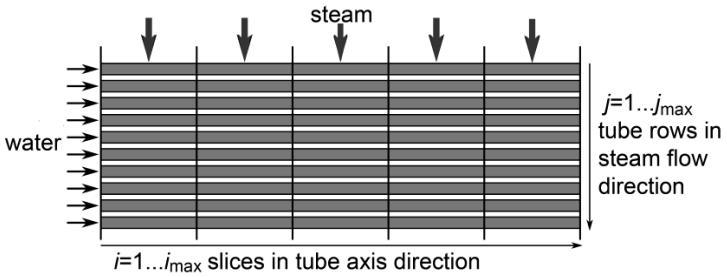

Figure 6.2: Division of one condensing pass into $i_{max} \times j_{max}$ calculation elements.

The calculation of each element is based on assumptions of constant condensation temperature and U. The water outlet temperature to element (i+1, j) and vapour-phase mass flow rate to element (i, j+1) are calculated from the heat transfer rate $\Phi_{i,j}$ in the element applying the ε-NTU method according to equations (6.2) to (6.7). Steam pressure drop is calculated after the heat transfer calculations.

$$U_{i,j} = \left[\frac{d_o}{d_i} \left(R''_{tf} + \frac{1}{h_{c,i,j}} \right) + R''_{w} + \frac{1}{h_{h,i,j}} \right]^{-1} \tag{6.2}$$

$$NTU_{i,j} = \frac{U_{i,j} A_{i,j}}{\dot{m}_{c,j} c_{p,c,i,j}} \tag{6.3}$$

$$\varepsilon_{i,j} = 1 - e^{-NTU_{i,j}} \tag{6.4}$$

$$\Phi_{\mathrm{i,j}} = \varepsilon_{\mathrm{i,j}} \dot{m}_{\mathrm{c,j}} c_{\mathrm{p,c,i,j}} \left(T_{\mathrm{h,i,j}} - T_{\mathrm{c,i,j}} \right) \tag{6.5}$$

$$T_{\mathrm{c,i+1,j}} = T_{\mathrm{c,i,j}} + \frac{\Phi_{\mathrm{i,j}}}{\dot{m}_{\mathrm{c,j}} c_{\mathrm{p,c,i,j}}} \tag{6.6}$$

$$\dot{m}_{\mathrm{h,V,i,j+1}} = \dot{m}_{\mathrm{h,V,i,j}} - \frac{\Phi_{\mathrm{i,j}}}{h_{\mathrm{fg,i,j}}} \tag{6.7}$$

6.2.2 Local heat transfer and pressure drop calculation

The tube inside heat transfer coefficient h_{c} for cold water is determined from the Nusselt number *Nu*, obtained from the correlation originally published by Petukhov and Popov (1963) as cited in (Shah & Sekulic, 2003),

$$Nu_{\mathrm{c}} = \frac{h_{\mathrm{c}} d_{\mathrm{i}}}{k_{\mathrm{c}}} = \frac{\frac{f}{8} \mathrm{Re}\,\mathrm{Pr}}{a + 12.7 \sqrt{\frac{f}{2}} \mathrm{Pr}^{2/3} - 1} \left(\frac{\mu}{\mu_{\mathrm{c}}} \right)^{0.14}, \quad a = 1.07 + \frac{900}{\mathrm{Re}} - \frac{0.62}{1 + 10\,\mathrm{Pr}} \tag{6.8}$$

The correlation is valid for $0.5 < Pr < 2000$ and $10^4 < Re < 5 \cdot 10^6$. The friction factor f is obtained from a formulation by for hydraulically smooth tubes originally published by Bhatti and Shah (1987) as cited in (Shah & Sekulic, 2003),

$$f = 0.00512 + 0.4572\, Re^{-0.311} \tag{6.9}$$

Condensation is affected by gravity, vapour shear, and condensate inundation. The combined effect of these is approximated by an averaging formula for gravity and shear-dominated heat transfer coefficients $h_{\mathrm{h,gr}}$ and $h_{\mathrm{h,sh}}$ originally published by Butterworth (1977) as cited in (Kakac, 1991),

$$h_{\mathrm{h}} = \sqrt{\frac{1}{2} h_{\mathrm{h,sh}}^2 + \sqrt{\frac{1}{4} h_{\mathrm{h,sh}}^4 + h_{\mathrm{h,gr}}^4}}, \tag{6.10}$$

An inundation correction by Kern originally published by Kern (1958) as cited in (Blangetti & Krebs, 1988) was applied to this to obtain the heat transfer coefficient of the j:th row $h_{\mathrm{h,j}}$:

$$h_{\mathrm{h,j}} = h_{\mathrm{h}} \left[j^{5/6} - (j-1)^{5/6} \right] \tag{6.11}$$

The gravity-dominated condensation heat transfer coefficient is determined from the Nusselt correlation (Nusselt, 1916), with the constant corrected from the original 0.725 to the more accurate solution of 0.728 by Butterworth (1983),

$$Nu_{\mathrm{h,gr}} = \frac{h_{\mathrm{h,gr}} d_{\mathrm{o}}}{k_{\mathrm{l}}} = 0.728 \left[\frac{\rho_{\mathrm{L}} (\rho_{\mathrm{L}} - \rho_{\mathrm{V}}) g h_{\mathrm{fg}} d_{\mathrm{o}}^3}{\mu_{\mathrm{L}} k_{\mathrm{L}} \Delta T} \right]^{\frac{1}{4}}, \tag{6.12}$$

where the temperature difference between steam and tube outside wall $\Delta T = T_{\mathrm{h}} - T_{\mathrm{o}}$ is obtained from the stationary-state energy balance, setting heat fluxes from steam to tube wall and steam to cooling water as equal,

$$\Delta T = T_{\mathrm{h}} - T_{\mathrm{o}} = \frac{U}{h_{\mathrm{h}}} (T_{\mathrm{h}} - T_{\mathrm{c}}) \tag{6.13}$$

The shear-dominated heat transfer coefficient is determined from the Shekriladze-Gomelauri correlation (Shekriladze & Gomelauri, 1966)

$$Nu_{\mathrm{h,sh}} = \frac{h_{\mathrm{h,sh}} d_{\mathrm{o}}}{k_{\mathrm{l}}} = 0.59 \sqrt{\tilde{Re}}, \quad \tilde{Re} = \frac{w_{\mathrm{V}} d_{\mathrm{o}} \rho_{\mathrm{L}}}{\mu_{\mathrm{L}}} \tag{6.14}$$

where $\tilde{Re}$ is a two-phase Reynolds number with steam velocity w_{v} defined as the average across the row of the tubes considered.

Steam pressure drop Δp_{h} in the tube bank is calculated from

$$\Delta p_{\mathrm{h}} = 2 C_{\mathrm{f}} \frac{G_{\mathrm{max}}^2}{\rho_{\mathrm{V}}}, \tag{6.15}$$

where G_{max} is the vapour mass velocity at the smallest cross-sectional area A_{min} between the tubes,

$$G_{\mathrm{max}} = \frac{\dot{m}_{\mathrm{h,V,i,j}}}{A_{\mathrm{min}}}, \tag{6.16}$$

In element (i,j) the minimum steam flow area $A_{\mathrm{i,j,min}}$ is obtained from

$$A_{\mathrm{i,j,min}} = \frac{L_{\mathrm{tb}}}{i_{\mathrm{max}}} N_{\mathrm{T,j}} (P - d_{\mathrm{o}}), \tag{6.17}$$

The friction factor C_{f} is based on the correlation originally published by Jacob (1938) as cited in (Holman, 1989),

$$C_{\mathrm{f}} = \left[0.25 + \frac{0.1175}{\left(\frac{P}{d_{\mathrm{o}}} - 1 \right)^{1.08}} \right] \left(\frac{d_{\mathrm{o}} w_{\mathrm{v,max}} \rho_{\mathrm{V}}}{\mu_{\mathrm{V}}} \right)^{-0.16} , \tag{6.18}$$

where velocity $w_{\mathrm{V,max}}$ is the maximum steam velocity at the smallest area between the tubes.

The fluid properties in equations (6.12), (6.14), (6.15) and (6.18) are evaluated at saturated state corresponding to local pressure.

6.2.3 **Average-U models: 0-D and HEI standards**

The 0-D model is based on the same equations (6.2) - (6.18) as the 2-D model. The values of pressure drop, shear-dominated heat transfer coefficient, mean hot flow temperature, and the hot-side properties are based on half of the incoming vapour remaining and half of the hot side pressure drop, with fluid properties evaluated at saturated state at this pressure.

Determining U according to the HEI Standards of Steam Surface Condensers is based on equations (6.19) - (6.24) below (Woodward *et al.*, 1999)

$$\Phi = UA \frac{T_{\mathrm{c,out}} - T_{\mathrm{c,in}}}{\ln \dfrac{T_{\mathrm{sat}}\left(p_{\mathrm{h,in}}\right) - T_{\mathrm{c,in}}}{T_{\mathrm{sat}}\left(p_{\mathrm{h,in}}\right) - T_{\mathrm{c,out}}}} , \tag{6.19}$$

$$\Phi = \dot{m}_{\mathrm{h}} h_{\mathrm{fg}} \tag{6.20}$$

$$\Phi = \dot{m}_{\mathrm{c}} c_{\mathrm{p,c}} \left(T_{\mathrm{c,out}} - T_{\mathrm{c,in}} \right) \tag{6.21}$$

$$U = U_1 F_1 F_2 F_3, \tag{6.22}$$

where F_1 to F_3 are the correction factor for tube material and gauge, cooling water inlet temperature, and cleanliness. In this work, the overall heat transfer coefficient of clean condenser U_{cl} is determined from a curve fit based on the cooling water flow velocity w_{c} and inlet temperature $T_{\mathrm{c,in}}$ recommended in Woodward *et al.* (1999) to approximate the HEI standards, and adjusted to account for the tube material and gauge with a correction factor F_{m} from Drbal *et al.* (1996):

$$U_{\mathrm{cl}} = 2.7\, w_{\mathrm{c}}^{0.5} (0.5707 + 0.0274\, T_{\mathrm{c,in}} - 0.00036\, T_{\mathrm{c,in}}^2)\, F_{\mathrm{m}} , \tag{6.23}$$

where $[T_{c,in}]$ = °C, $[w_{c,in}]$ = m/s and $[U_{cl}]$ = W/(m^{2}K). The material correction factor is F_m = 0.87 for type A condenser and F_m = 0.91 for types B and C (Woodward *et al.*, 1999). The overall heat transfer coefficient for the condenser with the tube inside fouling resistance R''_{tf} is obtained from

$$U = \left(\frac{d_o}{d_i} R''_{tf} + \frac{1}{U_{cl}} \right)^{-1}, \tag{6.24}$$

6.2.4 Validation at base load conditions

The change of the overall heat transfer coefficient U and condenser pressure $p_{h,in}$ is predicted with all models as a function of seawater temperature T_c and flow velocity w_c. As the U and steam saturation temperature both vary within the condenser, but this is not taken into account in the HEI standards curve, the simplified definition of U from Equation (6.19) is used for plotting the results of all models.

The effect of T_c at base load conditions is investigated with $\dot{m}_c$, w_c and Φ taken from the measurements and R''_{tf} assumed 0.5·10^{-5} m^{2}K/W during low-$\dot{m}_c$ and 1.0·10^{-5} m^{2}K/W during high-$\dot{m}_c$ periods. The results are shown in Figure 6.3.

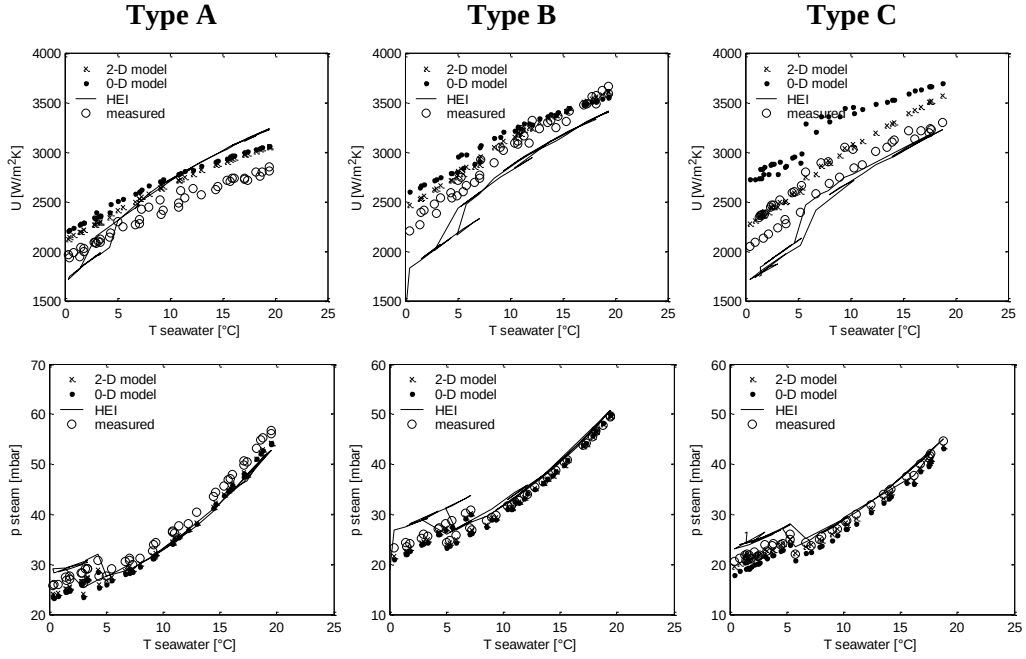

Figure 6.3: Condenser pressures and overall heat transfer coefficients as a function of seawater temperature.

Since the condenser pressure is largely a function of the cooling water inlet temperature (defining the starting point of the cooling water temperature curve) and mass flow rate (defining the rate of temperature increase), while the overall heat transfer coefficient only affects the temperature difference between the cold and hot flows, all models are able to predict p_h at any given coolant temperature within a few millibars even when differences in U are considerable.

The 2-D model tends to overestimate the performance of the condenser somewhat, but overall predicts it reasonably well for all tube bundle configurations at all conditions. The results of the 0-D model are broadly similar to the 2-D model with types A and B, but the 0-D model tends to overestimate the performance more, especially at the coldest water temperatures. With type C, this difference becomes quite large. This appears to be a result of several factors combining in the type C to magnify the importance of effects detrimental to performance that are difficult to account for in a single-point model.

Firstly, steam pressure drop Δp_h in the condenser is greatest at the cold end of tubes due to a higher local steam flow rate. With Δp_h greatest where most steam is condensed and roughly proportional to the square of velocity, the real effect is therefore greater than that resulting from a one-point average model based on flat steam flow distribution. Single-point averaging in steam flow direction also distorts the results towards higher-than-actual performance: most of the pressure drop takes place in the first few rows where the velocity is greatest, and the actual average effect is therefore greater than half of the total Δp_h calculated at half of the flow rate remaining.

Finally, heat transfer is highest in the first few tube rows due to the highest shear force improving the heat transfer coefficient, and the detrimental effects of both pressure drop and condensate inundation still low. The water in these tubes therefore warms faster than deeper in the tube bank. Particularly in the case of close temperature approach, this will limit the heat transfer potential left at the warm end of these tubes. Steam is then forced to flow through the first rows with comparatively little reduction in volumetric flow rate, resulting in significant pressure drop, and thus limiting the heat transfer rate available also deeper in the tube bank.

The type C condenser with the largest surface area, lowest pressure and closest temperature approach of all types is affected most by the above-mentioned effects. The net result can be seen in the values of U listed in Table 6.2 below for typical conditions of 1.8 m/s and +5 °C coolant velocity and temperature, and 105 kg/s steam mass flow rate (x = 0.91).

The effective overall heat transfer coefficient U_{eff}, based on Equation (6.19) and saturation temperature determined at $p_{h,in}$, is clearly lower than the U_{mean} based on the actual U determined from the heat transfer resistances according to Equation (6.2) (the arithmetic mean of local $U_{i,j}$ in case of 2-D model) in all cases, and the difference tends to be greater in the 2-D than in the 0-D model. Neglecting the issues of spatial variations in pressure and temperature produces the most optimistic results for the type C; as a result,

the 2-D and 0-D results diverge the most from each other with this type of condenser. The cold- and hot-side heat transfer coefficients are otherwise broadly similar between the models and condenser types.

Table 6.2: Condenser pressure and heat transfer coefficients with 0-D and 2-D models with +5 °C cooling water inlet temperature and 1.8 m/s tube-side velocity. U_{eff} is the effective overall heat transfer coefficient solved from Equation (6.19) with T_{sat} based on $p_{h,in}$, while U_{mean} is the arithmetic mean of local heat transfer coefficients calculated from Equation (6.2).

	Type A		**Type B**		**Type C**	
	0-D	**2-D**	**0-D**	**2-D**	**0-D**	**2-D**
$p_{h,in}$ [mbar]	27.8	28.4	25.2	25.7	21.4	22.9
$q_{m,c}$ [kg/s]	5147	5147	4860	4860	5329	5329
U_{eff} [W/m^{2}K]	2468	2400	2882	2788	3170	2691
U_{mean} [W/m^{2}K]	2855	2875	3246	3213	3331	3399
$h_{c,mean}$ [W/m^{2}K]	6347	6390	6502	6597	6533	6588
$h_{h,mean}$ [W/m^{2}K]	8403	8814	8470	8342	9071	9705

The plots confirm that the HEI standards curves predict a clearly stronger improvement of performance with increased coolant flow in all cases. There is also a noticeable difference between the results of the 2-D and 0-D models: although the tube inside heat transfer coefficient increases with increasing velocity, increasing U and decreasing p_h with all models, the aforementioned pressure drop related effects limit the 2-D model to a much lesser performance increase than the 0-D model. The effect is again particularly pronounced with type C.

For the purposes of on-line condition monitoring, an experimental correction factor as a function of cooling water temperature T_c was implemented to improve the accuracy. This was set on the basis of measurements taken soon after pressurized-water cleaning of the condenser tubes during periods of relatively fast seawater temperature change. The methodology of setting the correction factor is described in further detail in Publication I.

With the correction factor applied, the model can be used to determine the fouling thermal resistance R''_{tf} in the condenser tubes by adjusting the R''_{tf} value until the calculated condenser heat transfer performance matches the measured performance. This was the original purpose of the heat transfer model.

The calculated fouling thermal resistance R''_{tf} can also be used to validate the model at times of changing cooling water flow rate or steam flow rate by observing the change of R''_{tf} on a data series that includes an abrupt change of cooling water velocity w_c due to the switching of the sea water mass flow rate. As only the R''_{tf} is used to match the calculated to measured heat transfer, errors in predicting the change of convection resistance will result in an equal and opposite change of R''_{tf}, according to Equation (6.2). An abrupt jump of R''_{tf} when the water velocity changes can be a sign of this.

To compare the magnitude of the changes to random variations over time, R''_{tf} values for a 100-day period starting from T_c = 13 °C and cooling to 0 °C are plotted for types A and B in Figure 6.4. Measurement data needed to include condenser type C was not available.

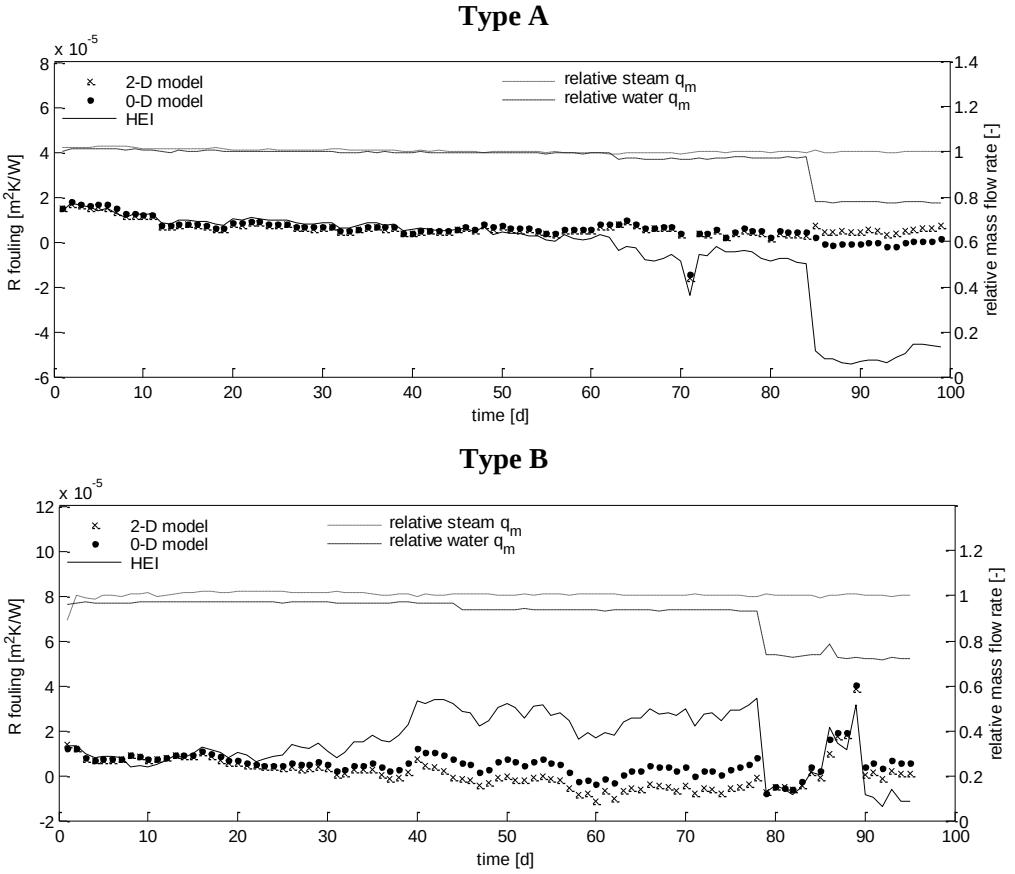

Figure 6.4: Condenser thermal fouling resistances and relative steam and coolant flow rates over a 100-day period. The measurements used are a continuous series of one-hour averages, of which every 24th value is represented in the figure.

When the coolant flow rate is reduced, the 2-D model produces a slight increase of R''_{tf} with type A and a decrease with type B, but the magnitudes of both are very small. The 0-D model yields an equally slight decrease of R''_{tf} with type A, but a clearer decrease with type B. The HEI curves produce a large reduction of R''_{tf} with both types to offset an overestimated impact of seawater flow rate reduction, however.

In addition to the fouling resistance change, other observations can be made from the results presented in Figure 6.4. Both the magnitude and rate of R''_{tf} variation of the type B condenser at days 80-90 appear too great to result from actual fouling changes. The

available data was insufficient to determine the actual cause, which may have been for example a measurement error or a problem in the gas venting system. It can also be seen that the values of R''_{tf} become negative with type B between days 45-85. This may be at least partly correct, however: a very small foulant growth at the surface of a smooth tube can reduce the convection resistance by more than the conduction resistance of the foulant. Given the small magnitude of R''_{tf}, the uncertainties of setting the baseline of $R''_{tf} = 0$, and the small coolant temperature change from which the heat transfer rate is calculated, the negative values may also in part or wholly result from inaccuracies of either the model or the measurements.

The behaviour of the models when the steam flow rate varies was studied using plant start-up data, and observing the R''_{tf} given by the three models. In the available data the steam flow rate increases from approximately 75% to full base load value. A pattern of R''_{tf} change that would either follow or mirror the steam flow change would indicate that the algorithm is likely correcting model errors with R''_{tf} to achieve the correct heat transfer rate. The results for types A and B at a seawater temperature of 15 °C are presented in Figure 6.5 below. Again, a complete set of necessary data was not available for type C.

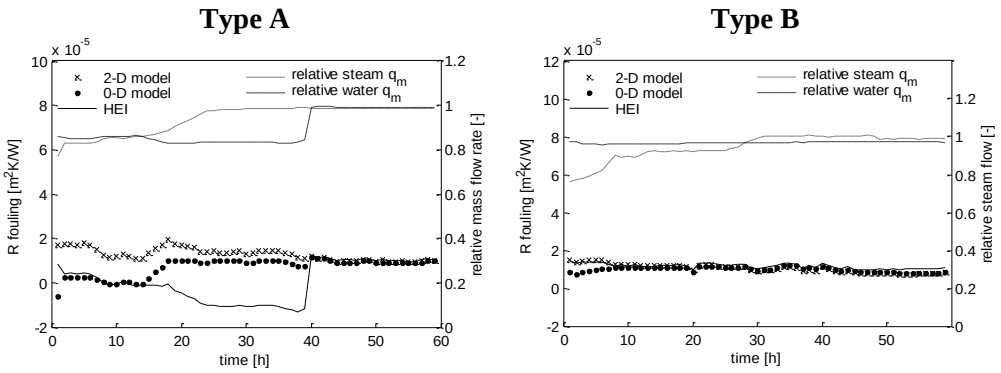

Figure 6.5: Condenser thermal fouling resistances and relative steam and coolant flow rates during start-up. The data points represent calculations on the basis of consecutive one-hour measurement averages over 60 hours.

In the case of type A, the HEI curve for R''_{tf} appears to mirror the steam flow rate to some extent, descending as the steam flow rate ascends. The 0-D model shows a lesser dependence on the steam flow rate, R''_{tf} increasing with the increasing steam flow and approaching the 2-D curve as the steam flow rate reaches 100 %. The R''_{tf} values calculated with the 2-D model show the least variation, and little signs of this variation following or mirroring either steam or coolant flow rates. In the case of type B both the HEI and 2-D R''_{tf} curves remain flat and nearly identical during the period of steam flow rate increase. The 0-D model again shows a reduction of R''_{tf} at 75-90 % steam flow rates.

For the purposes of a backpressure shell-and-tube condenser optimization, an experimental correction factor such as developed and used in Publication I, and utilized

in the R''_{tf} estimation in Figures 6.4 and 6.5, is obviously not available. Without a correction factor, Figure 6.3 indicates that the 2-D model is most accurate of the models, and particularly with Type C, the failure of the simpler models to account for the variations of pressure, temperature and heat transfer within the tube bundle lead to poor performance.

By implementing the correction factor – a simple linear function of cooling water temperature – and using the corrected model to estimate the fouling resistance, it also appears that the 2-D model yields the smallest systematic errors as functions of seawater or steam flow rates. On these grounds, and considering that a backpressure DH condenser would typically have a relatively close temperature approach, increasing the susceptibility of the model to the errors introduced by average-*U* simplification, the 2-D model was selected to be used as a basis of the CHP plant backpressure condenser heat transfer model.

6.3 Back pressure condenser

Two different types of district heat condensers (DHC) were considered. Initially, in Publication II, a DHC using extraction steam and designed for significant condensate subcooling was optimized from the manufacturer's point of view, i.e. finding the minimum-cost design to satisfy a fixed performance requirement. The final economic optimization of the backpressure condenser was modelled and optimized in Publication VI for the purpose of answering research question Q5. As the extraction steam DHC mass minimization is not directly related for this purpose, only the backpressure condenser model is described in the following.

For the backpressure condenser, a shell-and-tube U-tube condenser (Figure 6.6) with a round tube bundle and steam in pure cross flow was selected as the basic construction. Maximizing power production at any given DH load was assumed the goal, and thus there was no condensate subcooling section present. The heat transfer modelling of the tubular condenser follows in the main principles the 2-D modelling of the vacuum condenser described in chapter 6.2 above.

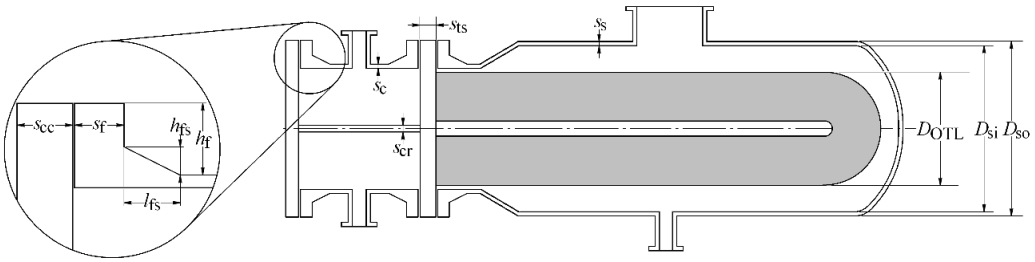

Figure 6.6: District heat condenser construction.

6.3.1 Fixed parameters and assumptions

250 °C design temperature and pressures of -1/+5 bar(g) for the shell and -1/+16 bar(g) for the tubes were assumed in sizing. P235GH carbon steel was used for the tubes, P355GH for the other parts. The yield strength of P355GH at 250 °C, σ_l = 210 N/mm^2, was used as the design stress in the mechanical sizing. An equilateral triangular tube pitch was chosen for the tightest possible packing of tubes at a given tube sheet ligament strength, since the need for mechanical cleaning requiring a square pitch was considered unlikely.

The loss coefficients for pressure drop were set according to (Sinnott, 2005). Lower fouling resistances than those of TEMA standards (Standards of the Tubular Exchanger Manufacturers Association, 2007), which were considered to represent pessimistic worst-case figures rather than typical ones, were used. The assumptions for fixed parameters in mechanical and thermal calculations are summarized in Table 6.3 below.

Table 6.3: Main sizing assumptions.

Mechanical		**Thermo-hydraulic**	
Corrosion allowance* [mm]	3.0	Tube wall thermal conductivity [W/mK]	56
Manufacturing tolerance* [mm]	2.0	Tube-side fouling resistance [m^{2}K/W]	$8.0 \cdot 10^{-5}$
Material design stress, P355GH [MPa]	210	Shell-side fouling resistance [m^{2}K/W]	$1.0 \cdot 10^{-5}$
Support plate thickness [mm]	10.0	Tube inside absolute roughness [mm]	0.04
Support plate spacing [mm]	1500	Tube arrangement	Δ 60°
Channel division rib thickness [mm]	15.0	Loss coefficient, inlet/outlet nozzle [-]	1.0/0.5
Tube-to-shell clearance [mm]	40	Loss coefficient, tube entry/exit [-]	0.5/1.0
		Loss coefficient, U-bend [-]	0.5

* not applied on heat transfer tubes

6.3.2 Heat transfer model

The heat transfer model is based on the 2-D model of the large vacuum condenser, with minor modifications and adaptations necessary for the shell-and-tube U-tube condenser. The model was designed to determine iteratively the performance of the condenser at different district heat load points. The load point data given as an input consists of the district heat power Φ_{DH}, and water output and return temperatures $T_{DH,out}$ and $T_{DH,ret}$.

The model solves the heat transfer coefficients and pressure drop. From this data the effective overall heat transfer coefficient U_{eff} can be obtained, and with it the effective conductance $G_{eff} = U_{eff} A$, defined similarly to Equation (6.19) in chapter 6.2.3 as

$$\Phi = G_{eff} \frac{T_{DH,out} - T_{DH,in}}{\ln \dfrac{T_{sat}\left(p_{h,nzl}\right) - T_{DH,in}}{T_{sat}\left(p_{h,nzl}\right) - T_{DH,out}}}, \tag{6.25}$$

where $p_{h,nzl}$ is the steam pressure at the nozzle, before the nozzle pressure drop. The G_{eff} is different from the actual mean conductance of the heat transfer surface: the local heat transfer rate is also affected by the pressure drop, since reducing pressure reduces also the saturation temperature. It is thus the G_{eff} and not the mean G that defines the terminal temperature difference (TTD) and turbine exhaust pressure, and thereby the impact of the condenser on the power production and boiler fuel consumption of the CHP plant.

The pressure at the nozzle $p_{h,nzl}$ is also the iteration variable: by adjusting it, the heat transfer model algorithm matches the calculated $\Phi_{DH,calc}$ to the required target $\Phi_{DH,tgt}$ from the input. The calculation procedure is outlined in the flow chart of Figure 6.7.

The straight part of the tubes in both passes of a U-tube of 2 passes is split in i_{max} slices in tube direction, and j_{max} circular segments in the steam flow direction. The outermost ring of tubes is denoted as $j = 1$, innermost $j = j_{max}$. A 180° U-turn element, $i_U = ½(i_{max}-1)+1$, joins the two passes. The flows entering element (i,j) are set by the outlet conditions of $(i-1,j)$ and $(i,j-1)$. Constant steam pressure, saturation temperature and heat transfer coefficients are assumed in each element.

The heat transfer in each element is calculated according to equations (6.2) to (6.6), but the vapour-phase flow entering element $(i, j+1)$ has been improved from Equation (6.7) by solving the remaining vapour from the energy balance considering the change of saturated vapour and condensate enthalpies due to pressure drop,

$$\dot{m}_{h,V,i,j+1} = \frac{\dot{m}_{h,V,i,j} h_{h,V,i,j} + \dot{m}_{h,L,i,j} h_{h,L,i,j} - \dot{m}_{h,V,i,1} h_{h,L,i,j+1} - \Phi_{i,j}}{h_{h,V,i,j+1} - h_{h,L,i,j+1}}, \qquad (6.26)$$

where $h_{h,V}$ and $h_{h,L}$ are the hot (steam) side saturated vapour and saturated liquid enthalpies at the inlet to the indicated element. This yields slightly improved accuracy over assuming a constant latent heat of evaporation h_{fg} at the mean pressure of the element, and ensures closing the energy balance precisely for each element.

The local heat transfer coefficients are obtained by using otherwise the equations (6.8) to (6.18), but obtaining the friction factor f from the iterative Colebrook-White equation for rough tubes,

$$\frac{1}{\sqrt{f}} = -2\log_{10}\left[\frac{2.51}{Re_c\sqrt{f}} + \frac{K/d_i}{3.71}\right]. \qquad (6.27)$$

instead of the Bhatti and Shah correlation of Equation (6.9) for hydraulically smooth tubes.

Steam pressure drop takes place at the nozzle and in the shell before the steam enters the tube bundle, and in the tube bundle itself. The tube bundle pressure drop is calculated according to equations (6.15) to (6.18) in each calculation element (i,j).

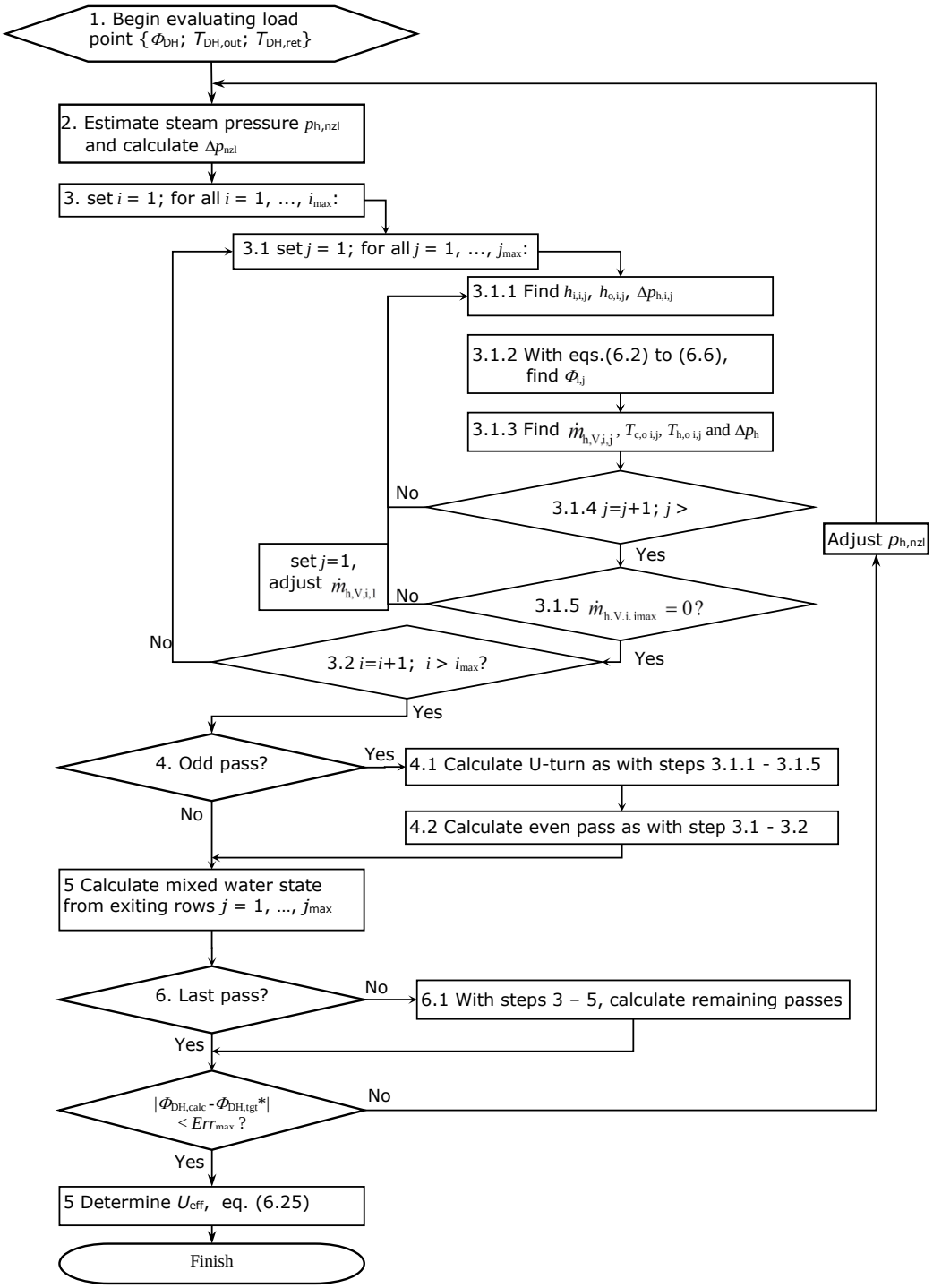

Figure 6.7: Flow chart of the back pressure district heat condenser heat transfer model.

The pressure drop before the tube bundle is denoted as Δp_{nzl}, and calculated assuming half a velocity head lost at the velocities at the nozzle, at the 90° turn from the nozzle into the shell, and in the free area between the bundle and shell:

$$\Delta p_{\mathrm{nzl}} = 0.5\frac{\rho_{\mathrm{V,nzl}}\dot{V}_{\mathrm{V,nzl}}^{\ 2}}{2A_{\mathrm{nzl}}^{\ 2}} + 0.5\frac{\rho_{\mathrm{V},90°}\dot{V}_{\mathrm{V},90°}^{\ 2}}{2A_{90°}^{\ 2}} + 0.5\frac{\rho_{\mathrm{V,ann}}\dot{V}_{\mathrm{V,ann}}^{\ 2}}{2A_{\mathrm{ann}}^{\ 2}}; \qquad (6.28)$$

$$A_{\mathrm{nzl}} = \frac{\pi D_{\mathrm{nzl}}^{\ 2}}{4};$$

$$A_{90°} = P_{\mathrm{nzl}}\left(\frac{D_{\mathrm{s,in}} - D_{\mathrm{OTL}}}{2} - h_{\mathrm{ip}}\right);$$

$$A_{\mathrm{ann}} = 2\cdot\left(\frac{\pi D_{\mathrm{s,in}}^{\ 2}}{4} - A_{\mathrm{bfl}}\right),$$

where P_{nzl} is the perimeter of an ellipse with a major axis of a_{nzl} and a minor axis of D_{nzl} obtained by using Ramanujan's approximation formula (Råde & Westergren, 1990). D_{bfl} is the diameter of the circular part of a baffle plate, h_{ip} is the height of the impingement plate from the tube bundle, and A_{bfl} is the area covered by the support plates in tube axis direction, shown with light grey in Figure 6.8.

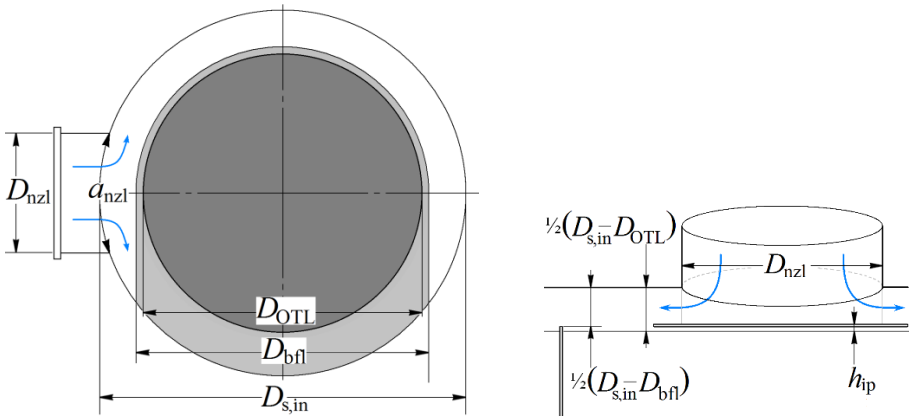

(a) (b)

Figure 6.8: Geometry at steam entry to the DHC shell.

The tube-side pressure drop Δp_{c} is obtained from the Darcy-Weisbach of Equation (6.29),

$$\Delta p_c = \frac{\rho_c w_c^2}{2}\left[f \frac{L_{tb}}{d_i} + K_{nzl,in} + K_{tb,in} + K_{U\text{-}tum} + K_{tb,out} + K_{nzl,out} \right], \tag{6.29}$$

Where the friction factor f is obtained from Equation (6.29), and the loss coefficients K are those listed in Table 6.3.

7 Condenser optimization

In the optimization of the CHP plant district heat condenser, only a pure CHP plant without integrated biomass conversion units was considered. The goal was to find which condenser performance parameters would maximize the profitability of the CHP plant at varying electricity prices, as well as to investigate suitable optimization methods for the problem.

This chapter focuses mainly on backpressure DHC optimization for the CHP plant profitability maximization presented in Publication VI. Material and conclusions from Publication II, where the total heat exchanged mass of an extraction steam DHC was minimized, is included to the extent that it supports investigating the main research questions of the thesis.

In the following, chapter 7.1 presents the background and existing literature on heat exchanger optimization related to the cost modelling and the optimization algorithms used. Chapter 7.2 describes the objective function, including the implementation of the cost function for the condenser, and determining the heat and power production and fuel consumption as a function of condenser operating parameters. Chapter 7.3 describes the optimization algorithms used, including the differential evolution (DE) and cuckoo search (CS) that were used in the initial studies, as well as genetic algorithm (GA) included later to serve as a benchmark for algorithm performance comparison. Chapter 7.4 presents the main results found in this part of the study; the focus is on the results obtained in Publication VI to answer the research question Q5, but the main findings of Publication II are also briefly summarized. Finally, chapter 7.5 presents the measures taken to reduce the calculation time of the optimization, including the performance comparison and control parameter tuning guidelines of the different optimization algorithms tested for the problem.

7.1 Background

The district heat condensers of combined heat and power (CHP) steam plants are typically U-tube heat exchangers with water on the tube side and steam condensing on the shell side. Particularly in condensers using bypass or bleed steam, sub-cooling the condensate is often desirable to minimize steam consumption: this was the case assumed in Publication II. In Publication VI, a backpressure condenser, more typical for a small-scale district heat -producing Nordic CHP plant, was considered. In a pure backpressure plant without two-stage heating of district heating water, subcooling the condensate will reduce electricity production for any given district heat load, which is usually not desirable. Intentional subcooling by submerging some of the tubes in condensate was therefore assumed not to take place. The configuration considered in publication VI was described in chapter 6.3 above.

Shell-and-tube heat exchanger optimization has been studied and published extensively, with several methods applied on cost estimation and the optimization itself. The following chapters outline commonly used methods in previous works by other authors.

7.1.1 Heat exchanger cost

In most published studies on heat exchanger optimization, including those of Hajabdollahi *et al.* (2011); Jegede & Polley (1992); Mizutani *et al.* (2003); Muralikrishna and Shenoy (2000); Ponce-Ortega *et al.* (2009); and Sanaye and Hajabdollahi (2010), the total cost of the heat exchanger is estimated as a function of the heat transfer area. When operating costs are not considered, this reduces cost optimization to area minimization, which has been done by Babu & Munawar (2007); Chaudhuri *et al.* (1997); Costa & Queiroz (2008); and Sanaye & Dehghandokht (2011). Usually this can be considered an adequate approximation if the shell has a high length-to-diameter ratio and is fully tubed, which is usually true if the shell-side fluid is a liquid. In a condenser with low-pressure steam on the shell side, a large fraction of the shell needs to be void of tubes to prevent high pressure drop and flow maldistribution, however. As a result, the shell, tube sheet and channel form a significant part of the total mass. These parts of the heat exchanger would be ignored in area minimization, which would then allow the optimizer to minimize the steam pressure drop and maintain saturation temperature by placing the tubes sparsely in a very large shell.

A more elaborate cost function proposed by Purohit (1983) was used in one of the cases considered by Ponce-Ortega *et al.* (2009). However, despite its complexity the Purohit method was found to be relatively inaccurate by Taal *et al.* (2003). In Publication II, minimizing the mass was assumed to be a better approximation than area minimization for finding the minimum-cost design. For this purpose, a simplified mechanical sizing algorithm to estimate the approximate dimensions of main components was created.

The drawback of the mass minimization approach is that it, too, ignores some manufacturing costs such as tube sheet and baffle drilling, which can be affected by design choices. It also implicitly assumes identical material costs for all sub-components, which is also a significant simplification. As a result, in Publication VI, a cost model based on a simplified version of Caputo *et al.* (2016) was implemented.

7.1.2 Optimization methods and algorithms

Many optimization methods have been used in shell-and-tube heat exchanger optimization. The optimization problem is made difficult by such characteristics as several constraints, non-differentiability, possible multimodality, and combination of discrete and continuous variables. These issues have been solved by various means, each with some drawbacks.

A deterministic, non-iterative solution combining pumping and area costs for segmentally baffled single-phase heat exchangers was presented by Jegede & Polley (1992) and

improved further by Serna & Jiménez (2005). Other methods include general disjunctive programming (Mizutani *et al.*, 2003), graphical analysis (Muralikrishna & Shenoy, 2000), and systematic screening of tube count tables with heuristic pruning of infeasible parts (Costa & Queiroz, 2008). Most of these methods involve significantly simplified shell-side calculation, and yield themselves poorly to multi-element calculation of condensing flows. There is also no guarantee of an optimum found being the global, not a local one.

During the last decade, several applications of various global optimization methods to the heat exchanger design optimization problem have been published. As stochastic methods they all suffer from much greater computational time, but as CPU speeds increase, this becomes less of a limit in contrast to the robustness and ease of implementation when confronted by difficult optimization problems combining discrete and continuous decision variables. Examples of stochastic methods applied to shell-and-tube heat exchanger optimization include simulated annealing (SA) (Chaudhuri *et al.*, 1997), particle swarm optimization (PSO) (Hajabdollahi *et al.*, 2011; Patel & Rao, 2010), and various evolutionary algorithms, such as differential evolution (DE) (Babu & Munawar, 2007), genetic algorithms (GA) (Hajabdollahi *et al.*, 2011; Ponce-Ortega *et al.*, 2009; Sanaye & Hajabdollahi, 2010; Sanaye & Dehghandokht, 2011), and harmony search (HS) (Fesanghary *et al.*, 2009). Of these, DE tends to outperform PSO and HS, particularly with multimodal functions (Xu & Li, 2007; Gao *et al.*, 2009), while between GA and DE, the former is considered more suitable for combinatorial problems while DE is said to be often faster and more robust in real-parameter optimization, particularly with non-separable problems (Price *et al.*, 2006).

As new stochastic metaheuristics are developed continuously, studies of their applications on shell-and-tube heat exchanger optimization are published frequently. These include the imperialist competitive algorithm (Hadidi *et al.*, 2013), gravitational search (Mohanty, 2016), and recently the so-called Jaya algorithm (Rao and Saroj, 2017). Many of the recent new metaheuristics algorithms are based on nature, often on the behaviours of some animal species. Such algorithms include the bat algorithm (BA) (Yang, 2010b), the firefly algorithm (FA) (Yang, 2010a), and two different algorithms inspired by cuckoo birds: the cuckoo search (CS) introduced by Yang and Deb (2009), and the cuckoo optimization algorithm (COA) by Rajabioun (2011). Despite the similar names, the last two are entirely different algorithms sharing nothing but the common source of inspiration in cuckoo birds.

Shell-and-tube heat exchanger optimization has been successfully performed using the FA (Mohanty, 2016) and COA (Asadi *et al.*, 2014), although in the latter the algorithm was erroneously referred to as cuckoo search. Recently Khosravi *et al.* (2015) compared the performance of FA and CS algorithms to a traditional GA in shell-and-tube heat exchanger optimization. Their finding was that both FA and CS were superior to GA in terms of reliability of finding the optimum, and between the two, CS clearly outperformed the FA at speed of convergence, requiring fewer objective function evaluation to reach the optimum.

In this thesis, DE was used first in Publication II for the design optimization of the DH condenser, where the objective function was simple mass minimization. The CS algorithm was implemented in Publication VI. The performance of some of the variants of both algorithms and the impact of control parameter settings on their performance is presented, with the standard MATLAB toolbox GA used as a benchmark to which the results are compared.

7.2 Objective function

In the initial optimization study presented in Publication II the objective function was simply the mass of the condenser, which was minimized. For the purposes comparison, also heat transfer area minimization was performed. The results confirmed that area minimization is not a useful approximation for condenser cost minimization. Mass minimization resulted in a condenser of 6.9 ton total mass with 331 m^2 heat transfer area. Area minimization reduced the heat transfer area to 284 m^2, but resulted in a very large shell almost void of tubes, and a total heat exchanger mass of 76.6 tons, which is clearly an uneconomical result.

For the main goal of the research, finding the optimal configuration and performance parameters for maximizing the profitability of a CHP plant, the objective function was set as the annual net cash flow rate of the plant. To determine this, a multi-period model similar to that described in chapter 2.1 was used. To minimize the calculation time of each objective function evaluation, only four periods were used to model the annual operating time. The parameters of each period P1 to P4 are listed in Table 7.1 below; the corresponding DH demand curve, and the multiperiod approximation of fuel consumption and power and heat production are shown in Figure 7.1.

Table 7.1: Average load points for the CHP plant.

Parameters	**P1**	**P2**	**P3**	**P4**
Period duration t [h]	1800	1400	1400	1400
Average ambient temperature [°C]	-8	0	+5	+10
DH water output/return T [°C]	90/55	80/50	75/45	75/45
DH power $\Phi_{DH,CHP}$ [MW]	20.0	18.0	14.0	10.0
Fuel moisture MC [%]	55	50	50	45
Fuel moisture [%] / LHV [MJ/kg]	7.4	8.5	8.5	9.6

The CHP plant model was used to obtain plant performance as function of condenser performance variables. An improved cost function was also developed for the condenser. These are described in chapters 7.2.1 and 7.2.2, and the evaluation of the objective function on the basis of this data in chapter 7.2.3.

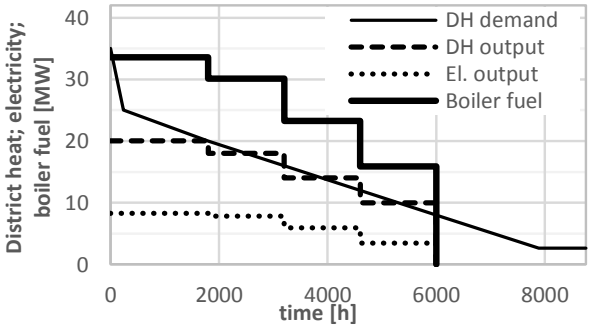

Figure 7.1: Annual CHP production and boiler consumption in the discretized multi-period model, and the DH demand curve.

7.2.1 Effect of condenser on plant performance

For the purposes of condenser optimization, the impact of condenser performance parameters on the plant performance was evaluated by using the plant model. The CHP plant IPSEpro model was not run directly during the optimization, which was carried out in MATLAB environment. For the optimization algorithm to be able to evaluate plant performance without access to the plant model, polynomial curve fits for obtaining the fuel consumption Φ_f and heat and power production Φ_{DH} and P_{el} at each load points as a function of condenser performance were created.

Two parameters define the condenser performance: effective conductance $G_{eff} = U_{eff} A$, and condensate sub-cooling ΔT_{SC}. Effective conductance is defined from the steam temperature $T_{h,in}$ and DH water outgoing and return temperatures $T_{DH,out}$ and $T_{DH,ret}$ as

$$G_{eff} = \Phi_{DH} \frac{\left(\ln \frac{T_{h,in} - T_{DH,out}}{T_{h,in} - T_{DH,ret}} \right)}{\left(T_{DH,ret} - T_{DH,out} \right)} . \tag{7.1}$$

The steam temperature $T_{h,in}$ is the saturation temperature at turbine exhaust pressure.

The curve fits were created so that first the plant power and heat production and fuel consumption figures would be obtained as a function of conductance G_{eff} while assuming zero subcooling, and the subcooling correction would then be applied to these figures. The curve fits were created separately for each load point P1 to P4.

Load point P1 represents the boiler-limited maximum load. The boiler fuel consumption Φ_f was thus fixed at that corresponding to the maximum continuous rating, and curve fits were created for P_{el} and Φ_{DH} as a function of G_{eff}. For the other load points, the district heat power was fixed at that defined by the DH load, and curve fits were created for P_{el} and Φ_f.

A very good agreement of $R^2 = 1.00$ was obtained for P_{el} and Φ_f as functions of G_{eff} within a range of 1000 kW/K < G_{eff} 1600 kW/K, corresponding to a terminal temperature difference TTD of approximately 2 °C to 8 °C at 20 MW district heat production. This was considered to be the range at which the optimum would very like be found. The plots of these correlations are presented in Figure 7.2. The curves appear to be relatively smooth, and extrapolation errors are likely to remain reasonable within 100…200 kW/K outside the range of the data points used.

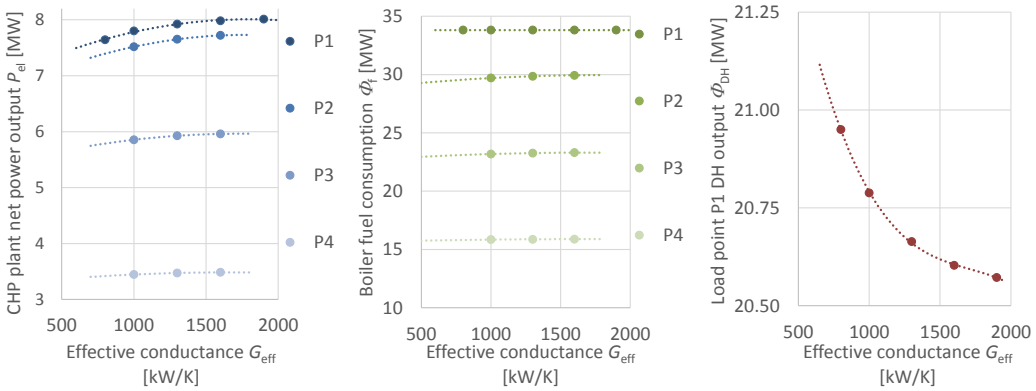

Figure 7.2: Variation of CHP plant net power output P_{el} and boiler fuel consumption Φ_f at load points P1 to P4, and district heat power at load point P1, as functions of condenser effective conductance G_{eff}.

The operation of the plant is assumed to be based on maximizing power output, and thus a good design should minimize subcooling; in a small condenser, such as the one considered here, more than one or two degrees of subcooling should be unlikely. The subcooling proved to have only limited impact on both power production P_{el} and boiler fuel consumption Φ_f, as well as the district heat production Φ_{DH} at load point P1. The changes of all aforementioned parameters were in all cases less than a 0.2 % change per each 1 °C of sub-cooling.

As the impact of subcooling at the likely range was found to be very small, a simpler single approximation accounting for the range of varying G_{eff}, load points, and ΔT_{SC} was considered adequate. The variation across the load points was accounted for by plotting the reduction of fuel power to boiler Φ_f and net electricity production P_{el} as a function of what the P_{el} would be with $\Delta T_{SC} = 0$ °C (see Figure 7.3). Three different values of G_{eff} were used: 1000, 1300 and 1600 kW/K. The change of fuel consumption and power production was then calculated for each load point with each value of G_{eff}. The results and the polynomial approximations are shown in Figure 7.3.

An acceptable figure of $R^2 > 0.9$ was obtained for the effect of subcooling at the range of $0 < \Delta T_{SC} < 3$ °C. While the accuracy left room for improvement, it was considered sufficient given the relatively small impact of the subcooling on the fuel consumption and

the power and heat production of the plant. In absolute terms, the variation of both net electricity production and boiler fuel consumption over the $0 < \Delta T_{SC} < 3$ °C range of variation considered was only 10…20 kW, as opposed to 100…200 kW variation of the same for the range of $1000 < G_{eff} < 1600$ kW/K.

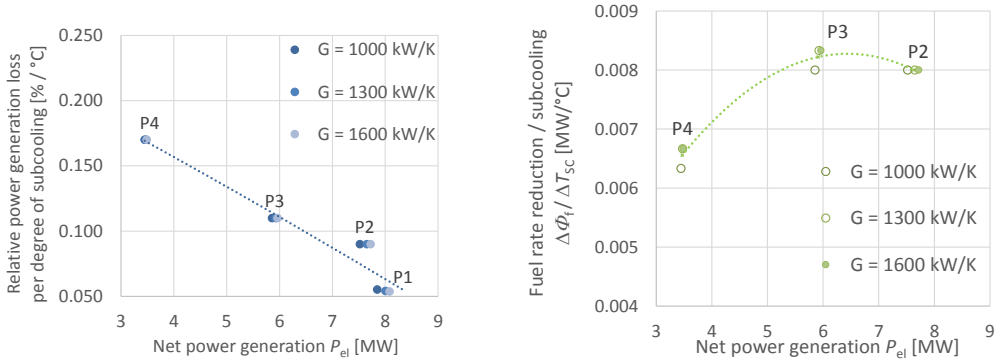

Figure 7.3: Relative loss of net power output P_{el} and absolute reduction boiler fuel consumption Φ_f at different values of G_{eff}, plotted as a function of P_{el} without subcooling (ΔT_{SC} = 0°C).

7.2.2 Condenser cost model

Mechanical sizing is necessary to obtain the dimensions, particularly the mass, of the main sub-components of a condenser. Exact mechanical design according to the latest standards was ruled outside the scope of the study. The main parts considered for estimating the mass and cost of the condenser were the tube bundle, shell, tubesheet, baffles, and the channel including the cover, rib and flanges. Nozzle size was assumed unaffected by the other dimensions and was thus not considered.

The size and mass were obtained by calculating the shell, channel and cover plate thicknesses against internal pressure and buckling at -1 bar vacuum according to the current pressure vessel code (Suomen standardoimisliitto, 2002). Instead of the stress and moment analysis of Suomen standardoimisliitto (2002), tubesheet thickness was estimated from the much simpler formula of the old 1996 standard (Suomen standardoimisliitto, 1996). The dimensions of the flanges were estimated as a function of shell diameter from curve fits made on flange dimensions for heat exchangers rated for 650 °F temperature and 300 psi(g) pressure. The sizing equations used are described in Appendix A of Publication II.

The investment cost TCI_{DHC} of the district heat condenser was obtained by setting the cost of installed equipment as 3.3 times the FOB cost (C_{FOB}) according to (Sinnott, 2005). The C_{FOB} was obtained from the manufacturing cost C_{man} by using a mark-up estimate consisting of 30 % overhead cost, 5 % contingency and 10 % manufacturer's profit.

The manufacturing cost C_{man} consists of material cost C_{mat} and processing cost C_{pr}, where C_{mat} is clearly the dominant factor. The following material costs were estimated in Publication VI: tubesheet cost $c_{m,ts}$ = 3.5 €/kg; shell, channel and flanges $c_{m,sh}$ = $c_{m,ch}$ = $c_{m,f}$ = 2.5 €/kg; and baffles $c_{m,bf}$ = 2.0 €/kg. The cost of the heat transfer tubes was set as a function of diameter based on a curve fit made on data available from commercial suppliers at the time of writing Publication VI,

$$c_{m,tb} = \left(2.40 + \frac{1.8 \cdot 10^{-4}\,\mathrm{m}^2}{{d_o}^2} \right) \frac{€}{\mathrm{kg}}, \tag{7.2}$$

where d_o [m] is the tube outside diameter. The tube length was unlimited, but a 10 % cost penalty was applied on tubes longer than 20 m before bending to U-tubes. The nozzle sizes were assumed unaffected by other dimensions, and were not considered in the cost model.

Of the processing cost, baffle-related costs are the largest one (Caputo *et al.*, 2016) and any attempt to minimize the baffle costs will also significantly impact the heat transfer surface geometry. Baffle processing costs were thus modelled in detail according to the methodology presented by Caputo *et al.* (2016), while the other processing costs were estimated at 10 % of C_{mat} based on the results presented by Caputo *et al.* (2016).

7.2.3 Objective function evaluation

The annual cash flow rate of the plant is obtained from equation

$$C_{tot} = \sum_{P=P1}^{P4} t_P \left(P_{el} c_{el} + \Phi_{DH} c_{DH} - \Phi_f c_f \right) - a TCI_{tot} - r_{O\&M} TCI_{tot}, \tag{7.3}$$

where a is the amortization factor for the total capital investment (TCI) at interest rate i and economic lifetime n. Table 7.2 lists these and other economic parameter values. The total capital investment of the plant TCI_{tot} is the sum of the DH condenser investment TCI_{DHC} and the plant investment excluding the district heat condenser, estimated at TCI_{CHP} = 26 million € based on data for a similar, but slightly smaller CHP plant found in Kuitunen (2007).

Table 7.2: Values of economic parameters.

Parameter	value
Maximum annual operating time t [h]	6000
Interest rate i [-]	0.10
Plant economic lifetime n [a]	20
Annual O&M cost ratio $r_{O\&M,}$ [%]	0.04
Wood chip price c_f [€/MWh$_{LHV}$]	20
District heat price c_{DH} [€/MWh]	60

The objective function value C_{tot} from Equation (7.3) is found by evaluating the condenser performance at conditions corresponding to periods P1 to P4 by using the heat transfer model presented in chapter 6.3.2, the curve fits described in chapter 7.2.1 to obtain plant heat and power production and fuel consumption, and the cost model of chapter 7.2.2 to find the DH condenser cost. The algorithm for this process is shown as a flow chart in Figure 7.4 below.

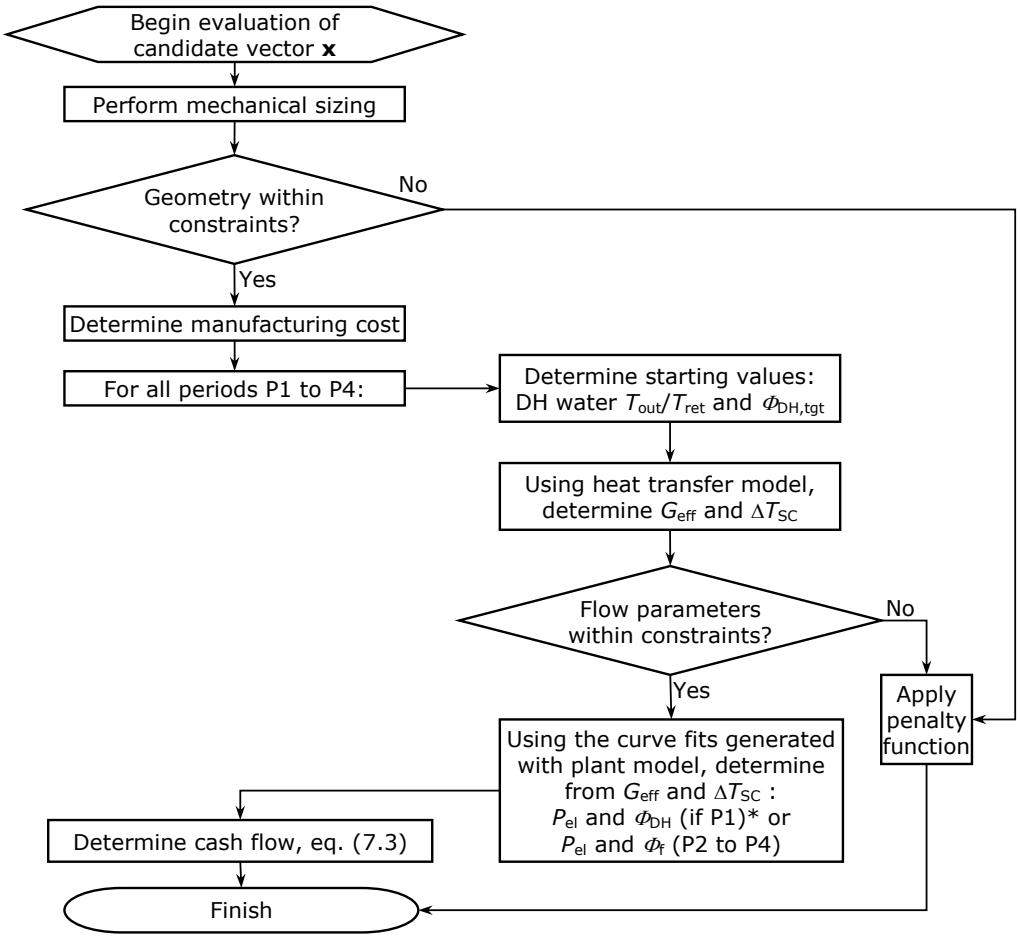

* For P1, the $\Phi_{DH,tgt}$ is adjusted during the iterative heat transfer calculation to a value that with the latest value of G_{eff} and ΔT_{SC} will yield a boiler fuel rate matching the boiler maximum continuous rating, thus making the variable Φ_f a de facto constant. For periods P2 to P4, $\Phi_{DH,tgt}$ is the Φ_{DH} listed in Table 7.1 heat transfer model is repeated until convergence.

Figure 7.4: Objective function evaluation flow chart.

The decision variables of the optimization are listed in Table 7.3. The straight length x_3 considers only the effective heat transfer area; the tube length covered by the support

plates or the tube sheet is not part of this variable, but is factored in the condenser mass and cost calculation.

Table 7.3: Decision variables x and their initialization ranges.

x	Definition	Initialization range
x_1	Ratio of shell to bundle $D_{sh,in}/D_{OTL}$	$0.5 < x_1 < 0.95$
x_2	Number of tube passes	$x_2 \in \{2,4\}$
x_3	Straight tube length per pass L_{str} [m]	$3.0 < x_3 < 12.0$
x_4	Tube outside diameter d_o [mm]	$x_4 \in \{10, 12, 14, 16, 18, 20, 22, 25, 28, 30\}$
x_5	Tube pitch/ diameter ratio P/d_o	$1.25 < x_5 < 1.50$
x_6	Water free-flow area $A_{fr.c}$ [m^2]	$0.2 < x_6 < 1.0$

Constraints are listed in Table 7.4. Maximum tube-side velocity was set at the maximum water velocity in carbon steel tubes according to Taborek (1983). Maximum shell-side velocity, defined as the maximum velocity at the tightest spacing between the tubes, was set at the upper end of the recommended range for vapours at approximately atmospheric pressure according to Sinnott (2005).

Tube pitch P must provide a strong enough tubesheet ligament between the holes. A limit of $P > 1.25d_o$ is recommended by Suomen standardoimisliitto (1996) and Sinnott (2005). TEMA (2007) permits even tighter spacing, but often with small tubes a minimum ligament of at least 3.2 to 6.4 mm is recommended for drilling tolerance and to allow tight rolling of the tubes to the tubesheet (Rohsenow *et al.*, 1998). Here tube pitch was limited at $1.25d_o$ with an additional 5 mm ligament limit.

Table 7.4: Constraints.

Variable	Constraint	Variable	Constraint
Tube-side velocity	$w_c \leq$ 3.0 m/s	Shell-side velocity	$w_h \leq 30$ m/s
Tube pitch	$P \geq 1.25d_o$	Tubesheet ligament	$(P - d_o) \geq 5$ mm
Condenser length	$L_{HX} \leq 15.0$ m	Condenser diameter	$D_{HX} \leq 3.5$ m

At any point of the calculation when any constraint of the optimization is violated, either mechanical or flow-related, the objective function evaluation is stopped. This is done to prevent unnecessary time-consuming evaluations of the multi-element, iterative heat transfer model.

Penalty functions are applied to solutions that violate constraints so as to ensure that any legal solution, no matter how poor, is guaranteed to be superior to any solution that violates one or more constraint. Selection pressure towards legal solutions is reinforced by ensuring that between solutions that violate multiple constraints, the one violating the fewest has always the better objective function value, and if only one constraint is violated, the one violating it less has the better objective function value.

7.3 Optimization algorithms

Two metaheuristic algorithms, differential evolution (DE) and cuckoo search (CS), were initially used in this work. At first in Publication II, DE was selected for its record of good performance with multimodal and non-separable real-valued functions (Price *et al.*, 2006; Xu & Li, 2007). In an attempt to find an even better-performing algorithm for the relatively time-consuming optimization task, cuckoo search was used in Publication VII. While both CS and DE were considered successful, the optimization time was significant with both: initially in the order of hours with a desktop computer even after efforts were made to reduce the computation time of the objective function. Consequently, as a final stage a number of optimizers were tested and their control parameter settings evaluated to find which type of algorithm would perform best at condenser optimization, and also establish guidelines on how to set the control parameters for best performance.

7.3.1 Differential evolution

Differential evolution (DE), a type of evolutionary algorithm, was used in the extraction steam district heat condenser optimization (Publication II). Evolutionary algorithms (EAs) are stochastic global optimization algorithms often able to find a global optimum even if the objective function is multimodal, multiconstrained, non-differentiable, non-continuous, or noisy. The cost of robustness is a far greater computational time than what is needed by derivative-based algorithms, or even deterministic direct methods not based on derivatives.

EAs work by mimicking evolution in the nature, dealing not with single points in the optimization space, but populations of trial solutions competing for survival and chance of producing offspring (new trial solutions) to the next generation. Random mutations are used to preserve diversity and ensure a thorough search of the objective function scope. The better the objective function value of a trial solution, the better its chance of surviving to the next generation. Genetic algorithms emphasize crossover over mutation and apply selection pressure also on selecting parents for the crossover, whereas evolution strategies rely mainly on mutation and offspring selection.

DE resembles evolution strategies in being a real-valued optimizer with mutation emphasized over crossover, and only offspring but no parent selection. Discrete variables are dealt with by dividing the allowable range to slots, any real number from one slot translating to a single value in objective function evaluation. An important characteristic of DE is that the magnitude of the mutations is adjusted by basing the mutation on a difference vector between two randomly chosen vectors $\mathbf{x}_{r1}$ and $\mathbf{x}_{r2}$. This ensures that as the population converges and the search proceeds from global exploration to fine-tuning the solution (so-called local exploitation stage), the mutations become gradually smaller.

The process of creating a new generation G+1 of candidate solutions from generation G is shown in Figure 7.5. Each vector serves once as a target vector $\mathbf{x}_i^G$, surviving to G+1 if it yields a better objective function value than a trial vector $\mathbf{u}_i^G$. Generating the trial vector

begins by creating a mutant vector $\mathbf{v}_i^G$ by randomly choosing a base vector $\mathbf{x}_{r0}^G$ and perturbing it by differential mutation,

$$\mathbf{v}_i^G = \mathbf{x}_{r0}^G + F\left(\mathbf{x}_{r1}^G - \mathbf{x}_{r2}^G\right), \tag{7.4}$$

where $F \in (0,1)$ is a weight factor and $\mathbf{x}_{r0}^G \neq \mathbf{x}_{r1}^G \neq \mathbf{x}_{r2}^G$. The trial vector is then built by crossover between the target vector and mutant vector. This is typically a binomial (uniform) crossover, where the value of each decision variable d is chosen from either the mutant or target vector:

$$u_{i,d}^G = \begin{cases} v_{i,d}^G & \text{if } \varepsilon_d \le CR \\ x_{i,d}^G & \text{otherwise} \end{cases}, \tag{7.5}$$

where ε_d is a uniform-distributed random number, $\varepsilon_d \in [0,1]$, and CR is an adjustable crossover parameter, $CR \in [0,1]$.

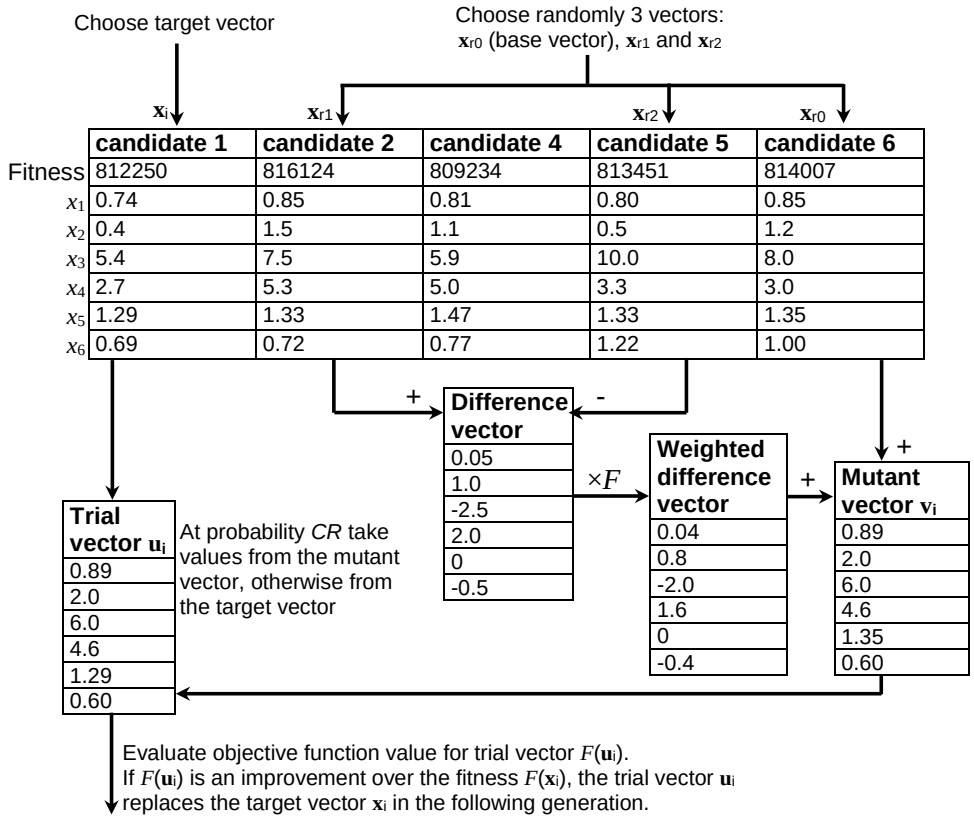

Figure 7.5: Creating new generation in DE/rand/1/bin: each population member (candidate solution or candidate) serves once as a target vector, surviving to the next generation if its fitness (objective function value) is better than that of the trial vector. Here NP=6 and F=0.8.

If the objective function is not separable, i.e. the 'goodness' of one variable value cannot be determined in isolation but depends on other variables, differential mutation provides a rotationally invariant search that can easily move in multiple variable axes simultaneously. High values of *CR*, emphasizing mutation over crossover are thus necessary for non-separable problems, while low *CR* promoting search along variable axes may yield better results for separable problems (Price *et al.*, 2006).

The form of DE described above is known as DE/rand/1/bin for *rand*om selection of base vector perturbed in differential mutation by *1* vector difference followed by *bin*omial crossover with the target vector. Different strategies have been proposed for both base vector selection and performing the crossover, each having some advantages and disadvantages over each other and the original DE. Initially in Publication II, the DE/rand/1/bin was used for the extraction steam DH condenser mass minimization. Later, the DE/local-to-best/1/bin and DE/rand/1/either-or were also tested in search for a way to reduce the computational time without sacrificing reliability.

DE/local-to-best/1/bin is otherwise similar to DE/rand/1/bin, but as the name suggests, the basis of differential mutation is set not at the base vector $\mathbf{x}_{r0}{}^{G}$ itself, but on the line between $\mathbf{x}_{r0}{}^{G}$ and the best solution found so far, $\mathbf{x}_{best}{}^{G}$. The mutant is thus obtained from

$$\mathbf{v}_i^G = \mathbf{x}_{r0}^G + F\left(\mathbf{x}_{best}^G - \mathbf{x}_{r0}^G\right) + F\left(\mathbf{x}_{r1}^G - \mathbf{x}_{r2}^G\right). \tag{7.6}$$

In case of DE/rand/1/either-or, an attempt is made to replace the uniform crossover, which is effective only at separable problems, with a rotationally invariant three-vector recombination. The trial vector is either the mutant from Equation (7.4) as is, or the recombinant, based on an adjustable probability p_F:

$$\mathbf{u}_i^G = \begin{cases} \mathbf{x}_{r0}^G + F\left(\mathbf{x}_{r1}^G - \mathbf{x}_{r2}^G\right) & \text{if } \varepsilon \le p_F \\ \mathbf{x}_{r0}^G + \dfrac{F+1}{2}\left(\mathbf{x}_{r1}^G + \mathbf{x}_{r2}^G - 2\mathbf{x}_{r0}^G\right) & \text{otherwise} \end{cases}, \tag{7.7}$$

where ε is a uniform-distributed random number, $\varepsilon \in [0,1]$.

Population size (number of parents, *NP*) of 10 times the number of decision variables *D* is often recommended. Reducing *F* improves convergence rate at the cost of reliability. As real-world problems tend to be non-separable, $0.8 < F < 1.0$ and $CR \approx 0.9$ are often recommended for an initial, conservative guess emphasizing reliability over speed (Price *et al.*, 2006).

7.3.2 Cuckoo search

First introduced in 2009 (Yang & Deb, 2009a), the Cuckoo Search (CS) is one of the most recent metaheuristic optimization algorithms. Like many metaheuristics, it is inspired by processes observed in nature: in this case, the well-known brood parasitic behaviour of

many cuckoo species (Yang, 2014), as well as a search pattern known as Lévy flights which maximises the efficiency of resource search (Focardi *et al.*, 2009) and has been observed in several mobile foraging species in nature (Focardi *et al.*, 2009; Yang, 2014).

Similarly to evolutionary, particle swarm and many other nature-inspired algorithms, the CS also operates not with a single point that it tries to improve, but a population of candidate solutions, which in CS represent cuckoo eggs. Each cuckoo lays one egg to one nest per generation. As this number is fixed, there is no practical distinction to be made between a cuckoo, an egg, and a nest.

Unfortunately, there is some discrepancy in the literature as to what, precisely, constitutes a cuckoo search. Specifically, while the ways the algorithm is described in (Yang & Deb, 2009a, 2009b) and (Yang, 2010a) are for the most part similar, the description in the text of (Yang, 2014) differs somewhat from these, and the actual MATLAB code provided in (Yang, 2014) provides a yet another, significantly different implementation. In the following, the algorithm as it was understood to work in its originally published form is referred to as CS-1. The slightly modified, but still broadly similar version described in the text of (Yang 2014) is referred to as CS-1mod. The implementation as MATLAB code in the attachment of (Yang, 2014) is referred to as CS-2, and a version based on the latter but modified by the candidate during the thesis work is referred to as CS-3.

In the original form as first introduced, the CS-1 algorithm was based heavily on so-called Lévy flights, i.e. random walks where the step length is drawn from a Lévy distribution. The Lévy distribution is a relatively heavy-tailed one compared to for example Gaussian distribution, which enables the algorithm to sufficiently often take the longer leaps necessary to effectively explore the search space, and not become stuck in a local optimum. The random walk that results from a series of Lévy-distributed steps is typically characterized by clusters of short steps connected by less common longer leaps.

All versions of CS are based on a two-stage iteration, where the first stage is typically one of Lévy flights based on the best candidate solution (egg) of the population, and the second is one of abandoning the worst solutions.

According to Yang (2009a), some of the new candidates should be generated by Lévy flights around the best solution, but a significant fraction should be created by far-field randomization. Many interpretations of the original CS, such as those described in (Walton *et al.*, 2011) and (Walton, 2013), state that the Lévy flights should be taken from randomly chosen eggs, but both the description in (Yang & Deb, 2009a) and (Yang, 2010a) as well as the MATLAB code in (Yang, 2010a) clearly indicate that the Lévy flights in the original version, denoted by CS-1 here, were to be based on the best egg of the population.

A Lévy flight around the best candidate can then be created by basing it on a difference vector $\Delta\mathbf{x}_{\text{best}}$ between the best egg $\mathbf{x}_{\text{best}}{}^{G}$ of the current generation G and a randomly chosen egg $\mathbf{x}_{\text{r0}}{}^{G}$. A new trial egg for generation G+1, which replaces a randomly chosen

egg $\mathbf{x}_{r1}{}^{G}$ if it yields a better objective function value, can then be created by using the best vector as the starting point, and adding to it a random walk step generated according to the implementation used in the MATLAB code included in (Yang, 2014):

$$\mathbf{u}^{G} = \mathbf{x}_{best}^{G} + \alpha \cdot \Delta\mathbf{x}_{best} \circ \mathbf{s} \circ \mathbf{n}, \tag{7.8}$$

where α is a scaling factor, **s** is a Lévy-distributed step size vector and **n** is a vector of random numbers with a standard normal distribution. Operator $\circ$ refers to the Hadamard product (entrywise multiplication) of vectors. All vectors have a size of *D*. The step size vector **s** is found with Mantegna's algorithm originally published in (Mantegna, 1994) as cited in (Yang, 2014) using two normal-distributed random variable vectors **p** and **q** of size *D* and a Lévy exponent β:

$$\mathbf{s} = \mathbf{p} \circ \mathbf{q}^{\circ -1/\beta}, \tag{7.9}$$

where all elements of **p** and **q** have a mean of zero, and variances of 1 and σ^2, respectively. σ^2 is calculated from

$$\sigma^2 = \left[\frac{\Gamma(1+\beta)}{\beta \cdot \Gamma(½ + ½\beta)} \cdot \frac{\sin(½\pi\beta)}{2^{½(1+\beta)}} \right]^{1/\beta}, \tag{7.10}$$

where Γ is the gamma function, $\Gamma(n) = (n\text{-}1)!$.

At the second stage the worst egg is abandoned at probability p_a. While the description in (Yang & Deb, 2009a) implies random re-initialization of the abandoned solutions both in the text and in the pseudo-code, the presentation (Yang & Deb, 2009b) unambiguously states Lévy flight as a method, and the simplified MATLAB code presented in (Yang, 2010a) specifies the abandoned solution as the starting point for the random step. If the worst egg of the population is abandoned, it is replaced by a new egg whether the new egg improves the objective function value or not. While the precise updating function is not given in any of the references, the simplified code of (Yang, 2010a) strongly implies this should be the same as used in the first step, Equation (7.8), but based on the worst member. The Lévy flight implementation of (Yang, 2014) was thus adapted to this concept as

$$\mathbf{x}^{G+1} = \mathbf{x}_{worst}^{G} + \alpha \cdot \Delta\mathbf{x}_{worst} \circ \mathbf{s} \circ \mathbf{n}. \tag{7.11}$$

As good solutions are less likely to be found near the worst solutions, choosing a much larger value of α for Equation (7.11) than for Equation (7.8) would likely be a good choice.

The process is summarized in Algorithm 7.1. It should be noted that unlike most population-based metaheuristics where each iteration through the algorithm typically

involves a similar number of function evaluations as there are population members, in case of CS-1 each iteration involves only one or two function evaluations, and only the best and worst member of the population serve as starting points for the Lévy flights.

Later, in reference (Yang, 2014), a broadly similar description of the algorithm is given in the text, differing mainly in the second stage of abandoning some of the eggs. The updating function could be interpreted as

$$\mathbf{x}^{G+1} = \mathbf{x}_{\text{worst}}^{G} + \alpha \cdot \mathbf{s} \circ H(p_a - \varepsilon) \circ (\mathbf{x}_{r1}^{G} - \mathbf{x}_{r2}^{G}), \tag{7.12}$$

where α and **s** are the scaling factor and step size vector as used in Equation (7.8), p_a is the switching probability, and ε is a uniformly distributed random variable. H refers to the Heaviside step function, which yields an output of 1 for positive inputs, otherwise 0.

Yang (2014) describes the second stage of the iteration using Equation (7.12) as a local search as opposed to the global random walk, although basing an exploitative local search on the worst population member would appear unlikely to be effective. This would also contradict the earlier references which stress the importance of far-field randomization in addition to the random walk around the best candidate (Yang & Deb, 2009a), or use the same updating function as for the first step (Yang, 2010a). The use of Equation (7.12) is thus considered a slightly modified implementation of the cuckoo search, and labelled here CS-1mod.

Algorithm 7.1. Original Cuckoo Search (CS-1) to maximize function $f(\mathbf{x})$, $\mathbf{x} = (x_1, \ldots, x_D)^T$.

begin
  Create a random population of *NP* parent cuckoos $\mathbf{x}_i$, $i = 1, 2, \ldots, NP$
  for all $\mathbf{x}_i$ **do**
    Find objective function value $F_i = f(\mathbf{x}_i)$
  end for
  Rank the solutions to find $\mathbf{x}_{\text{best}}{}^1$ and $\mathbf{x}_{\text{worst}}{}^1$
  while $NFE < NFE_{\max}$ **do**
    Select a random egg $\mathbf{x}_{r0}{}^G$, $\mathbf{x}_{r0}{}^G \neq \mathbf{x}_{\text{best}}{}^G$
    Create a new trial egg $\mathbf{u}^G$ by taking a Lévy flight from $\mathbf{x}_{\text{best}}{}^G$, Equation (7.8)
    Find objective function value $F_u{}^G = f(\mathbf{u}^G)$
    Select a random egg $\mathbf{x}_{r1}{}^G$
    if ($F_u{}^G > F_{r1}{}^G$)
      $\mathbf{x}_{r1}{}^{G+1} \leftarrow \mathbf{u}^G$
      $F_{r1}{}^{G+1} \leftarrow F_u{}^G$
    end if
    The worst egg of the population $\mathbf{x}_{\text{worst}}{}^G$ is abandoned at probability p_a
    If abandoned, a replacement is generated by Lévy flight from $\mathbf{x}_{\text{worst}}$, Equation (7.11)
    Rank the solutions to find new $\mathbf{x}_{\text{best}}{}^{G+1}$ and $\mathbf{x}_{\text{worst}}{}^{G+1}$.
  end while
end

As noted by the algorithm's author in (Yang, 2014), the updating equation (7.12) resembles differential mutation with the weight factor randomized by Lévy distribution; this is evident by comparing Equation (7.4) to Equation (7.12).

While the earlier descriptions and the broad outline of the simplified code in (Yang, 2010a) are mostly consistent with Algorithm 7.1, the MATLAB code of (Yang, 2014) differs significantly from it. This version, referred to as the CS-2 here, also consists of two steps where the first is one is based on Lévy flights according to Equation (7.8), only in this case performed for all eggs of the population rather than only the best member. The new egg replaces the original if it improves the objective function value. The main difference is in the second stage. Instead of replacing the worst or some of the worst eggs at probability p_a, a new trial solution is generated from each egg. Another change is that the candidate replaces the original only if it yields an improved objective function value. The updating function for each decision variable d of the trial solution $\mathbf{u}_i^G$ is

$$u_{i,d}^G = \begin{cases} x_{i,d}^G & \text{if } \varepsilon_d \le p_a \\ x_{i,d}^G + \gamma_d \left(x_{r1,d}^G - x_{r2,d}^G \right) & \text{otherwise} \end{cases}, \tag{7.13}$$

where ε_d and γ_d are uniform-distributed random numbers, ε_d, $\gamma_d \in (0,1)$. This process, as noted by Walton *et al.* (2013a), is even more similar to differential evolution than Equation (7.12). Equation (7.13) is essentially a DE/rand/1/bin with the target and base vectors being the same, crossover parameter $CR = 1 - p_a$, and a uniform-distributed random $F \in (0,1)$. The role of p_a has changed from a probability of abandoning the worst solution of the population, to the probability of a variable value remaining unchanged in a trial solution. The process is summarized as pseudo-code in Algorithm 7.2.

The CS-2 algorithm was used in Publication VI. The CS is said to be relatively insensitive to the values of α and β, with values of $\alpha = 0.01$ and $\beta = 1.5$ being usable for most problems (Yang, 2014). While there is some doubt as to whether this applies to all variants of CS that appear to exist, these parameters were used in Publication VI, and proved effective. Switching probability $p_a = 0.25$, population size of $NP = 60$ parent cuckoos, and a stopping condition of 300 generations were also used in Publication VI. Later, the optimal tuning of p_a and NP were determined; this is described in chapter 7.5.

It is clear that an intrinsic capability of DE and differential mutation is to focus the search from global exploration to local exploitation as the search goes on and population converges. At this stage, based on findings made during the progress of this work as well as those reported in (Walton *et al.*, 2013), it was concluded that the good performance of CS-2 may owe as much or more to the DE-like second step according to Equation (7.13) than to the Lévy flights on which the algorithm was originally based on.

Algorithm 7.2. Cuckoo Search (CS-2) to maximize function $f(\mathbf{x})$, $\mathbf{x} = (x_1, \ldots, x_D)^T$, as implemented in the MATLAB code of reference (Yang, 2014).

begin
  Create a random population of NP parent cuckoos $\mathbf{x}_i$, $i = 1, 2, \ldots, NP$
  for all $\mathbf{x}_i$ **do**
    Find objective function value $F_i = f(\mathbf{x}_i)$
  end for
  while $NFE < NFE_{max}$ **do**
    for all $\mathbf{x}_i$ **do**
      Create a trial egg $\mathbf{u}_i^G$ by taking a Lévy flight from $\mathbf{x}_i^G$, Equation (7.8)
      Find objective function value $F_{u(i)}^G = f(\mathbf{u}_i^G)$
      if $(F_{u(i)}^G > F_i^G)$
        $\mathbf{x}_i^{G+1} \leftarrow \mathbf{u}_i^G$
        $F_i^{G+1} \leftarrow F_{u(i)}^G$
      end if
    end for
    for all $\mathbf{x}_i$ **do**
      Create a trial egg $\mathbf{u}_i^G$ by random-weight differential mutation, Eq. (7.13)
      Find objective function value $F_{u(i)}^G = f(\mathbf{u}_i^G)$
      if $(F_{u(i)}^G > F_i^G)$
        $\mathbf{x}_i^{G+1} \leftarrow \mathbf{u}_i^G$
        $F_i^{G+1} \leftarrow F_{u(i)}^G$
      end if
    end for
    Rank the solutions
  end while
end

DE and differential mutation are not without weaknesses, however; as the population converges, the ability to perform global exploration is lost. This creates a risk of stagnation to a local optimum, particularly if a too small mutation weight or population size is used for optimizing a multimodal function. The Lévy flights on the other hand do maintain their ability to explore the entire objective function space. Based on this conclusion, a new hybrid Lévy flight / differential mutation algorithm, henceforth referred to as CS-3, was developed.

The new algorithm relies even more on differential mutation than Lévy flights. The role of Lévy flights is to add robustness by maintaining some amount of global exploration throughout the search by applying it on a minority fraction of the worst eggs. The differential mutation step, which was presumed to be overall more efficient at searching and thus the main search method, was applied on the whole population in each generation.

The DE/rand/1/bin with $\mathbf{x}_i = \mathbf{x}_{ro}$ was implemented as the first stage of the CS-3 iteration. In the second stage, the number of worst eggs abandoned was set as $p_a \cdot NP$, maintaining the original idea of CS-1 where the p_a is the fraction of abandoned eggs. There is no inherent connection between this definition of p_a and the crossover with the base/target

vector in Equation (7.13); thus using the nomenclature of Equation (7.4) and (7.5), the trial vector $\mathbf{u}_i^G$ is created at the second stage by generating each of its D members by

$$u_{i,d}^G = \begin{cases} x_{i,d}^G & \text{if } \varepsilon_d \geq CR \\ x_{i,d}^G + F_d\left(x_{r1,d}^G - x_{r2,d}^G\right) & \text{otherwise} \end{cases}, \tag{7.14}$$

where the scalar F of Equation (7.4) is replaced by a vector $\mathbf{F}$ of size D, $F_d \in (0.5,1)$, and base vector $\mathbf{x}_{r0}$ is set as the target vector $\mathbf{x}_i$. The magnitude of the mutation scale was increased from Equation (7.13) as implemented in the MATLAB code in (Yang, 2014) as it was evident that DE becomes prone to converge on local optimums if F is too small. The new algorithm is shown as pseudo-code in Algorithm 7.3.

Algorithm 7.3. Cuckoo Search (CS-3) to maximize function $f(\mathbf{x})$, $\mathbf{x} = (x_1, \ldots, x_D)^T$

begin
  Create a random population of NP parent cuckoos $\mathbf{x}_i$, $i = 1, 2, \ldots, NP$
  for all $\mathbf{x}_i$ **do**
    Find objective function value $F_i = f(\mathbf{x}_i)$
  end for
  while $NFE < NFE_{max}$ **do**
    for all $\mathbf{x}_i$ **do**
      Create a trial egg $\mathbf{u}_i^G$ by Eq. (7.4) and (7.5); $F_D \in (0.5,1)$, and $\mathbf{x}_{r0} = \mathbf{x}_i$.
      Find objective function value $F_{u(i)}{}^G = f(\mathbf{u}_i^G)$
      if $(F_{u(i)}{}^G > F_i^G)$
        $\mathbf{x}_i^G \leftarrow \mathbf{u}_i^G$
        $F_i^G \leftarrow F_{u(i)}{}^G$
      end if
    end for
    Rank the solutions
    for worst $(p_a \cdot NP)$ solutions **do**
      Create a trial egg $\mathbf{u}_i^G$ by taking a Lévy flight from $\mathbf{x}_i^G$, Equation (7.8)
      Find objective function value $F_{u(i)}{}^G = f(\mathbf{u}_i^G)$
      if $(F_{u(i)}{}^G > F_i^G)$
        $\mathbf{x}_i^{G+1} \leftarrow \mathbf{u}_i^G$
        $F_i^{G+1} \leftarrow F_{u(i)}{}^G$
      end if
    end for
  end while
end

Different ways of setting the p_a and CR were evaluated experimentally. Constant values of p_a ranging from 0.15 to 0.5, as well as a varying p_a increasing from 0.1 to 0.5 linearly or decreasing from 0.5 to 0.1 as a function of NFE approaching the termination criterion NFE_{max}. The impact of p_a appeared relatively small, but becoming slightly worse particularly towards the higher values of $p_a = 0.5$.

Finally, also replacing the DE/rand/1/bin with the greedier DE/local-to-best/1/bin strategy was tested as the first step of the CS-3 iteration. The performance test results and analysis are presented in chapter 7.5.

7.3.3 Genetic Algorithm

The genetic algorithm is one of the first and best-known metaheuristic optimization algorithms, and as such, is often used as a benchmark against which new methods are compared. In this work, an implementation supplied with the MATLAB Global Optimization toolbox is used. As an evolutionary algorithm, the GA uses populations of trial solutions, mimicking natural evolution to optimize a given objective function. In each iteration of the algorithm a generation of new trial solutions is produced by crossover and mutation. Solutions of current generation G are known as parents, those of G+1 as offspring. Elitism ensures the survival of the best solutions: a number of best solutions, defined by the elite count parameter N_E, survive without changes to the new generation.

The main search method of the GA is typically crossover, where an offspring is created by taking two solutions of the current generation, and creating the offspring for generation G+1 as a recombination of both. In this work, the so-called scattered crossover, where variable values of the offspring are chosen randomly from one or the other parent, was used. Parents are selected by stochastic universal sampling: the population is laid out as a line where each individual's length is proportional to its fitness value to be maximized, and selection traverses this line with equal step length set to cover the entire length, selecting each individual the pointer lands on with each step. The fraction of offspring generated by crossover is defined by the crossover fraction $CF \in [0,1]$.

Mutation is used to generate the remainder of new offspring needed for G+1. A mutant is created from a parent, chosen by stochastic universal sampling as with crossover, by adding to it a vector of Gaussian-distributed random variables with a mean of zero. The standard deviation of the distribution reduces as the search continues. At generation G = 1, the standard deviation of each decision variable d is set with a mutation scale parameter MS and the upper and lower bounds of the variable,

$$\sigma_{1,\mathrm{d}} = MS \cdot \left(x_{d,\max} - x_{d,\min}\right). \tag{7.15}$$

The standard deviation of each generation is then obtained from the standard deviation of the previous generation $\sigma_{\mathrm{G-1}}$, a shrink parameter S and maximum number of generations $G_{\max}$:

$$\sigma_{\mathrm{G}} = \sigma_{\mathrm{G-1}}\left(1 - S\frac{G}{G_{\max}}\right). \tag{7.16}$$

7.4 Results

7.4.1 Extraction steam DHC mass minimization

The results from the extraction steam condenser optimization, while somewhat tangential to the main research questions of this thesis, nevertheless showed that the heat transfer area *A*, which is often used for minimizing single-phase shell-and-tube heat exchanger costs in existing literature, cannot be used as the basis of a cost function for low-pressure steam condenser optimization. The details of the heat transfer and sizing models can be found in Publication II; the resulting dimensions from using mass or area minimization as objective functions can be seen in Table 7.3 below.

Table 7.5: Extraction steam DHC cost minimization results with two objective functions.

Variable		Minimum *m*	Minimum *A*
m_{HX}	Heat exchanger mass [kg]	6 913	76 578
A	Heat transfer area [m^2]	331	284
L_{HX}	Heat exchanger total length [m]	6.900	6.088
D_{HX}	Heat exchanger total diameter over flanges [m]	1.050	3.491
s_s	Shell thickness [mm]	13	35
s_{ts}	Tube sheet thickness [mm]	99	304
s_{cc}	Channel cover thickness [mm]	47	166

While Min(*A*) does give a smaller heat transfer area than Min(*m*), it is clear that being over 10 times heavier than the Min(*m*) result, this cannot approximate a minimum-cost design. Min(*A*) as an objective function allows steam pressure drop minimization by minimizing vapour velocity with a large, mostly empty shell. By maintaining high steam T_{sat} and thereby temperature difference, a smaller heat transfer area is sufficient.

7.4.2 Back pressure DHC optimization

Optimization of the back pressure condenser was performed at varying electricity prices, ranging from 40 to 80 €/MWh. While the low-end scenarios for future electricity prices in Nordic countries include even lower prices, unsubsidized biomass-fired CHP production is unlikely to be profitable in these scenarios, and condenser optimization for such scenarios was thus considered meaningless. Three cases of heat exchanger cost were considered: base, -20% optimistic and +20% pessimistic. The main parameters corresponding to 40, 60 and 80 €/MWh electricity price and base case of condenser price are listed in Table 7.4.

The condenser optimized for 40 €/MWh electricity price is far smaller than the other two, which are relatively similar to each other. While the smaller exchanger is much cheaper, the shorter design increases the relative share of shell, channel and tube sheet, which results in an almost 50 % greater specific cost of heat transfer area.

When the parameters used for plant performance estimation, G_{eff} and ΔT_{SC}, are plotted over the range of electricity price c_{el} for all condenser cost cases (Figure 7.6), a clear step change at approximately 50 €/MWh$_{el}$ becomes evident. At c_{el} values above the step change, G_{eff} varies from 1350 to 1550 kW/K and sub-cooling remains stable at ΔT_{SC} = 0.6±0.5 °C; below, the ranges vary from 400 to 600 kW/K and 0.2 to 0.4 °C. Above the step change, condenser manufacturing cost case has less than 5% impact on optimal conductance and heat transfer area at any given c_{el}.

It is evident that although a large step change takes place in condenser size and cost, the design optimized for an electricity price immediately below the step change price level does not yet represent the minimum condenser size within the constraints; conductances continue to reduce towards the lower electricity prices. The CHP plant also remains profitable with a positive net cash flow rate even assuming an expected return rate of 10 % for the investment, and in fact no similar step change in net cash flow rate takes place (Figure 7.7). It appears that the step change represents the point at which increasing the DH production during period P1 at the expense of power generation starts to outweigh the benefit that could be achieved by increased power output at part load.

Table 7.6: Condensers optimized for different electricity prices. Baseline case for the manufacturing cost is assumed.

	P_{el} [€/MWh$_{el}$]	**40**	**60**	**80**
Decision variables	$x_1=D_{OTL}/D_s$	0.737	0.750	0.740
	$x_2=N_{tbp}$	2	2	2
	$x_3=L_{str}$	4.000	8.054	8.066
	$x_4=d_o$ [mm]	18.0	16.0	16.0
	$x_5=P/d_o$ [-]	1.278	1.313	1.313
	$x_6=A_{fr,c}$ [m^2]	0.045	0.079	0.086
Optimized DHC dimensions	L_{tot} [m]	4.982	9.345	9.386
	D_{tot} [m]	0.821	1.096	1.148
	D_{ch} [m]	0.677	0.898	0.926
	D_s [m]	0.821	1.064	1.134
	L_s [m]	4.376	8.543	8.557
	s_{ts} [mm]	92	116	121
	s_{chc} [mm]	34	43	45
	m_{tot} [kg]	3 633	10 760	11 515
	$N_{tb/pass}$ [-]	255	599	645
	A_{tot} [m^2]	120	497	536
Costs	C_{tot} [10^6 €], Equation (7.3)	0.08	0.82	1.58
	C_{FOB} [10^3 €]	37	107	114
	c_{FOB} [€/m^2]	307	216	213

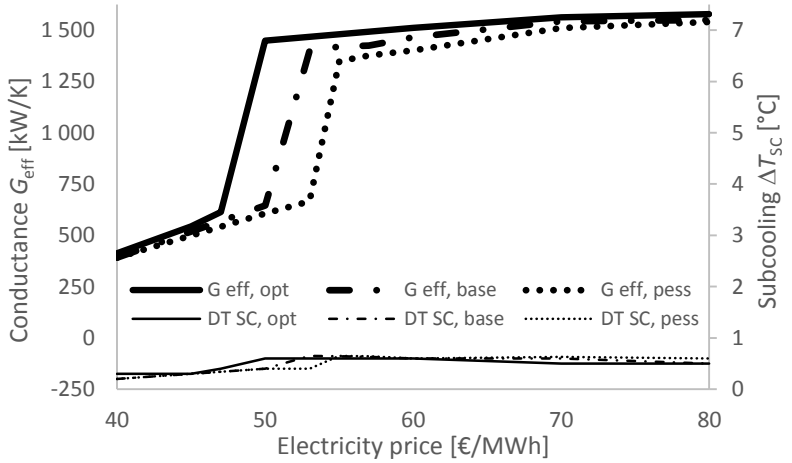

Figure 7.6: Conductance (thick line) and subcooling (thin) in optimized condensers at varying electricity price and optimistic (-20%), baseline and pessimistic (+20%) cost assumption.

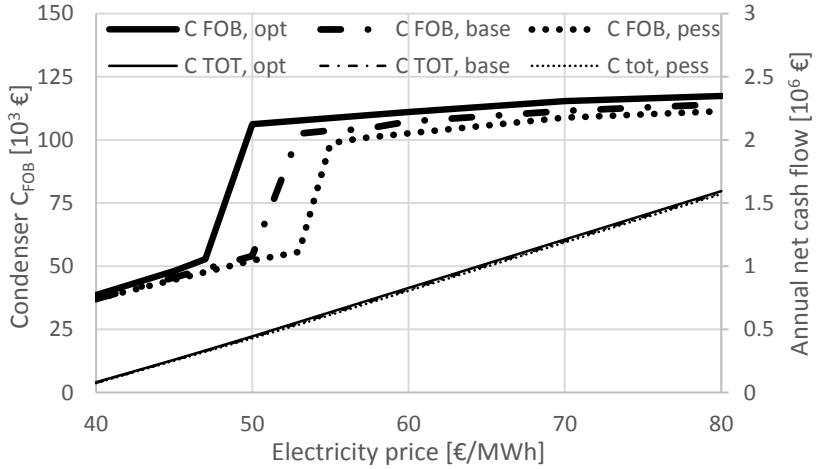

Figure 7.7: Condenser FOB cost and plant annual net cash flow as function of electricity price.

Figure 7.8 presents the optimal values of maximum-load (period P1) TTD and water pressure drop Δp_c as a function of electricity price above the step change. The optimum values fall within a relatively narrow range at all electricity prices and condenser cost scenarios; mostly 2-3 °C TTD and 0.4-0.5 bar Δp_c.

TTD becomes smaller at a reducing rate towards increasing electricity prices as could be expected, while the Δp_c curves tip downwards at the high end of electricity prices in all cases. The tip downwards in Δp_c could be an indication of the role of the pumping power

becoming relatively more important as the cost of obtaining more power output from the turbine increases with what is already a relatively large, low-TTD condenser design.

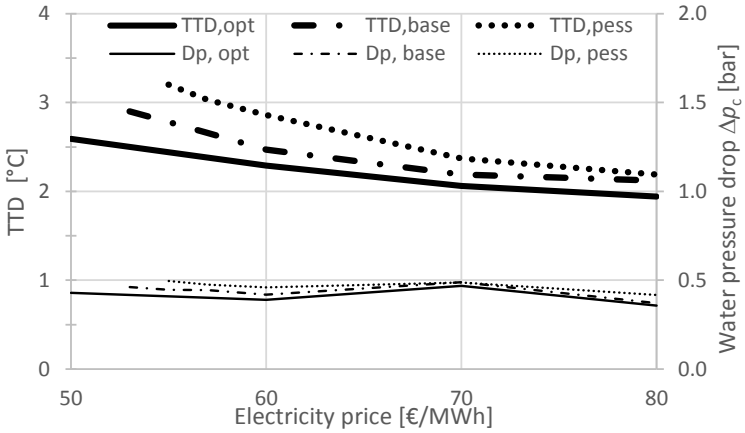

Figure 7.8: Terminal temperature difference and DH water pressure drop in optimized condensers as function of electricity price.

The possibility of altering the conductance by varying condensate level in the condenser shell was not considered here. A design where condensate level could be allowed to raise in the tube bundle to submerge some of the heat transfer tubes would allow a given condenser design both deliver high conductance and thus maximum electricity output at part load, and reduce the power output for increased DH production during the full-load period. This would likely be the best strategy in a situation when electricity price is less than district heat price, but still sufficiently high that the CHP plant is profitable.

7.5 Improving the optimization speed

Particularly the extraction steam DHC mass minimization proved to be a computationally heavy process taking a considerable amount of time to find a solution, and efforts were taken to reduce this. Firstly, significant calculation time reduction was achieved by adjusting the model to use the first or second-order numerical derivatives from the previous calculation elements both in steam and water flow direction to obtain good initial guesses for the each element (i,j) being calculated whenever applicable. The number of iterations through the calculation elements could be approximately halved by this method, and objective function evaluation time by almost as much.

The initial trials with the optimization showed that the choice of decision variables is important. Although a rotationally invariant search such as DE or CS can succeed well with completely non-separable problems, usually they, too, can perform somewhat better if such a choice of decision variables is made that the scale of the possible values is narrow, and the probability of constraint violations resulting from crossover is low. For

this reason for example the tube-side free flow area or flow velocity is a better choice of decision variable than the number of tubes, whose appropriate value will vary greatly depending on the chosen diameter.

The results of Table 7.5 were found with DE/rand/1/bin strategy using a population of NP=60 and parameters F = 0.8 and CR = 0.9. The algorithm was set to stop when reaching 600 generations, or after complete convergence. Convergence was considered complete when all population member had identical values of discrete variables, and the coefficient of variation of objective function values was $c_v < 0.001$. The coefficient of variation is calculated from

$$c_v = \sigma / \mu, \tag{7.15}$$

where σ is the standard deviation of objective function values and μ the mean value.

To ensure that the solution was the actual optimum at a high probability, four consecutive optimization runs were performed; each found the same minimum mass within 10 kg, all but one reaching the 600 generations. Based on repeatable results with parameters tending towards robustness over speed, this was considered likely to be the global optimum. In a PC with a 2.4 GHz CPU, the average run time was approximately 15 hours.

The 15-hour run time for 600 generations was achieved after the aforementioned measures had already been taken to reduce the calculation time. Some further time reduction was achieved by using a cheaper surrogate function in the initial run period of the algorithm, where the population had not yet converged. The surrogate function was implemented by simplifying the heat transfer model by using only two calulation elements in the water flow (tube) direction, and allowing less strict termination criteria for the iteration of both an individual calculation element, and through the tube rows. The computationally much heavier full-precision model would be used to evaluate a trial vector only if the objective function value obtained using the surrogate was close enough to that of the target vector to warrant the CPU usage. This had a noticeable impact on the computation time, since the surrogate could be evaluated in only a fraction of the time it would take to evaluate the full-precision model, which particularly in the earlier stages of population convergence would then be only rarely be used.

During the work the performance of DE and its sensitivity to the tuning parameters was also investigated to find ways of improving the performance. It was found that considerable performance improvement was possible also by this method: good results could still be found with reduced mutation weight factors of $F \approx 0.5$ in approximately 200…300 generations.

For the back pressure condenser optimization, cuckoo search (CS) was used. Khosravi *et al.* (2015) had compared the CS to other algorithms in shell-and-tube heat exchanger optimization and found it the fastest of the tested methods, although the comparison did not include DE. Together with the candidate's own experience with both algorithms in

different problem areas, improved performance from using the CS appeared to be possible, and significantly worse behaviour unlikely. As the back pressure condenser optimization was necessary to be run over a range of combinations of condenser cost and electricity price assumptions, good performance of the algorithm was an important consideration. For this purpose the decision to switch to the CS was initially made.

It became quickly evident in the process of the work that the objective function evaluation time in back pressure DHC optimization was much shorter than with the extraction steam DHC mass minimization: in the order of approximately just 10 %. This was the case even though the heat transfer model was run at four load points during each objective function evaluation, and the extraction steam condenser at only one.

The much shorter objective function evaluation time of the back pressure DHC optimization was a result of several reasons. The heat transfer model iteration converged clearly faster due to the simpler geometry of the tube bundle: without the need to iteratively solve the state and magnitude of steam flow through the second pass into the first, much fewer iterations were required. By using a fixed number of elements in steam flow direction rather than treating each tube row as a calculation element, also the number of calculation elements was clearly reduced. Finally, it appeared that using the incoming steam pressure as the iteration variable in the outermost loop required much fewer iterations to converge, than using the condenser dimensioning to match the heat transfer rate requirement did.

While the calculation time was reduced by an order of magnitude, the time was still significant, particularly considering that the optimization would in practice be useful to be run at a number of different price scenarios. For this reason, a process of algorithm tuning and comparison was carried out to find the best algorithm to use for the problem, and suitable control parameter settings for it. This process is described in the following chapter.

7.5.1 Evaluation of algorithm performance and control parameter settings

Algorithm performance comparison and control parameter tuning was performed only for the main subject of investigation, the backpressure condenser optimization. An electricity price of c_{el} = 60 €/MWh, and baseline investment cost were assumed; other economic variables were those of Table 7.2.

First, the DE/rand/1/bin algorithm was run multiple times with parameters set at F = 0.9 and CR = 0.9, and NP = 60, yielding consistent results of 816487 € ± 2 €. Although it cannot be easily proven that this is the global optimum, based on the consistency of the results with settings tending towards reliability over performance, it was considered likely to be the case.

Next, the algorithms were tested over a range of control parameter settings to find how to tune them correctly, and their tuned performances. Initially, the testing focused on

different variants of CS and DE, while using GA as a benchmark. The attempts to use CS-1 were largely unsuccessful, despite attempts to vary the step length α at a range of 0.001 to 0.1 separately for the Lévy flights based on the best solution and for replacing the abandoned solutions, different population sizes, and trying different ways of implementing the re-building of the abandoned nests (by Equation (7.11) or (7.12), or by random re-initialization of the worst solution).

Also particle swarm optimization (PSO) by Eberhart and Kennedy (1995) was tested; based on the results, it, too, could be considered successful, although slightly slower and less reliable than GA. The results obtained with CS-1 variants and PSO are omitted for brevity from the following.

For each algorithm two most important parameters were identified. Parameters which were either considered to have a relatively small impact on performance, or for which a good recommended values were found from literature, were kept fixed. The range of values for the varied parameters and the values used for the fixed parameters are listed in Table 7.7 below.

Table 7.7: Optimization algorithm control parameter settings.

Algorithm	**Varied control parameters**	**Fixed control parameters**
GA*	Mutation scale $MS \in [0,1]$ Crossover fraction $CF \in [0,1]$	Number of parents $NP = 10D$ Elite count $N_E = 0.05NP$ Shrink parameter $S = 1$
DE/rand/1/bin	Mutation weight $F \in (0,1)$ Crossover rate $CR \in [0,1]$	Number of parents $NP = 10D$
DE/local-to-best	Mutation weight $F \in (0,1)$ Crossover rate $CR \in [0,1]$	Number of parents $NP = 10D$
DE/either-or	Mutation weight $F \in [0,1]$ Mutation probability $P_F \in [0,1]$	Number of parents $NP = 10D$ Recombination scale $K = ½(F+1)$
CS-2	Switching probability $p_a \in [0,0.5]$ Number of parents $NP \in [5,10D]$	Step length parameter $\alpha = 0.01$ Lévy exponent $\beta = 1.5$
CS-3	Crossover parameter $(1\text{-}CR) \in [0,0.5]$ Number of parents $NP \in [5,10D]$	Step length parameter $\alpha = 0.01$ Lévy exponent $\beta = 1.5$ Fraction of abandoned eggs $p_a = 0.2$

* stochastic universal sampling parent selection, scattered crossover, and Gaussian mutation

For assessing the impact of the varied control parameters, the range of each varied parameter was divided in 10 parts, resulting in a 10-by-10 grid. In each square of the grid, 10 random pairs of control parameter values were generated, and the algorithm was run with these settings. If the run was successful, the pair of parameter values was plotted as a circle; if all 10 runs were successful, the circles were filled. Figure 7.9 shows the success rates obtained with the GA, three DE variants, and two CS variants. The criterion for a successful run was finding an objective function value within 0.025 %, or 200 €, of the best value found with the very long runs initially performed by DE/rand/1/bin at $F = CR$

= 0.9. The other termination criterion was reaching the maximum number of objective function evaluations $NFE_{max} = 1.5 \cdot 10^4$, i.e. the equivalent of 250 generations with GA or DE. Figure 7.10 presents the average NFE required to reach the objective function value required for a run to be successful.

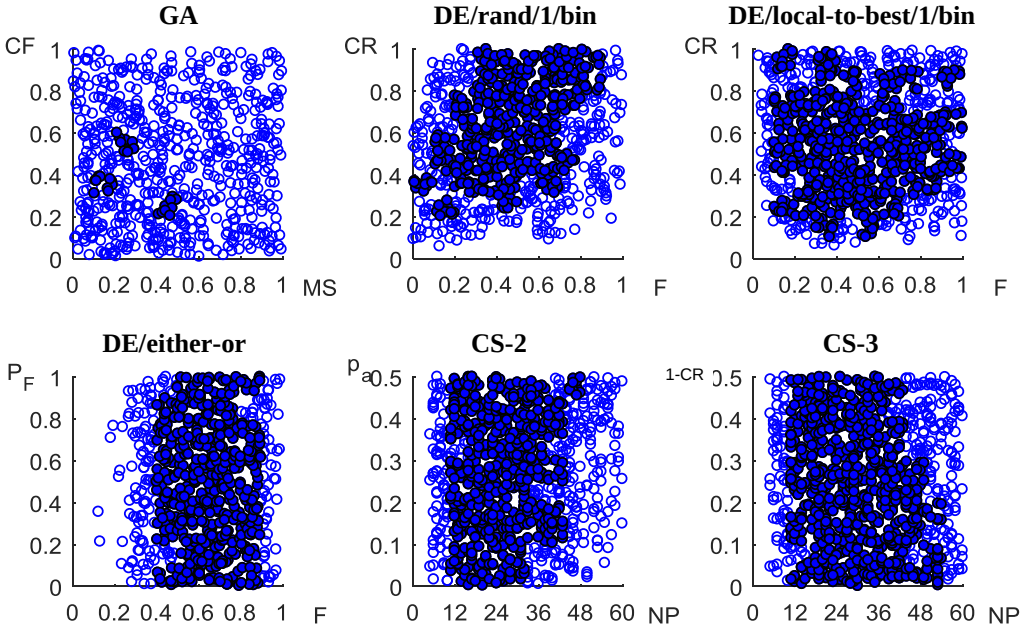

Figure 7.9: Successful optimization runs with different control parameter values.

It is evident that while there are differences in speed and reliability, all algorithms could be considered successful. The impact of control parameter settings on performance is also clear. For example the DE/rand/1/bin, while reliable at high values of *F*, could perform clearly faster with lower mutation weights without losing reliability.

Another interesting observation can be made on the CS-2 and CS-3: although these CS variants are based on a search very similar to the DE/rand/1/bin, they succeed with far smaller population sizes of only approximately 2…3*D*. Any DE variant would tend to converge prematurely with such a small population.

It was concluded that it is the Lévy flights which enable these DE-like methods to remain reliable with such a small population. The DE/local-to-best/1/bin was unsurprisingly the fastest as it was the greediest of the attempted strategies. As a drawback, it appeared to suffer from occasional misconvergence with high values of *CR* where its performance would otherwise be the fastest.

As a final stage, the convergence behaviour of all considered algorithms was tested with what was considered the best settings for each based on Figure 7.9 and 7.10. Termination

criterion was set as $NFE_{max} = 5000$, as it was evident that the earlier maximum of $1.5 \cdot 10^4$ was excessive for a well-tuned algorithm.

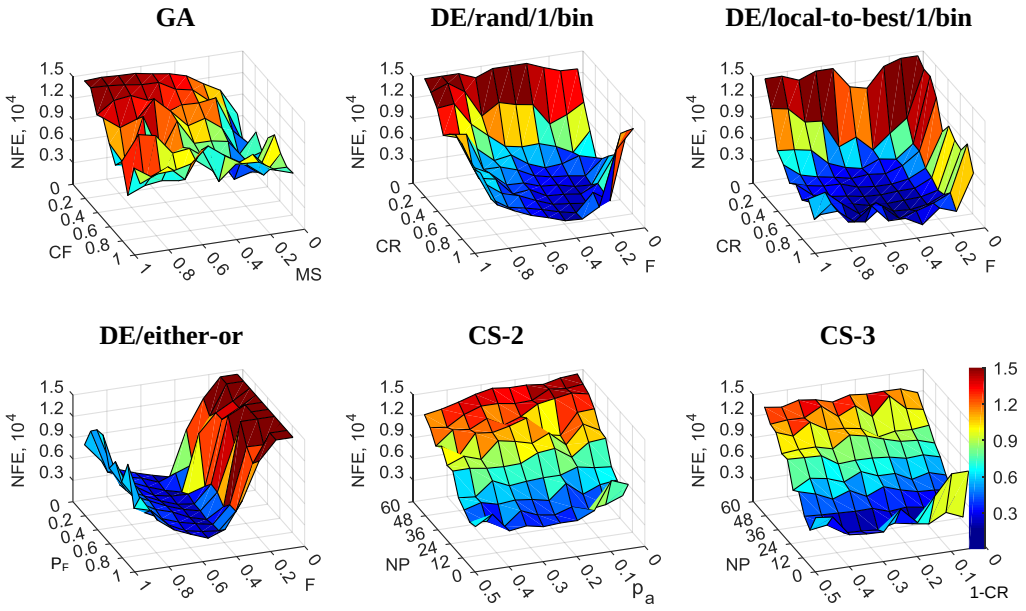

Figure 7.10: Average NFE required to converge to within 0.025% (i.e. within 200 € of best found annual net cash flow rate) of best found objective function value.

Also a one last modification of the CS-3 was tested at this stage; as it was evident that the Lévy flights were able to preserve diversity with quite small populations, it was also tested if they could do so with the classic differential mutation used in CS-2 and CS-3 replaced by the greedier local-to-best mutation strategy of Equation (7.6). This final modification is referred to as the CS-3mod. The control parameter settings used are listed in Table 7.8, and resulting convergence histories of 10 test runs per algorithm are plotted in Figure 7.11. Both the mean and worst objective function values are plotted.

Table 7.8: Control parameter values used for different algorithms for plotting the convergence graphs of Figure 7.11.

Algorithm	**Control parameter settings**
GA*	$NP = 60$; $N_E = 3$; $S = 1$; $MS = 0.4$; $CF = 0.5$
DE/rand/1/bin	$NP = 60$; $F = 0.4$; $CR = 0.95$
DE/local-to-best	$NP = 60$; $F = 0.5$; $CR = 0.7$
DE/either-or	$NP = 60$; $F = 0.5$; $P_F = 0.7$; $K = ½(F+1)$;
CS-2	$NP = 15$; $p_a = 0.1$; $\alpha = 0.01$; $\beta = 1.5$
CS-3	$NP = 15$; (1-CR) = 0.1; $p_a = 0.2$; $\alpha = 0.01$; $\beta = 1.5$
CS-3mod	$NP = 18$; (1-CR) = 0.25; $p_a = 0.2$; $\alpha = 0.01$; $\beta = 1.5$

* stochastic universal sampling parent selection, scattered crossover, and Gaussian mutation

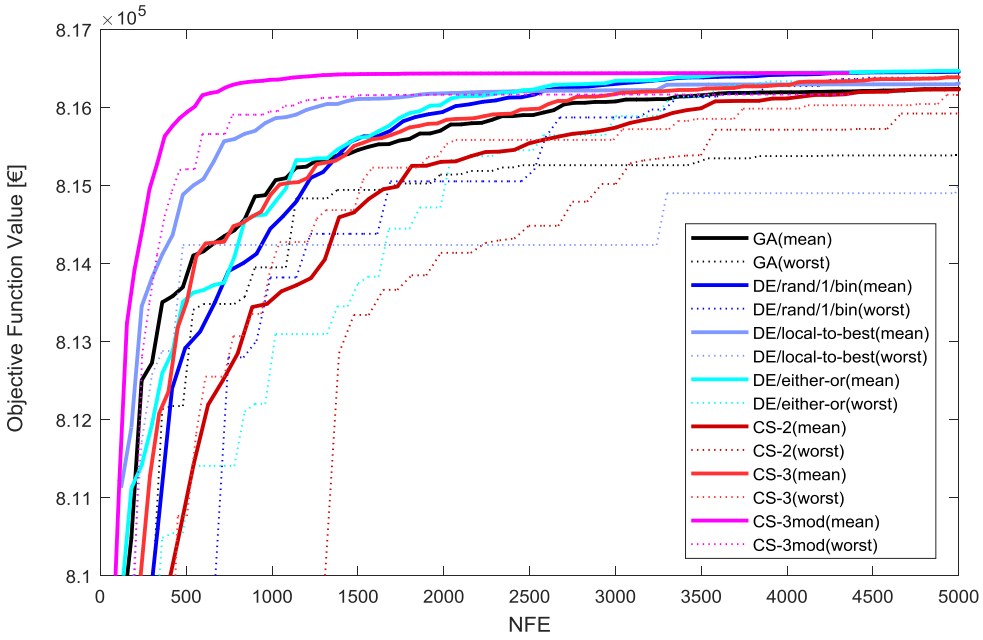

Figure 7.11: Convergence plots of the tested algorithms using the control parameter settings of Table 7.6. Each algorithms was ran 10 times; the mean progress and the worst of the runs are plotted.

While the graph confirms that all algorithms are capable of solving the task at hand, the differences in performance are also clear. Particularly, both GA and DE with local-to-best mutation strategy have their worst-case results at clearly lower levels than the other tested algorithms at the end of the 5000 function evaluation run. Another clear conclusion is the very good performance of the CS-3mod, where the original CS-2 as published in the appendix of (Yang, 2014) was modified by reducing the fraction of Lévy flights to the worst 25% of the population, and changing the mutation strategy. Even its worst performance is mostly superior to the mean performance of any other algorithm, and average time to stabilize to the final value appears to be in the order of 20-30 % of the other optimizers.

The good performance of the CS-3mod algorithm is clearly of value for the task of optimizing a CHP plant condenser, where in practice many runs with varying economic scenarios would likely be performed. On a desktop computer with a 3.50 GHz, 6-core CPU used in this last stage of optimization, the time of one run was reduced from the initial of over 1 hour, to approximately 20-30 minutes with a well-tuned DE or CS variant, and finally to less than 10 minutes with the CS-3mod.

The finding can be of interest also in the wider scope of metaheuristic optimizers; this would require much deeper investigation of its performance with a variety of test

functions, however. The promising results with this algorithm also raise the question whether mating the Lévy flights with an even greedier mutation strategy such as DE/best/1/bin could work well. These issues were ruled beyond the scope of this thesis work, and not investigated in detail.

8 Conclusions

The possibilities of improving the efficiency and profitability of biomass thermal conversion processes were studied in the thesis. The focus was on a small-scale district heat producing CHP plant using Nordic forest biomass as fuel. The topic was studied from two different aspects by using different approaches. Integrating the CHP process with low-temperature thermochemical conversion processes was investigated to learn about the possibilities of improving the technical and economic performance of the plant. Secondly, a component design optimization approach was taken to study the optimal condenser performance parameters at varying electricity prices. The main findings of the study, as well as notable areas identified for further study, are summarized in the following.

8.1 Main findings of the study

Q1 How are CHP plant operation and economics affected by integration with a biomass conversion process other than combustion?

The integration studies showed that integration with a thermochemical biomass conversion process has a significant impact on plant operation and economics. The studied case assumed a plant that is sized to operate 6000 hours annually, a typical figure for Nordic district heat producing CHP plants. Integrating a biomass conversion process to the CHP plant could increase this by almost 1500 (torrefaction) or 2000 hours (hydrothermal carbonization, or HTC).

Significantly improving the energy efficiency by means of process integration proved to be impossible. Economically, however, integration showed clear benefits through reduced investment costs and increased operating time of the CHP process. The extension of the annual operating time proved to be crucial for integrated plant economics. The best economic performances were found in the configurations offering the longest operating times, as this translates directly for maximum production of heat and biochar, and in practice often also electricity. In the case of HTC, the economically best-performing case was in fact the one which had the poorest overall energy efficiency, but also the longest operating time and smallest investment cost.

The economic benefit of the integration was clear: although the integrated plant concepts were smaller investments producing generally less energy products annually than co-located plants of same nominal output as the integrates, the best integration scenarios proved to yield not only a higher rate of return and shorter payback period, but also clearly greater annual net cash flow rates and higher net present values.

Q2 What are the best ways of integrating biomass conversion processes with co-generation plants?

The main benefits of integration result from investment cost saving, and operating time extension, while loss of power production reduced the profitability of the integrated plants. Operating time extension and loss of power output from the CHP plant both depend much on the integration concept on the power production.

In the case of torrefaction, the longest operating time as well as highest power production of the integration options was found by utilizing backpressure steam for the feedstock dryer and live steam for the reactor. Although maintaining heat production at winter conditions required largely bypassing the turbine, this loss was almost entirely compensated for by the combination of increased operating time and part-load power generation.

In the case of HTC, which is the more complex and expensive of the two thermochemical conversion processes, the simplest integration scenario proved to be the most economical. By replacing the complex heat recovery scheme of the stand-alone HTC process with pressurized hot water from the CHP plant steam cycle, the HTC plant cost was significantly reduced while simultaneously obtaining the greatest operating time extension for the CHP process.

Q3 Can integration with a biomass conversion process serve as a buffer against uncertain electricity prices in Nordic co-generation plants?

A biomass-fired CHP plant requires a sufficiently high electricity price to be profitable and preferable to a heat-only boiler. The future price of electricity is currently uncertain due to a number issues such as policy decisions regarding nuclear power and renewable energy subsidies, future costs of CO_2 emissions, and also the future cost developments of such technologies as wind and solar power, energy storage technology, and 4^{th} generation nuclear power plants. The results obtained in this thesis show that the introduction of a third energy product in the form of hydrochar or torrefied biochar can clearly reduce the vulnerability of CHP generation to electricity price fluctuations, if a sufficiently high price can be obtained for these products.

On the other hand, it is also clear that as both of the biochars are new energy products without developed markets, the price risk related to these is significant as well. An attempt to predict the market development was not made in this thesis, and thus only a tentative answer could be found for the research question Q3. Any attempt to predict the market development would also inevitably require predictions about future policy decisions, which together with the inherent difficulty of predicting market developments would have made any predictions highly uncertain, even if attempted.

Q4 What biochar price levels are required for mild pyrolysis of wood biomass to be profitable?

Using the baseline economic assumptions for investment costs and price of electricity, the stand-alone torrefaction plant proved reaches break-even profitability at a biochar price of 39 €/MWh$_{LHV}$; for hydrochar, a higher price of approximately 46 €/MWh$_{LHV}$ is needed for the stand-alone HTC plant to reach break-even. With the economically best-performing integration concepts, the prices are reduced to 30 and 37 €/MWh$_{LHV}$, respectively.

Compared to a simple CHP plant, the best-performing integrated plant with torrefaction would probably be economically preferable if a price of approximately 30…35 €/MWh$_{LHV}$ could be obtained for the torrefied biochar. A higher price was again required for hydrochar: nearly 40 €/MWh$_{LHV}$.

Although hydrochar proved to be more expensive to produce, this does not necessarily make HTC an inferior technology, since hydrochar has some advantages over torrefied biochar as a fuel. The price at which either biochar plant would become economically beneficial was somewhat sensitive to the assumed scenarios for the various prices and costs.

Q5 How is the optimal district heat condenser design affected by varying equipment and electricity costs?

While the plant profitability is highly sensitive to the price of electricity, the optimal design of the condenser proved to be much less so, provided electricity price is higher than approximately 45…50 €/MWh.

Below the 45…50 €/MWh price range, there was a clear change in the optimal design and performance of the condenser. This was likely affected by the assumptions applied to the problem. The operating strategy was not considered as a variable in the optimization. Allowing for varying strategies at maximum load depending on the prices of electricity and heat – for example raising the level of the condensate in the heat exchanger, or partially bypassing the turbine through a reduction valve – different results could have been obtained for prices slightly lower than where the step change in optimal configuration now took place. At much lower electricity prices, it is unlikely that the CHP plant would be economically preferable to a heat-only boiler.

Q6 What lessons can be learned from the practical solving process of these problems?

Additional findings somewhat tangential to the topic of the thesis were made particularly in the condenser optimization stage. In this work, the heat exchanger being a low-pressure steam condenser required an iterative multi-element heat transfer model to be implemented. The drawback of such a model is a long calculation time for each time it

was run; minimizing the number of objective function evaluations thus became a particularly serious concern. It became evident that when dealing with a computationally heavy optimization problem, several means can be used that each can reduce the computational time noticeably. These include cheap surrogates to pre-evaluate new solutions and applying the full model only on promising candidates, careful choice of decision variables and problem formulation, selection of a suitable algorithm, and correctly tuning the control parameters.

Particularly if the optimization is a task that is expected to be repeated several times, careful effort to correctly tune the control parameters can yield significant benefits. All of the methods considered in this thesis, with the exception of the CS-1 variants, could be considered effective in the sense that with one or at most a small number of runs, they were able to find a high-quality solution. By experimentation, a modified hybrid algorithm created by combining the cuckoo search and local-to-best mutation strategy of differential evolution proved to be clearly more powerful than the existing algorithms.

Another important aspect is the formulation of the problem. A heat exchanger is defined by a certain number of variables, so that the remaining variables are then unambiguously defined and can be calculated. Depending on which variable is made a decision variable and which a function thereof, the decision variable may be strongly dependent or relatively independent of other variables, and may have a relatively narrow range of good values, or a wide one. While several algorithms, such as both DE and CS, are capable of robust rotationally invariant search, they, too, still clearly benefit from a problem formulation that makes the decision variables as independent of each other as possible.

8.2 Future research needs

A number of additional questions became evident during the research. In the study of integrating the CHP and HTC processes, the residence times considered were relatively long. In future research the possibility of using shorter residence times should be investigated. Particularly at the high end of the HTC temperature range, the residence times could probably be significantly reduced while still allowing a sufficient level of carbonization to be reached. This would allow much smaller and thus cheaper equipment, and could improve the economic performance of the HTC plants, even if some of the advantage would be lost due to the more complex heat recovery schemes that would probably be required.

On the other hand, in a larger CHP plant with more and higher-pressure turbine extractions, an even lower carbonization temperature in the range of 180 to 200 °C could be beneficial, if it would permit using intermediate pressure turbine extraction steam for HTC reactor heating. This would show as increased power generation.

In terms of condenser optimization, the problem formulation which did not allow for varying operating strategies of the plant was limiting: different results at low electricity price range could be obtained from a more flexible scenario.

Finally, it was found that the combination of local-to-best differential mutation strategy with Lévy-distributed random walks was highly efficient at the backpressure district heat condenser optimization. This initial finding is only applicable for the single problem on which it was tested here, but based on the very good results obtained, further study of the capabilities of such hybridization of the two algorithms would appear worthwhile. More generally, using the potential of the greedier differential mutation strategies for fast convergence, balanced with the ability of Lévy flights to maintain global exploration as the population converges, appears promising.

References

Ackermann, G. (1937). *Heat transfer and molecular mass transfer in the same field over large temperature and partial pressure differences (in German: Wärmeübergang und molekulare Stoffübertragung im gleichen Feld bei großen Temperatur und Partialdruckdifferenzen).* Research bulletin (Forschungsheft) 382, 1-16.

Alakangas, E. (2000). *Properties of fuels used in Finland (in Finnish: Suomessa käytettävien polttoaineiden ominaisuuksia).* Espoo, Finland: Valtion Teknillinen Tutkimuskeskus VTT (Technical Research Center of Finland).

Alatalo, S. M., Repo, E., Mäkilä, E., Salonen, J., Vakkilainen, E., & Sillanpää, M. (2013). Adsorption behavior of hydrothermally treated municipal sludge & pulp and paper industry sludge. *Bioresource technology*, 147, 71-76.

Al-Sanea, S., Rhodes, N., Tatchell, D., & Wilkinson, T. (1983). A computer model for detailed calculation of the flow in power station condensers. *Condensers: Theory and Practice. Symposium*, 70-88.

Al-Sanea, S., Rhodes, N., & Wilkinson, T. (1985). Mathematical modeling of two-phase condenser flows. In: *2nd International Conference on Multi-Phase Flow, London, United Kingdom June 1985*, 19-21.

Arpiainen, V., & Wilen, C. (2013). *Report on optimisation opportunities by integrating torrefaction into existing industries*. SECTOR project Deliverable D3.2.

Asadi, M., Song, Y., Sunden, B., & Xie, G. (2014). Economic optimization design of shell-and-tube heat exchangers by a cuckoo-search-algorithm. *Applied Thermal Engineering*, 73(1), 1032-1040.

Babu, B., & Munawar, S. (2007). Differential evolution strategies for optimal design of shell-and-tube heat exchangers. *Chemical Engineering Science*, 62(14), 3720-3739.

Bach, Q., Tran, K., Skreiberg, Ø., & Trinh, T. T. (2015). Effects of wet torrefaction on pyrolysis of woody biomass fuels. *Energy*, 88, 443-456.

Bach, Q.V. & Skreiberg, Ø. (2016). Upgrading biomass fuels via wet torrefaction: A review and comparison with dry torrefaction. *Renewable and Sustainable Energy Reviews*, 54, 665-677.

Bajpai, P. (2015). *Management of pulp and paper mill waste*. Switzerland: Springer International Publishing.

Basu, P., Sadhukhan, A. K., Gupta, P., Rao, S., Dhungana, A., & Acharya, B. (2014). An experimental and theoretical investigation on torrefaction of a large wet wood particle. *Bioresource Technology*, 159, 215-222.

Batidzirai, B., Mignot, A., Schakel, W., Junginger, H., & Faaij, A. (2013). Biomass torrefaction technology: Techno-economic status and future prospects. *Energy*, 62, 196-214.

Bergman, P. C., Boersma, A., Zwart, R., & Kiel, J. (2005). Torrefaction for biomass co-firing in existing coal-fired power stations. *Energy Centre of Netherlands, Report No. ECN-C-05-013*. Netherlands.

Bergman, P. C., & Kiel, J. H. (2005). Torrefaction for biomass upgrading. In: *Proceedings of the 14th European Biomass Conference, Paris, France,* 17-21.

Bhatti, M., & Shah, R. (1987). Turbulent and transition flow convective heat transfer in ducts. In: *Handbook of Single-Phase Convective Heat Transfer*, Editors: Kakaç, S., Shah, R. K., & Aung, W. 4.1-4.166. New York, United States: Wiley.

Blangetti, F., & Krebs, R. (1988). Film condensation of pure vapours (in German: Filmkondensation reiner dämpfe). *VDI Wärmeatlas, section Ja.* Düsseldorf, West Germany: VDI-Verlag Gmbh.

Bobleter, O. (1994). Hydrothermal degradation of polymers derived from plants. *Progress in polymer science*, 19(5), 797-841.

Bridgeman, T. G., Jones, J. M., Shield, I., & Williams, P. T. (2008). Torrefaction of reed canary grass, wheat straw and willow to enhance solid fuel qualities and combustion properties. *Fuel*, 87(6), 844-856.

Butterworth, D. (1977). Developments in the design of shell and tube condensers. *ASME Paper, 77.*

Butterworth, D. (1983). Film condensation of pure vapor. *Heat Exchanger Design Handbook 2, section 2.6.* New York, United States: Hemisphere Publishing Corporation.

Caputo, A. C., Pelagagge, P. M., & Salini, P. (2016). Manufacturing cost model for heat exchangers optimization. *Applied Thermal Engineering*, 94, 513-533.

Chaudhuri, P. D., Diwekar, U. M., & Logsdon, J. S. (1997). An automated approach for the optimal design of heat exchangers. *Industrial & Engineering Chemistry Research*, 36(9), 3685-3693.

Chen, W. H., & Kuo, P. C. (2010). A study on torrefaction of various biomass materials and its impact on lignocellulosic structure simulated by a thermogravimetry. *Energy*, 35(6), 2580-2586.

Chen, W. H., & Kuo, P. C. (2011). Torrefaction and co-torrefaction characterization of hemicellulose, cellulose and lignin as well as torrefaction of some basic constituents in biomass. *Energy*, 36(2), 803-811.

Chen, W. H., Ye, S. C., & Sheen, H. K. (2012). Hydrothermal carbonization of sugarcane bagasse via wet torrefaction in association with microwave heating. *Bioresource technology*, 118, 195-203.

Colburn, A. P., & Hougen, O. A. (1934). Design of cooler condensers for mixtures of vapors with noncondensing gases. *Industrial & Engineering Chemistry*, 26(11), 1178-1182.

Costa, A. L., & Queiroz, E. M. (2008). Design optimization of shell-and-tube heat exchangers. *Applied Thermal Engineering*, 28(14), 1798-1805.

Deng, J., Wang, G. J., Kuang, J. H., Zhang, Y. L., & Luo, Y. H. (2009). Pretreatment of agricultural residues for co-gasification via torrefaction. *Journal of Analytical and Applied Pyrolysis*, 86(2), 331-337.

Dittus, F., & Boelter, L. (1930). University of California publications on engineering. *University of California Publications in Engineering*, 2, 371.

Drbal, L., Boston, P., & Westra, K. (1996). *Power plant engineering.* New York, United States: Springer Science+Business Media.

Dupont, C., Chiriac, R., Gauthier, G., & Toche, F. (2014). Heat capacity measurements of various biomass types and pyrolysis residues. *Fuel*, 115, 644-651.

Eagle, A., & Ferguson, R. (1930). On the coefficient of heat transfer from the internal surface of tube walls. *Proceedings of the Royal Society of London A: Mathematical, Physical and Engineering Sciences*, 127(806), 540-566.

Eberhart, R.C., & Kennedy J. (1995). A new optimizer using particle swarm theory. In: *Proceedings of the Sixth International Symposium on Micro Machine and Human Science (MHS '95), Nagoya, Japan, 4-6 Oct 1995.* 39-43.

Eriksson, G., & Kjellström, B. (2010). Assessment of combined heat and power (CHP) integrated with wood-based ethanol production. *Applied Energy*, 87(12), 3632-3641.

Erlach, B., & Tsatsaronis, G. (2010). Upgrading of biomass by hydrothermal carbonisation: Analysis of an industrial-scale plant design. In: *Proceedings of the 23rd International Conference on Efficiency, Cost, Optimization, Simulation and Environmental Impact of Energy Systems. Lausanne, Switzerland*, 14-17.

Erlach, B., Wirth, B., & Tsatsaronis, G. (2011). Co-production of electricity, heat and biocoal pellets from biomass: A techno-economic comparison with wood pelletizing. In: *Proceedings of World Renewable Energy Congress (Bioenergy Technology), Sweden, 8-13 May, 2011, Linköping*. 57, 508-515. Linköping, Sweden: Linköping University Electronic Press.

Erlach, B. (2014) *Biomass upgrading technologies for carbon-neutral and carbon-negative electricity generation*. Doctoral dissertation. Berlin, Germany: Technische Universität Berlin.

European Committee for Standardisation CEN (2003). *SFS-EN 12952-15 water-tube boilers and auxiliary installations - part 15: Acceptance tests*. Brussels, Belgium: European Committee for Standardisation (CEN).

Fagernäs, L., Brammer, J., Wilén, C., Lauer, M., & Verhoeff, F. (2010). Drying of biomass for second generation synfuel production. *Biomass and Bioenergy*, 34(9), 1267-1277.

Fahlén, E., & Ahlgren, E. O. (2009). Assessment of integration of different biomass gasification alternatives in a district-heating system. *Energy*, 34(12), 2184-2195.

Fesanghary, M., Damangir, E., & Soleimani, I. (2009). Design optimization of shell and tube heat exchangers using global sensitivity analysis and harmony search algorithm. *Applied Thermal Engineering*, 29(5), 1026-1031.

Finnish Meteorological Institute. (2015). *Monthly statistics (in Finnish: Kuukausitilastot*). [referred: October, 2015]. URL: http://www.ilmatieteenlaitos.fi/kuukausitilastot

Focardi, S., Montanaro, P., & Pecchioli, E. (2009). Adaptive lévy walks in foraging fallow deer. *PLoS One*, 4(8), e6587.

Frangopoulos, C. A., Von Spakovsky, M. R., & Sciubba, E. (2002). A brief review of methods for the design and synthesis optimization of energy systems. *International Journal of Thermodynamics*, 5(4), 151-160.

Funke, A., & Ziegler, F. (2010). Hydrothermal carbonization of biomass: A summary and discussion of chemical mechanisms for process engineering. *Biofuels, Bioproducts and Biorefining*, 4(2), 160-177.

Funke, A., & Ziegler, F. (2011). Heat of reaction measurements for hydrothermal carbonization of biomass. *Bioresource Technology*, 102(16), 7595-7598.

Gao, X., Wang, X., & Ovaska, S. J. (2009). Uni-modal and multi-modal optimization using modified harmony search methods. *International Journal of Innovative Computing, Information and Control*, 5(10), 2985-2996.

Gao, Y., Wang, X., Wang, J., Li, X., Cheng, J., Yang, H., & Chen, H. (2013). Effect of residence time on chemical and structural properties of hydrochar obtained by hydrothermal carbonization of water hyacinth. *Energy*, 58, 376-383.

Gao, P., Zhou, Y., Meng, F., Zhang, Y., Liu, Z., Zhang, W., & Xue, G. (2016). Preparation and characterization of hydrochar from waste eucalyptus bark by hydrothermal carbonization. *Energy*, 97, 238-245.

Goss, W. P., & Miller, R. G. (1992). Thermal properties of wood and wood products. In: *Proceedings of the Thermal Performance of the Exterior Envelopes of Whole Buildings International Conference.* 28, 193-203. Atlanta, Georgia, United States.

Gupta, M., Yang, J., & Roy, C. (2003). Specific heat and thermal conductivity of softwood bark and softwood char particles. *Fuel*, 82(8), 919-927.

Hadidi, A., Hadidi, M., & Nazari, A. (2013). A new design approach for shell-and-tube heat exchangers using imperialist competitive algorithm from economic point of view. *Energy Conversion and Management*, 67, 66-74.

Hajabdollahi, H., Ahmadi, P., & Dincer, I. (2011). Thermoeconomic optimization of a shell and tube condenser using both genetic algorithm and particle swarm. *International Journal of Refrigeration*, 34(4), 1066-1076.

Harada, T., Hata, T., & Ishihara, S. (1998). Thermal constants of wood during the heating process measured with the laser flash method. *Journal of Wood Science*, 44(6), 425-431.

Hoekman, S. K., Broch, A., & Robbins, C. (2011). Hydrothermal carbonization (HTC) of lignocellulosic biomass. *Energy & Fuels, 2*5(4), 1802-1810.

Hoekman, S. K., Broch, A., Robbins, C., Zielinska, B., & Felix, L. (2013). Hydrothermal carbonization (HTC) of selected woody and herbaceous biomass feedstocks. *Biomass Conversion and Biorefinery,* 3(2), 113-126.

Holman, J. P. (1989). *Heat transfer*. Singapore: McGraw-Hill.

Holmström, P. (1982). *Condensers: Theory and practice (in Finnish: Lauhduttimet : Teoria ja käytäntö*). Tampere, Finland: Sonator.

Ilic, D. D., Dotzauer, E., & Trygg, L. (2012). District heating and ethanol production through polygeneration in Stockholm. *Applied Energy*, 91(1), 214-221.

Ilic, D. D., Dotzauer, E., Trygg, L., & Broman, G. (2014). Integration of biofuel production into district heating–part I: an evaluation of biofuel production costs using four types of biofuel production plants as case studies. *Journal of Cleaner Production*, 69, 176-187.

Incropera, F. P., & DeWitt, D. P. (2002). *Fundamentals of heat and mass transfe*r (5th edition). United States: Wiley.

Intergovernmetal Panel on Climate Change (IPCC) (2011). *IPCC special report on renewable energy sources and climate change mitigation.* Cambridge, United Kingdom: Cambridge University Press.

Intergovernmetal Panel on Climate Change (IPCC) (2012). *Special Report on Renewable Energy Sources and Climate Change Mitigation.* Revised edition, Editors Pichs-Madruga, R., Edenhofer, O., Sokona, Y., Seyboth, K., Eickemeier, P., Matschoss, P., Hansen, G., Kadner, S., Schlömer, S., Zwickel, T., & Stechow, C.. ISBN 978-92-9169-131-9. Page 52, Figure TS.1.6. New York, United States: Cambridge University Press.

Jacob, M. (1938). Heat transfer and flow resistance in cross flow of gases over tube banks. *Trans.ASME,* 60(38), 384-386.

Jegede, F., & Polley, G. (1992). Optimum heat exchanger design: Process design. *Chemical Engineering Research & Design,* 70(A2), 133-141.

Jüdes, M., Vigerske, S., & Tsatsaronis, G. (2009). Optimization of the design and partial-load operation of power plants using mixed-integer nonlinear programming.

Optimization in the energy industry, 193-220. Berlin, Germany: Springer Berlin Heidergberg.

Kakaç, S. (1991). *Boilers, evaporators, and condensers*. John Wiley & Sons.

Kambo, H. S. & Dutta, A. (2014). Strength, storage, and combustion characteristics of densified lignocellulosic biomass produced via torrefaction and hydrothermal carbonization. *Applied Energy*, 135, 182-191.

Kern, D. Q. (1958). Mathematical development of tube loading in horizontal condensers. *AIChE Journal*, 4(2), 157-160.

Kludze, H., Deen, B., & Dutta, A. (2013). Impact of agronomic treatments on fuel characteristics of herbaceous biomass for combustion. *Fuel processing technology*, 109, 96-102.

Khosravi, R., Khosravi, A., Nahavandi, S., & Hajabdollahi, H. (2015). Effectiveness of evolutionary algorithms for optimization of heat exchangers. *Energy Conversion and Management*, 89, 281-288.

Koch, P. (1969). Specific heat of oven dry spruce, pine wood and bark. *Wood Science*, 1, 203-214.

Kohl, T., Laukkanen, T., Järvinen, M., & Fogelholm, C. (2013). Energetic and environmental performance of three biomass upgrading processes integrated with a CHP plant. *Applied Energy*, 107, 124-134.

Kohl, T., Laukkanen, T. P., & Järvinen, M. P. (2014). Integration of biomass fast pyrolysis and precedent feedstock steam drying with a municipal combined heat and power plant. *Biomass and Bioenergy*, 71, 413-430.

Kohl, T., Moises, T., Melin, K., Laukkanen, T., Järvinen, M., Park, S. W., & Guidici, R. (2015). Exergoeconomic assessment of CHP-integrated biomass upgrading. *Applied Energy* 156, 290-305.

Komulainen, S. (2012). *Definition of the run-time optimization of a power plant (in Finnish: Voimalaitoksen käytönaikaisen optimoinnin määrittely)*. M. Sc. Thesis. Lappeenranta, Finland: Lappeenranta University of Technology.

Koppejan, J., Sokhansanj, S., Melin, S., & Madrali, S. (2012). IEA Bioenergy Task 32 Report. Final Report. *Status overview of torrefaction technologies.* Enschede.

Koskelainen, L., Saarela, R., & Sipilä, K. (2006). *Handbook of distrcit heat (in Finnish: Kaukolämmön käsikirja).* Energiateollisuus Ry, Finland.

Kruse, A., Funke, A., & Titirici, M. (2013). Hydrothermal conversion of biomass to fuels and energetic materials. *Current Opinion in Chemical Biology*, 17(3), 515-521.

Kuitunen, T. (2007). *Subsidy systems for renewable power generation in the european union, and their effect on the profitability of biomass-fired power plants (in Finnish: Uusiutuvista energialähteistä tuotetun sähkön tukijärjestelmät euroopan unionissa ja niiden vaikutus biomassavoimalaitosten kannattavuuteen).* M. Sc. Thesis. Lappeenranta, Finland: Lappeenranta University of Technology.

Li, J., Henriksson, G., & Gellerstedt, G. (2007). Lignin depolymerization/re-polymerization and its critical role for delignification of aspen wood by steam explosion. *Bioresource technology*, 98(16), 3061-3068.

Libra, J. A., Ro, K. S., Kammann, C., Funke, A., Berge, N. D., Neubauer, Y., & Kern, J. (2011). Hydrothermal carbonization of biomass residuals: A comparative review of the chemistry, processes and applications of wet and dry pyrolysis. *Biofuels*, 2(1), 71-106.

Malin, M. (1997). Modelling flow in an experimental marine condenser. *International Communications in Heat and Mass Transfer*, 24(5), 597-608.

Mantegna, R. N. (1994). Fast, accurate algorithm for numerical simulation of Lévy stable stochastic processes. *Physical Review E*, 49(5), 4677.

Medic, D., Darr, M., Shah, A., & Rahn, S. (2012). The effects of particle size, different corn stover components, and gas residence time on torrefaction of corn stover. *Energies*, 5(4), 1199-1214.

Megginson, W., & Smart, S. (2008). *Introduction to corporate finance.* Cengage Learning.

Minaret, J., & Dutta, A. (2016). Comparison of liquid and vapor hydrothermal carbonization of corn husk for the use as a solid fuel. *Bioresource Technology*, 200, 804-811.

Mizutani, F. T., Pessoa, F. L., Queiroz, E. M., Hauan, S., & Grossmann, I. E. (2003). Mathematical programming model for heat-exchanger network synthesis including detailed heat-exchanger designs. 1. shell-and-tube heat-exchanger design. *Industrial & Engineering Chemistry Research,* 42(17), 4009-4018.

Mohanty, D. K. (2016). Application of firefly algorithm for design optimization of a shell and tube heat exchanger from economic point of view. *International Journal of Thermal Sciences,* 102, 228-238.

Mohanty, D. K. (2016). Gravitational search algorithm for economic optimization design of a shell and tube heat exchanger. *Applied Thermal Engineering,* 107, 184-193.

Muralikrishna, K., & Shenoy, U. (2000). Heat exchanger design targets for minimum area and cost. *Chemical Engineering Research and Design,* 78(2), 161-167.

Nusselt, W. (1916). Surface condensation of water vapour (in German: Die Oberflachenkondesation des Wasserdampfes). *Zeitsehrift des Vereines Deutscher Ingenieure,* 60, 541-546.

Official Statistics of Finland (OSF) (2016). Energy supply and consumption [e-publication]. ISSN 1799-7976. 1st quarter 2016. Helsinki: Statistics Finland [referred: August 10th, 2016]. URL: http://www.stat.fi/til/ehk/2016/01/ehk_2016_01_2016-06-22_tie_001_en.html

Ohliger, A., Förster, M., & Kneer, R. (2013). Torrefaction of beechwood: A parametric study including heat of reaction and grindability. *Fuel,* 104, 607-613.

Pach, M., Zanzi, R., & Björnbom, E. (2002). Torrefied biomass a substitute for wood and charcoal. In: *6th Asia-Pacific International Symposium on Combustion and Energy Utilization* (20).

Patel, V., & Rao, R. (2010). Design optimization of shell-and-tube heat exchanger using particle swarm optimization technique. *Applied Thermal Engineering,* 30(11), 1417-1425.

Patel, B., Gami, B., & Bhimani, H. (2011). Improved fuel characteristics of cotton stalk, prosopis and sugarcane bagasse through torrefaction. *Energy for Sustainable Development,* 15(4), 372-375.

Peduzzi, E., Boissonnet, G., Haarlemmer, G., Dupont, C., & Maréchal, F. (2014). Torrefaction modelling for lignocellulosic biomass conversion processes. *Energy,* 70, 58-67.

Pellegrini, L. F., & de Oliveira Junior, S. (2011). Combined production of sugar, ethanol and electricity: thermoeconomic and environmental analysis and optimization. *Energy,* 36(6), 3704-3715.

Peters, M., Timmerhaus, K., & West, R. (2003). *Plant design and economics for chemical engineers* (5th ed.) New York, United States: McGraw-hill. Inc.

Pethukov, B., & Popov, V. (1963). Theoretical calculation of heat exchange in turbulent flow in tubes of an incompressible fluid with variable physical properties. *High Temperature Heat Physics,* 1, 69-83.

Phanphanich, M., & Mani, S. (2011). Impact of torrefaction on the grindability and fuel characteristics of forest biomass. *Bioresource Technology,* 102(2), 1246-1253.

Pina, E. A., Palacios-Bereche, R., Chavez-Rodriguez, M. F., Ensinas, A. V., Modesto, M., & Nebra, S. A. (2015). Reduction of process steam demand and water-usage through heat integration in sugar and ethanol production from sugarcane–Evaluation of different plant configurations. *Energy.* Article in press, available: http://dx.doi.org/10.1016/j.energy.2015.06.054

Ponce-Ortega, J. M., Serna-González, M., & Jiménez-Gutiérrez, A. (2009). Use of genetic algorithms for the optimal design of shell-and-tube heat exchangers. *Applied Thermal Engineering,* 29(2), 203-209.

Pöyry Management Consulting. (2015). Adequacy of power capacity in finland and the development of capacity structure until 2030. [referred: November 1st, 2015]. URL: http://www.tem.fi/files/42541/Translation_Capacity_development_in_Finland.pdf

Price, K., Storn, R. M., & Lampinen, J. A. (2006). *Differential evolution: A practical approach to global optimization.* Springer Science & Business Media.

Prieto, M., Suarez, I., & Montanes, E. (2003). Analysis of the thermal performance of a church window steam condenser for different operational conditions using three models. *Applied Thermal Engineering,* 23(2), 163-178.

Prins, M. J., Ptasinski, K. J., & Janssen, F. J. (2006a). Torrefaction of wood: Part 1. weight loss kinetics. *Journal of Analytical and Applied Pyrolysis,* 77(1), 28-34.

Prins, M. J., Ptasinski, K. J., & Janssen, F. J. (2006b). Torrefaction of wood: Part 2. analysis of products. *Journal of Analytical and Applied Pyrolysis*, 77(1), 35-40.

Prins, M. J. (2005). *Thermodynamic Analysis of Biomass Gasification and Torrefaction*, Doctoral dissertation, Eindhoven, Netherlands: Technische Universiteit Eindhoven.

Purohit, G. (1983). Estimating costs of shell-and-tube heat exchangers. *Chemical Engineering*, 90(17), 56-67.

Råde, L., & Westergren, B. (1990). *Beta mathematics handbook: Concepts, theorems, methods, algorithms, formulas, graphs, tables*. CRC Press, Boca Raton, Florida, United States.

Ragland, K., Aerts, D., & Baker, A. (1991). Properties of wood for combustion analysis. *Bioresource Technology*, 37(2), 161-168.

Rajabioun, R. (2011). Cuckoo optimization algorithm. *Applied Soft Computing*, 11(8), 5508-5518.

Ramke, H., Blöhse, D., Lehmann, H., & Fettig, J. (2009). Hydrothermal carbonization of organic waste. In: *Proceedings of Twelfth International Waste Management and Landfill Symposium, Sardinia, Italy.*

Ramke, H., Blöhse, D., Lehmann, H., & Fettig, J. (2010). Hydrothermal carbonization of organic municipal waste (In German: Hydrothermale carbonisierung organischer Siedlungsabfälle). In: *22. Abfall-wirtschaftsforum*, Gießen, Germany.

Ramón, I. S., & González, M. P. (2001). Numerical study of the performance of a church window tube bundle condenser. *International Journal of Thermal Sciences*, 40(2), 195-204.

Rao, R. V., & Saroj, A. (2017). Constrained economic optimization of shell-and-tube heat exchangers using elitist-Jaya algorithm. *Energy*, 128, 785-800.

Rautalin, A. & Wilén, C. (1992). *Feeding biomass into pressure and related safety engineering.* Technical Research Centre of Finland, Laboratory of Fuel and Process Technology.

Repellin, V., Govin, A., Rolland, M., & Guyonnet, R. (2010). Modelling anhydrous weight loss of wood chips during torrefaction in a pilot kiln. *Biomass and Bioenergy*, 34(5), 602-609.

Reza, M. T., Lynam, J. G., Uddin, M. H., & Coronella, C. J. (2013). Hydrothermal carbonization: fate of inorganics. *Biomass and Bioenergy*, 49, 86-94.

Rohsenow, W. M., Hartnett, J. P., & Cho, Y. I. (1998). *Handbook of Heat Transfer*. New York, USA: McGraw-Hill.

Sanaye, S., & Dehghandokht, M. (2011). Modeling and multi-objective optimization of parallel flow condenser using evolutionary algorithm. *Applied Energy*, 88(5), 1568-1577.

Sanaye, S., & Hajabdollahi, H. (2010). Multi-objective optimization of shell and tube heat exchangers. *Applied Thermal Engineering*, 30(14), 1937-1945.

Sanders, W. P. (2004). *Turbine steam path vol. 3a - mechanical design and manufacture*. Tulsa, Oklahoma, United States: PennWell.

Sermyagina, E., Saari, J., Kaikko, J., & Vakkilainen, E. (2015). Hydrothermal carbonization of coniferous biomass: Effect of process parameters on mass and energy yields. *Journal of Analytical and Applied Pyrolysis*, 113, 551-556.

Serna, M., & Jiménez, A. (2005). A compact formulation of the Bell–Delaware method for heat exchanger design and optimization. *Chemical Engineering Research and Design*, 83(5), 539-550.

Shah, R. K., & Sekulic, D. P. (2003). *Fundamentals of heat exchanger design*. John Wiley & Sons.

Shekriladze, I., & Gomelauri, V. (1966). Theoretical study of laminar film condensation of flowing vapour. *International Journal of Heat and Mass Transfer*, 9(6), 581-591.

Sinnott, R. K. (2005). In Richardson J. F., Sinnott R. K. (Eds.), *Coulson & Richardson's chemical engineering design, vol 6*. (4th Ed.). Oxford, United Kingdom: Butterworth-Heinemann.

Skaar, C. (1988). *Wood-water relations*. Springer-Verlag.

Starfelt, F., Thorin, E., Dotzauer, E., & Yan, J. (2010). Performance evaluation of adding ethanol production into an existing combined heat and power plant. *Bioresource technology*, 101(2), 613-618.

Starfelt, F., Daianova, L., Yan, J., Thorin, E., & Dotzauer, E. (2012). The impact of lignocellulosic ethanol yields in polygeneration with district heating–a case study. *Applied energy*, 92, 791-799.

Starfelt, F., Aparicio, E. T., Li, H., & Dotzauer, E. (2015). Integration of torrefaction in CHP plants–A case study. *Energy Conversion and Management*, 90, 427-435.

Stevanović, Ž., Ilić, G., Radojković, N., Vukić, M., Stefanović, V., & Vučković, G. (2001). Design of shell-and-tube heat exchangers by using CFD technique, part one: Thermo-hydraulic calculation. *Facta Universitatis-Series: Mechanical Engineering*, 1(8), 1091-1105.

Suomen standardoimisliitto SFS (1996). *SFS-handbook 13, pressure vessels. dimensioning. (in Finnish: SFS-käsikirja 13, paineastiat. mitoitus.).* Helsinki, Finland: Suomen standardoimisliitto SFS.

Suomen standardoimisliitto SFS (2002). *SFS-EN 13445-3 unfired pressure vessels (in Finnish: SFS-EN 13445-3 lämmittämättömät painesäiliöt).* Helsinki, Finland: Suomen standardoimisliitto SFS.

Taal, M., Bulatov, I., Klemeš, J., & Stehlík, P. (2003). Cost estimation and energy price forecasts for economic evaluation of retrofit projects. *Applied Thermal Engineering*, 23(14), 1819-1835.

Taborek, J. (1983). Shell-and-tube exchangers: Single-phase flow. *Heat Exchangers Design Handbook 3*. Hemisphere Publishing Corporation, New York, United States.

TEMA inc. (2007). *Standards of the Tubular Exchanger Manufacturers Association.* 9th ed., TEMA inc. New York, United States.

TenWolde, A., McNatt, J. D., & Krahn, L. (1988). *Thermal Properties of Wood and Wood Panel Products for use in Buildings*. (No. DOE/USDA-21697/1; ORNL/Sub-87-21697/1). Oak Ridge National Lab., TN (USA); Forest Service, Madison, WI (USA). Forest Products Lab.

Thunman, H., Niklasson, F., Johnsson, F., & Leckner, B. (2001). Composition of volatile gases and thermochemical properties of wood for modeling of fixed or fluidized beds. *Energy & Fuels*, *1*5(6), 1488-1497.

Traupel, W. (1966). *Thermal turbomachinery: 1. Thermodynamic and fluid flow calculation. (in German: Thermische Turbomaschinen: 1. Thermodynamisch-*

Strömungstechnische Berechnung). Springer-Verlag, Berlin, Federal Republic of Germany.

Tveit, T., Savola, T., & Fogelholm, C. (2005). Modelling of steam turbines for mixed integer nonlinear programming (MINLP) in design and off-design conditions of CHP plants. In: *Proceedings of the 46th Conference on Simulation and Modeling (SIMS 2005),* Trondheim, Norway.

U.S. Environmental Protection Agency. (2007). *Biomass combined heat and power, catalog of technologies*.

Vallejos, M. E., Felissia, F. E., & Area, M. C. (2017). Hydrothermal treatments applied to agro- and forest-industrial waste to produce high added-value compounds. *BioResources*, 12(1), 2058-2080.

van der Stelt, M. J. C. (2011). *Chemistry and reaction kinetics of biowaste torrefaction*. Doctoral dissertation. Eindhoven, Netherlands: Technische Universiteit Eindhoven.

Wahlund, B., Yan, J., & Westermark, M. (2002). A total energy system of fuel upgrading by drying biomass feedstock for cogeneration: a case study of Skellefteå bioenergy combine. *Biomass and Bioenergy*, 23(4), 271-281.

Walton, S., Hassan, O., Morgan, K., & Brown, M. R. (2011). Modified cuckoo search: A new gradient free optimisation algorithm. *Chaos, Solitons & Fractals*, 44(9), 710-718.

Walton, S. (2013a). *Gradient free optimisation in selected engineering applications* Doctoral dissertation. Swansea, United Kingdom: Swansea University.

Walton, S., Brown, M. R., Hassan, O., & Morgan, K. (2013b). Comment on Cuckoo search: A new nature-inspired optimization method for phase equilibrium calculations by V. Bhargava, S. Fateen, A. Bonilla-Petriciolet. *Fluid Phase Equilibria*, 352, 64-66.

Winterton, R. (1998). Where did the dittus and boelter equation come from*? International Journal of Heat and Mass Transfer,* 41(4), 809-810.

Woodward A. R., Howard D. L., & Andrews E. F. C. (1999). *Modern Power Station Practice, 3rd Edition, Vol C (Turbines, Generators and Associated Plant), Chapter 4: Condensers, pumps and cooling water plant.* British Electricity International Ltd.

Xu, X., & Li, Y. (2007). Comparison between particle swarm optimization, differential evolution and multi-parents crossover. *International Conference on Computational Intelligence and Security, 2007*, 124-127.

Yan, W., Acharjee, T. C., Coronella, C. J., & Vásquez, V. R. (2009). Thermal pretreatment of lignocellulosic biomass. *Environmental Progress & Sustainable Energy*, 28(3), 435-440.

Yan, W., Hastings, J. T., Acharjee, T. C., Coronella, C. J., & Vásquez, V. R. (2010). Mass and energy balances of wet torrefaction of lignocellulosic biomass. *Energy & Fuels*, 24(9), 4738-4742.

Yang, X., & Deb, S. (2009a). Cuckoo search via Lévy flights. In: *Nature & Biologically Inspired Computing, 2009. NaBIC 2009. World Congress on*, 210-214. IEEE.

Yang, X., & Deb, S. (2009b). Cuckoo search via Lévy flights. *Nature & Biologically Inspired Computing, 2009. NaBIC 2009. World Congress on*. IEEE. [Retrieved: October 6th 2017] URL: http://www.cs.cmu.edu/~02317/slides//lec_20.pdf.

Yang, X. (2010a). *Nature-inspired metaheuristic algorithms*. 2nd edition. Luniver press, Cambridge, United Kingdom.

Yang, X. (2010b). A new metaheuristic bat-inspired algorithm. In: *Nature inspired cooperative strategies for optimization (NICSO 2010*). 65-74. Springer.

Yang, X. (2014). *Nature-inspired optimization algorithms*. Elsevier.

Zeng, H., Meng, J., & Li, Z. (2012). Numerical study of a power plant condenser tube arrangement. *Applied Thermal Engineering*, 40, 294-303.

Zhang, C., Sousa, A., & Venart, J. (1993). The numerical and experimental study of a power plant condenser. *Journal of Heat Transfer, 115*(2), 435-445.

Žukauskas, A. (1987). Heat transfer from tubes in cross-flow. *Advances in Heat Transfer*, 8, 93-160.

Publication I

Saari, J., Kaikko, J., Vakkilainen, E., and Savolainen, S.
Comparison of power plant steam condenser heat transfer models for on-line condition monitoring.

Reprinted with permission from
Applied Thermal Engineering
Vol. 62, pp. 37-47, 2014

Applied Thermal Engineering 62 (2014) 37–47

Contents lists available at ScienceDirect

Applied Thermal Engineering

journal homepage: www.elsevier.com/locate/apthermeng

Comparison of power plant steam condenser heat transfer models for on-line condition monitoring

Jussi Saari [a, *], Juha Kaikko [a], Esa Vakkilainen [a], Samuli Savolainen [b]

[a] Lappeenranta University of Technology, P.O. Box 20, FI-53851 Lappeenranta, Finland
[b] Fortum Power and Heat Oy, P.O. Box 100, FI-00048 Fortum, Finland

HIGHLIGHTS

- Models are based on effectiveness-NTU calculation as single heat exchanger, or in many elements.
- The multi-element condenser model is significantly more accurate at low pressures and close temperature approach.
- With experimental correction factor the difference in accuracy is considerably reduced.
- The HEI standards could not be adjusted by a simple correction to accurately predict heat transfer coefficient.

ARTICLE INFO

Article history:
Received 23 August 2012
Accepted 1 September 2013
Available online 13 September 2013

Keywords:
Heat exchanger
Condenser
Steam surface condenser
Fouling

ABSTRACT

In this paper heat transfer models for large power plant condenser were examined. The goal was to develop a model capable of predicting not only the condenser pressure but the overall heat transfer coefficient. Such a model can be used for condenser condition monitoring. The results of a two-dimensional (2-D) condenser heat transfer model and single-point, zero-dimensional (0-D) model are presented together with the results from Heat Exchanger Institute (HEI) standards curves. Both 0-D and 2-D models can account for the effects of steam-side pressure drop and in a simplified manner also some effects of tube bundle geometry. For all models an experimental correction as a function of cooling water temperature was implemented to improve their accuracy. The results are presented in comparison with the measured plant data for three different tube bundle geometries, with and without the experimental correction factor. The 2-D model proved to be the most consistently accurate of the models both without the correction, and at varying steam and coolant flow with the correction applied. The results indicate significant local variation of pressure drop related effects, which the 0-D model failed to accurately predict particularly in cases of close temperature approach. In predicting the heat transfer coefficient the HEI model was the least accurate, significantly overestimating the impact of coolant flow rate change, and failing to match the measurements even with a correction applied.

1. Introduction

This paper concerns the development of a heat transfer model for seawater condensers of a large steam power plant, providing a reasonable compromise between computational time and accuracy of the results. The model should provide results fast enough to be used as a part of an on-line condition monitoring system, while also accurate enough for determining foulant layer development inside the seawater tubes, as well as showing likely changes in condenser performance if the plant operating parameters are slightly varied.

Predicting the heat transfer in a large condenser is challenging. Depending on the required accuracy and maximum acceptable computation time, different approaches are possible. The fastest but least accurate option are correlations provided by Heat Exchanger Institute (HEI) or British Electrotechnical and Allied Manufacturers Association (BEAMA), giving the overall heat transfer coefficient U as a function of cooling water flow and inlet temperature, and various tabulated correction factors [1]. While simple, this method fails to account for several phenomena affecting heat transfer and is unlikely to yield accurate results for heat transfer coefficients, though condenser pressure prediction is satisfactory. A calculation based on an average U determined from heat transfer coefficients at average flow conditions was also considered questionable given the vast local variations in flow conditions in a large condenser.

* Corresponding author. Tel.: +358 294 462 111; fax: +358 5 411 7201.
E-mail addresses: saari@lut.fi, jussi.saari@lut.fi (J. Saari).

1359-4311/$ – see front matter © 2013 Elsevier Ltd. All rights reserved.
http://dx.doi.org/10.1016/j.applthermaleng.2013.09.005

Nomenclature

A	area [m^2]
B	width [m]
C	experimental correction factor for condensation heat transfer coefficient: $C = h_{adjusted}/h_{correlation}$ [−]
C_f	friction factor [−]
c_p	specific heat in isobaric process [J kg^{-1} K^{-1}]
d	diameter [m]
f	friction factor (Darcy) [−]
F_x	correction term for U in HEI standards [−]
G	mass velocity [kg s^{-1} m^{-2}]
g	gravitational acceleration [m s^{-2}]
h	1. heat transfer coefficient [W m^{-2} K^{-1}]2. specific enthalpy [kJ kg^{-1}]
h_{fg}	latent heat of condensation [kJ kg^{-1}]
i_{max}	number of calculation segments in tube axis direction [−]
j_{max}	number of tube rows in steam flow direction [−]
k	thermal conductivity [W m^{-1} K^{-1}]
L	length [m]
$\dot{m}$	fluid mass flow rate [kg s^{-1}]
N	number of tubes [−]
n	index of calculation elements [−]
NTU	number of transfer units (dimensionless conductance) [−]
Nu	Nusselt number [−]
P	tube pitch [m]
p	pressure [Pa]
Pr	Prandtl number [−]
R	thermal resistance [K W^{-1}]
Re	Reynolds number [−]
R''	thermal resistance per surface area [m^2 K W^{-1}]
s	tube wall thickness [m]
T	temperature [°C]
w	velocity [m s^{-1}]
x	steam quality [−]
U	overall heat transfer coefficient [W m^{-2} K^{-1}]

Greek symbols

Δp	pressure drop [Pa]
ε	heat exchanger effectiveness [−]
Φ	heat transfer rate [W]
μ	dynamic viscosity [Pa s]
ρ	density [kg m^{-3}]

Subscripts

C	cumulative
c	cold (sea water) side
cl	clean
gr	gravity
h	hot (steam) side
i	1. tube inside2. calculation element index in tube axis direction
in	inlet
j	calculation element index in tube row direction
L	liquid phase
o	tube outside
out	outlet
s	tube surface
sh	1. shell2. shear
T	transverse to steam flow direction
tb	tube
TOT	total
TRU	true value (according to measurements)
V	vapour phase

At the other extreme, detailed 2-D and 3-D numerical models have been developed to model the behaviour of both large power plant condensers and laboratory-scale test equipment. Al-Sanea et al. used a single-phase 2-D model [2]. Later Al-Sanea et al. [3] and Bush et al. [4] implemented two-phase 2-D models. A quasi-3-D method was used to model power station condensers by Zhang et al. [5], and laboratory-scale test condenser by Zhang and Bokil [6]. Malin used a 3-D model [7] to model a marine condenser. Ramon and Gonzalez developed a 3-D model of a church window type condenser [8], and Prieto et al. compared the results of similar model to both HEI correlations and a 2-D simplification of the 3-D model [9]. Hu and Zhang developed improvements to turbulence [10] and inundation [11] modelling for numerical condenser simulations. Zeng et al. [12] developed 3-D models of three power plant condenser configurations, and compared the results to HEI correlations. While the 3-D models are likely the most accurate option in the absence of extensive proprietary data available to condenser manufacturers, the difficulties of modelling two-phase flow, phase change and interaction of the two phases will still produce significant uncertainties in the results. For on-line condition monitoring purposes or a use as a component module of a larger power plant model, the computational complexity of such numerical models would also be excessive.

The approaches studied in this paper are a 2-D model based on a geometrical simplification broadly similar to that presented by Prieto et al. in Ref. [9] calculating the condenser as a heat exchanger network of smaller condensers, and a 0-D model based on an average U calculated at average flow conditions. The possibility of an even simpler implementation was investigated by comparing these results to calculation with an average U obtained from the HEI standards for steam surface condensers. All three methods were implemented for three separate condenser types, one of which is similar to the church window type analysed by Prieto et al. All condensers considered are of two-pass configuration with seawater in horizontal tubes.

The 2-D method described in this paper differs from that of Prieto et al. mainly in the treatment of condensation heat transfer, and in the inclusion of an experimental parameter to fit the model to measured performance. In Ref. [9] the vapour phase heat transfer coefficient was determined according to Taborek [13] and the phase change and heat and mass transfer were modelled according to film theory by Colburn and Hougen [14], corrected by Ackermann's factor according to [15]. The condensate film heat transfer coefficient was obtained from Nusselt's correlation for single horizontal tube without vapour shear, originally presented in Ref. [16], and modified by a shear correction from Ref. [17].

In this work it was assumed that given the simplification of actual flow patterns into 2-D or 0-D models and the difficulties of modelling condensate behaviour and the possible formation and effects of inert gas pockets in the tube bundle, a purely theoretical model could not achieve sufficient accuracy. An experimental correction factor C was introduced to fit the model results to measurements by adjusting the condensation heat transfer coefficient obtained from heat transfer correlations (i.e. $C = h_{adjusted}/h_{correlation}$). The unadjusted $h_{correlation}$ is based on correlations of Nusselt number Nu for gravity- and shear-dominated cases. With an experimental correction applied to account for the uncertainties in condensation modelling, it appeared unlikely that the more

elaborate approach of Ref. [9] would be advantageous over the simpler method presented here.

The sensitivity of the developed 2-D and 0-D models and HEI standards curves to changes in steam and coolant flow rates is investigated and compared to measurement data for three different condenser types to the extent that available data allowed. Results are studied both with and without the experimental correction factor in order to also obtain information on the relative usefulness of the models for predicting condenser performance if data for fitting the correction factor is not available.

2. The studied condensers and their 2-D simplifications

Three tube bundle configurations were studied. Labelled A, B, and C, these are shown in Fig. 1, with the simplified geometries to illustrate the treatment of steam flow in the models. The simplification resulted from assuming steam to enter the tube bank perpendicularly, and estimating the average number of rows j_{max} that the steam would flow across in the bundle. Each tube bundle has two water-side passes, splitting the shown tube bundles to top and bottom passes in A and left and right-side passes in B and C.

In the 2-D model the steam flow is assumed to be in perfect cross flow across the tubes, with parallel directions for vapour and liquid phase flows. In geometries A and C the number of tubes N_T transverse to the steam flow was estimated to remain relatively constant so that there would be N_{TOT}/j_{max} tubes in each row. The geometry B represents the church window type in which the cross-sectional area for steam flow reduces more clearly after each row. The tube bank is estimated to narrow steadily until finally $N_{T,jmax} = 0.30N_{T,1}$.

The tube arrangement in each condenser is equilateral triangular. The main physical characteristics as well as typical operating conditions are described in Table 1. All condensers are used in large condensing power plants with seawater cooling. The plants operate at base load, with the seawater flow rate switched between a lower value during winter and higher in summer. The condensers are equipped with an on-line cleaning system continuously rotating cleaning balls through the tubes.

3. Model description

In the model the heat transfer in a condenser is determined by four separate thermal resistances. Presented for a unit area, these are the tube outside condensation resistance R_o'', tube wall conduction resistance R_w'', tube inside convection resistance R_i'', and tube inside fouling thermal resistance R_{tf}''. The last term represents the net effect caused by the foulant layer, including changes in convective heat transfer due to surface changes. The effects of tube-side flow maldistribution, heat conduction in tube axis direction, tube outside fouling, inert gases in steam, leakages, and heat losses to the environment were considered negligible and not considered in the model.

Table 1
Main specifications and typical base load operating conditions of the studied condenser types.

	A	B	C
Number of tubes per pass [−]	5225	6500	8800
Tube material	SMO steel	Titanium	Titanium
Tube thermal conductivity [W/mK]	14	21	21
Tube outer diameter [mm]	28.0	24.0	22.0
Tube pitch [mm]	35.0	32.5	27.5
Tube wall thickness [mm]	0.8	0.5	0.5
Tube length [m]	8.89	8.97	9.27
Shell width [m]	6.7	6.7	6.7
Cooling water mass flow rate [kg/s]	4800 or 6200	4500 or 5900	4400 or 5800
Cooling water temperature [°C]	0–20	0–20	0–20
Steam mass flow rate [kg/s]	105	105	105
Steam pressure at inlet [mbar]	25–60	20–55	20–55

If the model is used to find condenser pressure $p_{h,in}$ at a given cooling water mass flow rate $\dot{m}_c$ and inlet temperature $T_{c,in}$ and steam mass flow rate $\dot{m}_h$, a value for R_{tf}'' must be assumed. If the condenser pressure is known, R_{tf}'' can be determined using the model. R_{tf}'' or $p_{h,in}$ is found in all models by adjusting the unknown parameter to such a value that the calculated heat transfer rate Φ matches the actual, as described in Algorithm 1 in Appendix A. The pressure $p_{h,in}$ is steam pressure immediately above the tube bundle; it is assumed that two velocity heads, based on velocity determined at unobstructed free flow area of the shell above the tube bundle, $A_{sh} = L_{tb}B_{sh}$, are lost as the steam flow accelerates, decelerates and turns into the tube bank. The actual heat transfer rate can be determined from the cold-side measurements or estimated from the hot-side.

To determine the fouling resistance the algorithm accounts for all discrepancies between calculated and measured results by adjusting the R_{tf}''. A sufficiently accurate modelling of biofouling was considered impossible and the available data is insufficient to identify measurement problems, leaks or other possible causes of poor indicated condenser performance. This is an inherent limitation of the model, resulting in the indication of a possibly increased R_{tf}'' as a result of any operating problem, even if fouling is not the actual physical cause.

3.1. Calculation procedure

The algorithm divides each water-side pass in i_{max} segments in tube axis direction, and j_{max} rows in steam flow direction (Fig. 2). With data for the incoming water and steam flow rates and states to element (i,j) obtained from the outlet conditions of elements $(i-1,j)$ and $(i,j-1)$, the calculation is performed iteratively for both

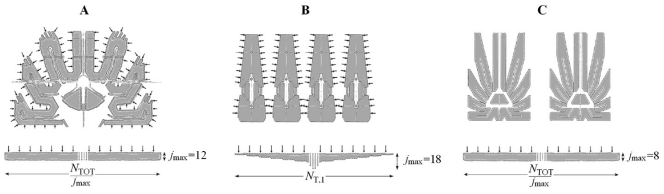

Fig. 1. Studied tube bundle configurations. The green area in the top figures represents the actual tube bundle configuration viewed in tube axis direction, the lower figures the 2-D model simplification. (For interpretation of the references to color in this figure legend, the reader is referred to the web version of this article.)

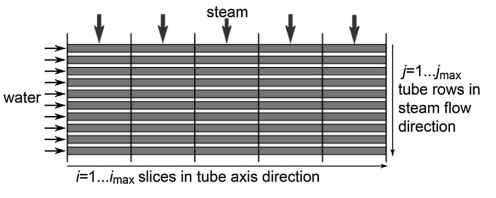

Fig. 2. Division of one condensing pass into $i_{max} \times j_{max}$ calculation elements.

passes, one segment i at a time starting with an initial guess of steam mass flow rate into element $(i,1)$, and adjusting this until the vapour-phase flow after (i,j_{max}) becomes zero. Water is assumed to be mixed between the passes. Steam pressure drop before entry to tube bank $\Delta p_{h,in}$ is calculated separately for each segment i,

$$\Delta p_{h,in,i} = \tfrac{1}{2}\rho_{h,V,i} w_{h,V,i}^2 \cdot 2, \tag{1}$$

where velocity $w_{h,V,i}$ is based on free flow area in shell to segment i, $L_{tb}B_{sh}/(2i_{max})$.

Calculation of each element is based on assumptions of constant condensation temperature and U. The water outlet temperature to element $(i+1,j)$ and vapour-phase mass flow rate to element $(i,j+1)$ are calculated from the heat transfer rate $\Phi_{i,j}$ in the element applying the ε-NTU method according to Eqs. (2)–(7). Steam pressure drop is calculated after the heat transfer calculations.

$$U_{i,j} = \left[\frac{d_o}{d_i}\left(R''_{tf} + \frac{1}{h_{c,i,j}}\right) + R''_w + \frac{1}{h_{h,i,j}}\right]^{-1} \tag{2}$$

$$\mathrm{NTU}_{i,j} = \frac{U_{i,j}A_{i,j}}{\dot{m}_{c,j}c_{p,c,i,j}} \tag{3}$$

$$\varepsilon_{i,j} = 1 - e^{-\mathrm{NTU}_{i,j}} \tag{4}$$

$$\Phi_{i,j} = \varepsilon_{i,j}\dot{m}_{c,j}c_{p,c,i,j}\left(T_{h,i,j} - T_{c,i,j}\right) \tag{5}$$

$$\dot{m}_{h,V,i,j+1} = \dot{m}_{h,V,i,j} - \frac{\Phi_{i,j}}{h_{fg,i,j}} \tag{6}$$

$$T_{c,i+1,j} = T_{c,i,j} - \frac{\Phi_{i,j}}{\dot{m}_{c,j}c_{p,c,i,j}} \tag{7}$$

3.2. Local heat transfer and pressure drop calculation

Tube inside heat transfer coefficient h_c for cold water was determined from the Nusselt number Nu, obtained using the correlation by Petukhov and Popov originally published in Ref. [18] as cited in Ref. [19],

$$Nu_c = \frac{h_c d_i}{k_c} = \frac{\frac{f}{8}Re\,Pr}{a + 12.7\sqrt{\frac{f}{2}}Pr^{2/3} - 1}\left(\frac{\mu}{\mu_c}\right)^{0.14}, \quad a = 1.07 + \frac{900}{Re} - \frac{0.62}{1+10Pr} \tag{8}$$

The correlation is valid for valid for $0.5 < Pr < 2000$ and $10^4 < Re < 5\cdot10^6$. The friction factor f was obtained from a formulation by Bhatti and Shah for hydraulically smooth tubes originally published in Ref. [20] as cited in Ref. [19],

$$f = 0.00512 + 0.4572\,Re^{-0.311} \tag{9}$$

Condensation is affected by gravity, vapour shear, and condensate inundation. The combined effect of these was approximated by an averaging formula for gravity and shear-dominated heat transfer coefficients $h_{h,gr}$ and $h_{h,sh}$ originally published in Ref. [21] as cited in Ref. [22],

$$h_h = \sqrt{\frac{1}{2}h_{h,sh}^2 + \sqrt{\frac{1}{4}h_{h,sh}^4 + h_{h,gr}^4}}. \tag{10}$$

An inundation correction by Kern originally published in Ref. [23] as cited in Ref. [24] was applied to this to obtain the heat transfer coefficient of the j:th row $h_h(j)$:

$$h_h(j) = h_h\left[j^{5/6} - (j-1)^{5/6}\right] \tag{11}$$

The gravity-dominated condensation heat transfer coefficient was determined from the Nusselt correlation [16], with the constant corrected from the original 0.725 to the more accurate solution of 0.728 by Butterworth [25],

$$Nu_{h,gr} = \frac{h_{h,gr}d_o}{k_l} = 0.728\left[\frac{\rho_L(\rho_L - \rho_V)gh_{fg}d_o^3}{\mu_L k_L \Delta T}\right]^{\frac{1}{4}}, \tag{12}$$

where the temperature difference between steam and tube outside wall $\Delta T = T_h - T_o$ is obtained from stationary-state energy balance, setting heat fluxes from steam to tube wall and steam to cooling water as equal,

$$\Delta T = T_h - T_o = \frac{U}{h_h}(T_h - T_c). \tag{13}$$

The shear-dominated heat transfer coefficient was determined from the Shekriladze–Gomelauri correlation [26]

$$Nu_{h,sh} = \frac{h_{h,sh}d_o}{k_l} = 0.59\sqrt{\tilde{R}\,e}, \quad \tilde{R}\,e = \frac{w_V d_o \rho_L}{\mu_L} \tag{14}$$

where $\tilde{R}\,e$ is a two-phase Reynolds number with the steam velocity w_v defined as the average across the row of the tubes considered.

Steam pressure drop Δp_h in the tube bank was calculated from

$$\Delta p_h = 2C_f\frac{G_{max}^2}{\rho_V}, \tag{15}$$

where G_{max} is the vapour mass velocity at the smallest cross-sectional area A_{min} between the tubes,

$$G_{max} = \frac{\dot{m}_{h,V,i,j}}{A_{min}}, \tag{16}$$

At element (i,j) the minimum steam flow area $A_{i,j,min}$ is obtained from

$$A_{i,j,min} = \frac{L_{tb}}{i_{max}}N_{T,j}(P - d_o). \tag{17}$$

The friction factor C_f is based on the correlation originally published by Jakob in Ref. [27] as cited in Ref. [28],

$$C_f = \left[0.25 + \frac{0.1175}{\left(\frac{P}{d_o} - 1\right)^{1.08}}\right]\left(\frac{d_o w_{V,max}\rho_V}{\mu_V}\right)^{-0.16}, \tag{18}$$

where velocity $w_{V,max}$ is the maximum steam velocity at the smallest area between the tubes.

Fluid properties in Eqs. (12), (14), (15) and (18) were evaluated at saturated state corresponding to local pressure.

3.3. Average-U models: 0-D and HEI standards

The 0-D model is based on the same Eqs. (2)–(18) as the 2-D model. The values of pressure drop, shear-dominated heat transfer coefficient, mean hot flow temperature, and the hot-side properties are based on half of the incoming vapour remaining and half of the hot-side pressure drop, with fluid properties evaluated at saturated state at this pressure.

Determining U according to the HEI Standards of Steam Surface Condensers is based on Eqs. (19)–(24) below [1]

$$\Phi = \mathrm{UA}\frac{T_{\mathrm{c,out}} - T_{\mathrm{c,in}}}{\ln\frac{T_{\mathrm{sat}}(p_{\mathrm{h,in}}) - T_{\mathrm{c,in}}}{T_{\mathrm{sat}}(p_{\mathrm{h,in}}) - T_{\mathrm{c,out}}}} \tag{19}$$

$$\Phi = \dot{m}_{\mathrm{h}} h_{\mathrm{fg}} \tag{20}$$

$$\Phi = \dot{m}_{\mathrm{c}} c_{p,\mathrm{c}} \left(T_{\mathrm{c,out}} - T_{\mathrm{c,iin}}\right) \tag{21}$$

$$U = U_1 F_1 F_2 F_3, \tag{22}$$

where F_1 to F_3 are the correction factor for tube material and gauge, cooling water inlet temperature, and cleanliness. In this work the overall heat transfer coefficient of clean condenser U_{cl} was determined from a curve fit based on the cooling water flow velocity w_{c} and inlet temperature $T_{\mathrm{c,in}}$ recommended in Ref. [1] to approximate the HEI standards, and adjusted to account for the tube material and gauge with a correction factor F_{m} from Ref. [29]:

$$U_{\mathrm{cl}} = 2.7 w_{\mathrm{c}}^{0.5}\left(0.5707 + 0.0274 T_{\mathrm{c,in}} - 0.00036 T_{\mathrm{c,in}}^2\right) F_{\mathrm{m}}, \tag{23}$$

where $[T_{\mathrm{c,in}}] = {}^\circ\mathrm{C}$, $[w_{\mathrm{c,in}}] = \mathrm{m/s}$ and $[U_{\mathrm{cl}}] = \mathrm{W/(m^2K)}$. $F_{\mathrm{m}} = 0.87$ for type A condenser and $F_{\mathrm{m}} = 0.91$ for types B and C [1]. The overall heat transfer coefficient for the condenser with the tube inside fouling resistance R_{tf}'' was obtained from

$$U = \left(\frac{d_0}{d_{\mathrm{i}}} R_{\mathrm{tf}}'' + \frac{1}{U_{\mathrm{cl}}}\right)^{-1}. \tag{24}$$

4. Condensation correction factor

Condensation heat transfer calculation is subject to several potential sources of errors mostly related to the simplified flow patterns, condensate behaviour, and inert gases. The 2-D model not only simplifies the steam flow pattern, but also neglects the different directions of vapour and condensate flows. In the 0-D model also the highly non-linear changes of condensation heat transfer coefficient and steam saturation temperature due to pressure drop are lost. With the knowledge that experimental data on inundation effects is very scattered [22] and the inundation correction of Eq. (11) is purely experimental, the treatment of inundation must also be considered very imprecise. The effect of inert gases is significant in gravity-dominated condensation and becomes pronounced at low pressures, but forced flow is much less affected [30]. Overall, the effect of inert gases should be small in well-designed condensers with appropriate equipment for removing the gases [1].

Many of the greatest sources of uncertainties are clearly influenced by coolant temperature T_{c}. Condensate behaviour is affected by viscosity which changes significantly with temperature for liquid water, and pressure, which itself depends on T_{c}, also has an indirect effect through steam velocity on the shear effects on condensate. The changes in viscosity and shear effects are likely to affect the flow and distribution of the condensate film within the tube bundle, which is not modelled in either 2-D or 0-D models, but simply approximated to be in parallel to the steam flow. Steam pressure drop both before and within the tube bank is another significant source of uncertainty due to the difficulty of estimating the actual loss coefficients, varying flow velocities before steam entry to the tube bank, and the inherent uncertainty of pressure drop correlations. Pressure drop is significantly affected by velocity, and therefore by steam pressure and thus indirectly by T_{c}. Although inert gases should not have a significant effect in a well-designed condenser, the possible presence of air pockets in the condensers cannot be completely ruled out, and satisfactory removal of non-condensables may also be affected by pressure. Since many of the main uncertainties appear likely to depend on coolant temperature, the correction factor C was set as a function of T_{c}.

Determining the correction factor was complicated by the unknown fouling thermal resistance R_{tf}''. The best approximation was assumed to be $R_{\mathrm{tf}}'' = 0$ with data collected immediately after the yearly maintenance stop, which includes washing the tubes. This is not necessarily true, as some of the foulant may remain, and fouling may also permanently change the surface for example through oxidization or mechanical deformation. Without better information or possibility of investigating the surface, these effects were assumed negligible.

Plant start-ups after the maintenance occurred in autumn when T_{c} sometimes changes rapidly. The best data series provided a range of $T_{\mathrm{c}} = 6\ldots13\ {}^\circ\mathrm{C}$ in 6 weeks for the condenser type A: a change of $6\ {}^\circ\mathrm{C}$–$13\ {}^\circ\mathrm{C}$ in 4.5 weeks followed by a decrease to $10\ {}^\circ\mathrm{C}$. Foulant growth was assumed low on the basis of biofouling rates presented in Ref. [31], further confirmed by nearly identical values of U at $T_{\mathrm{c}} = 10\ {}^\circ\mathrm{C}$ with 4 weeks of time in between the data points. The correction factor was determined with data for the washed A-type condenser collected from 30-day period, each data point representing a 1-h average from varying times of day. The data was based on the higher coolant flow rate. Calculation of C was done by setting $R_{\mathrm{tf}}'' = 0$ and modifying C instead of R_{tf}'' or $p_{\mathrm{h,in}}$. The results together with linear curve fits are presented in Fig. 3, confirming the presumption that $C = f(T_{\mathrm{c}})$. Correction factors were determined similarly for 0-D, 2-D and HEI standards models.

Because a period of fast temperature change immediately after washing was not found for the B and C-type condensers, the model was run initially only on type A, using data from three years to estimate typical R_{tf}'' variation. Two periods of rapid temperature change were found for types B and C, one at each water flow rate. These periods were used for determining the correction factors of B- and C-type condensers but using the R_{tf}'' values obtained from the model for type A at those times: $0.5 \times 10^{-5}\ \mathrm{m^2K/W}$ at the low $\dot{m}_{\mathrm{c}}$ data and $1.0 \times 10^{-5}\ \mathrm{m^2K/W}$ at the high $\dot{m}_{\mathrm{c}}$ data. The low-$\dot{m}_{\mathrm{c}}$ series includes also some high-$\dot{m}_{\mathrm{c}}$ data points.

A weakness of this approach is that biofouling rate is known to be a function of the tube material and flow conditions [31] which differ between the types A, B and C. This approach was still considered better than using post-washing data from a long time period and thus with varying fouling levels, or using only a small T_{c} range causing uncertainty in finding the slope for the correction. Data from as short time and wide T_{c} range as possible should ensure that while errors in absolute R_{tf}'' value may appear, systematic errors as a function of T_{c} resulting in erroneous information on fouling trends are minimized. The resulting correction factors are plotted in Fig. 3.

The data collected from two separate times with different temperatures and water flow rates results in $C_{0\mathrm{D}}$ and $C_{2\mathrm{D}}$

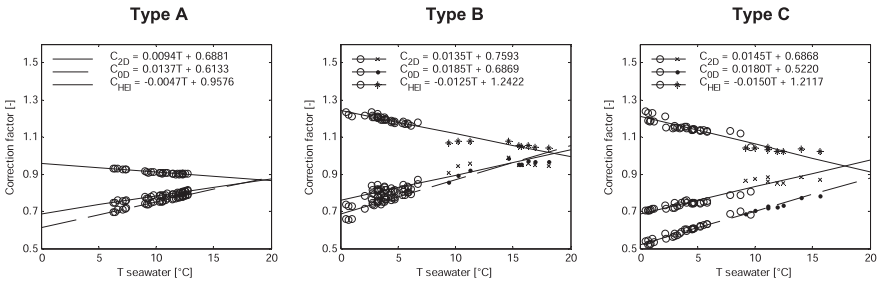

Fig. 3. Correction factors as a function of the seawater temperature, one data point per day. In Type B and Type C the circle represents the low-$\dot{m}_c$ data ($R_{tt}'' = 0.5 \times 10^{-5}$ m^{2}K/W), the remainder high-$\dot{m}_c$ data ($R_{tt}'' = 1.0 \times 10^{-5}$ m^{2}K/W).

distributions each fitting well within the same line for both type B and C. The trend with all geometries is for the 0-D and 2-D models to overestimate the heat transfer coefficient particularly at low T_c. This is in agreement with the presumption that the main deficiencies in the model are related to the condensate behaviour, hot-side pressure drop and inert gases, as all could be expected to decrease the performance especially at cold temperatures, i.e. low pressure and high condensate viscosity. Only increased vapour shear effects on the condensate would produce the opposite effect.

Compared to the correction factors C_{0D} and C_{2D}, C_{HEI} exhibits the opposite behaviour. Without exact knowledge of the data on which the HEI curves are based on, the reasons for the difference are impossible to pinpoint reliably. One possible explanation is that this could indicate a higher relative importance of tube inside convection resistance in HEI data than what is the case with the condensers considered here: the tube inside convection resistance depends more strongly on temperature than the condensation resistance. With condensation the increased vapour shear at low pressures compensates for the decrease in gravity-dominated coefficient.

It is also noteworthy that with the high-$\dot{m}_c$ data points of the geometries B and C, the correction factors points of HEI and 2-D models remain essentially constant, unlike C_{0D} points which continue approximately on the path established by the low-T_c, mainly low-$\dot{m}_c$ points. This may indicate that the effect of coolant temperature reduces at 10–20 °C range, but given the limited amount of data may also be simply a result of random fluctuations in measurements and/or actual performance. In the absence of a larger set of reliable data to base a more detailed correction factor on, and given the proximity of data points to the simple linear fit,

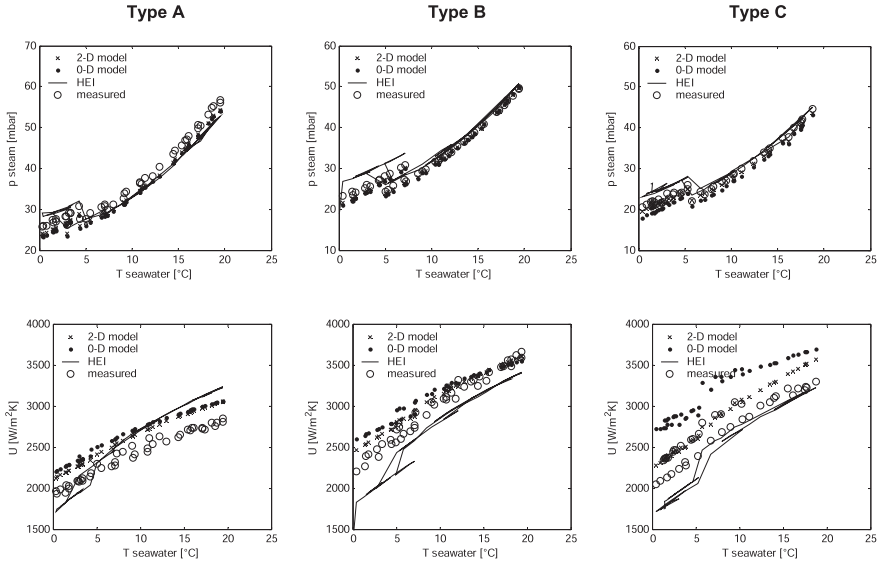

Fig. 4. Condenser pressures and overall heat transfer coefficients without correction factor as a function of seawater temperature.

the linear approximation was considered adequate for the purpose and implemented.

5. Results and validation

The change of the overall heat transfer coefficient U and condenser pressure $p_{h,in}$ was predicted with all models as a function of seawater temperature T_c and flow velocity w_c. Two cases were studied: without any applied correction, and using a linear approximation for the correction factor as presented in Fig. 3. As U and steam saturation temperature both vary within the condenser but this is not taken into account in the HEI standards curve, the simplified definition of U from Eq. (19) was used for plotting the results of all models.

5.1. Base load conditions without correction factor

The effect of T_c at base load conditions was investigated with $\dot{m}_c$, w_c and Φ taken from the measurements and R_{tf}'' assumed 0.5×10^{-5} m^{2}K/W during the low-$\dot{m}_c$ and 1.0×10^{-5} m^{2}K/W during high-$\dot{m}_c$ periods. The results are shown in Fig. 4.

Since condenser pressure is largely a function of T_c (defining the starting point of the cooling water temperature curve) and $\dot{m}_c$ (defining the rate of temperature increase), while U only affects the temperature difference between the cold and hot flows, all models are able to predict p_h at any given coolant temperature within a few millibars even when differences in U are considerable.

The 2-D model tends to overestimate performance, but overall predicts the condenser performance reasonably well for all types and at all conditions. The results from the 0-D model are broadly similar to the 2-D model with types A and B, but the 0-D model tends to overestimate the performance more especially at the coldest water temperatures. With type C this difference becomes quite large. This appears to be a result of several factors combining in type C to magnify the importance of effects detrimental to performance that are difficult to account for in a single-point model.

Firstly, steam pressure drop Δp_h in the condenser is greatest at the cold end of tubes due to higher local steam flow rate. With Δp_h greatest where most steam is condensed and the roughly proportional to square of velocity, the real effect is therefore greater than that resulting from a one-point average model based on flat steam flow distribution. A single-point averaging in steam flow direction also distorts the results towards higher-than-actual performance: most of the pressure drop takes place in first few rows where the velocity is greatest, and the actual average effect is therefore greater than half of total Δp_h calculated at half of the flow rate remaining.

Finally, heat transfer is highest in the first few tube rows due to highest shear force improving the heat transfer coefficient, and the detrimental effects of both pressure drop and condensate inundation still low. The water in these tubes therefore warms faster than deeper in the tube bank. Particularly in case of close temperature approach, this will limit the heat transfer potential left at the warm end of these tubes. Steam is then forced to flow through the first rows with comparatively little reduction in volumetric flow rate, resulting in significant pressure drop, and thus limiting the heat transfer rate available also deeper in the tube.

The type C condenser with the largest surface area, lowest pressure and closest temperature approach of all types is most affected by the above-mentioned effects. The net result can be seen in the values of U listed in Table 2 below for typical conditions of 1.8 m/s and +5 °C coolant velocity and temperature, and 105 kg/s steam flow rate ($x = 0.91$). The overall heat transfer coefficient U based on Eq (19) and saturation temperature determined at $p_{h,in}$ is clearly lower than the U_{mean} based on the actual U based on the heat transfer resistances according to Eq. (2) (the arithmetic mean of local $U_{i,j}$ in case of 2-D model) in all cases, and the difference tends to be greater in 2-D than 0-D model. Neglecting the issues of spatial variations in pressure and temperature produces the most optimistic results for the type C; as a result, the 2-D and 0-D results diverge the most from each other with this type of condenser. The cold- and hot-side heat transfer coefficients are otherwise broadly similar between models and condenser types.

Table 2
Condenser pressure and heat transfer coefficients with 0D and 2D models with +5 °C cooling water inlet temperature and 1.8 m/s tube-side velocity. U is the overall heat transfer coefficient solved from Eq. (19) with T_{sat} based on $p_{h,in}$, while U_{mean} is the arithmetic mean of local heat transfer coefficients calculated from Eq. (2).

	Type A		Type B		Type C	
	0-D	2-D	0-D	2-D	0-D	2-D
$p_{h,in}$ [mbar]	27.8	28.4	25.2	25.7	21.4	22.9
$q_{m,c}$ [kg/s]	5147	5147	4860	4860	5329	5329
U [W/m^{2}K]	2468	2400	2882	2788	3170	2691
U_{mean} [W/m^{2}K]	2855	2875	3246	3213	3331	3399
$h_{c,mean}$ [W/m^{2}K]	6347	6390	6502	6597	6533	6588
$h_{h,mean}$ [W/m^{2}K]	8403	8814	8470	8342	9071	9705

From Fig. 4 it could be seen that the HEI curves overestimate the effect of coolant flow rate has on U. The predicted effect of changing w_c could not be plotted over a range of data points from the measurements as only two values were ever used. In order to examine the effects according to the three models typical conditions $\dot{m}_h = 105$ kg/s, $x = 0.91$, $T_{c,in} = +5.0$ °C and $R_{tf}'' = 1 \times 10^{-5}$ m^{2}K/W were used instead, with w_c and $\dot{m}_c$ as the only varying parameters. The results are presented in Fig. 5.

The plots confirm that the HEI standards curves predict a clearly stronger improvement of performance with increased coolant flow in all cases. There is also a noticeable difference between the results of the 2-D and 0-D models: although the tube inside heat transfer coefficient increases with increasing velocity, increasing U and decreasing p_h with all models, the aforementioned pressure drop related effects limit the 2-D model to a much lesser performance increase than the 0-D model. The effect is again particularly pronounced with the type C.

5.2. Base load conditions with correction factor

Fig. 6 shows the behaviour of the models at different seawater temperatures when the correction factors (Fig. 3) are applied. The actual correction factors of types B and C remaining almost constant at higher temperatures in Fig. 3 indicates that at that range of T_c, unlike at lower temperatures, particularly the HEI curves and the 2-D model approximated the slope of $U = U(T_c)$ fairly well. Figs. 4 and 5 showed that the HEI curves overestimate the effect of coolant flow rate change. As a result, the correction curve appeared to aim along the low-$\dot{m}_c$ data points and at the middle of the cluster of high-$\dot{m}_c$ points. In case of type A condenser the HEI curve did fit well the high-$\dot{m}_c$ part of the curve, but the impact of the switch to low $\dot{m}_c$ was clearly too large. To fit the HEI curves to the measurements a more complex function of T_c as well as factoring in the effect of water flow rate would be required.

Both 0-D and 2-D models predicted the U and p_h changes accurately and amost identically with the correction applied. With 2-D model the high-$\dot{m}_c$ correction factors for types B and C also remained relatively constant in Fig. 3, but in contrast to the HEI curves, the 2-D predictions of Fig. 6 appear accurate. In addition to better accuracy with changing coolant flow rates, this may also be an indication that the relatively constant correction factor values at high T_c in Fig. 3 for 2-D model results with types B and C may be partly the result of measurement noise and/or actual temporary

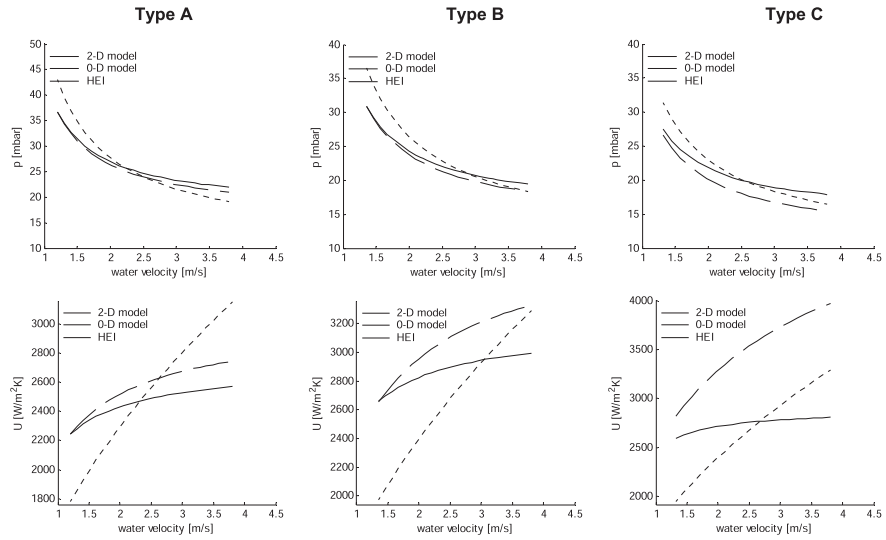

Fig. 5. Condenser pressures and overall heat transfer coefficients without correction factor as a function of sea water flow velocity.

performance anomalies. The experimental data from type C is considerably more scattered than the other two types in Fig. 6; an explanation was not found, but the variation appears to be too large to be due to fouling and may indicate problems with the measured data.

The accuracy of the models in predicting the change of condenser performance as a result of changing w_c can be seen more clearly by observing the change of R_{tf}'' on a data series that includes an abrupt change of w_c due to the switching of the sea water mass flow rate. As the algorithm uses only R_{tf}'' to match the calculated to

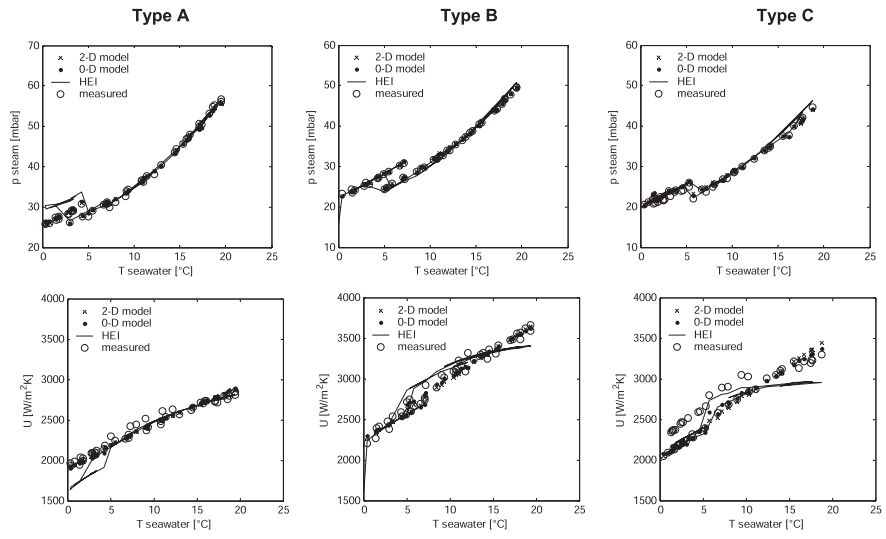

Fig. 6. Condenser pressures and overall heat transfer coefficients with correction factor as a function of the sea water temperature.

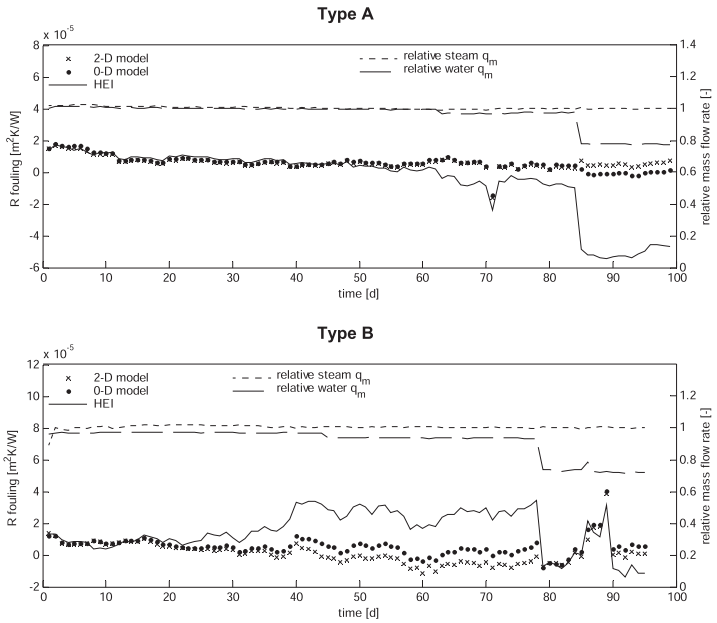

Fig. 7. Condenser thermal fouling resistances and relative steam and coolant flow rates over a 100-day period. Measurements used were a continuous series of 1-h averages, of which every 24th value is represented above.

the measured heat transfer, errors in predicting the change of convection resistance will result in an equal and opposite change of R_{tf}'', as can be seen in Eq. (2). An abrupt jump of R_{tf}'' when w_c changes can be a sign of this. The R_{tf}'' may also actually change if the foulant surface changes enough to affect convection; this effect will change as velocity changes, resulting in R_{tf}'' changing even if the foulant itself does not. In this study inspecting the tube inside surface during operation or immediately after washing was not possible.

To compare the magnitude of the changes to random variations over time, R_{tf}'' values for a 100-day period starting from $T_c = 13$ °C and cooling to 0 °C are plotted for types A and B in Fig. 7. Measurement data needed to include condenser type C was not available.

When coolant flow rate is reduced, the 2-D model produces a slight increase of R_{tf}'' with type A and a decrease with type B, but the magnitudes of both are very small. The 0-D model yields an equally slight decrease of R_{tf}'' with type A, but a more clear decrease with type B. The HEI curves produce a large reduction of R_{tf}'' with both types to offset the overestimated impact of seawater flow rate reduction, however.

In addition to the R_{tf}'' change, other observations can be made from the results of Fig. 7. Both the magnitude and rate of R_{tf}'' variation of the type B condenser at days 80–90 appear too great

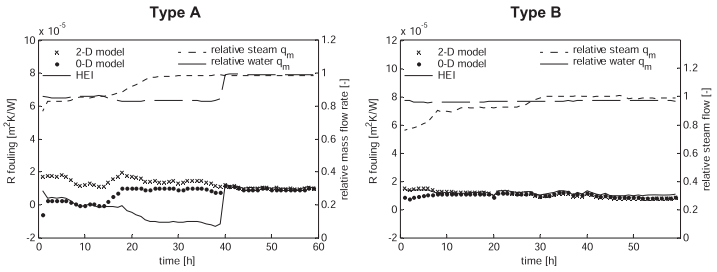

Fig. 8. Condenser thermal fouling resistances and relative steam and coolant flow rates during start-up. Data points represent calculations on the basis of consecutive 1-h measurement averages over 60 h.

to result from actual fouling changes. Available data was insufficient to determine the actual cause, which may have been for example a measurement error or a problem in the gas venting system.

Another interesting result is the values of $R_{tf}'' < 0$ with type B between days 45–85. This may be at least partly correct, however: a very small foulant growth at the surface of a smooth tube can reduce the convection resistance by more than the foulant's conduction resistance [31]. Given the small magnitude of R_{tf}'', the uncertainties of setting the baseline of $R_{tf}'' = 0$, and the small coolant temperature change from which the heat transfer rate is calculated, the negative values may also in part or whole result from inaccuracies of the model or the measurements.

5.3. Model behaviour at lower steam flow rate

Behaviour of the models when steam flow rate varies was studied using start-up data where the steam flow rate increases from approximately 75% to full base load value, and observing the R_{tf}'' given by the three models. A pattern of R_{tf}'' change that would either follow or mirror the steam flow change would indicate that the algorithm is likely correcting model errors with R_{tf}'' to achieve the correct heat transfer rate. Results for types A and B at a seawater temperature of 15 °C are presented in Fig. 8 below. Again, a complete set of necessary data was not available for type C.

In case of type A, the HEI curve for R_{tf}'' appears to mirror the steam flow rate to some extent, descending as the steam flow rate ascends. The 0-D model shows a lesser dependence on steam flow rate, R_{tf}'' increasing with increasing steam flow and approaching the 2-D curve as steam flow rate reaches 100%. The R_{tf}'' values calculated with the 2-D model show the least variation, and little signs of this variation following or mirroring either steam or coolant flow rates. In case of type B both the HEI and 2-D R_{tf}'' curves remain flat and nearly identical during the period of steam flow rate increase. The 0-D model again shows a reduction of R_{tf}'' at 75–90% steam flow rates.

6. Conclusions

Two condenser heat transfer models applying significant simplifications were developed, a 0-D model based on an average overall heat transfer coefficient U, and a 2-D model dividing the condenser into elements in both steam and coolant flow directions. In addition to the two models, the HEI standards curves were used for predicting the condenser performance. Plant measurement data was used to determine a linear correction factor as a function of seawater temperature to match the calculated to measured performance. The correction was applied entirely on the condensation heat transfer coefficient, as this was considered to be the main source of calculation uncertainties.

Without the correction the 2-D model was the most consistently accurate model in predicting condenser performance. With two of the condensers the 0-D and HEI models were only slightly less accurate, but with the type C the 0-D model deviated significantly more from the measurements. This was estimated to be mostly a result of greater importance of local variations in temperature, pressure and heat transfer coefficient with the lower pressures, higher steam velocities and closer temperature approaches of the type C condenser. The HEI curves clearly overestimated the effect of coolant flow rate change compared to measurements and the other models.

When the experimental correction factor was applied, the 2-D model appeared again to be the most accurate one, showing little signs of significant errors when either steam or coolant flow rate were changed. With the 0-D model there were indications of unlikely reduction of R_{tf}'' at reduced steam flow rate, and an overestimation of the impact of cooling water flow rate change with type B. The HEI curve performed poorly with changing coolant flow rate, and appeared to show some inaccuracy with reduced steam flow rate as well.

The HEI standards curves proved to be too inaccurate for more than a rough heat transfer coefficient prediction, and unsuitable for on-line condition monitoring. If great simplicity and minimal computational time is desired for a model for base load operation, a more complex correction factor would be required that would essentially amount to an entirely new experimental function $U = f(\dot{m}_c, T_c)$, thus also rendering the usefulness of the HEI curve as a basis for correction questionable compared to simply creating an experimental function for the condenser at hand.

The 2-D model was overall the most accurate when predicting the performance with or without a correction factor, also when somewhat outside of the scope of flow conditions used for determining the correction factor. This benefit must be weighed against the clear increase in calculation and model development time. The computational time of the 2-D model is still quite short, but if it is used as a component module of a larger power plant model, it may prove to be excessive. Depending on the condenser in question, required accuracy, expected operating conditions and variation thereof, the 0-D model may be sufficient, but it may be a poor choice particularly at low pressures, small temperature differences and in the presence of significant pressure drop.

The 2-D model provided sufficient accuracy and consistency that it could be considered useful for rough initial sizing and evaluation of condensing heat exchanger designs, but due to the typically complex tube bundle configurations of large vacuum condenser and the steam flow patterns that cannot be fully modelled with the applied simplifications, it's utility for such purposes must be considered limited. The authors are currently working on extending the use of a model similar to the 2-D model of this study to an optimization of a backpressure shell-and-tube condenser for a combined heat and power plant.

Acknowledgements

Fortum Power and Heat Oy is gratefully acknowledged for providing the funding and plant data that made this work possible.

Appendix A

Algorithm 1. Determining the fouling resistance or condenser pressure.

1. Calculate actual heat transfer rate $\Phi_{TRU} = \dot{m}_c c_p (T_{c,out} - T_{c,in})$ or $\Phi_{TRU} = \dot{m}_h x h_{fg}$
2. Guess tube inside fouling thermal resistance R_{tf} or condenser pressure $p_{h,in}$
3. Calculate steam pressure drop before tube bundle
4. Calculate Φ in the condenser. Using as incoming flows the exit flows from previous elements, calculate for each element n, $n = 1,\ldots,N$, $N = 2 \cdot i_{max} \cdot j_{max}$ in 2-D model and $N = 1$ in 0-D and HEI models:
   - U_n and Φ_n
   - cumulative $\Phi_{C,n} = \Phi_{C,n-1} + \Phi_n$.
5. After last element N:
   - If $\Phi_{C,N} < (\Phi_{TRU} -$ maximum allowable error) reduce R_{tf}'' or increase $p_{h,in}$, move to step 3.
   - If $\Phi_{C,N} > (\Phi_{TRU} +$ maximum allowable error) increase R_{tf}'' or reduce $p_{h,in}$, move to step 3.

References

[1] A.R. Woodward, D.L. Howard, E.F.C. Andrews, Modern power station practice, in: (Turbines, Generators and Associated Plant), Chapter 4: Condensers, Pumps and Cooling Water Plant, third ed., vol. C, British Electricity International Ltd., 1999.

[2] S.A. Al-Sanea, N. Rhodes, D.G. Tatchell, T.S. Wilkinson, A computer model for detailed calculation of the flow in power station condensers, I. Chem. E. Sympos. Ser. 75 (1983) 70–88.

[3] S.A. Al-Sanea, N. Rhodes, T.S. Wilkinson, Mathematical modeling of two-phase condenser flows, in: 2nd International Conference on Multi-phase Flow, London, UK, 1985.

[4] A.W. Bush, G.S. Marshall, T.S. Wilkinson, The prediction of steam condensation using a three component solution algorithm, in: Proceedings of the 2nd Int. Sympos. on Condensers and Condensation, University of Bath, UK, 1990.

[5] C. Zhang, A.C.M. Sousa, J. Venart, The numerical and experimental study of a power plant condenser, J. Heat Transfer 115 (1993) 435–445.

[6] C. Zhang, A. Bokil, A quasi-three-dimensional approach to simulate the two-phase fluid flow and heat transfer in condensers, Int. J. Heat Mass Transfer 40 (15) (1997) 3537–3546.

[7] M.R. Malin, Modelling flow in an experimental marine condenser, Int. Commun. Heat Mass Transfer 24 (1997) 597–608.

[8] I.S. Ramon, M.P. Gonzalez, Numerical study of the performance of a church window tube bundle condenser, Int. J. Thermal Sci. 40 (2001) 195–204.

[9] M.M. Prieto, I.M. Suarez, E. Montanes, Analysis of the thermal performance of a church window steam condenser for different operational conditions using three models, J. Appl. Therm. Eng. 23 (2003) 163–178.

[10] H.G. Hu, C. Zhang, A modified k-epsilon turbulence model for the simulation of two-phase flow and heat transfer in condensers, Int. J. Heat Mass Transfer 50 (2007) 1641–1648.

[11] H.G. Hu, C. Zhang, A new inundation correlation for the prediction of heat transfer in steam condensers, Numer. Heat Transfer 54 (2008) 34–46.

[12] H. Zeng, J. Meng, L. Zhixin, Numerical study of a power plant condenser tube arrangement, J. Appl. Therm. Eng. 40 (2012) pp.294–pp.303.

[13] J. Taborek, Heat Exchanger Design Handbook, Hemisphere Publishing Corporation, New York, USA, 1983.

[14] A.P. Colburn, O.A. Hougen, Design of cooler condensers for mixture of vapours with noncondensing gases, Ind. Eng. Chem. 26 (1934) 1178–1782.

[15] G. Ackermann, Heat transfer and molecular mass transfer in the same field over large temperature and partial pressure differences (Wärmeübergang und Molekulare Stoffübertragung im Gleichen Feld bei Großen Temperatur und Partialdruckdifferenzen), Res. Bull. (1937) 382 (in German).

[16] W. Nusselt, Surface condensation of water vapour (Die Oberflachenkondensation des Wasserdampfes), Z. Vereines Deutsch. Ing. 60 (1916) 541–546, 569–575 (in German).

[17] W.M. Rohsenow, J.P. Hartnett, E.N. Ganic, Handbook of Heat Transfer Fundamentals, second ed., McGraw-Hill, New York, USA, 1985.

[18] B.S. Petukhov, V.N. Popov, Theoretical calculation of heat exchange in turbulent flow in tubes of an incompressible fluid with variable physical properties, High Temp. 1 (1) (1963) 69–83.

[19] R.K. Shah, D.P. Sekulic, Fundamentals of Heat Exchanger Design, John Wiley & Sons, Inc., Hoboken, New Jersey, USA, 2003.

[20] M.S. Bhatti, R.K. Shah, Turbulent and transition convective heat transfer in ducts, in: S. Kakaç, R.K. Shah, W. Aung (Eds.), Handbook of Single-phase Convective Heat Transfer, John Wiley & Sons, Inc., New York, USA, 1987 (chapter 4).

[21] D. Butterworth, Developments in the design of shell-and-tube condensers, Asme Winter Annual Meeting, Atlanta, ASME Preprint-77-WA/HT-24.

[22] S. Kakac, Boilers, Evaporators and Condensers, John Wiley & Sons, Inc., New York, USA, 1991.

[23] D.Q. Kern, Mathematical developments of tube loading in horizontal condensers, Am. Inst. Chem. Eng. J. 4 (1958) 157–160.

[24] F. Blangetti, R. Krebs, Film Condensation of Pure Vapours (Filmkondensation reiner Dämpfe), VDI-Verlag Gmbh, Düsseldorf, West Germany, 1988. Section Ja. (in German).

[25] D. Butterworth, R.G. Sardesai, P. Griffith, A.E. Bergles, Condensation, Heat Exchanger Design Handbook, Chapter 2.6, Hemisphere, Washington DC, USA, 1983.

[26] I.G. Shekriladze, V.I. Gomelauri, Theoretical study of laminar film condensation of flowing vapour, Int. J. Heat Mass Transfer 9 (6) (1966) 581–591.

[27] M. Jakob, Heat transfer and flow resistance in cross flow of gases over tube banks, Trans. ASME 60 (1938).

[28] J.P. Holman, Heat Transfer, McGraw-Hill Book Company – Singapore, Singapore, 1989.

[29] Black, Veatch, in: L.F. Drbal, P.G. Boston, K.L. Westra (Eds.), Power Plant Engineering, Chapman & Hall, New York, USA, 1996.

[30] E.M. Sparrow, W.J. Minkowycz, M. Saddy, Forced convection condensation in the presence of noncondensables and interfacial resistance, Int. J. Heat Mass Transfer 10 (12) (Dec 1967) 1829–1845.

[31] H. Müller-Steinhagen, Fouling of Heat Exchanger Surfaces (Verschmutzung von Wärmeübertragerflächen), VDI-Verlag Gmbh, Düsseldorf, West Germany, 1988. Section Oc. (in German).

Publication II

Saari, J., Afanasyeva, S., Vakkilainen, E., and Kaikko, J.
Heat transfer model and optimization of a shell-and-tube district heat condenser

Proceedings of the 27th International Conference on Efficiency, Cost, Optimization, Simulation and Environmental Impact of Energy Systems (ECOS)
Turku, Finland; 15-19 June, 2014

HEAT TRANSFER MODEL AND OPTIMIZATION OF A SHELL-AND-TUBE DISTRICT HEAT CONDENSER

Jussi Saari [a], Svetlana Afanasyeva[b], Esa Vakkilainen [c] and Juha Kaikko [d]

[a] *Lappeenranta University of Technology, Lappeenranta, Finland, saari@lut.fi,*
[b] *Lappeenranta University of Technology, Lappeenranta, Finland, svetlana.afanasyeva@lut.fi,*
[c] *Lappeenranta University of Technology, Lappeenranta, Finland, esa.vakkilainen@lut.fi,*
[d] *Lappeenranta University of Technology, Lappeenranta, Finland, juha.kaikko@lut.fi*

Abstract:

This paper presents a heat transfer model and optimization of a shell-and-tube U-tube district heat condenser of a CHP plant. A multi-element model, found important for accuracy in an earlier study by the authors, is used to account for spatial variation of heat transfer and steam pressure drop. The case considered is a condenser with specified requirements on thermal load, terminal temperature difference and drain cooler approach, constrained by maximum allowed pressure drops, as well as typical constraints dictated by manufacturing, operating and maintenance concerns.

To minimize steam pressure drop, a significant volume of the shell side must be void of tubes. It is shown that heat transfer area minimization cannot approximate a minimum-cost design, and would yield an excessively large shell diameter. An alternative method of minimizing the total mass of the condenser, based on approximate dimensioning of the main components, is presented. Differential evolution, a type of evolutionary algorithm, is used in the optimization.

Keywords:

Condensers, heat exchangers, optimization, differential evolution

1. Introduction

District heat condensers of combined heat and power (CHP) steam plants are typically U-tube heat exchangers with water on the tube side and steam condensing on the shell side. In condensers using bypass or bleed steam, sub-cooling the condensate is often desirable to minimize the steam consumption. This study concerns the modelling and optimization of such a condenser.

Shell-and-tube heat exchanger optimization has been studied and published extensively, with several methods applied on cost estimation, heat transfer modelling, and the optimization itself. In most published studies on heat exchanger optimization, including references [1-10], the total cost of the heat exchanger is estimated as a function of the heat transfer area. When operating costs are not considered, this reduces cost optimization to area minimization, which was done in papers [11-14]. This can usually be considered an adequate approximation if the shell has a high length-to-diameter ratio and is fully tubed, which is often true if the shell-side fluid is a liquid. In a condenser with low-pressure steam on the shell side a large fraction of the shell needs to be void of tubes to prevent high pressure drop and flow maldistribution, however. The shell, tube sheet and channel form a significant part of the total mass, and since these are ignored in area minimization, the optimizer can minimize pressure drop and maintain saturation temperature by using a very large shell.

A more elaborate cost function proposed by Purohit [15] was used in one of the cases considered by Ponce-Ortega et al. [6]. However, despite its complexity the Purohit method was found to be relatively inaccurate by Taal et al. [16]. In this study minimizing the mass was assumed to be a better approximation than area minimization for finding the minimum-cost design. For this the approximate dimensions of main components are estimated. Mass minimization, too, ignores some manufacturing costs such as tube sheet and baffle drilling that can be affected by design choices. Due to the lack of public data on manufacturing costs, mass minimization was still considered the best available option. For comparison purposes also results of area minimization are presented.

Most shell-and-tube heat exchanger optimization studies are based on rating the heat exchangers using an average overall heat transfer coefficient U to determine the heat transfer area. This is usually reasonable with single-phase heat exchangers, such as in studies [1-9] and [11-13]. With condensers, local variations are often taken into account. Hajabdollahi et al. accounted for the velocity reduction due to condensation by calculating U at steam inlet and outlet conditions and using their average in [10], while Sanaye et al. modelled a finned-tube condenser using multiple elements [14]. Other heat transfer evaluation methods have also been used in optimization, such as commercial software by Chaudhuri et al. [11], and computational fluid dynamics (CFD) by Stevanović et al.[17], both of which considered only single-phase heat exchangers.

In this paper the heat transfer model is based on the 2-D heat transfer model developed by the authors for large seawater vacuum condensers [18]. Calculating the condenser in elements was shown to yield significantly better accuracy over using a single averaged value of U particularly with a close temperature approach, which is typically the case with district heat condensers.

Many optimization methods have been used in shell-and-tube heat exchanger optimization. The optimization problem is made difficult by such characteristics as several constraints, non-differentiability, possible multimodality, and combination of discrete and continuous variables. These issues have been solved by various means, each with some drawbacks. A deterministic, non-iterative solution combining pumping and area costs for segmentally baffled single-phase heat exchangers was presented by Jegede and Polley [1] and further improved by Serna and Jiménez [5]. Other methods include general disjunctive programming by Mizutani et al.[2], graphical analysis by Muralikrishna and Shenoy [3], and systematic screening of tube count tables with heuristic pruning of infeasible parts by Costa and Queiroz [13]. Most of these methods involve significantly simplified shell-side calculation, and yield themselves poorly to multi-element calculation of condensing flows. There is also no guarantee of an optimum found being the global, not a local one.

During the last 15 years several applications of various global optimization methods to the heat exchanger design optimization problem have been published. As stochastic methods these all suffer from much greater computational time, but as CPU speeds increase, this becomes less of a limit in contrast to the robustness and ease of implementation when confronted by difficult optimization problems combining discrete and continuous decision variables. Examples of stochastic methods applied to shell-and-tube heat exchanger optimization include simulated annealing (SA) [11], particle swarm optimization (PSO) [8,10], and various evolutionary algorithms such as differential evolution (DE) [12], genetic algorithms (GA) [4,6,9,10,14], and harmony search (HS) [7]. Of these, DE tends to outperform PSO and HS particularly with multimodal functions [19,20] while between GA and DE, the former is considered more suitable for combinatorial problems while DE is usually faster and more robust in real-parameter optimization, particularly with non-separable problems [21]. In this study DE was used.

2. Problem definition and objective function

The case chosen for study was a district heat condenser operating with turbine bleed steam in a commercial small modular CHP plant with nominal boiler fuel power of 35 MW, producing 20.5 MW district heat at 50/90 °C input/output temperature levels, and 8 MW electricity [22,23]. The objective was set at finding the optimum configuration for a condenser for the 20.5 MW district heat load. A terminal temperature difference requirement of TTD = 5 °C and drain cooler approach of DCA = 10 °C were chosen with the design point flows shown in Table 1 below. Maximum cold (tube) and hot (shell) side pressure drops were set at $\Delta p_c = 0.5$ bar and $\Delta p_h = 0.2$ bar.

A two-pass shell-and-tube U-tube condenser with first tube pass below the second (Fig. 1) was chosen for the task. U-tube construction was selected for being the cheapest, as well as avoiding any problems from the different thermal expansions of tubes in condensing and subcooling sections. Tube flow was set bottom to top to enable significant subcooling of the condensate. The condenser is calculated in 4 separate sections: first pass with condensing section B and subcooling section A, second condensing pass C, and section U where sections A and B combine and turn 180 °.

Table 1. Condenser fluid stream data

Variable	*Steam*	*DH water*
Flow rate [kg/s]	8.60	119
Temperature, in / out [°C]	95 / 60	50 / 90
Pressure, inlet nozzle [bar]	0.85	16.0
Steam quality [-]	0.96	n/a

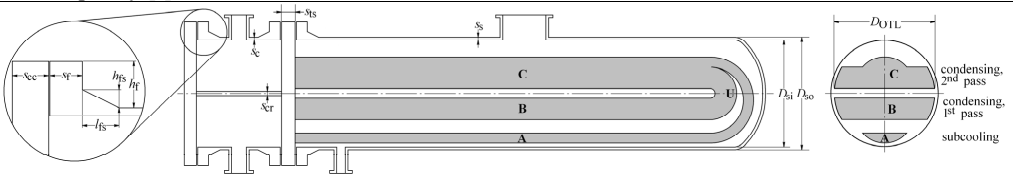

Fig. 1. District heat condenser construction

The problem was formulated with six decision variables x_n, listed in Table 2 below along with the range where the search is initiated. The initialization ranges are not constraints unless separately defined as such. A vector **x** of six values defines a candidate solution, and from this vector, flow data and fixed parameters the heat exchanger model can determine the remaining dimensions.

Table 2. Decision variables

Variable	Definition	Initialization range
x_1	Tube-side (water) flow velocity w_c [m/s]	$1.0 < x_1 < 2.5$
x_2	Tube outside diameter d_o [mm]	$x_2 \in \{10, 12, 14, 16, 18, 20, 22, 25, 28, 30\}$
x_3	Tube pitch to diameter ratio P/d_o	$1.25 < x_3 < 1.50$
x_4	Condensing tube rows in first pass $N_{L,B}$	$5 < x_4 < 25$
x_5	Fraction of first water-side pass tubes in the condensate sub-cooling section r_{SC} [-]	$0.05 < x_5 < 0.20$
x_6	Baffle spacing in section A $S_{B,A}/k_A$ [-]	$0.2 < x_6 < 1.0$

Two objective functions are compared, minimizing the heat exchanger mass m, and heat transfer area A, both determined by the condenser model. The model, described in detail in chapter 3, finds the tube length required to condense all incoming steam. When minimizing the area, the objective function value is obtained directly from the model, when mass is minimized, a simplified mechanical dimensioning is used to estimate the total mass.

Exact mechanical design was ruled outside the scope of the study. The mass is estimated as a sum of the main parts: tube bundle, shell, tubesheet, baffles, and the channel including cover, rib and flanges. Nozzle size was assumed unaffected by other dimensions and not considered. Shell, channel and cover plate thicknesses are calculated against internal pressure and buckling at -1 bar vacuum according to [24]. Instead of the stress and moment analysis of [24], tubesheet thickness was estimated from the simpler formula of the old [25] standard. Flange dimensions were estimated as a function of shell diameter from curve fits for flange dimensions for heat exchangers rated for 650 °F temperature and 300 psi(g) pressure. The sizing equations are described in Appendix A.

2.1. Fixed parameters and assumptions

250 °C design temperature and pressures of -1/+5 bar(g) for the shell and -1/+16 bar(g) for the tubes were assumed in sizing. P235GH carbon steel was used for the tubes, P355GH for other parts. Yield strength of P355GH at 250 °C, $\sigma_I = 210$ N/mm^2, was used as design stress in sizing calculations. An equilateral triangular tube pitch was chosen for tighter packing of tubes at a given tube sheet ligament strength, since need for mechanical cleaning requiring a square pitch was considered unlikely. Loss coefficients for pressure drop were set according to [26]. Lower fouling resistances

than those of TEMA standards [27], which were considered to represent pessimistic worst-case figures rather than typical ones, were used. The assumptions for fixed parameters in mechanical and thermal calculations are summarized in Table 2 below.

Table 2. Main sizing assumptions

Mechanical		Thermo-hydraulic	
Corrosion allowance* [mm]	3.0	Tube wall thermal conductivity [W/mK]	56
Manufacturing tolerance* [mm]	2.0	Tube inside fouling resistance [m^2K/W]	$8.0 \cdot 10^{-5}$
Material design stress, P355GH [MPa]	210	Tube outside fouling resistance [m^2K/W]	$1.0 \cdot 10^{-5}$
Baffle plate thickness, section A [mm]	10.0	Tube inside absolute roughness [mm]	0.04
Support plate thickness, sec. B/C [mm]	10.0	Baffle cut, section A [%]	25
Support plate spacing, sec. B/C [mm]	1500	Tube arrangement	Δ 60°
Channel division rib thickness [mm]	15.0	Loss coefficient, inlet/outlet nozzle [-]	1.0/0.5
Tube wall thickness [mm]	1.2	Loss coefficient, tube entry/exit [-]	0.5/1.0
Tube-to-shell clearance [mm]	40	Loss coefficient, U-bend [-]	0.5

* not applied on heat transfer tubes

2.2. Constraints

Heat exchanger designs are subject to several geometric and performance constraints, handled by penalty functions in this study. Among performance variables, the temperature approach and heat load requirements are handled by constraining DCA and fixing inlet states and flow rates: if DCA is acceptable, then energy balance dictates that so must be the water outlet temperature and TTD.

Flow velocities in heat exchangers are constrained by pressure drop, but must also be low enough to prevent vibration, yet high enough to prevent fouling. In this case with relatively clean fluids, w_{min} constraints were omitted, and the upper bounds set according to recommendations in [26] for liquid in tubes, liquid at shell side (section A) and vapour at shell side (sections B, C and U).

Tube pitch P must provide a strong enough tubesheet ligament between the holes. A limit of $P > 1.25d_o$ is recommended in [25,26]. TEMA [27] permits even tighter spacing, but often with small tubes a minimum ligament of at least 3.2 to 6.4 mm is recommended for drilling tolerance and to allow tight rolling of the tubes to the tubesheet [28]. Here tube pitch was limited at $1.25d_o$ with an additional 5 mm ligament limit. Baffle spacing $S_{B,A}$ in section A was limited to $0.2 < S_{B,A}/k_A < 1.0$, where k_A is the width of the condensate trough. All constraints are summarized in Table 4 below.

Table 4. Constraints

Performance variable	Constraint	Geometric variable	Constraint
Tube-side velocity	$w_c \leq$ 2.5 m/s	Tube pitch	$P \geq 1.25d_o$
Drain cooler approach	DCA ≤ 10 °C	Tubesheet ligament	$(P - d_o) \geq 5$ mm
Tube-side pressure drop	$\Delta p_c \leq$ 0.5 bar	Condenser length	$L_{HX} \leq 15.0$ m
Shell-side pressure drop	$\Delta p_h \leq$ 0.2 bar	Condenser diameter	$D_{HX} \leq 3.5$ m
Shell-side velocity, condensing	$w_{h,B/C/U} \leq 30$ m/s	Baffle spacing, subcooling	$0.2 < S_{B,A}/k_A < 1$
Shell-side velocity, subcooling	$w_{h,A} \leq 1.0$ m/s		

3. Heat exchanger sizing and objective function evaluation

The heat exchanger model and sizing algorithm takes as input the incoming flows, and a candidate solution vector **x** from the optimizer. From these the algorithm finds the heat transfer surface required to condense all incoming steam. The mechanical sizing module then finds the remaining dimensions and mass. Finally, the objective function evaluator compares the performance and size against the constraints, and applies penalties based on the number and severity of violations.

From the inputs to the heat transfer model, the number of tubes and their distribution between sections A and B in the first pass (see Fig.1) are defined. The number of tubes in each of the N_L

rows is then determined, and from this the bundle diameter D_{OTL} between outer surfaces of the outermost tubes. Heat transfer then determines tube length.

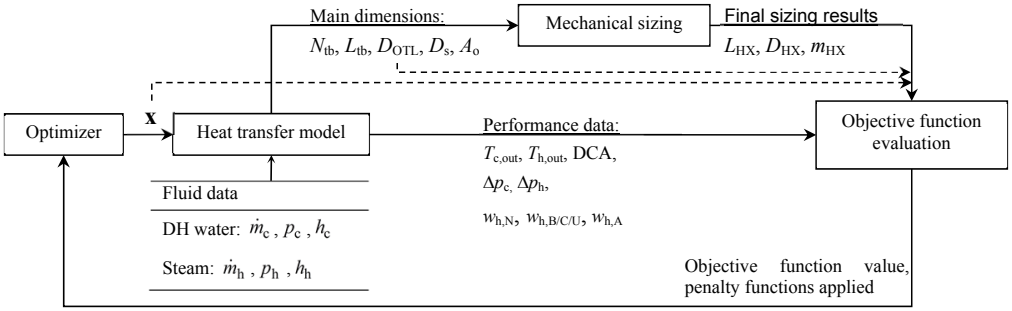

Fig. 2. Simplified data flow diagram and general topography of the optimization code

Condenser model is similar to that of [18]. The condensing parts B and C are split in i_{max} slices in tube direction, and j_{max} rows in steam flow direction (Fig. 3). Flows entering element (i,j) are set by outlet conditions of (i-1,j) and (i,j-1). Each element is calculated assuming of constant T_{sat} and U.

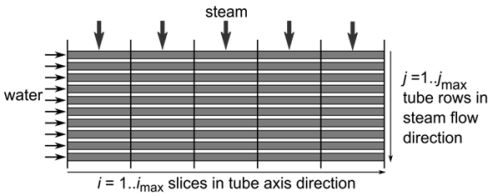

Fig. 3. Division of one condensing pass into i_{max}×j_{max} calculation elements.

Energy balance and ε-NTU method are used as in [18] to determine the heat transfer rate and water exit temperature from an element:

$$U_{i,j} = \left[\frac{d_o}{d_i} \left(R''_{tf,in} + \frac{1}{h_{c,i,j}} \right) + R''_w + \frac{1}{h_{h,i,j}} + R''_{tf,out} \right]^{-1} \quad (1)$$

$$NTU_{i,j} = \frac{U_{i,j} A_{i,j}}{\dot{m}_{c,j} c_{p,c,i,j}} \quad (2)$$

$$\varepsilon_{i,j} = 1 - e^{-NTU_{i,j}} \quad (3)$$

$$\Phi_{i,j} = \varepsilon_{i,j} \dot{m}_{c,j} c_{p,c,i,j} \left(T_{h,i,j} - T_{c,i,j} \right) \quad (4)$$

$$T_{c,i+1,j} = T_{c,i,j} + \frac{\Phi_{i,j}}{\dot{m}_{c,j} c_{p,c,i,j}} \quad (5)$$

The vapour-phase mass flow rate from an element is solved from energy balance considering the change of saturated vapour and condensate enthalpies due to pressure drop,

$$\dot{m}_{h,V,i,j+1} = \frac{\dot{m}_{h,V,i,j} h_{h,V,i,j} + \dot{m}_{h,L,i,j} h_{h,L,i,j} - \dot{m}_{h,V,i,1} h_{h,L,i,j+1} - \Phi_{i,j}}{h_{h,V,i,j+1} - h_{h,L,i,j+1}} . \quad (6)$$

The performance of a given condenser is calculated iteratively in water flow direction one slice i at a time, starting with an estimated steam flow to (i,1), and continuing until the stopping conditions are met. For B and U this is no vapour exiting from (i,j_{max}), for C the steam exit from (i, j_{max}) matching the pressure and flow rate of (i_{max}-i+1,1) in B. The algorithm is shown in Fig. 4 below.

The tubes from section A are combined to those from B in section U, forming there an additional element first in steam flow direction. In C the tubes of j=1 and j=2 in U are combined to a single j=1 approximated as a simple tube bank of same width as row j_{max} of section B, with the tubes from A evenly spread over the full width. State of water entering element (1,1) in C is set as an mass-weighted average of j=1 and j=2 in U. Section A is calculated as a single element with an average heat transfer coefficient U_A. After each iteration, the condensed steam is compared to the requirement, and tube length adjusted. Calculation finishes when all incoming is condensed, and the step change of pressure from C to B is sufficiently small for all i.

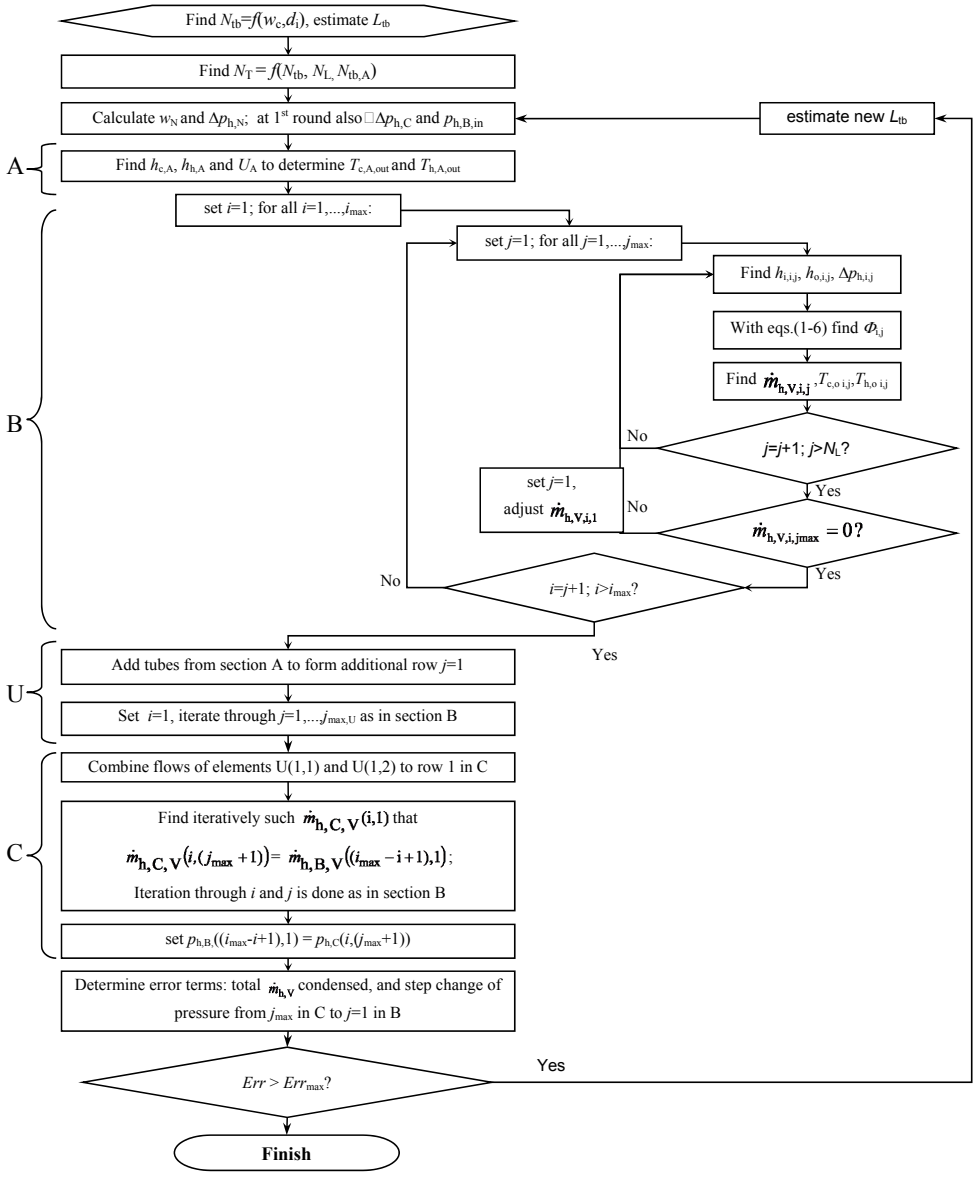

Fig. 4. Flow chart of the heat transfer model.

Tube inside heat transfer coefficient h_c was based on the Petukhov-Popov correlation [29], with the Darcy friction factor f obtained from a formulation of the iterative Colebrook-White equation [30]:

$$Nu_c = \frac{h_c d_i}{k_c} = \frac{0.125 f \cdot Re_c Pr_c}{a + 12.7\sqrt{½ f \cdot Pr_c^{2/3} - 1}} \left(\frac{\mu}{\mu_c}\right)^{0.14}, \quad a = 1.07 + \frac{900}{\mathrm{Re}} - \frac{0.62}{1+10\,\mathrm{Pr}}, \tag{7}$$

$$\frac{1}{\sqrt{f}} = -2\log_{10}\left[\frac{2.51}{Re\sqrt{f}} + \frac{K/d_i}{3.71}\right]. \tag{8}$$

Tube-side Δp_c was obtained from the Darcy-Weisbach equation with loss coefficients of Table 2.

$$\Delta p_c = ½\rho_c w_c^2 \left[f\left(L_{tb}/d_i\right) + K_{\text{entry nozzle}} + K_{\text{tb-entry}} + K_{\text{U-turn}} + K_{\text{tb-exit}} + K_{\text{exit nozzle}}\right]. \tag{9}$$

The hot-side flow in the sub-cooling section is arranged in a covered trough with baffle plates. The Kern correlation [31] was used for estimating the heat transfer coefficient and pressure drop:

$$Nu_{h,A} = \frac{h_{h,A} k_{h,A}}{d_o} = 0.36 Re_{h,A}^{0.55} Pr_{h,A}^{1/3} \left(\frac{\mu_h}{\mu_w}\right)^{0.14}. \tag{10}$$

$Re_{h,A}$ is based on velocity at minimum free-flow area A_{ff}, using dimensions shown in Fig. 5 below.

$$A_{ff} = \frac{P}{P - d_o} H_A S_{B,A}, \tag{11}$$

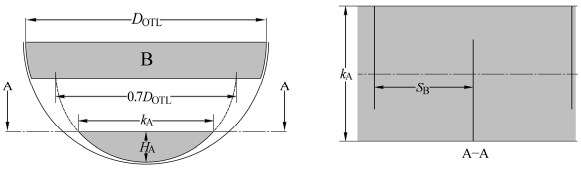

Fig. 5. Dimensions of shell-side flow in section A.

Condensation heat transfer at the tube outside is affected by gravity, vapour shear, and condensate inundation. The net effect of these is approximated from gravity- and shear-dominated heat transfer coefficients $h_{h,gr}$ and $h_{h,sh}$ with an averaging formula (12) and inundation correction (13) as in [18]:

$$h_h = \sqrt{\frac{1}{2}h_{h,sh}^2 + \sqrt{\frac{1}{4}h_{h,sh}^4 + h_{h,gr}^4}} \text{ [32]}, \tag{12}$$

$$h_h(j) = h_h\left\lfloor j^{5/6} - (j-1)^{5/6}\right\rfloor \text{ [32]}, \tag{13}$$

$$Nu_{h,gr} = \frac{h_{h,gr} d_o}{k_l} = 0.728\left[\frac{\rho_L(\rho_L - \rho_V) g h_{fg} d_o^3}{\mu_L k_L \Delta T}\right]^{\frac{1}{4}} \text{ [33]}, \tag{14}$$

$$Nu_{h,sh} = \frac{h_{h,sh} d_o}{k_l} = 0.59\sqrt{\tilde{Re}}, \qquad \tilde{Re} = \frac{w_V d_o \rho_L}{\mu_L}, \tag{15}$$

Steam pressure drop was obtained from Jakob correlation based on vapour mass velocity at the smallest cross-sectional area between the tubes G_{max}:

$$\Delta p_h = 2C_f \frac{G_{max}^2}{\rho_V}, \tag{16}$$

$$C_f = \left[0.25 + 0.1175\left(\frac{P}{d_o} - 1\right)^{-1.08}\right]\left(\frac{d_o w_{v,max}\rho_V}{\mu_V}\right)^{-0.16} \text{ [34]}. \tag{17}$$

4. Optimization

Differential evolution (DE), a type of evolutionary algorithm, was used in the optimization. Evolutionary algorithms (EAs) are stochastic global optimization algorithms often able find a global optimum even if the objective function is multimodal, multiconstrained, non-differentiable, non-continuous or noisy. The cost of robustness is a far greater computational time than what is needed by derivative-based algorithms, or even deterministic direct methods not based on derivatives.

EAs work by mimicking evolution in nature, dealing not with single points in the optimization space, but populations of trial solutions competing for survival and chance of producing offspring (new trial solutions) to the next generation. Random mutations are used to preserve diversity and ensure thorough search of the objective function scope. The better the objective function value of a trial solution, the better its chance of surviving to the next generation. Genetic algorithms emphasize crossover over mutation and apply selection pressure also on selecting parents for the crossover, whereas evolution strategies rely mainly on mutation and offspring selection.

DE resembles evolution strategies in being a real-valued optimizer with mutation emphasized over crossover and only offspring but no parent selection. Discrete variables are dealt by dividing the allowable range to slots, any real number from one slot translating to a single value in objective function evaluation. An important characteristic of DE is that the magnitude of mutations is adjusted by basing the mutation on a difference vector between two randomly chosen vectors $\mathbf{x}_1$ and $\mathbf{x}_2$. This ensures that as the population converges and the search proceeds from finding the right area to fine-tuning the solution, the mutations become gradually smaller.

A new generation G+1 of candidate solutions is created from generation G by having each vector serve once as a target vector, surviving to G+1 if it wins the comparison with a trial vector $\mathbf{u}$ generated by crossover between a noise vector $\mathbf{v}$ and the target vector itself. In crossover decision variables of $\mathbf{u}$ are taken from $\mathbf{v}$ at a probability defined by the crossover parameter CR, otherwise from the target vector. The noise vector $\mathbf{v}$ is created by differential mutation from a base vector $\mathbf{x_0}$ chosen from generation G by adding to it the difference vector $\mathbf{x}_1$-$\mathbf{x}_2$ scaled with weight factor F.

If the objective function is not separable, i.e. the 'goodness' of one variable value cannot be determined in isolation but depends on other variables, differential mutation provides a rotationally invariant search that can easily move in multiple variable axes simultaneously. High values of CR emphasizing mutation are thus required for non-separable problems, while low CR promoting search along variable axes may yield better results for separable problems [21].

A population size of 10 times the number of decision variables is often recommended. Small values of F tend to improve speed at the cost of reliability. As real-world problems tend to be non-separable, $0.8<F<1.0$ and $CR\approx0.9$ are often recommended for an initial, conservative guess emphasizing reliability of convergence over speed [21].

5. Results

Optimization results are shown in Table 5 below. While Min(A) yields a smaller heat transfer area than Min(m), it is clear that this cannot approximate a minimum-cost design: the Min(A) design is over 10 times heavier than the Min(m) result. The difference results from Min(A) allowing vapour pressure drop Δp to be minimized by minimizing vapour velocity with a large, mostly empty shell. By maintaining higher steam T_{sat} and thereby higher temperature difference, a smaller heat transfer area is sufficient. The resulting heavy shell, tube sheet and channel prevent such a solution with mass minimization.

The results were found with a population of NP=60 and parameters F=0.8 and CR=0.9. The algorithm was set to stop when reaching G=600, or after complete convergence. Convergence was considered complete when the whole population had identical values of d_o and N_L, and the coefficient of variation of objective function values was $c_v<0.001$. The coefficient of variation is calculated from

$$c_v = \sigma / \mu, \tag{18}$$

where σ is the standard deviation of objective function values and μ the mean value.

To ensure that the solution was the actual optimum, four consecutive optimization runs were performed; each of these found the same minimum mass within 10 kg, all but one reaching the 600 generations. On the basis of repeatable results obtained with a set of parameters tending towards robust convergence over speed, this was considered to be the global optimum. In a PC with a 2.4 GHz CPU, the average run time was approximately 15 hours.

Table 5. Optimization results.

	Variable		Minimum m	Minimum A
Decision variables	x_1	Tube-side (water) flow velocity w_c [m/s]	1.79	1.84
	x_2	Tube outside diameter d_o [mm]	14.0	10.0
	x_3	Tube pitch to diameter ratio P/d_o [-]	1.357	1.550
	x_4	Condensing tube rows in first tube pass $N_{L,B}$ [-]	12	5
	x_5	Fraction of first pass tubes in section A [-]	0.119	0.143
	x_6	Baffle spacing in section A $S_{B,A}/k_A$ [-]	0.742	0.200
Solution dimensions	m_{HX}	Heat exchanger mass [kg]	6 913	76 578
	A	Heat transfer area [m^2]	331	284
	L_{HX}	Heat exchanger total length [m]	6.900	6.088
	D_{HX}	Heat exchanger total diameter over flanges [m]	1.050	3.491
	s_s	Shell thickness [mm]	13	35
	s_{ts}	Tube sheet thickness [mm]	99	304
	s_{cc}	Channel cover thickness [mm]	47	166

Sensitivity to tuning parameters F and CR was investigated by dividing the F and CR space in 0.1×0.1 squares, and running the mass minimization with three random pairs of F and CR in each square. The results are shown in Fig. 6 below; if optimization found a solution with $m_{HX} < 6930$ kg, the run was considered to be close enough to the optimum to be considered successful and was plotted, otherwise not.

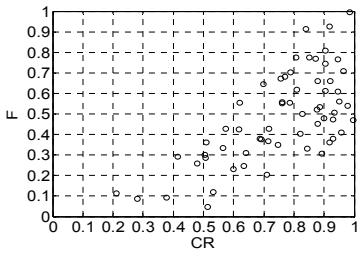

Fig. 6. Successful mass minimization trials with different combinations of F and CR (NP=60).

The results show that in addition to high F and CR, some success was also found with low values of both, although less reliably, indicating a partly separable problem [21]. Successful solutions were concentrated at high values of CR and moderate to high F. Since low F values can often result in faster convergence, speed and reliability was compared between F=0.8 and F=0.55 with CR=0.9 and NP=60. The results of four runs with each set of tuning parameters (Fig. 7) demonstrate reliable behaviour with both, but F=0.55 converging clearly faster. From the figure it is also evident that the algorithm converges fairly quickly to area of the optimum, and spends most of the time fine-tuning the solution.

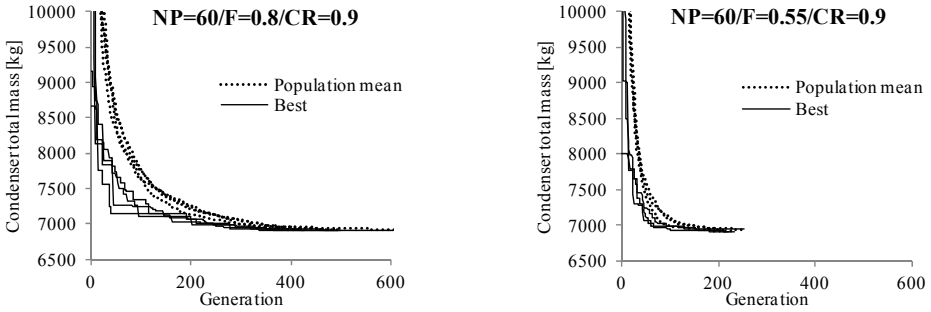

Fig. 7. Convergence histories with a) F=0.8 and CR=0.9, and b) F=0.55 and CF=0.9.

6. Conclusions

The results show that heat transfer area is not a practical objective function to minimize for finding a minimum-cost design for a low-pressure steam condenser. Without considering other parts of the condenser than the heat transfer area, the optimization will find a solution where steam pressure drop is kept very low by using a very large shell. This maximizes the temperature difference between steam T_{sat} and water to minimize the heat transfer area, but results in an impractically heavy condenser.

The more balanced design found by mass minimization is clearly a better approximation for a minimum-cost design. It, too, neglects some aspects of true cost, such as labour costs and the different prices of metal in different components. Accurate economic optimum could well have fewer, larger tubes to reduce the cost of drilling the tube sheet and baffle plate holes, for example. Publically available cost data did not permit accounting for such factors here, but to a heat exchanger manufacturer such data could be readily available, and could be easily implemented in the objective function.

Differential evolution proved to be successful in finding the optimal solution. Optimization was relatively slow, but a run time of 10-15 hours can still be considered acceptable for a practical method. Since DE converges to the general area of the global optimum fairly fast, but spends a long time finding the exact solution, transferring the problem to a deterministic algorithm after finding the approximate solution and fixing the discrete parameters could also reduce the solution time considerably.

Appendix A. Determining heat exchanger mass

The condenser mass is calculated from m = 7850 kg/m^3·V_{HX}, where V_{HX} is the sum of component metal volumes. Metal volume in tubes is calculated from

$$V_{tb} = N_{tb} N_{passes} L_{pass} \cdot \tfrac{1}{4}\pi(d_o^2 - d_i^2) \,. \qquad \text{(A.1)}$$

The shell is assumed to have a circular end cover at same distance from tube bundle as the cylinder:

$$V_s = \tfrac{1}{4}\pi \left\{(L_{pass} + \tfrac{1}{2} D_{s,i}) \cdot [(D_{s,i} + 2s_s)^2 - D_{s,i}^2] + s_s (D_{s,i} + 2s_s)^2\right\} \,. \qquad \text{(A.2)}$$

The shell thickness is the sum of required thickness $s_{s,0}$, corrosion allowance c_1 and manufacturing tolerance c_2,

$$s_s = s_{s,0} + c_1 + c_2, \qquad \text{(A.3)}$$

where $s_{s,0}$ is the maximum of required thicknesses from sizing against elastic buckling $s_{s,eb}$, non-elastic buckling $s_{s,neb}$, and against internal pressure $s_{s,ip}$:

$$s_{\mathrm{s,ip}} = \frac{D_{\mathrm{s,i}} p}{\frac{2\sigma}{n} - p} \tag{A.4}$$

$$s_{\mathrm{s,neb}} = Max(s_{\mathrm{a}}, s_{\mathrm{b}}); \qquad s_{\mathrm{a}} = \frac{D_{\mathrm{s,i}}}{\frac{2\sigma}{p} - 2} \qquad s_{\mathrm{b}} = 1.04 L_{\mathrm{s}} \sqrt{\frac{pn}{3\sigma}} \tag{A.5}$$

$$s_{\mathrm{s,eb}} = \mathrm{Min}\ |p_{\mathrm{calc}} - p_{\mathrm{external}}(\mathrm{a})|, \tag{A.6}$$

where p_{calc} for a thickness s is obtained from

$$p_{\mathrm{calc}}(n_{\mathrm{k}}) = \frac{E_{\mathrm{t}}}{k_{\mathrm{E}} n_{\mathrm{K}}} \left\{ 2\left(k^2 - 1\right)^{-1} \left[1 + (k/B)^2\right]^{-2} \left(s_{\mathrm{s}}/D_{\mathrm{s,i}}\right) + \frac{8}{12\left(1 - \nu^2\right)} \left[k^2 - 1 + \frac{2k^2 - 1 - \nu}{(k/B)^2 - 1} \right] \left(s_{\mathrm{s}}/D_{\mathrm{s,i}}\right)^3 \right\}, \quad B = \pi D_{\mathrm{s,o}} / \left(2 \cdot 1.04 L_{\mathrm{s}}\right). \tag{A.7}$$

The number of elastic buckling waves k is an integer, and $p_{\mathrm{calc}} = \min\{p_{\mathrm{calc}}[k \in (2,10)]\}$. The pressure difference $|p_{\mathrm{calc}} - p_{\mathrm{ext}}(\mathrm{a})|$ is found by golden section search described in [35]. Values of $s_{\mathrm{sh,eb,min}}$ and $s_{\mathrm{sh,eb,max}}$ are initialized so that $s_{\mathrm{sh,eb}}$ is trusted to be found between these. The minimization of $|p_{\mathrm{calc}} - p_{\mathrm{ext}}(\mathrm{a})|$ continues until the difference $s_{\mathrm{sh,eb,max}} - s_{\mathrm{sh,eb,min}}$ rounds to 0.00 mm.

The channel volume is the sum of cylinder, cover plate and rib, with volumes V_{c}, V_{cc}, and V_{cr}. V_{c} is found similarly as V_{s}. Thickness s_{cc} is the maximum of s_{s}, and thickness from (A.4) with p_{c} as internal p. Channel length is assumed $2 \times D_{\mathrm{nozzle}}$, assuming $w_{\mathrm{nozzle}} = 1.5 w_{\mathrm{c}}$. V_{cc} is obtained from

$$V_{\mathrm{cc}} = s_{\mathrm{cc}} \cdot \tfrac{1}{4} \pi D_{\mathrm{cc}}^2, \tag{A.8}$$

where D_{cc} is the same as flange diameter $D_{\mathrm{f}} = D_{\mathrm{s,i}} + 2h_{\mathrm{f}}$. The cover plate thickness s_{cc} is

$$s_{\mathrm{cc}} = C\left(D_{\mathrm{s,i}} + 2s_{\mathrm{c}}\right)\sqrt{\frac{pn}{\nu\sigma}} + c_1 + c_2, \tag{A.9}$$

where the $C = 0.35$, and factor ν for holes $\nu = 1$.The tubesheet thickness s_{ts} is determined from

$$s_{\mathrm{ts}} = C D_{\mathrm{s,o}} \sqrt{\frac{pn}{\nu\sigma}} + c_1 + c_2, \tag{A.10}$$

where $p = \mathrm{Max}(p_{\mathrm{c}}, p_{\mathrm{h}})$, $C = 0.40$ for a tubesheet held between two flanges, and ν determined from

$$\nu = \nu_{\mathrm{H}} \cdot \nu_{\mathrm{W}}, \tag{A.11}$$

where ν_{W} the correction for welding, assumed here at $\nu_{\mathrm{W}} = 1$, and ν_{H} the correction for holes,

$$\nu_{\mathrm{H}} = (P - d_{\mathrm{o}}) / P. \tag{A.12}$$

To find flange dimensions, the following curve fits (all dimensions in millimetres) were created from a manufacturer's catalogue for shell-and-tube heat exchangers rated for 650 °F and 300 psi(g):

$$h_{\mathrm{f}} = \tfrac{1}{2}\,(0.103 D_{\mathrm{s,i}} + 76.4 - 2 s_{\mathrm{s}}) \tag{A.13}$$

$$h_{\mathrm{fs}} = \tfrac{1}{2}\,(0.0442 D_{\mathrm{s,i}} + 21.2 - 2 s_{\mathrm{s}}) \tag{A.14}$$

$$s_{\mathrm{f}} = 56.6 \ln D_{\mathrm{sh,i}} - 304 \tag{A.15}$$

$$l_{\mathrm{fs}} = 19.8 \ln D_{\mathrm{s,i}} + 95 \tag{A.16}$$

Nomenclature

A	area, m^2
c_1	corrosion allowance, m
c_2	manufacturing tolerance, m
C_{f}	coefficient of friction, -
CR	crossover parameter in differential evolution, -
d	tube diameter, m
D	diameter, m
E_{t}	Young's modulus, Pa
f	Darcy friction factor, -

F scaling factor in differential mutation, -
G 1. mass velocity, kg / (m^2 s)
2. generation in differential evolution, -
H height, m
h heat transfer coefficient, W / (m^2K)
h_{fg} latent heat, kJ/kg
k 1. thermal conductivity, W / (mK)
2. width of circular segment (trough, tube bundle), m
3. number of elastic buckling waves, -
K 1. surface roughness, m
2. loss coefficient, -
L length, m
m mass, kg
$\dot{m}$ fluid mass flow rate , kg/s
n safety factor, -
N number of tubes, -
NP number of parents (population size in a generation), -
NTU Number of Transfer Units, -
Nu Nusselt number, -
P tube pitch, m
Pr Prandtl number, -
Re Reynolds number, -
s thickness, m
u trial vector in differential evolution
v noise vector in differential evolution
w velocity, m / s
x decision variable
x vector of decision variable values

Greek symbols

ε heat exchanger effectiveness, -
μ dynamic viscosity, Pa s
ν Poisson's ratio, -
ρ density, kg / m^3
σ_l design stress, Pa

Subscripts and superscripts

c 1. cold (district heating water) side
2. channel
cc channel cover
cr channel rib
f flange
fs flange shoulder
gr gravity-dominated

h hot (steam) side
i 1. inside
2. calculation element index in tube axis direction
j calculation element index in steam flow direction
L 1. longitudinal direction
2. liquid phase of hot side fluid
o outside
OTL outer tube limit, tube bundle furthest edge
s 1. tube wall surface
2. shell
sh shear-dominated
T transverse direction
tb tube
ts tubesheet
V vapor phase of hot side fluid

References

[1] Jegede F.O., Polley G.T., Optimum Heat Exchanger Design. Trans IchemE 1992;70(A): 133-141.

[2] Mizutani F., Pessoa F.L.P., Queiroz E.M., Mathematical Programming Model for Heat-Exchanger Network Synthesis Including Detailed Heat-Exchanger Designs. 1. Shell-and-Tube Heat-Exchanger Design Ind. Eng. Chem. Res. 2003;42(17):4009-4018

[3] Muralikrishna K., Shenoy U.V., Heat exchanger design targets for minimum area and cost. Chem.Eng.Res.Des. 2000;78(2):161-167

[4] Kizilkan R.Ö., Reppich M., A new design approach for shell-and-tube heat exchangers using genetic algorithms from economic point of view. Chem. Eng. Process. 2006;45:268-275

[5] Serna M., Jiménez A., A compact formulation of the Bell-Delaware method for heat exchanger design and optimization. Chem.Eng.Res.Des.2005;83(5):539-550

[6] Ponce-Ortega J.M., Serna-González M., Jiménez-Gutiérrez A., Use of genetic algorithms for the optimal design of shell-and-tube heat exchangers. J.App.Therm.Eng. 2008;29(2):203-209

[7] Fesanghary M., Damangir E., Soleimani I., Design optimization of shell-and-tube heat exchangers using global sensitivity analysis and harmony search algorithm. J.App.Therm.Eng. 2009;29:1026-1031

[8] Rao R.V., Patel V.K., Design optimization of shell-and-tube heat exchangers using global sensitivity analysis and harmony search algorithm. J.App.Therm.Eng. 2010;30:1417-1425

[9] Sanaye S., Hajabdollahi H., Multi-objective optimization of shell-and-tube heat exchangers. J.App.Therm.Eng. 2010;30: 1937-1945

[10] Hajabdollahi H., Ahmadi P., Dincer I., Thermoeconomic optimization of a shell and tube condenser using both genetic algorithms and particle swarm. International Journal of Refrigeration 2010;34:1066-1076

[11] Chaudhuri P.D., Urmila M.D. Jefery S.L., An automated approach for the optimal design of heat exchangers, Ind. & Engg. Chem. Res. 1993;36:3685-3693

[12] Babu B.V., Munawar S.A., Differential evolution strategies in the optimization of shell-and-tube heat exchangers. Chemical Engineering Science 2007;62(14):3720-3739

[13] Costa A.L.H., Queiroz E.M., Design optimization of shell-and-tube heat exchangers. J.App.Therm.Eng. 2008;28:1798-1805

[14] Sanaye S., Dehghandokht M., Modeling and multi-objective optimization of parallel-flow condensers using evolutionary algorithm. Applied Energy 2010;88:1568-1577

[15] Purohit G.T., Estimating costs of shell and tube heat exchangers. Ch.Eng.1983;90(17):57-67

[16] Taal M., Bulatov I., Klemeš J., Stehlík P., Cost estimation and energy price forecasts for economic evaluation of retrofit projects. J.App.Therm.Eng. 2003;23:1819-1835

[17] Stevanović Z., Ilić G., Radojković N., Vukić M., Stefanović V., Vučković G. Design of shell-and-tube heat exchangers by using CFD technique – Part one: thermo-hydraulic calculation. Mechanical Engineering 2001;1(8):1091-1105

[18] Saari J., Kaikko J., Vakkilainen E.K., Savolainen S., Comparison of power plant steam condenser heat transfer models for on-line condition monitoring. J.App.Therm.Eng. 2014;62(1): 37-47

[19] Xu X., Li Y.. Comparison between Particle Swarm Optimization, Differential Evolution and Multi-Parents Crossover. In: Wang Y., Cheung Y-m., Zhang Q., Wang P.S., editors. CIS '07 Proceedings of the 2007 International Conference on Computational Intelligence and Security, IEEE Computer Society; 2007 Dec 15-19; Harbin, China. doi:10.1109/CIS.2007.113

[20] Gao Z-X., Wang X., Ovaska J., ,Uni-modal and multi-modal optimization using modified harmony search methods. Int.J.Innov.Comput.I. 2009;5(10):2985-2998

[21] Price K.V., Storn R.M., Lampinen J. Differential Evolution: A Practical Approach to Global Optimization, Berlin, Germany: Springer-Verlag; 2005

[22] Komulainen, S., Voimalaitoksen käytönaikaisen optimoinnin määrittely. (Eng. Definition of power plant on-line optimization) [master's thesis]. Lappeenranta, Finland: Lappeenranta University of Technology; 2012

[23] Kuitunen, T., Uusiutuvista energialähteistä tuotetun sähkön tukijärjestelmät Euroopan unionissa ja niiden vaikutus biomassaoimalaitosten kannattavuuteen. (Eng. Subsidy systems for electricity produced from renewable sources in the European Union and their effect on the profitability of biomass power plants) [master's thesis]. Lappeenranta, Finland: Lappeenranta University of Technology; 2011

[24] SFS-EN 13445-3, Lämmittämättömät painesäiliöt. (Eng. Unfired pressure vessels). Helsinki, Finland: Suomen Standardisoimisliitto SFS; 2002

[25] SFS-Käsikirja 13, Paineastiat. Mitoitus. Helsinki, Finland: Suomen Standardisoimisliitto SFS; 1996

[26] Sinnott R.K., Coulson & Richardson's Chemical Engineering Design, Vol.6, 4th edition. Oxford, UK: Butterworth-Heinemann; 2005

[27] Standards of the Tubular Exchanger Manufacturers Association, 9th Edition. New York, USA: Tubular Exchanger Manufacturers Association, Inc.; 2007

[28] Rohsenow W.M., Hartnett J.P., Cho Y.I., Handbook of Heat Transfer, 3rd Edition. New York, USA: McGraw-Hill; 1998

[29] Shah R.K., Sekulic D.P., Fundamentals of Heat Exchanger Design. Hoboken, New Jersey, USA: John Wiley & Sons, Inc.; 2003

[30] Kast W., Druckverlust (Eng.pressure drop). Düsseldorf, Germany: VDI-Verlag; 1988.

[31] Kern D.Q., Process Heat Transfer. New York, USA: McGraw-Hill; 1950

[32] Kakac S., Boilers, Evaporators and Condensers. New York, USA: John Wiley & Sons;1991

[33] Nusselt W., Die Oberflachenkondensation des Wasserdampfes. (Eng. Film condensation of water vapour). Z. Vereines Deutsch. Ing. 1916;60:541-546,569-575

[34] Holman J.P., Heat Transfer. Singapore, Singapore: McGraw-Hill Book Company; 1989

[35] Rao S., Optimization: Theory and Applications. New Delhi, India: Wiley, cop.; 1979

Publication III

Sermyagina, E., Saari, J., Zakeri B., Vakkilainen, E., and Kaikko, J.
Effect of heat integration method and torrefaction temperature on the performance of an integrated CHP-torrefaction plant

Reprinted with permission from
Applied Energy
Vol. 149, pp.24-34, 2015

Applied Energy 149 (2015) 24–34

Contents lists available at ScienceDirect

Applied Energy

journal homepage: www.elsevier.com/locate/apenergy

Effect of heat integration method and torrefaction temperature on the performance of an integrated CHP-torrefaction plant

Ekaterina Sermyagina [a,*], Jussi Saari [a], Behnam Zakeri [a,b], Juha Kaikko [a], Esa Vakkilainen [a]

[a] Laboratory of sustainable energy systems, LUT Energy, Lappeenranta University of technology, Skinnarilankatu 34, FI-53850 Lappeenranta, Finland
[b] Energy Economics and Power Plant Engineering Lab., Department of Energy Technology, Aalto University, PL 14100, FI-00076 Aalto, Finland

HIGHLIGHTS

- Torrefaction process is modelled on the basis of mass and energy balances.
- Models for two biomass fired CHP plants were developed.
- Six scenarios of torrefaction integration into CHP plant were applied.
- Fuel consumption, power output and trigeneration efficiency were evaluated.

ARTICLE INFO

Article history:
Received 6 November 2014
Received in revised form 19 March 2015
Accepted 21 March 2015
Available online 7 April 2015

Keywords:
Torrefaction
Biomass
Modelling
Integration
CHP

ABSTRACT

An important factor for industrial-scale implementation of torrefaction – a thermal pre-treatment technology that enhances the fuel characteristics of biomass – is the requirement for a low-cost source of heat energy. Significant benefits can be achieved if torrefaction is integrated with a large heat producer. To study this possibility, a new model for the energy and mass balances of the torrefaction process was developed on the basis of available experimental data. The torrefaction model was then integrated into steam power plant simulations, and the performance of different integration schemes was evaluated. To investigate the effect of plant size and operating mode, the same configurations were studied for both large and small combined heat and power (CHP) plants. Large plant operates at full boiler load, and capturing a portion of heat from the plant reduces the power output for all integration cases. At the same time, higher trigeneration efficiencies in comparison with non-integrated case together with fuel consumption decrease due to torrefaction gas co-firing indicate that integration of torrefaction and CHP plant at full load could be beneficial. In case of small plant, free boiler capacity at reduced-load conditions allows to cover the torrefaction heat demand and simultaneously increase the electricity generation for almost all integration cases. Trigeneration efficiency is changing within a relatively narrow range for most of the cases, while the solid fuel consumption is higher than in design case. This work shows that integration method together with process temperature and plant operation mode are the important factors that could have an effect on CHP plant integration with torrefaction process.

1. Introduction

Many different types of biomass are available, for example, agricultural residues, herbaceous crops and the material most commonly used in industry, woody biomass. Wood has a number of properties that make it suitable for energy production; the comparatively high energy content, the low demand for fertilizers and herbicides, and the high yield per land area [1]. On the other hand, wood as such has several shortcomings, for example, low density, high moisture content, a hydrophilic nature, poor grindability and inconsistent quality. These characteristics increase transport, storage and handling costs, limiting possible applications [2]. Torrefaction, also known as roasting or mild pyrolysis, is a form of thermochemical treatment that improves some of the unfavourable properties of biomass as a fuel. In the torrefaction process, biomass is heated in an inert atmosphere at 200–300 °C, losing mass and energy with the gas produced. The remaining solid product is more brittle and hydrophobic than the original material [1–3], and subsequent pelletizing of the torrefied wood yields a product with high energy density. Several studies have reported positive results on the technical and economic feasibility of

* Corresponding author. Tel.: +358 469067661.
E-mail address: Ekaterina.Sermyagina@lut.fi (E. Sermyagina).

http://dx.doi.org/10.1016/j.apenergy.2015.03.102
0306-2619/

torrefied pellet production [4–6]. Small-scale pellet combustion for heating, entrained-flow gasification, replacement of coal or co-firing in coal-fired power plants have all been proposed as potential uses for torrefied pellets [1,5–7].

Woody biomass is a quite important commodity, and its role increases in many spheres worldwide. The global solid biofuel trade, consisting mainly of forest wood biomass, experienced a nearly sixfold growth from 56 to 300 PJ annually in the decade 2000–2010 [8]. According to the International Energy Agency 'BLUE Map' scenario, to attain a clean yet competitive energy supply, biomass use for energy would have to increase threefold by 2050 compared with levels in 2005 [9]. The European Union is promoting the use of renewable energy, including biomass, and is encouraging a decrease in primary energy consumption through improved efficiency in energy generation, transmission and end-use. Directive 2012/27/EU offers comprehensive measures for reaching the EU's 20% energy efficiency target by 2020 [10]. Solid biofuel with improved properties can substitute a higher share of coal in coal-fired plants: while a co-firing rate of less than 20% of energy content is currently assumed feasible for untreated biomass in coal-fired plants, torrefied biomass can replace more than 50% of the coal fuel [11,12]. Optimal heat integration of biomass conversion into power production thus offers a potentially valuable approach that can contribute considerably to meeting goals for the energy supply of the future.

The torrefaction process requires heat for both drying of the biomass and the torrefaction itself. In addition to the torrefied biomass, the process produces a fuel gas stream as a side product and waste heat from cooling of the torrefied solid product. A biomass-fired combined heat and power (CHP) plant is in many ways an excellent candidate for integration with the torrefaction process as the feedstock logistics, storage and handling facilities already exist, and potential heat sources and sinks for heating and cooling needs are available.

A number of studies of polygeneration systems that integrate CHP plants with various biomass conversion technologies have been published. Studies have found benefits in integrating ethanol production [13–17], gasification [18–20] or pelletization [21] with existing CHP plants. Kohl et al. [22] compared pelletization, torrefaction and pelletization, and fast pyrolysis integrated with a CHP plant, concluding that energy efficiency improved as a result of the increased yearly boiler workload in comparison with stand-alone operation.

Reported data on combining torrefaction with CHP plants is, however, limited. An investigation of an integration case with a 120 MW_{th} CHP has been presented by Håkansson et al. [23]. In another study, Li et al. [24] investigated the potential and effects of co-firing torrefied biomass in a coal-fired boiler. The impacts of various integration concepts of the CHP plant and torrefaction process have, however, not been studied in detail. In addition, the question of CHP plant size has not received proper attention. Research on the most favourable economic and technical integration concept is of considerable interest since the results are applicable also to currently operating plants. In view of the significant consumption of woody biomass by the pulp and paper industry, e.g. in the Nordic area, the development and integration of torrefaction into the CHP cycle is deemed to have an essential potential.

The aim of this study is to investigate different integration concepts and the effect of plant size on the thermodynamic performance of a CHP-torrefaction polygeneration system. A mass and energy balance model is created to predict solid- and gas-phase mass yields and heating values on the basis of published experimental data on the torrefaction of typical Scandinavian wood biomasses (pine, spruce, birch, and mixed-species logging residues). Development of the models is described and results of simulation of the integration scenarios are presented.

2. Modelling of torrefaction

2.1. Model development

IPSEpro process simulation software [25] was used to investigate integration of the torrefaction process into CHP plants. The software does not offer a ready-made torrefaction process model, but does provide standard CHP plant components and includes a model development kit to design new process components to complement the standard component library.

The industrial-type torrefaction equipment considered consists of three parts: a dryer, torrefaction reactor, and cooler for the solid product. Indirect heating and cooling are assumed, but detailed component operation is not considered. The gas-phase product is directed to combustion, e.g., in a boiler or furnace. Fig. 1 shows a schematic diagram of the developed model.

2.2. Torrefaction products

The main components of wood are three polymeric structures: hemicellulose, cellulose and lignin, of which mainly hemicellulose is affected by torrefaction. Torrefaction occurs at a temperature range of 200...300 °C. At temperatures below 250 °C, hemicellulose devolatilization and carbonization are limited, but at higher temperatures, decomposition of all the main components becomes extensive as lignin and cellulose also begin limited devolatilization below 300 °C [26]. Mass loss increases with time, but based on experiments with willow, beech and spruce, the rate of mass loss slows down considerably after the first 20 to 30 min [27,28].

Solid product mass and energy yields of 70% and 90%, respectively, for a 30% increase in LHV are often quoted, citing the report by Bergman et al. [6], but somewhat lower energy retention appears more common in most experiments with European woods. The results are quite diverse, ranging from 95.1% and 96.5% (willow, [31]) to 52% and 71% (pine, [30]) for mass and energy yields, respectively. Fig. 2 summarizes a selection of published yields from torrefaction experiments with pine [30,32], birch [32], spruce [29], willow [31], wood briquettes [33], and logging residues [30].

The torrefaction model used in this study is based on an assumption that the sum of the available energy of feedstock dry matter and heat of reaction is divided between available heats of the gaseous and solid products:

$$\dot{m}_d(LHV_d + h_{react}) = \dot{m}_g LHV_g + \dot{m}_{torr} LHV_{torr} \quad (1)$$

where h_{react} [kJ/kg] is the heat of reaction; $\dot{m}_d$, $\dot{m}_g$ and $\dot{m}_{torr}$ [kg/s] are the mass flows of feedstock dry matter, torrefaction gas and

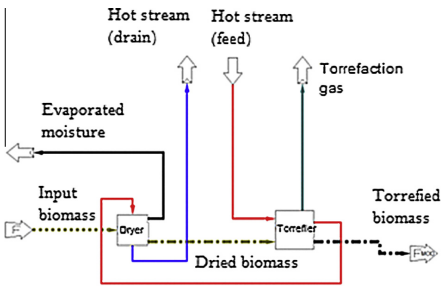

Fig. 1. Torrefaction process model in IPSEpro software.

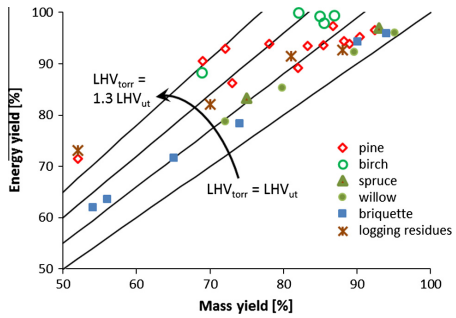

Fig. 2. Mass and energy yields for torrefaction of different wood biomasses [31,30,32,29,33]. The lines represent the increase in torrefied product heating value LHV_{torr} relative to untreated feed LHV_{ut} (both dry, ash-free).

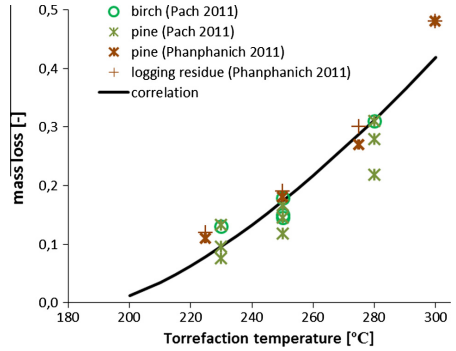

Fig. 3. Mass loss as a function of torrefaction temperature. Correlation curve represents Eq. (2).

torrefied biomass; LHV_d, LHV_g and LHV_{torr} [MJ/kg] are their lower heating values correspondingly.

Available data on the parameters of interest – mass yield, gaseous product heating value, and solid product heating value – suffer from being somewhat limited and from being dispersed among references using different assumptions, measurement approaches, and experimental parameters.

To close the energy balance, solid product mass yield, gas heating value, and heat of reaction were estimated on the basis of published experimental results. Solid product heating value was then solved using Eq. (1). This approach was considered necessary, because being roughly an order of magnitude less than the solid product heating value, the gas-phase heating value would otherwise be subject to potentially very large relative errors from comparatively uncertain solid product LHV estimates.

The mass yield M [−], or ratio of solid product to feedstock dry fraction, was determined from the correlation expressed in Eq. (2).

$$M = \frac{m_{torr}}{m_d} = 1 - a(T_{torr} - T_{ini})^b \quad (2)$$

The constants $a = 4.47 \cdot 10^{-4}$, $b = 1.46$ and temperature $T_{ini} = 190$ °C were obtained with data from [31,30] by minimizing the residual sums of squares. The resulting curve and the initial data on which it was based are shown in Fig. 3.

Although softwood is known to be less reactive than hardwood, due to differences in the hemicellulose structure [27,34], the data in Fig. 3 is too limited to clearly demonstrate this. Difference in the torrefaction time, 30 min by Phanphanich and Mani [30] and 1–3 h by Pach et al. [31], appears to have little effect. This can be explained by the low heat conductivity of wood, meaning the temperature inside a chip changes slowly, and the fact that the mass loss rate slows after the first 20–30 min. Logging residues appear slightly more reactive than wood, possibly due to the higher ash content and thus greater presence of catalytic components. Overall, the correlation appears to be an adequate approximation for the mass yield of typical Scandinavian forest biomasses at >30 min residence time and varying temperatures.

Prins et al. [3] and Prins [35] published experimental results for the gas-phase product for willow and larch, as well as some non-woody biomasses. These results were used in the thermochemical model by Bates and Ghoniem [36]. For use in this study, the data given in [3] and [35] pose some difficulties. Firstly, mass balances were not closed; the unknown rate of the missing mass leaves a significant uncertainty for the comparatively small mass fraction in the gas phase. Secondly, only the true gas-phase components are considered, but in industrial equipment solids and tar are likely to be transported out of the reactor as dust and droplets with the gas stream. These components may have heating values an order of magnitude greater than the gas, and may have a notable effect on the total heating value transported with the gas flow.

In the absence of more accurate information, the data for woody biomasses (larch and willow, approximately 10% moisture) from [3] and [35] were used to obtain a simple curve fit for the heating value of the torrefaction gas, shown in Eq. (3) and Fig. 4. Due to the limitations in material library of the IPSEpro software, this gas flow was simulated as a mixture of carbon dioxide, methane and water vapour, providing the lower heating value.

$$LHV_{TG} = 2.00 + 5.28 \cdot 10^{-5} \cdot (T_{torr} - 190°C)^{2.49} \quad (3)$$

Data on the heat of reaction of wood decomposition during torrefaction also suffer from a high degree of uncertainty and are partly contradictory. Bergman [4] suggests that reaction enthalpy will be within ±1% of feedstock heating value, while Prins et al. [3] measured endothermic reaction enthalpies of 87 ± 400 kJ/kg for willow when torrefied for 30 min at 260 °C, and 124 ± 449 kJ/kg for 10 min of torrefaction at 300 °C [34]. The stated uncertainty range, however, ignores the uncertainty resulting from failure to close the mass balances.

Recent research suggests that torrefaction reactions can be considered a two-stage process. The first stage consumes oxygen from the hemicellulose (and at higher temperatures from the cellulose)

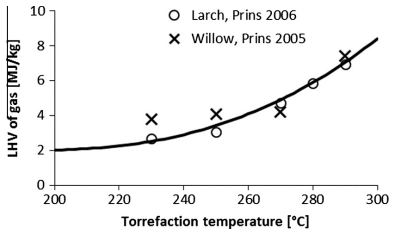

Fig. 4. Lower heating value of torrefaction gas as a function of torrefaction temperature. Experimental data from [3,33], correlation curve represents Eq. (3).

with clearly exothermic reactions. In the following stage, both endo- and exothermic reactions are present [37,38].

Bates and Ghoniem [36] used a two-step model with three correlations to estimate the higher heating value (HHV). Regardless of the HHV correlation and torrefaction temperature, the first step reaction enthalpy always remained exothermic. The second step reaction enthalpy varied from 300 kJ/kg endothermic to −200 kJ/kg exothermic at 200 °C, depending on HHV correlation, and from −50 kJ/kg exothermic to −550 kJ/kg exothermic at 300 °C.

Ohliger et al. [39] measured heat of reaction in beech torrefaction. Results with 10% moisture beech ranged from 0... + 150 kJ/kg endothermic to −150...0 kJ/kg exothermic, with the more exothermic reactions coinciding mostly with the highest mass losses, i.e. long time and/or high temperature. High moisture content caused more endothermic reactions, probably due to vapour flow flushing the volatiles needed in the exothermic second-stage reactions from the reactor [38]. Results of van der Stelt [37] also indicate a trend towards increasingly exothermic behaviour at increasing temperatures, although the results of 1.5 MJ/kg endothermic to −1.2 MJ/kg exothermic had significant uncertainty from the mass balance not being closed. Experimental co-torrefaction of hemicellulose, cellulose and lignin for 60 min by Chen and Kuo [38] indicated the opposite behaviour, with net exothermic reactions at 230 °C, less exothermic reactions at 260 °C, and even slightly endothermic reactions at 290 °C. Recently, Peduzzi et al. [40] estimated the heat of reaction for unspecified wood biomass at 250 °C as −170 kJ/kg exothermic, and Basu et al. [41] found a heat of reaction of −360 kJ/kg for poplar wood at unspecified temperature.

Although there appears a tendency for torrefaction to exhibit slightly exothermic heat of reaction more often than not, the data were considered too dispersed and contradictory to serve as a basis for a model that could predict accurately the change of heat of reaction as a function of temperature. A constant −500 kJ/$kg_{feed,dry}$ heat of reaction, considered a conservative estimate for determining the solid product energy yield, was used in the model. The resulting energy yield and solid matter heating value behaviour appear reasonably close to published results. The relative change of solid product dry fraction LHV (energy ratio ER [−]) and energy yield E [−], defined as in Eqs. (4) and (5)

$$ER = \frac{LHV_{torr}}{LHV_{d}} \tag{4}$$

$$E = ER \cdot \frac{m_{torr}}{m_{d}} \tag{5}$$

are plotted as a function of torrefaction temperature together with experimental data from Refs. [31,30] in Fig. 5.

The experimental results used for torrefaction modelling in current study are derived from laboratory-scale units. The various sizes and shapes of feedstock material together with inevitable impurities would affect the reaction kinetics in case of industrial-scale operation, Medik et al. [42] found that this effect is weaker than influence of temperature and residence time. The results of several studies indicate that larger particles would react slower [43], however, with sufficient reaction time these differences in behaviour become less pronounced [41,42]. Consequently, it was suggested that within the framework of existing limitations, the torrefaction model developed in current work could be applied to industrial-scale units.

2.3. Torrefaction heat requirement

Before torrefaction, the feedstock is typically dried to a moisture content of approximately 10% [4,22]. Drying consumes most of the heat required for the whole torrefaction process. The dryer type is not specified in the model, but a belt dryer would enable flexibility in selecting the heat source and would allow use of fairly low-temperature sources [44]. A specific heat consumption of 1.2 kW h/$kg_{H2O-evaporated}$, considered to represent a typical or conservative estimate for belt dryer heat consumption [44,45], was assumed. Dryer heat can be supplied by flue gas, hot water, or low pressure steam.

From dried biomass storage the biomass feed is assumed to enter the torrefaction reactor at a temperature of 60 °C and moisture of 10%. The feed is then torrefied by heating it to the specified reaction temperature and maintaining the temperature for a sufficiently long period, typically 30–60 min. Indirect heating of the biomass was assumed in this study, allowing the use of any flow at a sufficient temperature for heat supply. Although torrefaction requires a higher temperature than drying, the total heat demand of torrefaction is much lower.

As industrial torrefaction reactors are not yet common equipment with known typical heat consumption rates, a model-based approximation had to be used. Accurate modelling of the heat consumption in torrefaction is challenging for several reasons, in particular because of variations in the specific heat of the wood, the heat of the reaction during torrefaction, and the magnitude of heat losses.

The model used in this study assumes that moisture content remains constant up to 100 °C, at which point all moisture is evaporated. The net heat consumption Φ_{TORR} [kW] in the torrefaction reactor can be considered to consist of five separate parts: (1) sensible heat of moist wood temperature change, $\Phi_{<100°C}$ [kW]; (2) latent heat of remaining evaporation, Φ_{evap} [kW]; (3) sensible heat

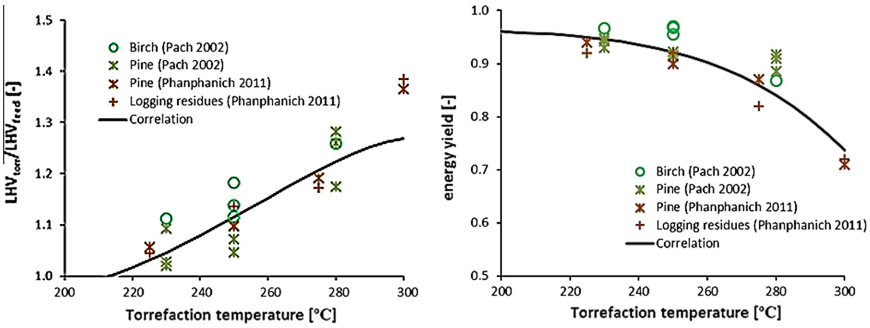

Fig. 5. Model-based solid product energy ratio (Eq. (4)) and energy yield (Eq. (5)) compared to experimental results from [31,30].

of dry wood and water vapour, $\Phi_{100°C\text{-}Torr}$ [kW]; (4) heat of reaction in torrefaction, Φ_{react} [kW], and (5) heat losses, Φ_{loss} [kW]. The sensible heats are obtained from Eqs. (6) and (7):

$$\Phi_{<100\ °C} = \dot{m}_{feed}\bar{c}_{p,<100°C}(100\ °C - T_{feed,in}) \quad (6)$$

$$\Phi_{100-Torr} = \dot{m}_{feed}(T_{torr} - 100)\left[(1 - MC_{feed})\bar{c}_{p,dry} + MC_{feed}\bar{c}_{p,vapour}\right] \quad (7)$$

where MC_{feed} is the moisture content of the feedstock.

The specific heat of wood has a strong dependence on temperature [46], but shows little [47] or no dependence [48] on the wood species. Moisture also affects the specific heat. Part of the moisture is not free liquid in the cells but bound to the fibres. As a result, the net specific heat of moist wood is greater than the weighted sum of dry and water components [48]. Decomposition of wood begins at approximately 150 °C, affecting the c_p [39]. The specific heat of moist wood $\bar{c}_{p,<100\ °C}$ [kJ/kg K] was estimated from a correlation by TenWolde [49] as cited in [50]

$$\bar{c}_{p,<100\ °C} = \frac{\bar{c}_{p,dry,<100\ °C} + 4.19MC_{db}}{1 + MC_{db}} + MC_{db}(0.02355\overline{T} - 1.32MC_{db} - 6.191) \quad (8)$$

where MC_{db} [−] is the fractional dry basis moisture content and $\overline{T}$ [K] is the average temperature. The dry wood specific heat $\bar{c}_{p,dry,<100\ °C}$ [kJ/kg K] is obtained from

$$\bar{c}_{p,dry,<100} = 0.1031 + 0.003867 \cdot \overline{T} \quad (9)$$

The specific heat of water vapour is assumed to be 1.95 kJ/kg K. The correlation in Eq. (9) is valid for dry wood up to 147 °C, from which point onwards wood decomposition begins [39]. Other correlations for dry wood c_p also exist, up to a maximum of 177 °C, for example those by Skaar [51], Koch [52], and Gupta et al. [53]. All suggest linear dependence to absolute temperature. Harada et al. [54] presents a linear correlation up to 260 °C. This correlation, however, differs significantly from the others. At 147 °C all correlations are within 0.25 kJ/kg K, but when extrapolated to torrefaction temperatures the range increases to almost 0.57 kJ/kg K at 300 °C.

Ohliger et al. [39] considered taking the c_p above 147 °C to be either that of char or an average of that of char and extrapolated wood c_p. However, char has a much lower c_p than wood, and given the relatively short duration of the heating phase, in this paper the properties were assumed to be much closer to those of wood than char. In the absence of a more accurate model, Eq. (9), yielding lowest c_p of the compared correlations, with the exception of that of Harada [54], was used also in the range of 147 °C < T < 300 °C, with the knowledge that considerable errors may thus be introduced.

The heat required for the evaporation of the last moisture from the wood was calculated from

$$\Phi_{evap} = \dot{m}_{feed}MC_{feed}h_{fg} \quad (10)$$

where *a* value of of h_{fg} = 2260 kJ/kg, corresponding to the latent heat of evaporation of free water at 100 °C, was assumed, ignoring the effect of bound moisture. The error thus introduced was assumed to be small and most likely of opposite direction compared to the error caused by the extrapolation of dry wood c_p.

Although the bulk of published data indicates somewhat exothermic heat of reaction, which was also assumed for determining the solid product heating value, the data can still be considered varied and sometimes contradictory. To avoid an overly optimistic estimate of the heating benefit from the exothermicity of the reactions, h_{react} was thus assumed to be zero when determining the heating requirement.

Some heat losses from the reactor are inevitable during the process. However, without considering the design of the reactor, it is hard to evaluate them properly. In current model this loss was assumed to be 10% of the total heat requirement.

Fig. 6 shows the total heat consumption of torrefaction reactor at three different temperatures and 10% moisture feedstock at a temperature of 60 °C. The heat consumption of drying the chips from 50% to 10% is also indicated for comparison. It is evident from the figure that water evaporation accounts for the vast majority of the energy demand in torrefaction, most of it in the dryer.

The heat requirement and energy recovery available from the torrefaction process are illustrated in Fig. 7. While at low temperatures the process is a clear net consumer of energy, as torrefaction severity increases, the gas stream volume and heating value increase rapidly, reaching the process heat need at 300 °C. The sensible heat recovered from the process is negligible in comparison.

3. Integration of torrefaction and cogeneration plants

3.1. CHP plant models

Two different CHP plants were considered for the integration analysis: a large-scale biomass fired plant with a 385 MW circulating fluidized bed (CFB) boiler and a condensing turbine [55], henceforth referred to as Plant A, and a smaller biomass fired backpressure plant with a 29 MW bubbling fluidized bed (BFB) boiler [56] (Plant B). Both plants are based on actual operating industrial plants and their performance has been modelled using IPSEpro software. They are assumed to run on the basis of required heat demand; integration of torrefaction will thus affect only electricity production and fuel consumption.

Plant A produces 103 MW electricity and 110 MW district heat at 90/50 °C supply/return temperature levels during the three month winter peak. In addition, 120 MW of process steam is supplied continuously for industrial purposes at 16.5 bar(a), 10 bar(a) and 4.5 bar(a) pressures. This type of plant is usually built to produce electricity. So, the assumption used for choosing the operation type for Plant A tries to run at maximum steam load while operating. As the plant tries to run at full boiler load, the condensing tail takes whatever steam remains after the steam extractions for thermal load fulfilment.

Plant B is an example of a small CHP plant that is typically utilized, e.g. in central Europe, to increase small-scale heat and power production from biomass. At full load it produces 7.9 MW electricity and 20.0 MW district heat. A different scenario is considered with this plant because this kind of plant is typically built to fulfil district heating demand. When the heat load of a backpressure plant is decreased (spring/autumn season), the steam flow through

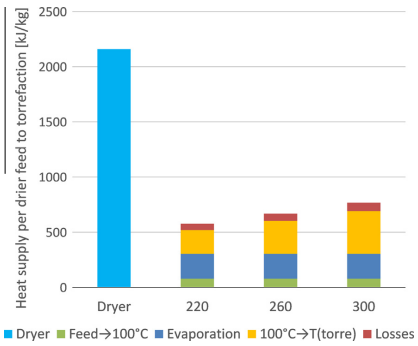

Fig. 6. Heat consumption of dryer and torrefier at three torrefaction temperatures [°C].

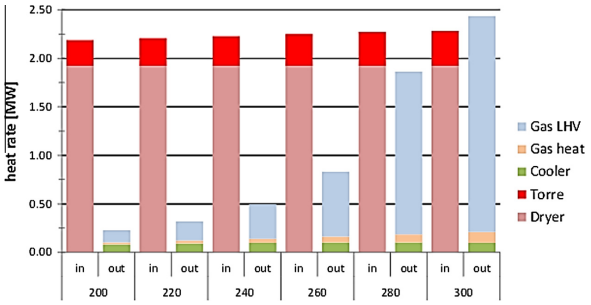

Fig. 7. Energy required and recovery of torrefaction process (1 kg/s feedstock with wet basis moisture content of 50%).

the turbine and therefore electricity output are inevitably reduced. Under these circumstances, an additional heat consumer in the form of a torrefaction plant can increase the electricity output by using the available free boiler capacity. In this study, a case of 60% district heat load (12 MW) at 90/50 °C temperature level was chosen to represent typical reduced-load conditions.

The main plant parameters at full load design point operation are summarized in Table 1; schematic diagrams of the design cases are shown in Figs. 8 and 9. For the wood chips used both as boiler fuel and torrefaction feedstock, a moisture content of MC = 50% and lower heating value of 18.8 MJ/kg on a dry basis were assumed based on data from Alakangas [57]. For both cases, the torrefied solid fuel could be either used internally, processed further in the plant, for example, by pelletizing, or sold on the market as torrefied chips; the scope of this study was limited to the integration of the torrefaction and CHP processes.

The boiler for both cases is modelled using four components: the furnace, including the steam drum, followed by a series of three heat exchangers in the flue gas flow direction, representing the superheater, economizer and air preheater. Heat transfer rate Φ [kW] in the three heat exchangers is determined from

$$\Phi = G\Delta T_{\mathrm{lm}} \tag{11}$$

where the conductance G [kW/K] is the product of the overall heat transfer coefficient U [kW/m^2 K] and heat transfer area A [m^2], and ΔT_{lm} [K] is the logarithmic temperature difference. Table 2 lists the values for design point conductance G of the main heat transfer surfaces for both plants.

Table 1
Main characteristics of CHP plants at full load design point.

Category	Parameter	Plant A	Plant B
Net production	Electricity	103 MW	7.9 MW
	District heat	110 MW	20.0 MW
	Process heat	120 MW	–
Boiler	Type	CFB	BFB
	Thermal output	385 MW	29 MW
	Stack temperature	150 °C	150 °C
Turbine	Inlet steam	110 bar/550 °C	90 bar/500 °C
	Back pressure (DH)	0.4 bar	0.8 bar
	Condenser pressure	50 mbar	n/a
	Extractions	50[a]/16.5/10/4.5 bar(a)	59[a]/8.5 bar(a)
Main losses	Boiler	55 MW	4.3 MW
	Condenser	37 MW	n/a
	Auxiliary power	8.1 MW	0.60 MW

[a] To obtain high-pressure steam for torrefaction, it is assumed that an extraction can be created in the settling chamber after the partial admission control stage at the turbine inlet.

Component performance changes in off-design conditions. In this study, variations in turbine and pump isentropic efficiencies were assumed to remain small and not considered. In the boiler, the conductances G of the superheater, economizer and air preheater are assumed to change in proportion to relative gas flow change [58]:

$$G = G_0 \left(\frac{\dot{m}_{\mathrm{FG}}}{\dot{m}_{\mathrm{FG},0}} \right)^{0.6} \tag{12}$$

where $\dot{m}_{FG}$ is the flue gas mass flow rate, with subscript 0 referring to the design point.

A steam coil air preheater is used to prevent flue gases from cooling below 150 °C. In some cases, the stack temperature may increase slightly above 150 °C. Full superheat can be maintained by reducing the water injection to superheater in most cases, but in some situations, especially with the smaller plant at part load, the live steam temperature will inevitably be slightly reduced.

With reduced loads, the auxiliary power consumption P_{aux} also drops. Part-load P_{aux} is estimated from:

$$P_{\mathrm{aux}} = \left(0.5 + 0.25 \frac{\dot{m}_{\mathrm{FG}}}{\dot{m}_{\mathrm{FG},0}} + 0.25 \frac{\dot{m}_{\mathrm{FW}}}{\dot{m}_{\mathrm{FW},0}} \right) P_{\mathrm{aux},0} \tag{13}$$

where $\dot{m}_{\mathrm{FW}}$ is the feed water flow rate, with subscript 0 referring to the design point.

3.2. Integration options

The heat required for the torrefaction process can be provided by various streams, such as hot water, flue gases from the boiler, or steam from the turbine. The thermodynamic performances of six different integration schemes (Table 3) were investigated. Case 0 represents a non-integrated operation of the CHP plant and torrefaction unit and was used as a reference point for comparison. In Case 0, the heat demand of the torrefier and dryer was supplied by flue gases from the combustion of torrefaction gas and additional fuel. In all cases studied, power consumption of the torrefaction process was assumed to be 200 kW/$\dot{m}_{\mathrm{H2O,evap}}$ in the dryer, 50 kW · $\dot{m}_{\mathrm{in}}$ in the torrefier, and 200 kW · $\dot{m}_{\mathrm{feed}}$ for the total sum of power consumption of other components.

In Cases 1 and 2, the water from the boiler drum is returned back to the steam-water system after supplying heat for the torrefaction process units. The temperature of the exhaust gases after the dryer for Cases 2 and 3 was set at 150 °C. In Case 4, flue gases are returned back to the boiler after the torrefier. Condensate from the dryer in Cases 4, 5 and 6 is mixed to the main condensate flow before the deaerator.

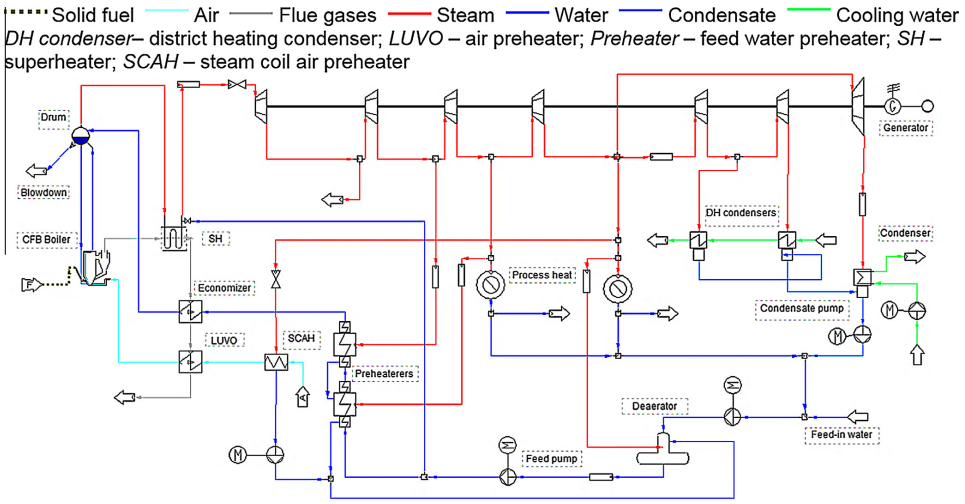

Fig. 8. Design case model for Plant A.

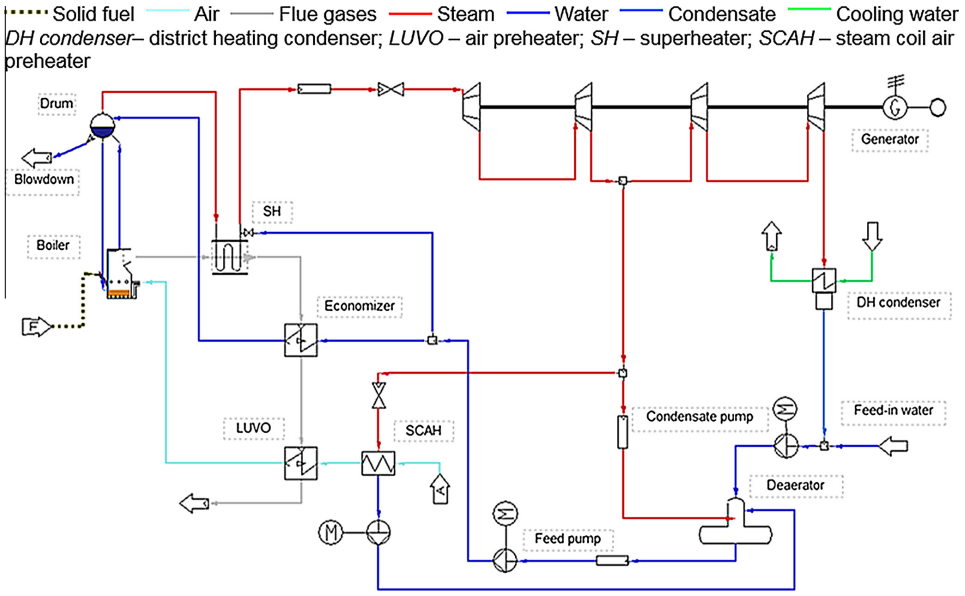

Fig. 9. Design case model for Plant B.

Table 2
Heat transfer surface conductance [kW/K] of boilers at design point.

Heat transfer surface	Plant A	Plant B
Steam generator	260	n/a
Superheater	420	26
Economizer	500	32
Air preheater	640	34
Steam coil air preheater	20	5

The following assumptions were applied to all cases:

- Heat from the torrefied biomass cooling is used for combustion air preheating.
- For all integration cases the torrefaction gas is co-fired in the boiler together with biomass.
- Torrefaction heat losses are independent of the heating media used.
- Live steam pressure is fixed at the design level.
- Constant mass flow of solid biomass to torrefaction is assumed (10 kg/s for Plant A and 1 kg/s for Plant B integration cases).

To compare the performance of the considered schemes, the trigeneration efficiency [%] was calculated:

$$\eta_{trig} = \frac{(P_{gen} - \sum P_{pump} - \sum P_{aux}) + (Q_{DH} + Q_{process}) + \dot{m}_{torr} \cdot LHV_{torr}}{\dot{m}_{tot\_fuel} \cdot LHV_{fuel}} \cdot 100\% \quad (14)$$

where P_{gen} is the power at the generator terminals [MW]; ΣP_{pump} is the electric power consumed by the pumps in the steam cycle (feed water pump and condensate pump) [MW]; ΣP_{aux} is the power used by other plant equipment (fans, fuel and ash handling, etc.); Q_{DH} is the district heating load [MW]; $Q_{process}$ is the process heat [MW]; $\dot{m}_{torr}$ [kg/s] is the mass flow rate of torrefied fuel; $\dot{m}_{tot\_fuel}$ [kg/s] is the combined mass flow rate of boiler solid fuel and torrefaction feedstock; and LHV_{fuel} and LHV_{torr} are the lower heating values of untreated and torrefied solids respectively [MJ/kg].

3.3. Simulation results and discussion

Fig. 10 illustrates solid fuel consumption as a function of torrefaction temperature for the studied integration cases. The solid fuel consumption reduces with increasing torrefaction temperature for both the large and the small CHP plant. This result is as expected since the higher the torrefaction temperature the greater is the mass loss at torrefaction. Thus, both the heating value and the mass flow rate of the torrefaction gases to the boilers increase with increased torrefaction temperature. As a result, a larger share of solid fuel can be substituted in the boiler. The increase in torrefaction reactor heat consumption (about 40% more for the highest temperature level than for the lowest one) is negligible in comparison.

Table 3
Heat sources for torrefaction process units.

Case	Heat source for section	
	Torrefaction	Drying
Case 1	Saturated water from the drum	Water after the torrefier
Case 2	Saturated water from the drum	Flue gases after air preheater
Case 3	Flue gases after the superheater	Flue gases after the torrefier
Case 4	Flue gases after the superheater	Backpressure steam
Case 5	Steam extraction from the HP turbine	Backpressure steam
Case 6	Steam extraction from the HP turbine	Steam after the torrefier

When the boiler of Plant A is operated at full load, increasing the share of torrefaction gas that is co-fired leads to growing economy of the main solid fuel use (Fig. 10(a)). In Cases 2 and 3, the relatively high heat demand of the dryer is covered by the heat of flue gases. Under these circumstances, the heat of flue gasses is not sufficient to maintain the necessary level of combustion air preheating in air-preheater. The steam coil with increased heat transfer area is used to fulfil the required air preheating. As a result of decreased heat transfer rate of air-preheater, the fuel mass flow rate to the boiler decreases. Case 2 demonstrates the highest decrease in fuel consumption among the integration cases: a 7.5% increase in fuel economy for the 300 °C torrefaction temperature in comparison with the non-integrated case. Case 3 achieves a 6.1% increase in fuel economy at the same conditions. Cases 1, 4, 5 and 6 exhibit virtually identical numbers within the studied temperature range (from 0.2% at the lowest temperature level to 5.4% increase in fuel economy at the highest temperature).

With regard to Plant B, the solid fuel consumption for all integration cases is higher in comparison with the design case (Fig. 10(b)). Similarly to integration options for Plant A, Cases 2 and 3, where heat from flue gasses is captured to torrefaction, behave noticeably differently from the other cases. Maintaining the combustion air temperature at the required level in these two cases leads to increased steam mass flow through the steam coil. As a result, mass flow of live steam and boiler fuel to produce it also increase. At the lowest temperature level, Cases 1, 4, 5 and 6 have fuel consumption that is 12% – 17% higher than the design values, and the fuel consumption gets relatively close to the design case consumption at 300 °C. Whereas cases 2 and 3 have an average increase of 38.1% and 46.1% respectively.

Power generation for both plants varies slightly with torrefaction temperature. The way of integration, however, has a rather strong effect. Averaged over the temperature range, the net power output at different integration cases for both plants is presented in Fig. 11. The power production of the larger Plant A is reduced when torrefaction is introduced, since the torrefaction heat demand either decreases steam production, or some of the generated steam needs to be extracted before expansion to condenser pressure. Heat that is taken from the boiler for torrefaction reduces the live steam mass flow to the turbine in Cases 1, 2 and 3, and as a consequence, electricity output is decreased: respectively 9.4%, 11% and 10%, compared to electricity production in the non-integrated plant. Another factor is the necessary level of air preheating that needs to be maintained by the steam coil in Cases 2 and 3. Higher consumption of steam results in a bigger loss of net power output for these two cases. In Cases 4 and 5, the boiler steam production is relatively close to the design value, and steam energy from the final expansion to condenser pressure is only lost due to torrefaction. Therefore, the reduction in power output is lowest in these two cases: correspondingly, 3.2% and 1.1% lower in comparison with the base Case 0.

A quite different situation is observed with the smaller Plant B integration options. The available free capacity of the boiler allows increase in power output for almost all integration cases. In order to fulfil the higher demand for steam mass flow to air preheating, steam mass flow through the turbine and, as a result, net electricity output increase significantly in Cases 2 and 3 (43.4% and 50.7% more than in the design case). In Case 6, meeting the heat demand of the dryer and torrefier with high pressure steam results in a loss of generation power. For this reason, the net power output for this case is 5.1% lower than the design value.

The impact of the chosen integration scheme and torrefaction temperature on trigeneration efficiency (Eq. (13)) is presented in Fig. 12. The amount of low-value heat that is produced and basically lost in the condenser decreases in Plant A quite significantly in all integration cases in comparison with the design case. As a

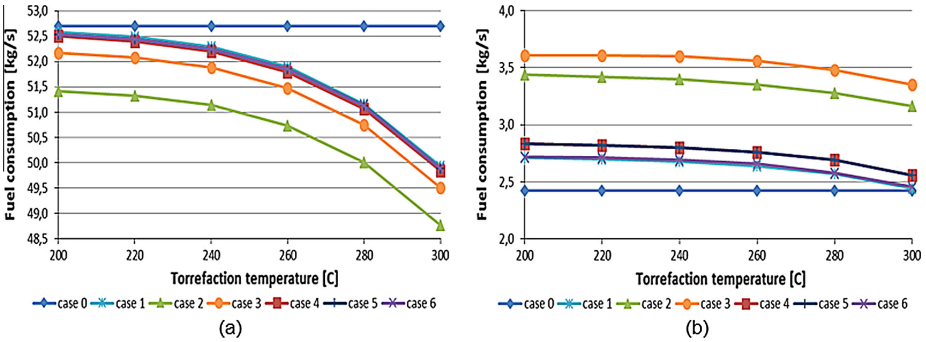

Fig. 10. Solid fuel consumption for Plant A (a) and Plant B (b) integration cases.

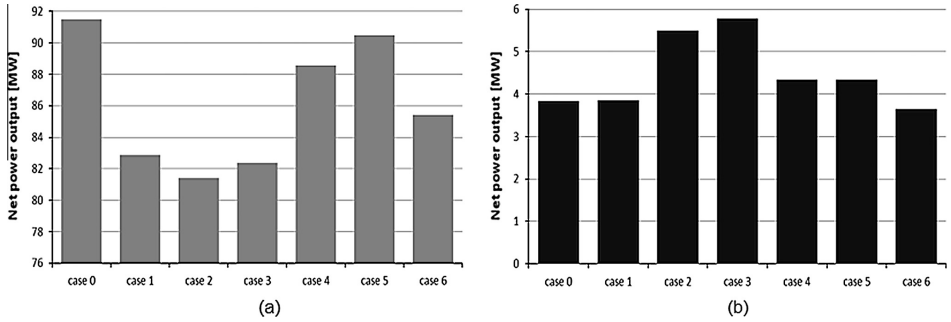

Fig. 11. Net power output averaged over torrefaction temperature range (200–300 °C) for Plant A (a) and Plant B (b) integration cases.

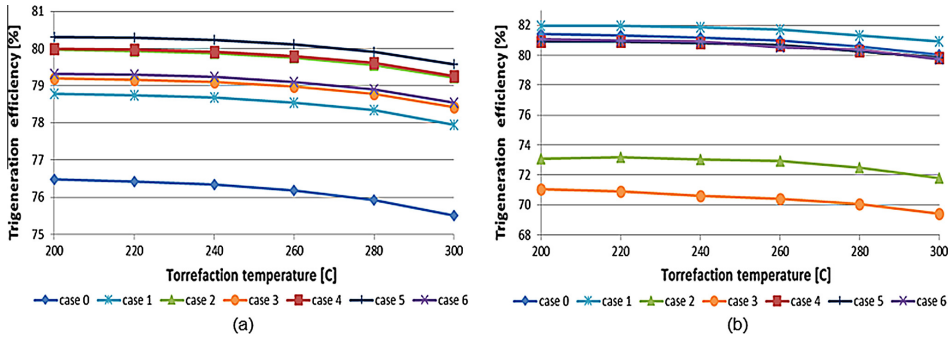

Fig. 12. Trigeneration efficiency for Plant A (a) and Plant B (b) integration cases calculated with Eq. (14).

consequence of the reduction of this loss in the overall plant balance, the trigeneration efficiency for all integration options is notably higher than in Case 0 (Fig. 12(a)). However, with the considerable decrease of torrefied fuel mass flow at high temperatures, trigeneration efficiency curves for all cases slope downwards. Of the integration options studied, Case 5 has the highest efficiency: on average 5.2% higher than the design case.

In Plant B, the impact of the increased fuel mass flow exceeds the effect of greater power generation; as a consequence, the trigeneration efficiency for most of the cases is lower than for the reference Case 0 (Fig. 12 (b)). The efficiency changes within a relatively narrow range close to the design level for most of the cases studied (from 0.4% loss on average for Cases 4, 5 and 6 to 0.9% increase for Case 1). For Cases 2 and 3, the increased amount of

steam for air preheating leads to higher steam mass flow through the turbine. Since this would increase the district heat production above the specified 12 MW, an auxiliary cooler to dump the excess heat from the DH network needed to be utilized in these cases. As a consequence of this additional heat loss in the energy balance of the plant, the lowest values for trigeneration efficiency are found in Cases 2 and 3: 9.7% and 12.2% lower than in the design case.

4. Conclusions

In order to investigate the effect of torrefaction process on power plant cycle, a torrefaction model was developed and then integrated with models of two different-sized CHP plants. The first plant represented a typical large-scale plant operated at full boiler load, while the second model was a smaller backpressure plant operated mostly at a reduced district heating load. Six integration concepts were implemented for both plants and the performance of the integrated plants was evaluated within the typical range of torrefaction temperatures.

The operation assumptions used in this work led to quite different results for the studied integration options. With the larger plant, maintaining maximum boiler output and simultaneous co-firing of torrefaction gas decreases fuel consumption and power output with torrefaction temperature increase. As for the smaller boiler at partial load operation, the fuel consumption was somewhat higher than in the design case, while increased steam flow led to additional electricity output. The efficiency of the feedstock conversion into useful energy streams (trigeneration efficiency) is determined mostly by the type of integration and differs only slightly with torrefaction temperature. The trigeneration efficiency for all integration options with the first plant is higher than for the non-integrated case. As for the second plant, the effect of the integration is relatively low for most of the studied cases. For both plants, the integration cases that used the heat of flue gases for torrefaction performed quite differently than the other studied scenarios: capture of a certain amount of heat from flue gases resulted in additional consumption of steam for the combustion air preheating.

The results of the simulations indicate the diverse effect of the various integration scenarios on the performance of CHP plants operated under different regimes. As expected, torrefaction parameters have an effect on integration performance: at higher torrefaction temperatures, a larger share of fuel can be substituted with torrefaction gas. Based on the analysis presented in this study, it can be concluded that the potential of integration of torrefaction with a cogeneration plant is highly dependent on the operation characteristics of both the CHP plant and the torrefaction process and each particular case requires individual evaluation from the point of view of both reduction in fuel consumption and additional cost analysis.

References

[1] Van der Stelt M, Gerhauser H, Kiel JHA, Ptasinski KJ. Biomass upgrading by torrefaction for the production of biofuels: A review. Biomass Bioenerg 2011;35:3748–62. http://dx.doi.org/10.1016/j.biombioe.2011.06.023.

[2] Verhoeff F, Adell A, Boersma AR, Pels JR, Lensselink J, Kiel JHA, et al. TorTech: Torrefaction as key technology for the production of (solid) fuels from biomass and waste. ECN Biomass, Coal and Environmental Research, Report ECN-E-11-039; 2011.

[3] Prins MJ, Ptasinski KJ, Janssen FJ. Torrefaction of wood. Part 2. Analysis of products. J Anal Appl Pyrol 2006;77:35–40. http://dx.doi.org/10.1016/j.jaap.2006.01.001.

[4] Bergman PCA, Boersma AR, Zwart RWR, Kiel JHA. Torrefaction for biomass co-firing in existing coal-fired power stations. ECN, Report ECN-C-05-013, Netherlands; 2005.

[5] Uslu A, Faaij AP, Bergman PCA. Pre-treatment technologies, and their effect on international bioenergy supply chain logistics. Techno-economic evaluation of torrefaction, fast pyrolysis and pelletisation. Energy 2008;33:1206–33. http://dx.doi.org/10.1016/j.energy.2008.03.007.

[6] Pirraglia A, Gonzalez R, Saloni D, Denig J. Technical and economic assessment for the production of torrefied ligno-cellulosic biomass pellets in the US. Energ Convers Manage 2013;66:153–64. http://dx.doi.org/10.1016/j.enconman.2012.09.024.

[7] Cocchi M, Nikolaisen L, Junginger M, Goh CS, Heinimö J, Bradley D. Global Wood Pellet Market Study 2011; IEA Bioenergy.

[8] Lamers P, Junginger M, Hamenlick C, Faaij A. Developments in international solid biofuel trade. An analysis of volumes, policies, and market factors. Renew Sust Energ Rev 2012;16(5):3176–99. http://dx.doi.org/10.1016/j.rser.2012.02.027.

[9] IEA. Technology roadmaps: International Energy Agency (IEA), IEA; 2010.

[10] Directive 2012/27/EU of European Parliament and of the Council. Official Journal of the European Union; 2012, L 315/1.

[11] Biomass co-firing. Technology brief. IEA-ETSAP and IRENA Technology Brief E21; 2013.

[12] Koppejan J, Sokhansanj S, Melin S, Madrali S. Status overview of torrefaction technologies. IEA Bioenergy Task 32 report 2012, Enschede.

[13] Eriksson G, Kjellström B. Assessment of combined heat and power (CHP) integrated with wood-based ethanol production. Appl Energ 2010;87(12):3632–41. http://dx.doi.org/10.1016/j.apenergy.2010.06.012.

[14] Ilic D, Dotzauer E, Trygg L. District heating and ethanol production through polygeneration in Stockholm. Appl Energ 2012;91(1):214–21. http://dx.doi.org/10.1016/j.apenergy.2011.09.030.

[15] Starfelt F, Daianova L, Yan J, Thorin E, Dotzauer E. The impact of lignocellulosic ethanol yields in polygeneration with DH—a case study. Appl Energ 2012;92:791–9. http://dx.doi.org/10.1016/j.apenergy.2011.08.031.

[16] Starfelt F, Thorin E, Dotzauer E, Yan J. Performance evaluation of adding ethanol production into an existing combined heat and power plant. Bioresource Technol 2010;101(2):613–8. http://dx.doi.org/10.1016/j.biortech.2009.07.087.

[17] Zhou W, Yang H, Rissanen M, Nygren B, Yan J. Decrease of energy demand for bioethanol-based polygeneration system through case study. Appl Energ 2012;95:305–11. http://dx.doi.org/10.1016/j.apenergy.2012.02.014.

[18] Brammer J, Bridgewater A. Drying technologies for an integrated gasification bio-energy plant. Renew Sust Energ Rev 1999;3(4):243–89. http://dx.doi.org/10.1016/S1364-0321(99)00008-8.

[19] Difs K, Wetterlund E, Trygg L, Söderström M. Biomass gasification opportunities in a DH system. Biomass Bioenerg 2010;34(5):637–51. http://dx.doi.org/10.1016/j.biombioe.2010.01.007.

[20] Fahlén E, Ahlgren E. Assessment of integration of different biomass gasification alternatives in DH systems. Energy 2009;88(5):2184–95. http://dx.doi.org/10.1016/j.energy.2008.10.018.

[21] Wahlund B, Yan J, Westermark M. A total energy system of fuel upgrading by drying biomass feedstock for cogeneration: a case study of Skellefteå bioenergy combine. Biomass Bioenerg 2002;23(4):271–81. http://dx.doi.org/10.1016/S0961-9534(02)00055-7.

[22] Kohl T, Laukkanen T, Järvinen M, Fogelholm C-J. Energetic and environmental performance of three biomass upgrading processes integrated with a CHP plant. Appl Energ 2013;107:124–34. http://dx.doi.org/10.1016/j.apenergy.2013.02.021.

[23] Håkansson K, Nordin A, Nordwaeger M, Olofsson I, Svanberg M. Process and system integration aspects of biomass torrefaction. In: 18th European biomass conference and exhibition proceedings, Lyon, France; 2010.

[24] Li J, Brzdekiewicz A, Yang W, Blasiak W. Co-firing based on biomass torrefaction in a pulverized coal boiler with aim of 100% fuel switching. Appl Energ 2012;99:344–54. http://dx.doi.org/10.1016/j.apenergy.2012.05.046.

[25] IPSEpro 4.0. © 1997–2015 SimTech GmbH.

[26] Bergman PC, Kiel JH. Torrefaction for biomass upgrading. In: 14th European biomass conference proceedings, Paris, France; 2005.

[27] Prins MJ, Ptasinski KJ, Janssen FJ. Torrefaction of wood. Part 1. Weight loss kinetics. J Anal Appl Pyrol 2006;77:28–34. http://dx.doi.org/10.1016/j.jaap.2006.01.002.

[28] Repellin V, Govin A, Rolland M, Guyonnet R. Modelling anhydrous weight loss of wood chips during torrefaction in a pilot kiln. Biomass Bioenerg 2010;34:602–9. http://dx.doi.org/10.1016/j.biombioe.2010.01.002.

[29] Larsson SH, Rudolfsson M, Nordwaeger M, Olofsson I, Samuelsson R. Effects of moisture content, torrefaction temperature, and die temperature in pilot scale pelletizing of torrefied Norway spruce. Appl Energ 2013;102:827–32. http://dx.doi.org/10.1016/j.apenergy.2012.08.046.

[30] Phanphanich M, Mani S. Impact of torrefaction on the grindability and fuel characteristics of forest biomass. Bioresource Technol 2011;102:1246–53. http://dx.doi.org/10.1016/j.biortech.2010.08.028.

[31] Bridgeman T, Jones J, Shield I, Williams P. Torrefaction of reed canary grass, wheat straw and willow to enhance solid fuel qualities and combustion properties. Fuel 2008;87(6):844–56. http://dx.doi.org/10.1016/j.fuel.2007.05.041.

[32] Pach M, Zanzi R, Björnbom E. Torrefied biomass: A substitute for wood and charcoal. In: 6th Asia–Pacific international symposium on combustion and energy utilization proceedings, Kuala Lumpur; 2002.

[33] Felfli FF, Luengo CA, Suárez JA, Beatón PA. Wood briquette torrefaction. Energy for Sustain Dev 2005;9(3):19–22. http://dx.doi.org/10.1016/S0973-0826(08)60519-0.

[34] Bates RB, Ghoniem AF. Biomass torrefaction: Modelling of reaction thermochemistry. Bioresource Technol 2013;134:331–40. http://dx.doi.org/10.1016/j.biortech.2013.01.158.
[35] Prins MJ, Ptasinski KJ, Janssen FJJG. More efficient biomass gasification via torrefaction. Energy 2006;31(15):3458–70. http://dx.doi.org/10.1016/j.energy.2006.03.008.
[36] Prins MJ. Thermodynamic analysis of biomass gasification and torrefaction [dissertation]. Eindhoven: Technical University of Eindhoven; 2005.
[37] Van der Stelt MJC. Chemistry and reaction kinetics of biowaste torrefaction [dissertation]. Eindhoven: Technical University of Eindhoven; 2011.
[38] Chen W-H, Kuo P-C. Torrefaction and co-torrefaction characterization of hemicellulose, cellulose and lignin as well as torrefaction of some basic constituents in biomass. Energy 2011;36:803–11. http://dx.doi.org/10.1016/j.energy.2010.12.036.
[39] Ohliger A, Förster M, Kneer R. Torrefaction of beechwood: a parametric study including heat of reaction and grindability. Fuel 2013;104:607–13. http://dx.doi.org/10.1016/j.fuel.2012.06.112.
[40] Peduzzi E, Boissonnet G, Haarlemmer G, Dupont X, Marechal F. Torrefaction modelling for lignocellulosic biomass conversion processes. Energy 2014. http://dx.doi.org/10.1016/j.energy.2014.03.086.
[41] Basu P, Sadhukhan AK, Gupta P, Rao S, Dhungana A, Acharya B. An experimental and theoretical investigation on torrefaction of a large wet wood particle. Bioresource Technol 2014;159:215–22. http://dx.doi.org/10.1016/j.biortech.2014.02.105.
[42] Medic D, Darr M, Shah A, Rahn S. The effects of particle size, different corn stover components, and gas residence time on torrefaction of corn stover. Energies 2012;5:1199–214. http://dx.doi.org/10.3390/en5041199.
[43] Kokko L. A method for finding suitable particle sizes for thermal conversion processes by using a simulation tool focusing on wood particle heat transfer and chemical kinetics [dissertation]. Tampere: Tampere University of Technology; 2014.
[44] Arpiainen V, Wilén C. Report on optimisation opportunities by integrating torrefaction into existing industries. Deliverable No. D3.2, Production of Solid Sustainable Energy Carriers from Biomass by Means of Torrefaction. SECTOR project, EU 7th Framework Programme; 2014.
[45] Fagernäs L, Brammer J, Wilén C, Lauer M, Verhoeff F. Drying of biomass for second generation synfuel production. Biomass Bioenerg 2010;34(9):1267–77. http://dx.doi.org/10.1016/j.biombioe.2010.04.005.
[46] Thunman H, Niklasson F, Johnsson F, Leckner B. Composition of Volatile Gases and Thermochemical Properties of Wood for Modeling of Fixed or Fluidized Beds. Energ Fuel 2001;15:1488–97. http://dx.doi.org/10.1021/ef010097q.
[47] Dupont C, Chiriac R, Guillaume G, Toche F. Heat capacity measurements of various biomass types and pyrolysis residues. Fuel 2014;115:644–51. http://dx.doi.org/10.1016/j.fuel.2013.07.086.
[48] Goss WP, Miller RG. Thermal properties of wood and wood products. In: Proceedings of thermal performance of the exterior envelopes of buildings, V: 193–203, Atlanta, GA: ASHRAE; 1992.
[49] TenWolde A, McNatt JD, Krahn L. Thermal properties of wood panel products for use in buildings. USDA Forest Products Laboratory, DOE/USDA-21697/1; Madison, USA; 1988.
[50] Ragland KW, Aerts DJ. Properties of wood for combustion analysis. Bioresource Technol 1991;37:161–8.
[51] Skaar C. Wood–water relations. Berlin, Germany: Springer-Verlag; 1988.
[52] Koch P. Specific heat of oven dry spruce, pine wood and bark. Wood Sci 1969;1:203–14.
[53] Gupta M, Yang J, Roy C. Specific heat and thermal conductivity of softwood bark and softwood char particles. Fuel 2003;82:919–27. http://dx.doi.org/10.1016/S0016-2361(02)00398-8.
[54] Harada T, Hata T, Ishihara S. Thermal constants of wood during the heating process measured with the laser flash method. J Wood Sci 1998;44(6):425–31.
[55] Ikonen O. Biomvoimalaitoksen energiatehokkuuden parantaminen ja osakuorma-ajon optimointi [master's thesis]. Lappeenranta: Lappeenranta University of Technology; 2013. Finnish.
[56] Komulainen S. Voimalaitoksen käytönaikaisen optimoinnin määrittely [master's thesis]. Lappeenranta: Lappeenranta University of Technology; 2012. Finnish.
[57] Alakangas E., 2000. Suomessa käytettävien polttoaineiden ominaisuuksia., VTT tiedotteita 2045. VTT Energia, Valtion Teknillinen Tutkimuskeskus, Espoo; 2000. <http://www.vtt.fi/inf/pdf/tiedotteet/2000/T2045.pdf> [accessed 15.04.14].
[58] Basu P. Combustion and gasification in fluidized beds. CRC Press; 2006.

Publication IV

Saari, J., Kuparinen, K., Sermyagina, E., Vakkilainen, E., Kaikko, J. and Sergeev V.
The effect of integration method and carbonization temperature on the performance of an integrated hydrothermal carbonization and CHP plant.

Submitted in 2017 to *BioResources*

Publication V

Saari, J., Sermyagina, E., Vakkilainen, E., Kaikko, J. and Sergeev V.
Integration of hydrothermal carbonization and a CHP plant: Part 2 - operational and economic analysis

Reprinted with permission from
Energy
Vol. 113, pp.574-585, 2016

Energy 113 (2016) 574–585

Contents lists available at ScienceDirect

Energy

journal homepage: www.elsevier.com/locate/energy

Integration of hydrothermal carbonization and a CHP plant: Part 2 —operational and economic analysis

Jussi Saari [a, *], Ekaterina Sermyagina [a], Juha Kaikko [a], Esa Vakkilainen [a], Vitaly Sergeev [b]

[a] Lappeenranta University of Technology, P.O. Box 20, FI-53851 Lappeenranta, Finland
[b] Peter the Great Saint Petersburg State Polytechnical University, 29, Polytechnicheskaya st., 195251, St. Petersburg, Russia

ARTICLE INFO

Article history:
Received 19 January 2016
Received in revised form
13 June 2016
Accepted 20 June 2016

Keywords:
HTC
Biomass
Modelling
Integration
CHP

ABSTRACT

Wood-fired combined heat and power (CHP) plants are a proven technology for producing domestic, carbon-neutral heat and power in Nordic countries. One drawback of CHP plants is the low capacity factors due to varying heat loads. In the current economic environment, uncertainty over energy prices creates also uncertainty over investment profitability. Hydrothermal carbonization (HTC) is a promising thermochemical conversion technology for producing an improved, more versatile wood-based fuel. Integrating HTC with a CHP plant allows simplifying the HTC process and extending the CHP plant operating time. An integrated polygeneration plant producing three energy products is also less sensitive to price changes in any one product. This study compares three integration cases chosen from the previous paper, and the case of separate stand-alone plants. The best economic performance is obtained using pressurized hot water from the CHP plant boiler drum as HTC process water. This has the poorest efficiency, but allows the greatest cost reduction in the HTC process and longest CHP plant operating time. The result demonstrates the suitability of CHP plants for integration with a HTC process, and the importance of economic and operational analysis considering annual load variations in sufficient detail.

1. Introduction

Biomass-fired combined heat and power (CHP) production using local wood sources is a strategy that combines carbon-neutral energy source with supply security and dispatchability. The main weaknesses with wood-based heat and power production are related to the limitations of untreated wood as fuel - low energy density, degradation in storage, and infeasibility for replacing fossil fuels in many existing plants. Often the low capacity factor of a CHP plant due to the significant annual variation of heat demand also has a detrimental effect on profitability.

Several technologies exist for converting raw biomass to better-quality fuels that can be more easily transported and stored. These high value bioproducts are more versatile fuels for various combustion technologies, including liquid fuels for traffic use. Depending on the biofuel and the scenario, the economic profitability of many of the biomass conversion technologies may currently depend on public subsidies. As the conversion processes typically require additional heat input and produce waste heat streams, process integration can sometimes yield benefits either by improving the overall energy efficiency or reducing the investment cost.

Numerous studies have investigated the integration of biomass conversion with power generation, CHP and other processes. Starfelt et al. showed that integrating ethanol production with a heat and power plant yields a clear improvement of efficiency, with less biomass used for a given amount of district heat (DH), power and ethanol in comparison to stand-alone plants [1]. In a later study the economic benefits of integration, attributed mainly to increased power production and extended operating time, were shown [2].

Co-generation of sugar, ethanol and electricity was shown to improve thermodynamic performance over stand-alone plants through decreasing the exergy destruction [3], and by heat integration of the processes, water and process steam consumption can be reduced [4]. Fahlen and Ahlgren [5] found integration of gasification with natural gas combined cycle CHP production economical under some scenarios. Integration of pelletization [6] and torrefaction [7] with CHP production have also been shown to yield energy efficiency benefits. Efficiency benefits were shown also in the integration of torrefaction with a large coal-fired CHP plant for the purpose of partial or complete fossil coal replacement in the

* Corresponding author.
E-mail address: Jussi.Saari@lut.fi (J. Saari).

http://dx.doi.org/10.1016/j.energy.2016.06.102
0360-5442/

boiler [8].

In northern European context, CHP plants are often backpressure steam plants. As heat load varies seasonally over the year, the annual operating time and power production of such plants is limited. Integration with a biomass conversion process has been shown to yield benefits in terms of increased operating time and higher power production during this period. Extending the annual operating time increases the capacity factors and incoming cash flow, thus increasing the value of the investment. This was found to be the case with ethanol production [1], pelletization and torrefaction [9], and biomass fast pyrolysis [10].

In this study the integration of hydrothermal carbonization (HTC) and a small-scale biomass-fired backpressure CHP plant is studied. HTC is a mild pyrolysis process similar to torrefaction. The biomass is typically mixed with liquid water to form a slurry, and heated to a temperature of 180–250 °C at saturated-state pressure. Compared to torrefaction, HTC achieves similar pyrolysis severity at a lower temperature. Using vapour instead of liquid water has also been studied, resulting in less severe carbonization than with liquid water when using otherwise similar parameters and the feedstock [11]. Possible feedstocks include various waste streams such as municipal and paper industry sludges [12], bark [13], corn husks [11] or weed plants [14] as well as woody biomass [15].

The published studies of HTC and CHP integration have so far been limited. An integration concept aiming at simplifying the HTC process was published by Erlach et al. first in [16]. This was later compared with two additional ones in [17]: a minimum-change integration where the only change to the stand-alone HTC process was using extraction steam from the CHP plant as a heat source, and one where the simplified process was further improved with a superheated steam drier for improved efficiency. While these integration studies did not reveal possibilities for significant efficiency improvements, they did show a potential for significant reduction in complexity, translating to reduced investment costs and likely improved operability as well. A wider variety of integration schemes were studied and compared on technical merits at full and low load in Part 1 of this study [18], yielding similar conclusions: while simplification of the HTC process is possible by integrating it with a CHP plant, a significant efficiency improvement is not.

None of the aforementioned studies investigated the plant operation throughout the annual variation of load and operating conditions in detail. As load variation is significant for CHP plants producing district heat (DH) in Nordic countries, this is an important topic for proper economic evaluation of plant configurations. In this study a discretized multi-period model of the annual variation of the DH load, fuel quality and ambient conditions is used. Multiperiod DH load approximation has been used in a number of earlier studies investigating CHP plants [19] or their integration with pelletization and torrefaction [9] or fast pyrolysis [10]. Of the seven concepts introduced in Part 1 of this study [18] – six integrated concepts and the case of separate stand-alone plants – three were ruled out as problematic or clearly inferior. The remaining four are evaluated here in terms of operability and economic performance.

A particular concern for the profitability of any energy sector investment in the current situation is the significant uncertainty over future energy prices, emission trading, as well as subsidies and taxes. As such, without subsidies or significantly increased CO_2 emission cost through taxation or emission trading, biochar is currently not a competitive alternative to coal. Electricity markets in the Northern Europe are at a period of change where uncertainty over renewable power subsidies and the future of nuclear power create serious doubts about the price of electricity. Using different scenarios for investment cost and electricity prices, the four different plant concepts are compared in terms of net present value (NPV), internal rate of return (IRR), and payback period (PBP). A sensitivity analysis is performed.

Preliminary studies often evaluate plant concepts at few loads. Then they are compared and using some criteria the promising ones are chosen for further study. In this paper this kind of ranking is compared to full economic ranking where operational characteristics at a large enough number of load points for good coverage are taken into account.

2. Studied cases

The economics of integrating a small-scale CHP plant and HTC process, and operation under different loads and conditions are considered. The CHP plant, as described in Part 1 of the study [18] and summarized in Table 1, is a wood chip fired back pressure plant with minimum and maximum district heat (DH) loads of 8 MW–20 MW, and a net electrical output of 8 MW_{el} at full load. The main characteristics of the plant are listed in Table 1.

Four different HTC and CHP plant concepts were considered, all of which are designed for hydrochar production of 5 tons per hour, or 1.39 kg/s. Case 0 is the reference case where both plants operate separately in stand-alone mode. The feed slurry is pressurized and pre-heated in stages before the HTC reactor with flash vapour from product slurry depressurization. For final heating to reactor temperature the stand-alone HTC plant has a grate-fired boiler of 5 MW design-point output, producing 30 bar steam at approximately 350 °C temperature. The LHV-based boiler efficiency at design point is 82%.

Before thermal dryer the product slurry is mechanically dewatered. The liquid from dewatering is mostly recirculated back to the process feed. The dryer is operated with low-pressure flash vapour from the product slurry cooling and depressurization, and hot waste water from the mechanical dewatering.

Three integration concepts were considered; Case 1, Case 5 and Case 6 of Part 1 of the study. Case 1 is the minimum-change variant from the basic stand-alone HTC process. The only difference between this and Case 0 is the replacement of the stoker boiler with the use of live steam from the BFB boiler of the CHP plant, throttled to 30 bar and cooled to 350 °C with feedwater injection.

Cases 5 and 6 are similar processes, representing more significant simplifications of the HTC process. Case 5 utilizes a mixture of feedwater and drum water to supply the water and heat necessary to reach the desired HTC reactor state. This eliminates the need for feed slurry heating, but also the sink where most heat from product slurry cooling is recovered in Case 0 and Case 1. In Case 5 the available heat is recovered by using the flash vapour in an additional low-pressure feedwater heater in the CHP plant, and cooling the hot water from dewatering by heating the process makeup water in a heat recovery heat exchanger. Case 5 is an entirely once-through process without water recirculation, which increases the waste water and makeup water flows significantly. The energy efficiency is also somewhat inferior to Case 0 and Case 1. Case 6 is similar to Case 5, but with limited HTC process water recirculation, allowing both more efficient heat recovery and reduced waste

Table 1
CHP plant main characteristics at full and minimum load.

Parameter	Full load	Minimum load
Net power output	8.0 MW	2.0 MW
District heat output	20.0 MW	8.0 MW
Total (CHP) Efficiency	85%	83%
Live steam parameters	90 bar/500 °C	90 bar/450 °C
Furnace temperature	900 °C	700 °C

water flow.

It is evident that co-locating CHP and HTC processes at the same site will have benefits particularly for wood chip logistics, storage and handling even if the processes themselves would not be integrated. The aim of this study is thus only to investigate the possible benefits obtained from the heat integration of the two processes.

CHP plants in DH production are base load plants, in Finland typically sized for producing approximately 40–60% of peak DH load and able to operate down to approximately 40–50% part load [20]. Typical district heat load duration curves vary significantly from country to country depending on climate. Also the types of heat consumers in the DH network also affect the load curve shape. In Northern Europe there is a fairly short period of peak winter load, minimum summer load being usually 10% or less of the peak winter load [20]. Year-to-year variation can be significant due to varying weather, and in the future the uncertainties related to climate change effects may increase this even more.

Typically the base load CHP plant heat production should amount to at least 4000 … 5000 annual full load hours, usually the equivalent of approximately 80% of the total annual heat consumption [20]. When the district heat load exceeds the maximum capacity of the CHP plant, or is less than the minimum load, auxiliary hot water boilers are used to provide heat. These are typically cheaper boilers burning more easily combusted fuels, such as pellets, light oil, or natural gas.

In this study a simple linear approximation of DH load curve was used to represent what was considered a typical Finnish DH load curve of a small municipality, with 35 MW peak winter load and 2.6 MW summer minimum load. This corresponds to total annual operating time of 6000 h, 1800 h of which are at full load, for the considered CHP plant. The annual DH production amounts to 4740 full-load hours.

2.1. Multi-period model

To consider the annual variation of DH load, ambient conditions and fuel properties, a multi-period model was implemented. A DH load duration curve was approximated by a peak load of 35 MW, 20 MW heat load at 1800 h, linear reduction to 2.6 MW at 7890 h, and finally steady 2.6 MW load for the remaining summer hours. This was represented by two full-load periods, P1 and P2, followed by steadily reducing DH load at 4 MW intervals (P3 to P6) until the summer period, which was split to a low-load P7 and minimum-load P8 (see Fig. 1).

Wood chip moisture was assumed to increase towards the winter. Temperature of boiler fuel and HTC feedstock was set at the average ambient temperature of each period. The combustion air temperature, taken from the boiler room, was assumed to be 20 °C higher than ambient temperature. The ambient temperatures are based on 30-year monthly average temperatures gathered by the Finnish Meteorological Institute [21] for Jyväskylä, a city in central Finland. District heating water output and return temperatures were based on ambient temperature according to [20]. Data for fuel properties and temperature levels for each period is listed in Table 2; the load curve approximation, and the multiperiod approximation of heat and power production are plotted on Fig. 2.

3. Plant operation and control

3.1. HTC plant

Part-load control must ensure maintaining the plant operating parameters within allowable limits. The HTC plant is simpler than the CHP plant and has fewer limitations. As the cases differ significantly, so do the operational limits. An important factor in the stand-alone process of Case 0 and it's minimum-change integrated equivalent Case 1 is ensuring that the slurry is kept from boiling at the vapour injections, and saturated conditions are avoided at pumps. A 5 °C margin to boiling point is maintained at the slurry heating line before the HTC reactor.

The amount of waste water produced as well as the slurry water that would need to be separated past the HTC reactor can also be problematic; this is a factor particularly in cases 5 and 6. To ensure that the piping, pumps and waste water handling equipment remain reasonable, a maximum capacity of 40 tons per hour of waste water flow rate was assumed for all cases.

3.2. CHP plant

The main parameters which can become boundaries to the CHP plant operation are listed in Table 3. The operating strategies are aimed at maximizing electricity production at any given load and, together with the HTC plant operation, for maximizing the operating period of the CHP plant. Hydrochar and heat production take priority over power production when full-rate output of all three is not possible. Although particularly with the integrated cases maximizing power production sometimes results in slightly different operation than maximizing the overall CHP efficiency, even at the low electricity price scenarios the fuel cost saving from efficiency maximization is insufficient to compensate for the income loss from reduced net power output.

Fig. 3 depicts the changes of selected significant plant operating parameters as functions of cumulative time in the heat load duration curve. Sub-figures (a) and (b) show the variation of boiler power fuel power (LHV input) and condenser pressure together with the district heat load and output temperature. Condenser pressure is not significantly affected by the integration concept as the variation of steam enthalpy at turbine exhaust is small enough to yield only a negligible effect. Boiler fuel input is increased in the integrated cases, however; the increase is slight at full load, but more significant at part loads, and leads to an increase of 1000–2000 h of annual operating time.

At full district heat load the stand-alone CHP plant has little capacity to increase boiler load. This small increase potential is used in the integrated cases at full and nearly full load. The boiler is then limited by flue gas flow rate (Fig. 3c). The maximum furnace temperature of 950 °C is approached, but not exceeded, in the integrated cases at 18 MW district heat production. At this load point the fuel moisture is assumed to reduce to 50% from the winter-time maximum of 55%, which yields the highest boiler fuel load and furnace temperature. Drum pressure does not approach it's maximum limit (Fig. 3f).

At 20 MW district heat load, HTC heat demand is enough that at boiler maximum continuous load steam flow to the turbine is significantly reduced; to maintain 20 MW heat output, a large fraction of steam is directed past the turbine through a reduction valve, desuperheated to saturated state with feedwater spraying, and routed to the DH condenser. Steam flow to the turbine is approximately halved as a result (Fig. 3d). As flow rate to the turbine is reduced at full load, HP turbine exhaust pressure and deaerator pressure reduce also in all cases (Fig. 3e and g). Flue gas stack temperatures are somewhat elevated from their design point value of 150 °C to approximately 160 °C at maximum boiler load, which slightly reduces the plant total efficiency.

As load and thus flue gas flow rate are reduced, the boiler heat transfer coefficients are reduced as well but relatively less than the gas flow rate, resulting in decreasing flue gas temperatures in the boiler. Full steam superheat can be maintained to load point P4 (14 MW DH load) in the stand-alone Case 0, or to P5 (10 MW DH) in Case 1 by reducing spraying in the superheater, but at low loads

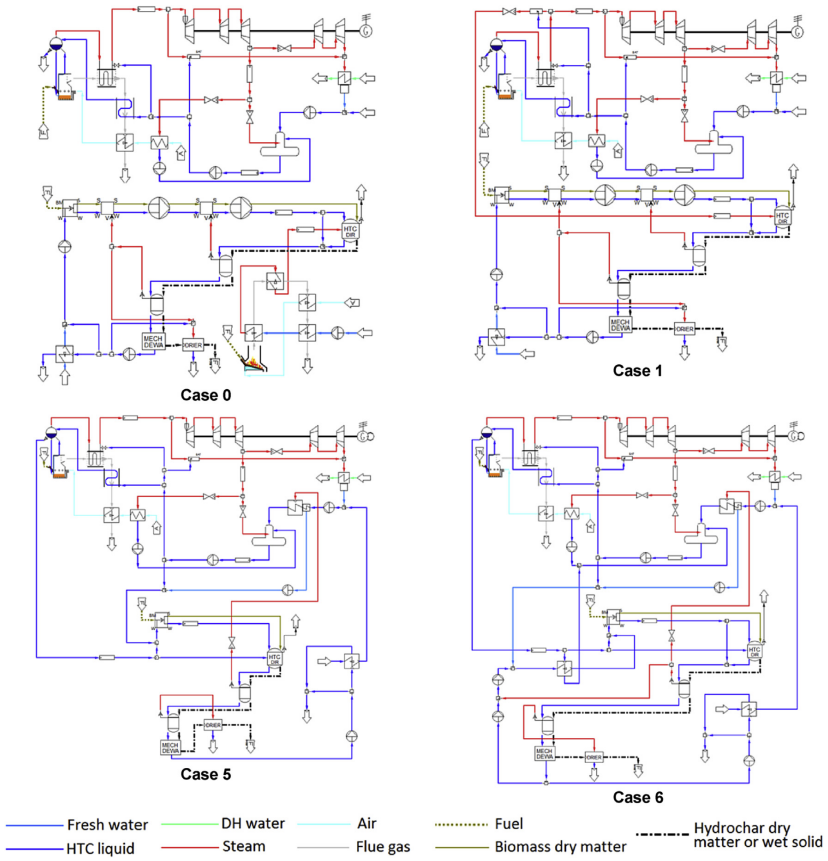

Fig. 1. Process flow diagrams of the stand-alone (Case 0) and the three integrates (Cases 1, 5 and 6).

Table 2
Summary of the load points and their duration during the year in the multi-period model.

Parameter	P0	P1	P2	P3	P4	P5	P6	P7	P8
Time									
period duration [h]	0	240	1560	1400	1400	1400	1400	490	870
cumulative at end [h	0	240	1800	3200	4600	6000	7400	7890	8760
Load and production									
mean heat load [MW]	35	30	22.5	18	14	10	6	4	2.6
CHP heat output [MW]	20	20	20	18	14	10	6	0	0
Temperatures									
ambient [°C]	−20	−10	−5	0	5	10	12	15	15
makeup water [°C]	5	5	5	5	10	10	10	10	10
DH water out [°C]	105	90	85	80	75	75	75	75	75
DH water return [°C]	60	50	50	50	45	45	45	45	45
Fuel									
moisture [$m_{H2O}/m_{dry+H2O}$]	0.55	0.55	0.55	0.50	0.50	0.45	0.45	0.40	0.40
temperature [°C]	−20	−10	−5	0	5	10	12	15	15
LHV [MJ/kg]	7.43	7.43	7.43	8.53	8.53	9.62	9.62	10.72	10.72

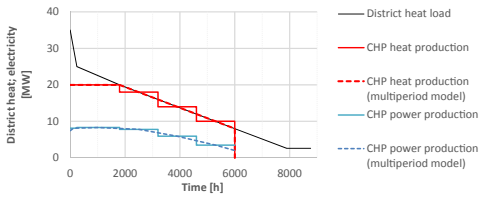

Fig. 2. Annual variation of the DH load, and CHP plant production of district heat and electricity.

steam temperature at turbine inlet is inevitably reduced in both cases. Full live steam superheat can, however, be maintained down to minimum boiler load in both Case 5 and Case 6. In these cases the HTC heating is taken from the drum as liquid, necessitating a high feedwater flow rate (Fig 3e). Since the fraction thermal load extracted from flue gas in the superheater is reduced relatively more than the total boiler load reduces as DH load is reduced but the HTC heat load remains relatively unchanged, maintaining 500 °C live steam temperature becomes possible in these cases.

At low enough load flue gas temperatures begin to approach the minimum limits of 135 °C stack temperature and 700 °C furnace temperature. Stack temperature is maintained at first by using the SCAH for preheating the air before the luvo from approximately 10 MW DH load downwards. Due to the combination of increasing heating need in SCAH and reducing pressure levels in the turbine, at load point P6 (8 MW DH) the LPT valve is used to maintain sufficient steam pressure at HPT exhaust to keeping the stack temperature at 135 °C. At a slightly lower DH load the same has to be done also with the integrated cases. Minimum operating point of 8 MW district heat output (40% DH load) is reached when furnace temperature reaches 700 °C at 6000 h of cumulative operating time.

With the integrated cases 5 and 6 an additional restriction at low loads is the reducing main condensate flow as the flow from the DH condenser reduces. Waste heat from HTC flash vapour is recovered to the condensate stream in a low pressure feed preheater (LPPH), but unlike the condensate flow, the flash vapour flow rate varies little between different load points. The significant HTC feedwater flow is also part of the main condensate in these cases, increasing the flow, but as DH power is reduced towards the minimum, boiling would still occur before the deaerator unless measures are taken to prevent this. Boiling is prevented by a combination of two means. Firstly, increasing deaerator pressure allows a higher condensate temperature. Secondly, by bypassing some of the HTC waste water past the heat recovery heat exchanger (HRX), the condensate entering the LPPH can be made colder, enabling more heat to be absorbed before reaching saturated state.

Increasing the deaerator pressure reduces power production slightly, but has little effect on plant losses or efficiency. The method is limited by the maximum deaerator pressure, and the ability to heat the main condensate stream only to the saturation temperature of the flash vapour, however. Bypassing part of the HTC wastewater past the HRX allows decreasing the DH output further in the CHP process, but at the cost of increased losses and reduced efficiency. As the heat recovery bypass allows a longer period of HTC operation and DH production to smaller loads, it is still economical to do so.

4. Annual production and consumption

The annual output and consumption rates of energy products was obtained with the multi-period approximation of annual production. The discretized variation of boiler fuel consumption (including the stoker boiler in Case 0) and DH and net power output are plotted in Fig. 4, together with the DH heat demand curve. The hydrochar output remains constant at 32.4 MW_{LHV} throughout the HTC operating period: 8000 h in Case 0, and the same as CHP operating time in the integrated cases. The HTC feedstock rate increases from 35.2 to 38.0 MW_{LHV} as the wood moisture reduces from winter 55% to summer 40%.

Table 4 shows the total annual net production and consumption figures. Electricity is separated to sold and purchased for the purposes of economic analysis, because these have a different price. The total efficiency of the polygeneration plant is also calculated and listed on Table 4. These are obtained in both LHV and HHV terms from net annual energy production of electricity $E_{el,net}$, district heat Q_{DH} and hydrochar Q_{hc}, and the wood chip input in boiler fuel Q_f and HTC feedstock Q_{feed}:

$$\eta_{LHV} = \frac{E_{el,net} + Q_{DH} + Q_{hc,LHV}}{Q_{feed,LHV} + Q_{f,LHV}}, \quad (1)$$

$$\eta_{HHV} = \frac{E_{el,net} + Q_{DH} + Q_{hc,HHV}}{Q_{feed,HHV} + Q_{f,HHV}}. \quad (2)$$

The stand-alone CHP process has a higher efficiency than the stand-alone HTC process in LHV terms, but as the HTC feedstock is not burnt, the water latent heat loss decreases, resulting in nearly the same HHV efficiencies for both. The differences in efficiencies between the integrated processes are relatively small, with figures mostly between those of CHP and HTC stand-alone processes as could be expected. Case 1 with the more complex HTC heat recovery scheme of the stand-alone process is the most efficient, in HHV terms more so than either stand-alone process. The good HHV efficiency is explained by extending the operation of the CHP process towards the low-moisture periods, where latent heat losses are reduced. The same reason explains why Case 5, the process with lowest LHV efficiency but longest operating time, is less behind the other processes in HHV efficiency than in LHV efficiency.

The relative fractions of annual outgoing energy flows from the process are shown in Fig. 5. The blue-green tones represent products, losses are shown in yellow-red tones. Here, too, the results are

Table 3
Off-design operating limits for the CHP plant.

Parameter	Design	min	max	Limitations
Flue gas flow rate $\dot{m}_{FG}$ [kg/s]	17.50		19.5	Fan capacity, tube bank vibration and erosion
Furnace temperature T_{furn} [°C]	904	700	950	Combustion; ash melting and agglomeration
Flue gas stack temperature T_{stack} [°C]	150	135		Flue gas condensation
Turbine inlet steam flow rate $\dot{m}_{t,in}$ [kg/s]	10.60	2.0	12.0	Output at minimal flow; swallowing capacity
Drum pressure p_D [bar]	100		110	Pressure vessel strength
Deaerator pressure p_{DA} [bar]	5.6	3.0	8.0	Steam velocity; pressure vessel strength

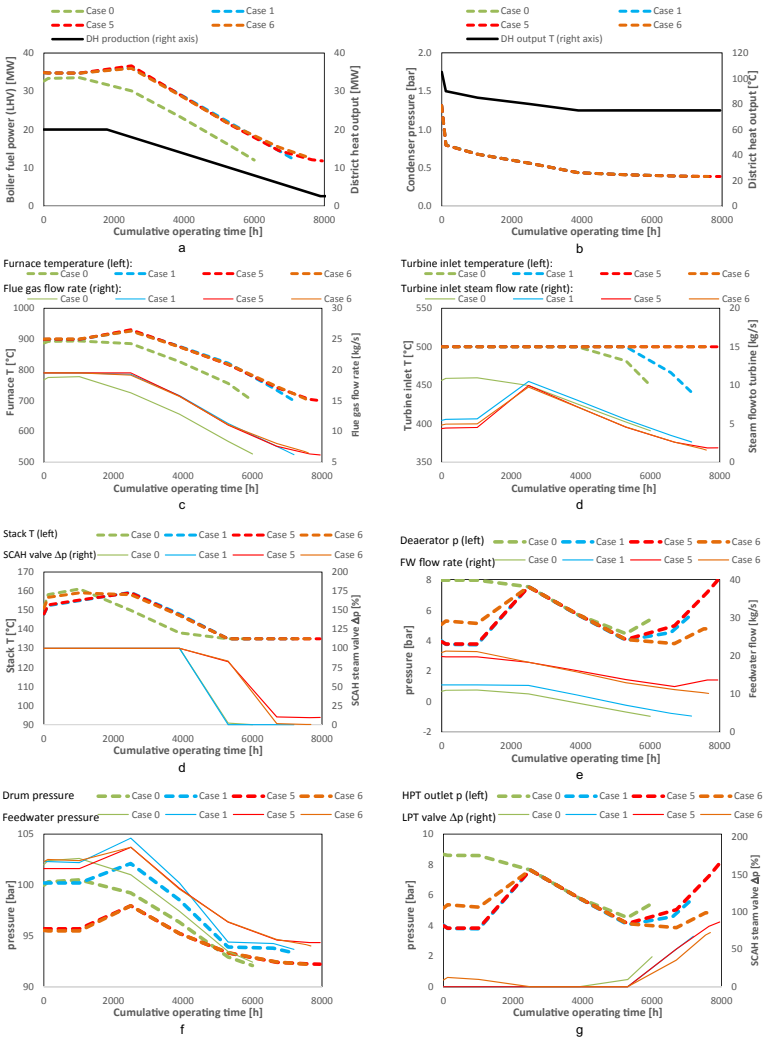

Fig. 3. Plant operating parameters as functions of cumulative time in the heat load duration curve.

broadly similar between the different cases. Among losses, the largest is the loss of HTC feedstock heating value into liquid and gas fractions, followed by dewatering and drying loss and boiler loss. Dewatering and drying loss consists only of losses in dewatering and storage, and the difference of thermal drier heat consumption and the latent heat of evaporated water: the heat of evaporation in thermal dryer is not considered a loss, as this heat is fully recovered in the increase of solid product LHV.

While a fairly small fraction of the total, the heat loss with the waste water is noticeably larger in Case 5, resulting in this scheme having the poorest overall efficiency. Case 6, which is similar to Case 5 but benefiting from a more complex recirculation and heating arrangement for reduced waste water flow rate and losses, has only slightly better overall efficiency than Case 5 as the waste water loss remains significantly greater than in Case 1.

The variation of LHV and HHV efficiencies as a function of

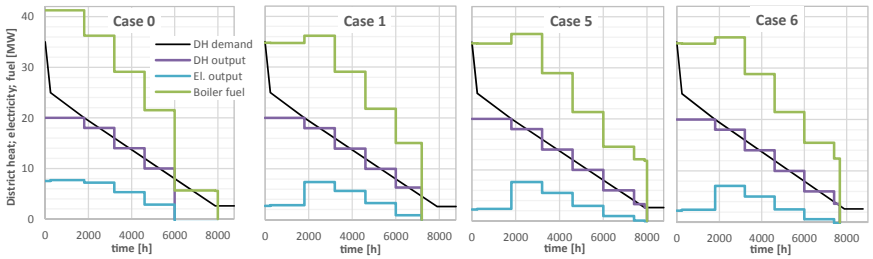

Fig. 4. Annual production of CHP products (power and heat) together with boiler fuel consumption using the multi-period model, and the DH demand curve. Case 0 includes the boiler fuel used in the separate HTC stoker boiler.

Table 4
Annual energy inputs and outputs of separate CHP and HTC plants, co-located separate plants (Case 0), and the three integrated cases.

Case	CHP	HTC	Case 0	Case 1	Case 5	Case 6
Fuel input						
CHP boiler fuel $Q_{f,BFB,LHV}$ [GWh_{LHV}]	157.3	–	157.3	201.8	212.2	208.4
HTC stoker boiler $Q_{f,S,LHV}$ [GW_{LHV}]	–	49.8	49.8	–	–	–
HTC feed $Q_{HTC,LHV}$ [GWh_{LHV}]	–	292.1	292.1	261.5	292.1	280.0
Total $Q_{chips,HHV}$ [GWh_{HHV}]	193.6	415.7	609.2	565.8	613.8	595.2
Total $Q_{chips,LHV}$ [GWh_{LHV}]	157.3	342.0	499.3	463.3	504.3	488.4
Other energy products						
Net electricity $E_{el,net}$ [GWh]	39.0	−4.85	34.1	28.79	24.53	25.64
Sold electricity $E_{el,s}$ [GWh]	39.0	0	35.3	28.79	24.77	25.69
Purchased electricity $E_{el,p}$ [GWh]	0	4.85	1.22	0	0.23	0.05
District heat output Q_{DH} [GWh]	94.8	0	94.8	102.3	105.1	104.2
Hydrochar output $Q_{hc,HHV}$ [GWh_{HHV}]	0	292.1	292.1	262.4	292.1	280.0
Hydrochar output $Q_{hc,LHV}$ [GWh_{LHV}]	0	259.2	259.2	233.0	259.2	248.8
Trigeneration efficiency						
η_{LHV} [%]	85.1	74.4	77.7	78.6	77.1	77.5
η_{HHV} [%]	69.1	69.1	69.1	69.4	68.7	68.9

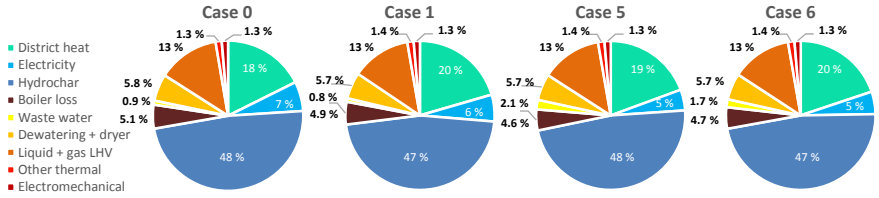

Fig. 5. Outgoing energy flows from the process in LHV terms.

cumulative operating time is plotted in Fig. 6a. The minimum-change integration scheme of Case 1 has the best efficiencies throughout the year, but only by a narrow margin until approximately 6000 h, or 8 MW DH load. At very low loads the efficiencies of Case 5 and Case 6 reduce faster, to become significantly worse than even stand-alone HTC plant at 8000 h.

Although the loss of feedstock LHV to liquid and gas fractions is the single greatest loss component, it remains constant and fixed by the choice of HTC parameters. The second largest component, drying and dewatering losses, varies only relatively little and cannot be significantly affected either by integration method or by plant operation. It is thus the boiler and waste water losses which actually vary the most between cases and load points; the variation of these losses are shown in Fig. 6b.

The waste water loss can be seen to increase significantly towards the low-load end of the curve in both Case 5 and Case 6. At high loads the Case 6 water loss is significantly less than that of Case 5 due to the improved HTC feed heating scheme, but towards low CHP load the Case 6 water loss increases to become even higher than that of Case 5. This is due to the need to bypass warm waste water past the heat recovery heat exchanger in order to maintain the ability of the LPPH to absorb the heat of condensing vapour from the flash tank. Case 6 with its reduced water flow needs bypassing already at a higher CHP load, negating part of the efficiency advantage of this arrangement. In terms of boiler losses the integrates are broadly similar. The lower efficiency of the stoker boiler shows as a slightly increased boiler losses at CHP part load. The greater combined load of the two boilers makes the stand-alone boiler loss much greater at full CHP load.

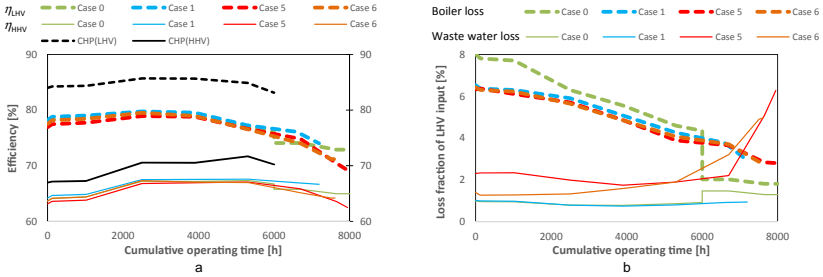

Fig. 6. Variation of (a) efficiency and (b) main losses (boiler and waste water) as a function of cumulative operating time for the different cases.

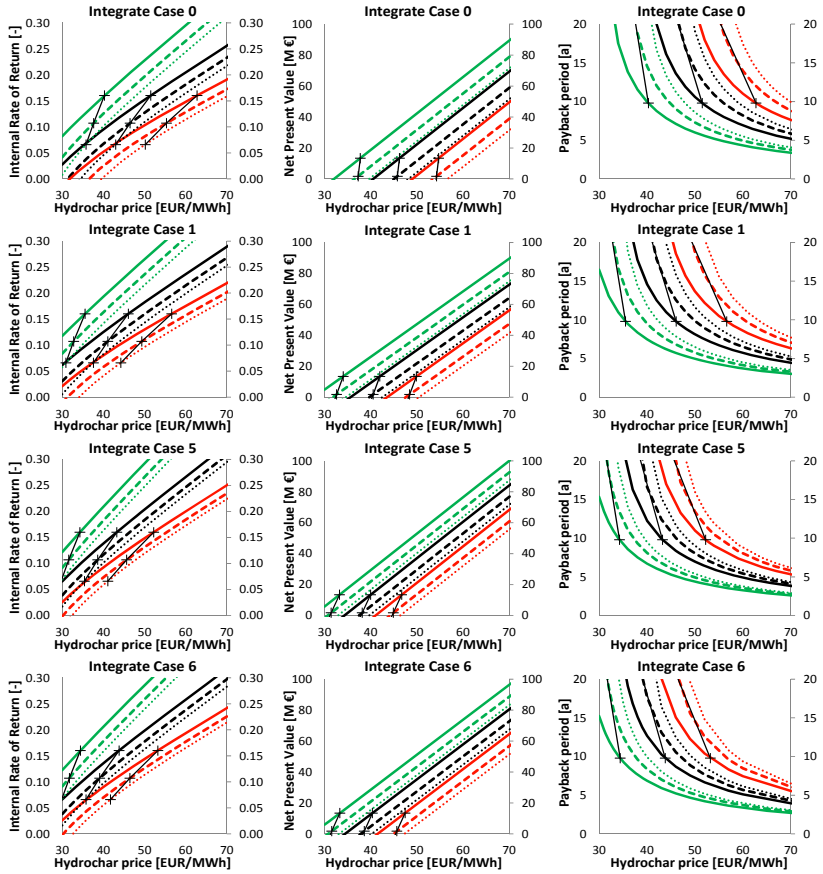

Fig. 7. Studied cases compared in terms of IRR, NPV and PBP. Crosses connected by black lines represent the hydrochar prices required to improve the economic parameter shown in the figure over stand-alone CHP. Green lines represent optimistic (−25%), red lines pessimistic (+25%) investment cost. Solid lines represent high, dashed medium, and dotted low electricity price. (For interpretation of the references to colour in this figure legend, the reader is referred to the web version of this article.)

5. Economic analysis

5.1. Capital investment

Capital investment is the total amount of money needed to purchase and install the equipment for constructing aplant. Plant equipment was sized on the basis of the maximum capacity level obtained from the simulation results and increased by typical industry overdesign factors. Recommended magnitudes of overdesign factors (1.1–1.2) are considered sufficient to mitigate potential changes in the operating performance and design uncertainties [22]. Table 5 summarizes cost data for different plant configurations.

Cost data for standard equipment, such as pumps, heat exchangers, reactors and tanks is taken from Refs. [22] and [23]. The cost of specialized processing equipment, such as HTC slurry pumps, pellet and filter presses, wood chips driers and conveyors, is based on vendor information presented by Erlach in Ref. [17]. CHP plant cost was estimated using data from [24] for the boiler costs [25], for the turbogenerator, and [22] and [23] for other equipment.

The cost of purchased equipment (PEC) was estimated using scaling factors and converted to base year 2014 using cost indexes [23]. Scaling factor allow estimating the cost of an item on the basis of available data for similar equipment of different size or capacity [17]:

$$Cost_a = Cost_b \left(\frac{X_a}{X_b}\right)^{\alpha} \quad (3)$$

where α is the scaling factor, and X is the capacity of the equipment.

Cost indexes are applied to forecast the costs of materials and equipment based on historical cost data. Chemical Engineering plant cost indexes (CEPCI) are recommended for process equipment investment estimates [22]. Cost data given in US dollars (USD) from year y is converted to year 2014 Euro (average annual exchange rate in 2014 is 0.695 €/USD):

$$C_{€,2014} = C_{USD,y} \frac{CPE_{2014}}{CPE_y} \frac{€_{2014}}{USD_{2014}} \quad (4)$$

Sum of PEC and cost of other factors directly related to the erection of the equipment (i.e. instrumentation and controls, piping, electrical installations, equipment erection and construction expenses) comprises the total module cost (CBM). CBM/PEC was assumed 2.88 when other cost data was not available [23]. The offsite costs (45% PEC) include cost for land, ancillary buildings, site development and utilities.

Engineering and supervision (12% PEC) covers cost for construction design together with purchasing, procurement and construction supervision. Start-up expenses (10% PEC) amount to the cost of possible start-up changes in materials and equipment and loss of income while plant is operating at partial capacity.

Contractor's fee (5% of indirect and direct costs) considers profit of contractor if employed. Contingencies (10% of indirect and direct costs) cover the expenses on unforeseen circumstances (e.g. strikes, price changes, storms, floods, design errors).

Working capital (15% FCI) estimates the total amount of money needed above the fixed capital to start the plant up and operate to the moment of the income received. Total capital investments consists of working and fixed capital. Assumptions for total capital investment components calculation are taken from Refs. [22] and [23].

Integrated plants offer clearly reduced total capital investment compared to the stand-alone plants of Case 0: 16.5% less for Case 1, increasing to 21.2% (Case 5) and 20.8% (Case 6). The major cost components in standalone case are the reactor (14% TCI) and boiler (15% TCI) total module costs together with working capital (13% TCI) and offsite costs (10% TCI); removing the need for a separate boiler is clearly a significant economic advantage. Hydrothermal treatment composes a significant investment in case of standalone operation – 69% of CBM – with HTC reactor, slurry pump, filter press, hydrochar dryer and pellet press as the main cost factors. As for integrated cases, the CHP plant represents over half of the capital investment. Configurations without slurry pumps (Case 5 and Case 6) clearly reduce the cost of HTC module even considering higher pressure requirements and consequently the cost of slurry mixing equipment.

5.2. Profitability evaluation

The profitabilities of the considered cases at different energy price assumptions are evaluated on the basis of net present value (NPV) and internal rate of return (IRR) and payback period (PBP). NPV is usually recommended as the best evaluation metric if only one is used [26]. All methods generally give the same accept/reject decision, but in case of mutually exclusive projects of different scope, they may suggest different ranking of the options; more than one metric is thus often used [26].

The NPV of a project is the sum of the total present worth of future cash flows during the economic project life time of n years discounted at an interest rate of i, minus the value of total capital investments TCI:

Table 5
Total capital investment calculation for studied cases. All numbers in millions of euros.

		HTC	CHP	Case 0	Case 1	Case 5	Case 6
direct costs	HTC purchased equipment cost (PEC)	3.7	–	3.7	3.7	3.2	3.2
	Stoker boiler PEC	1.6	–	1.6	–	–	–
	CHP plant PEC	–	5.8	5.8	5.8	5.8	5.9
	Total module cost	15.3	16.6	31.9	27.3	26.0	26.2
	Offsite cost	2.4	2.6	5.0	4.3	4.1	4.1
	Σ	17.7	19.2	36.9	31.6	30.1	30.3
indirect costs	Engineering	0.6	0.7	1.3	1.1	1.1	1.1
	Start-up	0.5	0.6	1.1	0.9	0.9	0.9
	Σ	1.2	1.3	2.4	2.1	2.0	2.0
	Contractor's fee	0.9	1.0	2.0	1.7	1.6	1.6
	Contingencies	1.9	2.0	3.9	3.4	3.2	3.2
Fixed-capital investment (FCI)		21.7	23.5	45.2	38.7	36.9	37.1
	Working capital	3.3	3.5	6.8	5.8	5.5	5.6
Total capital investment (TCI)		25.0	27.1	52.0	44.5	42.5	42.7

$$NPV = \frac{(1+i)^n - 1}{i\cdot(1+i)^n}\Big[E_{el,s}c_{el,s} + Q_{DH}\ c_{DH} + Q_{hc}c_{hc} - \Big(Q_{f,LHV} + Q_{HTC,LHV}\Big)c_f - E_{el,p}c_{el,p} - C_{O\&M}\Big] - TCI, \quad (5)$$

where the annual energy outputs and inputs E and Q are those shown in Table 4. The IRR is found using eq. (5) and solving iteratively such interest i that the NPV becomes zero. The PBP is found similarly by setting the NPV to zero in eq. (5), and solving for the number of years n. Results are shown in Fig. 7.

The assumed values of economic parameters in eq. (5) when not treated as variables are listed at Table 6. Three different electricity price scenarios were considered for market price of sold electricity. Constant electricity price throughout the plant operating time was assumed in each case. The electricity prices were estimated from the scenarios for electricity market price development presented in a report ordered by the Finnish Ministry of Employment and Economy [27].

The annual operating and maintenance cost $C_{O\&M}$ is determined as a fraction $r_{O\&M}$ of the TCI. For a small-scale bio-fired CHP plant an $r_{O\&M,CHP} = 4\%$ was assumed based on [28]. For the HTC plant there are no available references to estimate the operating and maintenance costs; since the plant operates on two-phase slurry and several components may be prone to fouling, clogging and corrosion, a higher O&M fraction of $r_{O\&M} = 8\%$ was assumed to obtain a conservative estimate. The combined $C_{O\&M}$ for each case was thus obtained using the mean $r_{O\&M}$ weighted with the fractions of CHP and HTC purchased equipment cost,

$$C_{O\&M} = \left(r_{O\&M,CHP}\frac{PEC_{CHP}}{PEC_{CHP+HTC}} + r_{O\&M,HTC}\frac{PEC_{HTC}}{PEC_{CHP+HTC}}\right)\cdot TCI. \quad (6)$$

Table 7 shows the cash flows for the considered cases, as well as the two stand-alone processes, when the investment is amortized in equal annual payments during the project economic lifetime. Two different scenarios are shown; if an interest rate of 10% is expected, the CHP plant returns only a marginally profitable net cash flow. Integration of a HTC process to the CHP plant according to Case 1 concept reduces this even further, while integration according to the concepts of Case 5 or Case 6 yields a small improvement. The stand-alone HTC plant is unprofitable, as is the combination of separate stand-alone CHP and HTC plants of Case 0.

Funding is likely available at a lower interest rate, however; assuming an interest rate of 5%, all of the integrated cases become more clearly profitable, with greater net cash flow rate than a pure CHP plant. The cash flow rate of the combined but non-integrated stand-alone plants of Case 0 also rises to a positive figure, although still inferior to the integrates. With either interest rate, the HTC stand-alone process is unprofitable, therefore making Case 0 inferior to pure CHP plant. All integration cases improve the annual net cash flow in comparison to having two separate processes, and except for Case 1 at the higher interest rate of 10%, also improve the cash flow of the pure CHP plant, with Case 5 providing the highest increase.

Sensitivity to parameters other than the hydrochar price is shown in Fig. 8; also the stand-alone HTC and stand-alone CHP plant are included in this comparison. Change of project IRR in percentage points is plotted in the charts as each of the considered parameters is varied by 20% up or down. Baseline investment cost and medium electricity cost scenario are assumed in this graph.

The profitability of the HTC stand-alone plant is clearly very sensitive especially to the wood feedstock price, and also to the investment and O&M costs. Stand-alone CHP plant profitability is much less affected by the price of wood chip, as both conversion efficiency and the price of the products are better than in the stand-alone HTC plant. The CHP plant is most sensitive to the price of district heat, which is the main product. Sensitivity to electricity price appears superficially low. Electricity price is likely by far the most volatile of the prices, however; while the 20% variation of parameters can be considered fairly large for most of the parameters, electricity price is subject to several times greater uncertainty.

The sensitivities of the different combined cases are broadly similar to each other. Changes in raw wood or investment cost will yield the biggest changes in profitability, but compared to a stand-alone HTC process, the sensitivity to these prices is much reduced. Compared to the CHP, the sensitivity to varying district heat or electricity price are also much reduced in the four cases combining both processes.

6. Results and conclusions

The process integration of CHP and HTC processes appear to be economically clearly advantageous over operating these as separate stand-alone plants. While integration does not offer significant energy efficiency advantages in this case, the increased CHP plant annual operating time and reduced overall investment cost make the integration clearly beneficial.

The actual profitability and choice of one integrated concept over another concept is less certain, although it does appear that the integration of small-scale CHP plant and HTC process according to the concepts of Case 5 (drum water use), and the similar Case 6, are likely to be profitable. Of the studied concepts of HTC and CHP co-production, these two were found to be superior to the alternatives under all considered scenarios and measured by all considered metrics, followed by Case 1 integrate, the separate plants of Case 0 being the consistently and clearly worst option.

Case 5 and Case 6 proved to yield the best economic performance although they had the lowest efficiencies and lowest net electricity production among the considered options at both full and part load. These weaknesses were more than compensated for by the reduced investment cost and increased production of district heat and, compared to Case 1, also increased production of hydrochar. These conclusions would have been difficult to see

Table 6
Values of economic parameters when not treated as variables in the analysis.

Parameter	Value	Energy product	Price
Maximum annual operating time t [h]	8000	Wood chip price c_f [€/MWh$_{LHV}$]	20
Interest rate i [%]	0.10	Sold electricity price (high) $c_{el,s}$ [€/MWh]	77
Plant economic lifetime [a]	25	Sold electricity price (medium) $c_{el,s}$ [€/MWh]	44
Annual CHP O&M cost ratio $r_{O\&M,CHP}$ [%]	0.04	Sold electricity price (low) $c_{el,s}$ [€/MWh]	21
Annual HTC O&M cost ratio $r_{O\&M,HTC}$ [%]	0.08	Purchased electricity price c_{DH} [€/MWh]	100
		District heat price $c_{el,p}$ [€/MWh]	60
		Hydrochar price c_{hc} [€/MWh$_{LHV}$]	40

Table 7
Annual cash flows of different cases.

	HTC	CHP	Case 0	Case 1	Case 5	Case 6
Investment amortization ($i = 10\%$) [M€]	−2.75	−2.98	−5.73	−4.91	−4.68	−4.70
Investment amortization ($i = 5\%$) [M€]	−2.19	−1.84	−4.03	−3.36	−3.17	−3.19
Operation and maintenance [M€]	−2.00	−1.08	−3.08	−2.48	−2.31	−2.33
Boiler fuel [M€]	−1.00	−3.15	−4.14	−4.04	−4.24	−4.24
HTC feedstock [M€]	−5.84	0	−5.84	−5.23	−5.84	−5.60
Purchased electricity [M€]	−0.48	0	−0.12	0	−0.02	−0.005
Sold electricity [M€]	0	1.71	1.55	1.27	1.09	1.13
Sold district heat [M€]	0	5.69	5.69	6.14	6.31	6.25
Sold hydrochar [M€]	10.37	0	10.37	9.32	10.37	9.96
Annual net cash flow ($i = 10\%$) [M€]	−1.70	0.19	−1.30	0.07	0.66	0.46
Annual net cash flow ($i = 5\%$) [M€]	−1.14	1.34	0.40	1.62	2.17	1.97

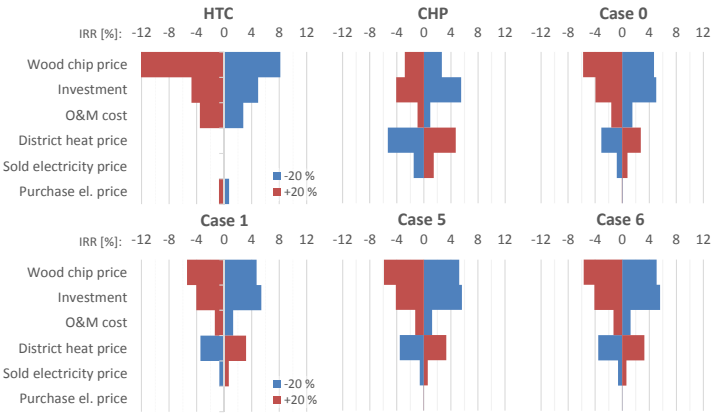

Fig. 8. Sensitivity analysis of IRR with ±20% change of parameters. IRR variation is shown in percentage points.

based on the pure thermodynamic analysis of Part 1 of this study; this emphasizes the necessity of careful operational and economic analysis when considering different plant configuration options.

At approximately 40 €/MWh price for hydrochar the profitability of an integrated Case 5 or Case 6 polygeneration plant starts to become increasingly likely. The uncertainty over the final investment cost of such a plant, and more importantly the uncertainty of the future prices of energy products (raw wood, electricity, district heat and the hydrochar), makes definitive conclusions difficult to draw, however. Particularly the prices of hydrochar, for which there is currently not yet an existing market, as well as electricity, are difficult to predict reliably.

A polygeneration plant can be considered also advantageous due the uncertainty of the economic environment: the profitability of an integrated CHP-HTC plant will be less vulnerable to fluctuations in electricity and district heat price. Although the vulnerability to wood chip price variation does increase in such a plant in comparison to a pure CHP plant, the price of raw wood is less likely to vary drastically than particularly the price of electricity.

The stand-alone HTC plant appears to be unprofitable under probable current economic input values. A different type of stand-alone HTC process could yield different results, however. An increased HTC pressure and thus temperature would allow shorter residence times and thus smaller volume flash tanks and reactors, while increasing the costs of most other components. The net effect of such process changes would require further study. Also the integration with a larger CHP plant, or a CHP plant supplying heat to process industry at a relatively constant rate rather than the significantly varying district heat load profile could yield different results, and should be investigated further.

Nomenclature

Roman letters

A	area [m^2]
c	energy price [€/MWh]
c_p	specific heat [kJ/kgK]
CBM	Cost, Bare Module [€]
E	energy (electric or mechanical) [MJ]
FCI	Fixed Capital Investment [€]
HHV	Higher Heating Value [MJ/kg]
i	interest rate [%]
IRR	Internal rate of return [−]
LHV	Lower Heating Value [MJ/kg]
N	plant economic lifetime [a]
NPV	net present value [€]
MC	biomass moisture content, water to total mass [−]
p	pressure [bar]
PBP	Payback Period [a]
PEC	Purchased Equipment Cost [€]
Q	heat [MJ]

$r_{O\&M}$	ratio of annual operation and maintenance cost to total capital investment [−]
t	time [h]
T	temperature [°C, K]
TCI	Total Capital Investment [€]

Greek letters

α	scaling factor [−]
η	efficiency [−]

Abbreviations

CEPCI	Chemical Engineering Plant Cost Index
CHP	Combined Heat and Power
DA	Deaerator
DH	District Heat
FG	Flue Gas
HPT	High Pressure Turbine
HTC	Hydrothermal Carbonization
LPPH	Low Pressure Preheater
LPT	Low Pressure Turbine
SCAH	Steam Coil Air Heater

Subscripts

D	drum
DA	deaerator
DH	district heat
el	electricity
FG	flue gas
furn	furnace
hc	hydrochar
in	inlet
O&M	operation and maintenance
out	outlet
p	purchased
s	sold

References

[1] Starfelt F, Thorin E, Dotzauer E, Yan J. Performance evaluation of adding ethanol production into an existing combined heat and power plant. Bioresour Technol 2010;101:613–8.

[2] Starfelt F, Daianova L, Yan J, Thorin E, Dotzauer E. The impact of lignocellulosic ethanol yields in polygeneration with district heating—a case study. Appl Energy 2012;92:791–9.

[3] Pellegrini LF, de Oliveira Junior S. Combined production of sugar, ethanol and electricity: thermoeconomic and environmental analysis and optimization. Energy 2011;36:3704–15.

[4] Pina EA, Palacios-Bereche R, Chavez-Rodriguez MF, Ensinas AV, Modesto M, Nebra SA. Reduction of process steam demand and water-usage through heat integration in sugar and ethanol production from sugarcane—Evaluation of different plant configurations. Energy 2015. http://dx.doi.org/10.1016/j.energy.2015.06.054. Article in press.

[5] Fahlén E, Ahlgren E. Assessment of integration of different biomass gasification alternatives in a district-heating system. Energy 2009;34:2184–95.

[6] Wahlund B, Yan J, Westermark M. A total energy system of fuel upgrading by drying biomass feedstock for cogeneration: a case study of Skellefteå bioenergy combine. Biomass Bioenergy 2002;23:271–81.

[7] Sermyagina E, Saari J, Zakeri B, Kaikko J, Vakkilainen E. Effect of heat integration method and torrefaction temperature on the performance of an integrated CHP-torrefaction plant. Appl Energy 2015;149:24–34.

[8] Starfelt F, Aparicio ET, Li H, Dotzauer E. Integration of torrefaction in CHP plants—a case study. Energy Convers Manag 2015;90:427–35.

[9] Kohl T, Laukkanen T, Järvinen M, Fogelholm C. Energetic and environmental performance of three biomass upgrading processes integrated with a CHP plant. Appl Energy 2013;107:124–34.

[10] Kohl T, Laukkanen TP, Järvinen MP. Integration of biomass fast pyrolysis and precedent feedstock steam drying with a municipal combined heat and power plant. Biomass Bioenergy 2014;71:413–30.

[11] Minaret J, Dutta A. Comparison of liquid and vapor hydrothermal carbonization of corn husk for the use as a solid fuel. Bioresour Technol 2016;200:804–11.

[12] Alatalo S, Repo E, Mäkilä E, Salonen J, Vakkilainen E, Sillanpää M. Adsorption behavior of hydrothermally treated municipal sludge & pulp and paper industry sludge. Bioresour Technol 2013;147:71–6.

[13] Gao P, Zhou Y, Meng F, Zhang Y, Liu Z, Zhang W, et al. Preparation and characterization of hydrochar from waste eucalyptus bark by hydrothermal carbonization. Energy 2016;97:238–45.

[14] Gao Y, Wang X, Wang J, Li X, Cheng J, Yang H, et al. Effect of residence time on chemical and structural properties of hydrochar obtained by hydrothermal carbonization of water hyacinth. Energy 2013;58:376–83.

[15] Bach Q, Tran K, Skreiberg Ø, Trinh TT. Effects of wet torrefaction on pyrolysis of woody biomass fuels. Energy 2015;88:443–56.

[16] Erlach B, Wirth B, Tsatsaronis G. Co-production of electricity, heat and biocoal pellets from biomass: a techno-economic comparison with wood pelletizing. In: World Renewable Energy Congress-Sweden; 8–13 May; 2011. Linköping; Sweden: Linköping University Electronic Press; 2011. p. 508–15.

[17] Erlach DB. Biomass upgrading technologies for carbon-neutral and carbon-negative electricity generation. Doctoral dissertation. Germany: TU Berlin; 2014.

[18] Saari J., Sermyagina E., Vakkilainen E., Kaikko J., Sergeev V. Integration of hydrothermal carbonization and a CHP plant: part 1-model description and effect of integration method on performance. Energy, submitted 2016.

[19] Savola T, Tveit T, Fogelholm C. A MINLP model including the pressure levels and multiperiods for CHP process optimisation. Appl Therm Eng 2007;27:1857–67.

[20] Koskelainen L, Saarela R, Sipilä K. Kaukolämmön käsikirja (In Finnish; eng. "Handbook of districtheating"). Energiateollisuus ry (Association of Finnish Energy Industry); 2006.

[21] Pirinen P, Simola H, Aalto J, Kaukoranta JP, Karlsson P, Ruuhela R. Tilastoja Suomen ilmastosta 1981-2010 (In Finnish; eng."Statistics about the climate of Finland 1981-2010"). Finnish Meteorological Institute; 2012. p. 96.

[22] Peters M, Timmerhaus K, West R. Plant design and economics for chemical engineers. 5th. New York: McGraw-Hill. Inc; 2003.

[23] Sinnott R. Chemical engineering design, section 13.5. Chemical engineering design. fourth ed. Oxford, United Kingdom: Elsevier; 2005. p. 815.

[24] US Environmental Protection Agency (EPA). EPA. Biomass combined heat and power catalog of technologies. 2007.

[25] Darrow K, Tidball R, Wang J, Hampson A. Catalog of CHP technologies. US Environmental Protection Agency; 2015. Accessed online at, http://www.epa.gov/chp/technologies.html.

[26] Megginson W, Smart S. Introduction to corporate finance. Cengage Learning; 2008.

[27] Pöyry Management Consulting. Adequacy of power capacity in Finland and the development of capacity structure until 2030. 2015. p. 27. URL: https://www.tem.fi/files/42541/Translation_Capacity_development_in_Finland.pdf. Referred: Nov 1st, 2015.

[28] Kuitunen T. Uusiutuvista energialähteistä tuotetun sähkön tukijärjestelmät Euroopan unionissa ja niidenvaikutus biomassavoimalaitosten kannattavuuteen (In Finnish; eng. "Subsidy systems for renewable power generation in the European Union, and their effect on the profitability of biomass-fired power plants."). M Sc thesis. 2007. p. 85.

Publication VI

Saari, J., Machado, M.d.O.C., Sermyagina, E., Kaikko, J., and Vakkilainen, E.
Optimization of a Shell-and-Tube District Heat Condenser for a Small Back Pressure CHP Plant

Reprinted with permission from
Proceedings of the 12th International Conference on Heat Transfer, Fluid Mechanics and Thermodynamics (HEFAT)
Malaga, Spain; 11-13 July, 2016

OPTIMIZATION OF A SHELL-AND-TUBE DISTRICT HEAT CONDENSER FOR A SMALL BACK PRESSURE CHP PLANT

Jussi Saari*, Mariana M.O. Carvalho, Ekaterina Sermyagina, Esa Vakkilainen, Juha Kaikko.
*Author for correspondence
LUT School of Energy Systems,
Lappeenranta University of Technology,
Lappeenranta, 53850, Finland.
E-mail: saari@lut.fi

ABSTRACT

Wood-fired combined heat and power (CHP) plants are a proven technology for producing domestic, carbon-neutral heat and power in Nordic countries. Such plants are often of back-pressure configuration, the district heat condenser replacing the vacuum condenser of a condensing power plant. The condenser is usually a shell-and-tube heat exchanger with district heating water on the tube side. In this paper, a new approach is presented to optimize the condenser design considering not only the design-point performance, but also variations in the operating conditions. A power plant model is used to determine the plant performance (net power output and boiler fuel consumption) as a function of the main performance parameters of the condenser at each point. Cuckoo search algorithm is used for the optimization. The results show that although electricity price variation has a significant impact on plant net cash flow rate, the effects of electricity price and heat exchanger specific cost on condenser design are low.

INTRODUCTION

Bio-fired combined heat and power (CHP) plants have several advantages; they convert a carbon-neutral local energy source to heat and power at high efficiency. One challenge in the design and optimization of such plants is the variation of load: peak winter heat demand is typically an order of magnitude greater than minimum summer load. Currently the changes in the electricity markets in the Northern Europe also complicate CHP investment decisions: questions over renewable power subsidies and the future of nuclear power have created unusually high uncertainty over the future prices of electricity. This creates also challenges for plant and component design and optimization.

The focus of this paper is the optimization of a district heat (DH) condenser considering the annual net cash flow of the CHP plant as the objective function. DH condensers of CHP plants are typically U-tube shell-and-tube heat exchangers (STHX) with water on the tube side and steam condensing on the shell side.

The variation of heat load and operating conditions and their effect on both plant and condenser performance is considered using a multi-period model where the annual operating profile is approximated using four load points. A power plant model developed with the process simulation software IPSEpro is used to determine the plant performance (net power output and boiler fuel consumption) as a function of the condenser's conductance and condensate subcooling at each point. The performance results together with the heat exchanger cost model output are used to determine the objective function value. A range of electricity prices is considered to investigate the effect of the price on optimal condenser design.

Shell-and-tube heat exchanger optimization has been studied extensively, with several methods applied to cost and heat transfer modelling, and the optimization itself. Most studies model the heat exchanger cost as a function of the heat transfer area [1-10]. This approach has been shown to have drawbacks in general [11], and in condenser optimization in particular [12]. In this paper, the condenser manufacturing costs are divided into material cost and processing cost [11]. These were estimated by a combination of mechanical sizing methods presented in [11] to find the mass of each component, and a simplified version of processing cost model from [12] where only the most important processing costs are determined in detail.

The heat transfer modelling of a condenser presents certain challenges. An average overall heat transfer coefficient U is often adequate to determine the performance of a liquid-liquid STHX, but this approach would yield optimistic results for a low-pressure steam condenser with close temperature approach [13]. As a result, a multi-element 2D model treating the tube bundle as a network of heat exchangers, is used here [12, 13].

STHX design optimization is also made difficult by characteristics, such as several constraints, non-differentiability, possible multimodality, and a combination of discrete and continuous variables. Many optimization methods have been used in STHX optimization. Deterministic, non-iterative solutions for segmentally baffled single-phase STHX have been presented by several authors [1-3,5,14]. Most of these methods involve significantly simplified shell-side calculation, and are not suitable for multi-element calculation of condensing flows. Deterministic methods may also present converging issues, especially as the number of decision variables increases.

During the last 15 years, several stochastic optimization methods have been applied to heat exchanger optimization. These algorithms tend to be computationally heavy, but as CPU speeds increase, this becomes less of a limit in contrast to the robustness and ease of implementation in difficult optimization problems. Stochastic algorithms applied to STHX optimization include simulated annealing (SA) [15], particle swarm optimization (PSO) [8,10], and various evolutionary algorithms such as differential evolution (DE) [16], genetic algorithms (GA) [4,6,9,10,17], and harmony search (HS) [7]. In this study cuckoo search (CS), a relatively new and promising stochastic metaheuristic optimizer inspired by and loosely based on the brood-parasitic behaviour of cuckoo birds, was used. It's performance on a number of common benchmark functions has been shown to compare favourably to PSO and GA [18, 19].

NOMENCLATURE

a	[-]	Annuity factor for capital investment amortization
a_{nzl}	[m]	Major axis of the elliptic nozzle-to-shell joint
A	[m^2]	Area
c	[€/MWh]	Specific cost of energy or heat exchanger
	[€/m^2]	
c_p	[J/kgK]	Specific heat
C	[€/a]	Cost; Annual cash flow rate
d	[m]	Tube diameter
D	[m]	1. Diameter
f	[-]	Friction factor (Darcy)
g	[m/s^2]	Standard gravity
G	[W/K]	1. Conductivity
	[(kg/s)/m^2]	2. Mass velocity
	[-]	3. Generation of cuckoos
h	[W/m^{2}K]	Heat transfer coefficient (condensation or convection)
i	[-]	Interest rate
k	[W/mK]	Thermal conductivity
K	[m]	1. absolute surface roughness
	[-]	2. loss coefficient
k	[W/mK]	Thermal conductivity
L	[m]	Length
LHV	[MJ/kg]	Lower Heating value
$\dot{m}$	[kg/s]	Mass flow rate
n	[a]	Plant economic lifetime
NP	[-]	Number of parents in a cuckoo generation
NTU	[-]	Number of transfer units; NTU = UA/($\dot{m}\ c_p$)$_{min}$
Nu	[-]	Nusselt number
p	[Pa]	Pressure
P	[W],	1. Power
	[m]	2. Tube pitch
Pr	[-]	Prandtl number
$r_{O\&M}$	[-]	Ratio of operating and maintenance cost tot TCI
Re	[-]	Reynolds number
R_{tf}"	[m^{2}K/W]	Thermal fouling resistance
s	[mm],	1. Material thickness
	[-]	2. Step size vector
t	[h]	Time (in plant operation)
T	[°C]	Temperature
T_{furn}	[K]	Absolute temperature in boiler furnace
ΔT_{lm}	[°C]	Logarithmic mean temperature difference
TCI	[€]	Total Capital Investment
u	[-]	Uniform-distributed random variable
U	[W/m^{2}K]	Overall heat transfer coefficient
v	[-]	Uniform-distributed random variable
w	[m/s]	Velocity
x	[-]	Decision variable

Special characters

α	[-]	Scaling factor in optimization local search
β	[m]	Lévy exponent
ε	[-]	1. Heat exchanger effectiveness
	[-]	2. Uniformly distributed random variable
Φ	[W]	Thermal power
Γ	[-]	Gamma function,
μ	[Pa s]	Dynamic viscosity
ρ	[kg/m^3]	Density
σ	[N/mm^2]	Stress
σ^2	[N/mm^2]	Variance

Subscripts

bfl	Baffle (support) plate
c	Cold (water) side
CHP	Combined Heat and Power plant
D	Design point
DA	Deaerator
DH	District heat
eff	Effective
el	Electricity
f	Fuel
FG	Flue gas
FOB	Free on board
gr	Gravity
h	Hot (steam) side
HX	Heat exchanger
i	Element index in water flow direction
in	Inside; inlet
j	Element index in steam flow direction
L	Saturated liquid state
man	Manufacturing
mat	Material
max	Maximum
nzl	Nozzle
OD	Off-Design
OTL	Outer Tube Limit
out	Outside; outlet
pr	Processing
SC	Sub-cooling
SG	Steam generator
s	shell
sh	shear
tb	tube
V	Saturated vapour state

PROBLEM DEFINITION

A commercial small modular backpressure CHP plant with a 29 MW thermal output bubbling fluidized bed (BFB) boiler is considered [20]. At design point, the plant has a 20 MW DH output with 90/50 °C outlet/return temperatures. The turbine has a partial admission regulating stage and separate high-pressure (HP) and low-pressure (LP) parts with an extraction at the HP exhaust, controlled by the LP turbine inlet valve. The single backpressure DH condenser is not directly connected to turbine exhaust arrangement, but receives steam through a pipe. The design-point parameters are summarized in Table 1; schematic diagram is shown in Figure 1. The fuel is forest chips with 19.5 MJ/kg dry matter lower heating value (LHV), wet-basis moisture content varying from 55% (winter) to 40% (summer).

Table 1 Design-point parameters of the CHP plant model.

Parameter	Value
Power output; generator/net	8.66 / 8.00 MW
District heat (DH)	20.00 MW
Boiler thermal power	28.9 MW
Total (CHP) Efficiency	85 %
Steam parameters	90 bar / 500 °C

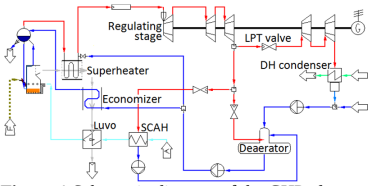

Figure 1 Schematic diagram of the CHP plant model.

The part-load modelling considers varying boiler and turbine performance. At off-design conditions (subscript OD), heat transfer rates Φ of those boiler surfaces where convection is the dominant heat transfer mode are calculated from design-point values (subscript D) assuming heat transfer to vary relative to 0.8:th power of flue gas mass flow rate $\dot{m}_{FG}$,

$$\Phi_{OD} = \Phi_D \left(\frac{\dot{m}_{FG,OD}}{\dot{m}_{FG,D}} \right)^{0.8} \frac{\Delta T_{lm,OD}}{\Delta T_{lm,D}}, \quad (1)$$

where ΔT_{lm} is the logarithmic mean temperature difference,

$$\Delta T_{lm} = \frac{(T_{h,in} - T_{c,out}) - (T_{h,out} - T_{c,in})}{\ln \frac{T_{h,in} - T_{c,out}}{T_{h,out} - T_{c,in}}}. \quad (2)$$

The steam generator heat transfer rate Φ_{SG} is estimated assuming an isothermal furnace where the heat transfer rate varies proportionally to the fourth power of absolute furnace temperature T_{furn},

$$\Phi_{SG,OD} = \Phi_{SG,D} \frac{T_{furn,OD}^4}{T_{furn,D}^4}. \quad (3)$$

Turbine pressure levels were determined using the ellipse law [21], and part-load efficiencies from polynomial curve fits based on [22] and [23]. The boundaries assumed for plant part-load operation are listed in Table 2.

Table 2 Off-design operating limits for the CHP plant.

Parameter	Design	min	max
Flue gas flow rate [kg/s]	17.27	-	19.5
Furnace temperature [°C]	904	700	950
Flue gas stack temperature [°C]	150	135	-
Turbine inlet steam flow rate [kg/s]	10.60	2.0	11.0
Deaerator pressure [bar]	5.6	3.0	8.0

Multi-period production model

A CHP plant is often sized for slightly over 50% of peak DH demand, resulting in 5000-7000 h annual operating time. Heat-only auxiliary boilers cover the peak consumption and demands below the CHP plant minimum load. The annual variation is approximated using a discretized model where each period is averaged to a single load point. The temperature levels of district heating water were set according to reference [24] based on the average ambient temperatures of each period. The ambient temperatures were estimated from Finnish Meteorological Institute monthly average temperature data in the central Finnish city of Jyväskylä. [25] The main parameters and the durations of the periods are listed in Table 3; Figure 2 shows the variation of heat and power production and fuel consumption.

Table 3 Average load points for the CHP plant.

Parameters	P1	P2	P3	P4
Period duration t [h]	1800	1400	1400	1400
Average ambient temperature [°C]	-8	0	+5	+10
DH water output/return T [°C]	90/55	80/50	75/45	75/45
DH power $\Phi_{DH,CHP}$ [MW]	20.0	18.0	14.0	10.0
Fuel: moisture [%] / LHV [MJ/kg]	55/7.4	50/8.5	50/8.5	45/9.6

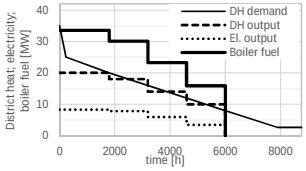

Figure 2 Annual CHP production and boiler consumption in the discretized multi-period model, and DH demand curve.

Condenser

A shell-and-tube U-tube condenser (Figure 3) in a round tube bundle and steam in pure cross flow was selected. Mechanical sizing was based on 250 °C design temperature and pressures of -1/+5 bar (shell) and -1/+16 bar (tubes). P235GH carbon steel was used for the tubes, P355GH for other parts. Yield strength of P355GH at 250 °C, σ_1 = 210 N/mm^2, was used as the design stress in calculations. 60° tube pitch was used. Loss coefficients for pressure drop were set according to [26]. Inside and outside fouling resistances of $R"_{tf,in} = 8 \cdot 10^{-5}$ and $R"_{tf,out} = 1 \cdot 10^{-5}$ m^{2}K/W were assumed. The values were set lower than figures in TEMA standards [27], which were considered to represent pessimistic rather than typical figures.

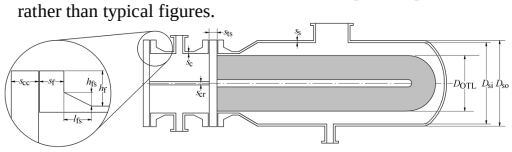

Figure 3 District heat condenser construction.

Objective function

The objective function to maximize is the annual net cash flow of the CHP plant, obtained from

$$C_{tot} = \sum_{P=1}^{4} t_P \left(P_{el} c_{el} + \Phi_{DH} c_{DH} - \Phi_f c_f \right) - aTCI_{tot} - r_{O\&M} TCI_{tot}, \quad (4)$$

where a is the amortization factor for the total capital investment (TCI) at interest rate i and economic lifetime n. Table 4 lists these and other economic parameter values. The cost the CHP plant excluding the condenser was estimated TCI_{CHP} = 26·10^6 € [28]. The DH condenser cost TCI_{DHC} was obtained by setting the cost of installed equipment as 3.3 times the FOB cost (C_{FOB}) [29]. The C_{FOB} was obtained from manufacturing cost C_{man} using a mark-up estimate consisting of 30% overhead cost, 5% contingency and 10% manufacturer's profit.

Table 4 Values of economic parameters.

Parameter	value
Maximum annual operating time t [h]	6000
Interest rate i [-]	0.10
Plant economic lifetime n [a]	20
Annual O&M cost ratio $r_{O\&M}$ [%]	0.04
Wood chip price c_f [€/MWh$_{LHV}$]	20
District heat price c_{DH} [€/MWh]	60

The manufacturing cost C_{man} consists of material cost C_{mat} and processing cost C_{pr}, where C_{mat} is clearly the dominant factor. Following material costs were assumed: tubesheet 3.5 €/kg; shell, channel and flanges 2.5 €/kg; and baffles 2.0 €/kg. Tube cost was set as a function of diameter based on a curve fit made on data available from commercial suppliers. Tube length was unlimited, but a 10% cost penalty was applied on tubes longer than 20 m before bending to U-tubes. Nozzle sizes were assumed unaffected by other dimensions and not considered.

Shell and channel are sized against internal pressure and buckling at -1 bar vacuum according to [31], and the tubesheet based on the simpler method of the older standard [26]. Flange dimensions were estimated from curve fits for standard flange sizes for heat exchangers as function of shell diameter.

Of the processing cost, baffle-related costs are the largest one [11] and any attempt to minimize the baffle costs will also significantly impact the heat transfer surface geometry. Baffle processing costs were thus modelled in detail according to the methodology of [11], while other processing costs were estimated at 10% of C_{mat} based on the results presented in [11].

The CHP plant fuel consumption Φ_f and heat and power production Φ_{DH} and P_{el} at each load points are functions of condenser performance: effective conductance $G_{eff} = U_{eff} A$, and condensate sub-cooling ΔT_{SC}. The effective conductance is defined as

$$G_{eff} = \Phi_{DH} \left(\ln \frac{T_{h,in} - T_{DH,out}}{T_{h,in} - T_{DH,return}} \right) / \left(T_{DH,return} - T_{DH,out} \right), \qquad (5)$$

where $T_{h,in}$ is the saturation temperature at the shell nozzle, $T_{sat}(p_{hzl})$. This is different from $G = UA$ based on an average of local U values, since local heat transfer rate in the bundle is also affected by varying vapour pressure, and hence $T_{sat}(p)$. It is the G_{eff} that determines the terminal temperature difference TTD, turbine exhaust pressure and thereby the effect on the CHP plant power production and boiler fuel consumption.

Sub-cooling may result from thick liquid inundation layer on the tubes, ineffective gas venting, or steam pressure drop. In a compact low-cost condenser design steam velocity may become high, the resulting pressure drop reducing $T_{sat}(p)$. This will manifest itself as sub-cooling as well as reduced G_{eff}. Subcooling due to thick inundation layers is unlikely in a small condenser considered here, and effective gas venting does not pose significant cost variations or restrictions to the design; these effects are thus not considered.

In the objective function evaluation the effects of G_{eff} and ΔT_{SC} on plant performance were determined using polynomial curve fits based on data generated with the plant model. A very good agreement of R^2=1.00 was obtained for $P_{el} = f(G_{eff})$ and $\Phi_f = f(G_{eff})$, and acceptable ($R^2 > 0.9$) also for ΔT_{SC} effect. The ΔT_{SC} proved to have relatively small impact on both P_{el} and Φ_f: <0.2 % per each 1 °C of sub-cooling.

The point P1 represents the boiler-limited maximum load. As the boiler load is at maximum during P1, increasing condenser G_{eff} increases power production at the expense of DH output. Since the Φ_{DH} production thus varies from the nominal value of 20 MW (Table 1), the period lengths of P1 and P2 are adjusted to prevent mean Φ_{DH} from exceeding the DH load curve.

The decision variables of the optimization are listed in Table 5. The straight length x_3 considers only effective heat transfer area; tube length covered by baffles or tube sheet is not part of this variable, but is factored in the condenser mass and cost calculation.

Table 5 Decision variables x and their initialization ranges.

x	Definition	Initialization range
x_1	Ratio of shell to bundle $D_{sh,in}/D_{OTL}$	$0.5 < x_1 < 0.95$
x_2	Number of tube passes	$x_2 \in \{2,4\}$
x_3	Straight tube length per pass L_{str} [m]	$3.0 < x_3 < 12.0$
x_4	Tube outside diameter d_o [mm]	$x_4 \in \{10, 12, 14, 16, 18, 20, 22, 25, 28, 30\}$
x_5	Tube pitch/ diameter ratio P/d_o	$1.25 < x_5 < 1.50$
x_6	Water free-flow area $A_{ff,c}$ [m^2]	$0.2 < x_6 < 1.0$

Constraints are listed in Table 6. Maximum tube-side velocity was set at the maximum water velocity in carbon steel tubes according to reference [30]. Maximum shell-side velocity, defined as the maximum velocity at the tightest spacing between the tubes, was set at the upper end of the recommended range for vapours at approximately atmospheric pressure in reference [29].

Table 6 Constraints.

Variable	Constraint	Variable	Constraint
Tube-side velocity	$w_c \leq$ 3.0 m/s	Shell-side velocity	$w_h \leq$ 30 m/s
Tube pitch	$P \geq 1.25 d_o$	Tubesheet ligament	$(P - d_o) \geq$ 5 mm
Condenser length	$L_{HX} \leq$ 15.0 m	Condenser diameter	$D_{HX} \leq$ 3.5 m

The optimization algorithm produces candidate solutions represented as vectors **x** of six design variable values. The outline of the algorithm to evaluate the objective function value for such a candidate vector is shown in Figure 4. The step of finding the district heat rate Φ_{DH} and adjusting the steam pressure until convergence is described in detail in the following chapter.

HEAT TRANSFER MODEL

The model determines iteratively the performance of the condenser at different load points by assuming a steam pressure p_h, solving the heat transfer rate given the water flow rate and return temperature, and correcting the pressure until DH production and water outlet temperature match the DH load.

The heat transfer calculation is based on reference [13]. Each U-tube of 2 passes pass is split in i_{max} slices in tube direction, and j_{max} circular segments in steam flow direction. A 180° U-element, $i_U = ½(i_{max}\text{-}1)+1$, joins the two passes. Flows entering element (i,j) are set by outlet conditions of $(i\text{-}1,j)$ and $(i,j\text{-}1)$. Constant T_{sat} and heat transfer coefficients are assumed in each element.

The flows are calculated iteratively in water flow direction from i=1 to i_{max} using equations (6) to (11). Each slice i is also calculated iteratively, starting with an estimated steam flow to $(i,1)$, and continuing until no vapour flow exits from (i,j_{max}).

$$U_{i,j} = \left[(d_o/d_i) \left(R''_{tf,in} + h_{c,i,j}^{-1} \right) + R''_w + h_{h,i,j}^{-1} + R''_{tf,in} \right]^{-1} \qquad (6)$$

$$NTU_{i,j} = \frac{U_{i,j} A_{i,j}}{\dot{m}_{c,j} c_{p,c,i,j}} \qquad (7)$$

$$\varepsilon_{i,j} = 1 - e^{-NTU_{i,j}} \qquad (8)$$

$$\Phi_{i,j} = \varepsilon_{i,j} \dot{m}_{c,j} c_{p,c,i,j} \left(T_{h,i,j} - T_{c,i,j} \right) \qquad (9)$$

$$T_{c,i+1,j} = T_{c,i,j} + \frac{\Phi_{i,j}}{\dot{m}_{c,j} c_{p,c,i,j}} \qquad (10)$$

$$\dot{m}_{h,V,i,j+1} = \frac{\dot{m}_{h,V,i,j} h_{h,V,i,j} + \dot{m}_{h,L,i,j} h_{h,L,i,j} - \dot{m}_{h,V,i,1} h_{h,L,i,j+1} - \Phi_{i,j}}{h_{h,V,i,j+1} - h_{h,L,i,j+1}} \qquad (11)$$

The tube inside heat transfer coefficient h_c is based on the Petukhov-Popov correlation [32], the friction factor f obtained from the iterative Colebrook-White equation:

$$Nu_c = \frac{h_{c,i,j} d_i}{k_c} = \frac{0.125 f \cdot Re_c Pr_c}{1.07 + \frac{900}{Re_c} - \frac{0.62}{1 + 10 Pr_c} + 12.7 \sqrt{\frac{Pr_c^{2/3} f}{2}} - 1} \left(\frac{\mu}{\mu_c} \right)^{0.14}, \qquad (12)$$

$$\frac{1}{\sqrt{f}} = -2 \log_{10} \left[\frac{2.51}{Re_c \sqrt{f}} + \frac{K/d_i}{3.71} \right]. \qquad (13)$$

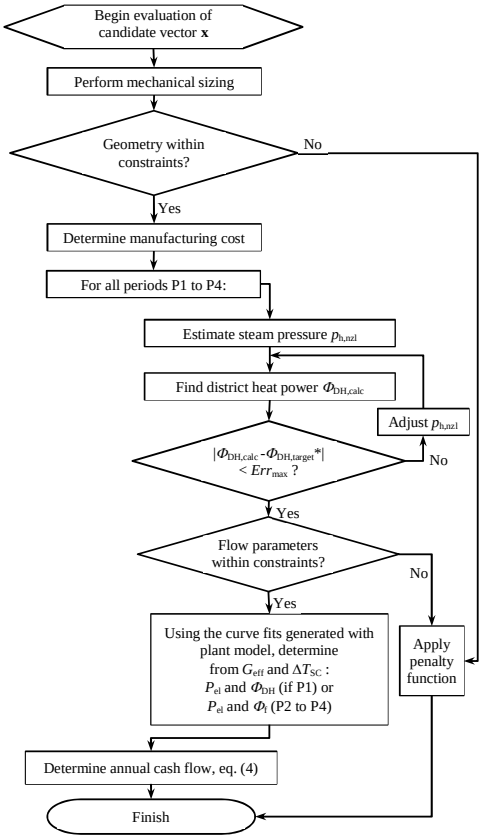

* In period P1 $\Phi_{DH,target}$ is adjusted during the iterative heat transfer calculation to a value that with the latest value of G_{eff} and ΔT_{SC} will yield a boiler fuel rate matching the boiler maximum continuous rating, thus making the variable Φ_f a de facto constant. For periods P2 to P4, $\Phi_{DH,target}$ is the Φ_{DH} listed in Table 3.

Figure 4 Flow chart for objective function evaluation.

Water pressure drop Δp_c was obtained from

$$\Delta p_c = \frac{\rho_c w_c^2}{2}\left(f\frac{L_{tb}}{d_i} + K_{nzl,c,in} + \frac{N_{tbp}}{2}\left(K_{tb,in} + K_U + K_{tb,out}\right) + K_{nzl,c,out}\right), \quad (14)$$

The condensation heat transfer coefficient at j:th segment $h_h(j)$ is obtained approximating the net effect of gravity- and shear-dominated coefficients $h_{h,gr}$ and $h_{h,sh}$ with an averaging formula (16) and an inundation correction (17):

$$Nu_{h,gr} = \frac{h_{h,gr} d_o}{k_l} = 0.728\left[\frac{\rho_L(\rho_L-\rho_V) g h_{fg} d_o^3}{\mu_L k_L \Delta T}\right]^{1/4} \text{ [33]}, \quad (15)$$

$$Nu_{h,sh} = \frac{h_{h,sh} d_o}{k_l} = 0.59\sqrt{\frac{w_V d_o \rho_L}{\mu_L}} \text{ [34]}, \quad (16)$$

$$h_h = \sqrt{0.5h_{h,sh}^2 + \sqrt{0.25h_{h,sh}^4 + h_{h,gr}^4}} \text{ [35]}, \quad (17)$$

$$h_h(j) = h_h\left[\left(j\cdot N_{Lj}\right)^{5/6} - \left(j\cdot N_{Lj}-1\right)^{5/6}\right] \text{ [35]}, \quad (18)$$

where N_{Lj} is the average number of tube rows in steam flow direction per each segment j.

Steam pressure drop takes place at the nozzle (Δp_{nzl}) and tube bundle. Δp_{nzl} was calculated assuming half a velocity head lost at velocities at nozzle, 90° turn from the nozzle, and the free area between the bundle and shell in shell axis direction,

$$\Delta p_{nzl} = 0.5\frac{\rho_{V,nzl}\dot{V}_{V,nzl}^2}{2A_{nzl}^2} + 0.5\frac{\rho_{V,90°}\dot{V}_{V,90°}^2}{2A_{90°}^2} + 0.5\frac{\rho_{V,ann}\dot{V}_{V,s,ax}^2}{2A_{s,ax}^2}; \quad (19)$$

$$A_{nzl} = \frac{\pi D_{nzl}^2}{4};$$

$$A_{90°} = P_{nzl}\cdot\left[\tfrac{1}{2}\left(D_{s,in} - D_{OTL}\right) - h_{ip}\right];$$

$$A_{s,ax} = 2\cdot\left(\frac{\pi D_{s,in}^2}{4} - A_{bfl}\right)$$

where P_{nzl} is the perimeter of an ellipse with major axis of a_{nzl} and minor axis of D_{nzl} obtained using Ramanujan's approximation formula [36], D_{bfl} is the diameter of the circular part of a baffle plate, h_{ip} is the height of the impingement plate from the tube bundle, and A_{bfl} is the area covered by the support plates in tube axis direction, shown as gray in Figure 5 below.

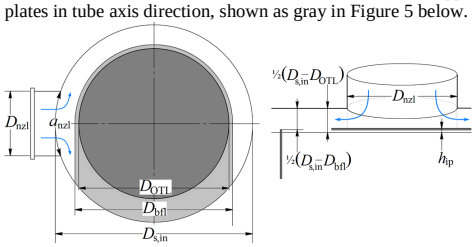

(a) (b)

Figure 5 Geometry at steam entry to the shell.

The pressure drop in the tube bundle was determined using Jakob correlation based on vapour mass velocity at the smallest area between the tubes G_{max}:

$$\Delta p_h = \frac{2\left[0.25 + 0.1175(P/d_o)^{-1.08}\right]\left(w_{V,max} d_o \rho_V \mu_V\right)^{-0.16} G_{max}^2}{\rho_V}. \text{ [37]} \quad (20)$$

OPTIMIZATION ALGORITHM: CUCKOO SEARCH

First introduced in 2009, the Cuckoo Search (CS) is one of the most recent metaheuristic optimization algorithms. Like many metaheuristics, such as evolutionary algorithms, wasp, ant, and bee colony algorithms, and bat algorithm, it is inspired by processes observed in nature: in this case, the well-known brood parasitic behaviour of many cuckoo species [38], as well as a search pattern known as Lévy flights [38] which maximises the efficiency of resource search [39] and has been observed in many mobile foraging species [38, 39].

Like many nature-inspired metaheuristics, the CS also operates not with a single point that it tries to improve, but a population of candidate solutions, which in CS represent cuckoo

eggs. Each cuckoo lays one egg to one nest per generation. As this number is fixed, there is no practical distinction to be made between a cuckoo, an egg, and a nest.

Each iteration begins with an attempt at global search by a so-called Lévy flight, a random walk where step length is drawn from Lévy probability distribution resulting in clusters of short steps connected by rare longer leaps. From each cuckoo i of generation G a new candidate solution is generated for generation G+1. The new candidate, which replaces the old one if it yields an objective function value better than the original, is obtained from

$$x_i^{G+1} = x_i^G + \alpha \cdot \Delta x_{best} \cdot s \cdot n, \quad (21)$$

where α is a scaling factor, vector Δx_{best} is the difference between current vector x_i^G and the so far best solution x_{best}, $\Delta x_{best} = x_{best}^G - x_i^G$, s is a Lévy-distributed step size vector and n is a vector of random variables with a standard normal distribution. All vectors have a size of D. The step size vector s is obtained with Mantegna's algorithm originally published in [40] as cited in [18] using two normal-distributed random variable vectors u and v of size D and a Lévy exponent β:

$$s = u \cdot v^{-1/\beta}, \quad (22)$$

where all elements of u and v have a mean of zero, and variances of 1 (v) and σ^2 (u), respectively. σ^2 is calculated from

$$\sigma^2 = \left[\frac{\Gamma(1+\beta)}{\beta \cdot \Gamma(½+½\beta)} \cdot \frac{\sin(½\pi\beta)}{2^{½(1+\beta)}} \right]^{1/\beta}, \quad (23)$$

where Γ is the gamma function, $\Gamma(n) = (n\text{-}1)!$. The second step is exploitative local search by replacing each element d of every egg (candidate vector) i at probability p_a, representing the detection of cuckoo eggs by the host bird. Each new decision variable d in a new candidate vector is obtained from

$$x_{i,d}^{G+1} = x_{i,d}^G + \alpha \cdot r \cdot H \cdot (p_a - \varepsilon) \cdot (x_{j,d}^G - x_{k,d}^G), \quad (24)$$

where H means the Heaviside function, α is the scaling factor as used in eq. (17), and r and ε are uniformly distributed random variables. Vectors x_j and are x_k are chosen randomly from the population. Again, the new candidate vector produced with eq. (20) replaces the previous solution – either the original x_i^G, or if the Lévy flight succeeded, the result of eq. (17) – if the new candidate vector yields a better objective function value.

The CS algorithm has proven to be relatively insensitive to the values of α and β; the values of 0.01 and 1.5, which can be used with most problems [18], were used in this study. A switching probability p_a = 0.25, population size of NP = 60 cuckoos, and stopping condition of 300 generations were used.

RESULTS

Optimization was performed with electricity price range of 40-80 €/MWh. While the low-end scenarios for future electricity prices in Nordic countries include even lower prices, unsubsidized bio-CHP production is unlikely to be profitable in these scenarios. Three cases of heat exchanger cost were considered: base, -20% optimistic and +20% pessimistic. The main parameters corresponding to 40, 60 and 80 €/MWh electricity price and base case of condenser price are listed in Table 7.

The condenser optimized for 40 €/MWh electricity price is far smaller than the other two, which are similar. While the smaller exchanger is much cheaper, the shorter design increases the relative share of shell, channel and tube sheet, which results in almost 50% greater specific cost of heat transfer area.

Table 7 Condensers optimized for different electricity prices, base case manufacturing cost assumed.

P_{el} [€/MWh$_{el}$]	40	60	80
$x_1=D_{OTL}/D_s$	0.737	0.750	0.740
$x_2=N_{tbp}$	2	2	2
$x_3=L_{str}$	4.000	8.054	8.066
$x_4=d_o$ [mm]	18.0	16.0	16.0
$x_5=P/d_o$ [-]	1.278	1.313	1.313
$x_6=A_{fr,c}$ [m^2]	0.045	0.079	0.086
L_{tot} [m]	4.982	9.345	9.386
D_{tot} [m]	0.821	1.096	1.148
D_{ch} [m]	0.677	0.898	0.926
D_s [m]	0.821	1.064	1.134
L_s [m]	4.376	8.543	8.557
s_{ts} [mm]	92	116	121
s_{chc} [mm]	34	43	45
m_{tot} [kg]	3 633	10 760	11 515
$N_{tb/pass}$ [-]	255	599	645
A_{tot} [m^2]	120	497	536
C_{tot} [10^6 €], eq.(1)	0.08	0.82	1.58
C_{FOB} [10^3 €]	37	107	114
c_{FOB} [€/m^2]	307	216	213

When the parameters used for plant performance estimation, G_{eff} and ΔT_{SC}, are plotted over the range of electricity price c_{el} for all condenser cost cases (Figure 6), a clear step change at approximately 50 €/MWh$_{el}$ becomes evident. At c_{el} values above the step change, G_{eff} varies from 1350 to 1550 kW/K and subcooling remains stable at ΔT_{SC} = 0.6±0.5 °C; below, the ranges vary from 400 to 600 kW/K and 0.2 to 0.4 °C. Above the step change, condenser manufacturing cost case has < 5% impact on optimal conductance and heat transfer area at any given c_{el}.

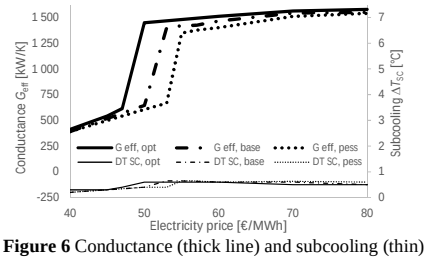

Figure 6 Conductance (thick line) and subcooling (thin) in optimized condensers at varying electricity price and optimistic (-20%), baseline and pessimistic (+20%) cost assumption.

It is evident that although a large step change takes place in condenser size and cost, the design optimized for an electricity price immediately below the step change price level does not yet represent the minimum condenser size within the constraints; conductances continue to reduce towards the lower electricity prices. The CHP plant also remains profitable with a positive net cash flow even assuming an expected return rate of 10% for the investment, and in fact no similar step change in net cash flow rate takes place (Figure 7). It appears that the step change

represents the point at which increasing the DH production during period P1 at the expense of power generation starts to outweigh the benefit that could be achieved by increased power output at part load.

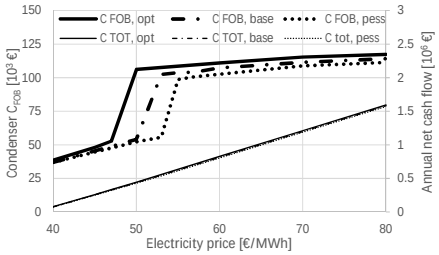

Figure 7 Condenser FOB cost and plant annual net cash flow as function of electricity price.

Figure 8 presents the optimal values of maximum-load (period P1) TTD and water pressure drop Δp_c as a function of electricity price above the step change. The optimum values fall within a relatively narrow range at all electricity prices and condenser cost scenarios; mostly 2-3 °C TTD and 0.4-0.5 bar Δp_c. TTD becomes smaller at a reducing rate towards increasing electricity prices as could be expected, while the Δp_c curves tip downwards at the high end of electricity prices in all cases. The tip downwards in Δp_c could be an indication of the role of the pumping power becoming relatively more important as the cost of obtaining more power output from the turbine increases with what is already a relatively large, low-TTD condenser design.

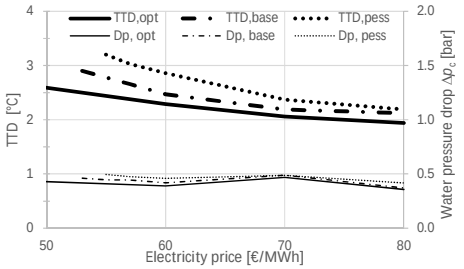

Figure 8 Condenser terminal temperature difference and water-side pressure drop at maximum load (load point P1).

CONCLUSIONS

Shell-and-tube district heat back pressure condenser optimization for a small modular power plant was studied using a multi-period model to account for annual variation of load and operating conditions. Cuckoo search algorithm was used in the optimization. A cost model incorporating elements from both Caputo et al. [11] and Saari et al. [12] was implemented to evaluate equipment cost.

The methods used were successful for the problem, and the resulting condenser configurations appear mostly typical for such equipment. While convergence proof for a stochastic metaheuristic is not possible, the curve shapes resulting from running the algorithm at gradually changing parameter values are relatively smooth with some notable but systematic exceptions, indicating reliable performance.

A steep step change occurs at approximately electricity price of 50 €/MWh$_{el}$. Above the step change price, the main finding was that while net cash flow rate for the investment is significantly affected by varying electricity price, variations in either electricity price or condenser cost have only little impact on what is the optimal design for the condenser.

For lower electricity price ranges the optimized designs were much smaller in size and cheaper in cost. Although the CHP plant remained profitable with a positive net cash flow rate down to the lowest electricity price considered, 40 €/MWh, the optimization result that appeared to maximize DH production at the expense of power output casts some doubt over the preferability of a CHP plant over a heat-only boiler at such conditions.

The possibility of altering the conductance by varying condensate level in the condenser shell was not considered here. A design where condensate level could be allowed to raise in the tube bundle to submerge some of the heat transfer tubes would allow a given condenser design both deliver high conductance and thus maximum electricity output at part load, and reduce the power output for increased DH production during the full-load period. This would likely be the best strategy in a situation when electricity price is less than district heat price, but still sufficiently high that the CHP plant is remains profitable.

REFERENCES

[1] F. Jegede and G. Polley, "Optimum heat exchanger design: process design", *Chemical Engineering Research & Design*, vol. 70, pp. 133-141, 1992.

[2] F. T. Mizutani, F. L. Pessoa, E. M. Queiroz, S. Hauan and I. E. Grossmann, "Mathematical programming model for heat-exchanger network synthesis including detailed heat-exchanger designs. 1. Shell-and-tube heat-exchanger design", *Ind Eng Chem Res*, vol. 42, pp. 4009-4018, 2003.

[3] K. Muralikrishna and U. Shenoy, "Heat exchanger design targets for minimum area and cost", *Chem. Eng. Res. Design*, vol. 78, pp. 161-167, 2000.

[4] R. Selbaş, Ö Kızılkan and M. Reppich, "A new design approach for shell-and-tube heat exchangers using genetic algorithms from economic point of view", *Chemical Engineering and Processing: Process Intensification*, vol. 45, pp. 268-275, 2006.

[5] M. Serna and A. Jiménez, "A compact formulation of the Bell–Delaware method for heat exchanger design and optimization", *Chem. Eng. Res. Design*, vol. 83, pp. 539-550, 2005.

[6] J. M. Ponce-Ortega, M. Serna-González and A. Jiménez-Gutiérrez, "Use of genetic algorithms for the optimal design of shell-and-tube heat exchangers", *Appl. Therm. Eng.*, vol. 29, pp. 203-209, 2009.

[7] M. Fesanghary, E. Damangir and I. Soleimani, "Design optimization of shell and tube heat exchangers using global sensitivity analysis and harmony search algorithm",

Appl. Therm. Eng., vol. 29, pp. 1026-1031, 2009.
[8] V. Patel and R. Rao, "Design optimization of shell-and-tube heat exchanger using particle swarm optimization technique", *Appl. Therm. Eng.*, vol. 30, pp. 1417-1425, 2010.
[9] S. Sanaye and H. Hajabdollahi, "Multi-objective optimization of shell and tube heat exchangers," *Appl. Therm. Eng.*, vol. 30, pp. 1937-1945, 2010.
[10] H. Hajabdollahi, P. Ahmadi and I. Dincer, "Thermoeconomic optimization of a shell and tube condenser using both genetic algorithm and particle swarm," *Int. J. Refrig.*, vol. 34, pp. 1066-1076, 2011.
[11] A. C. Caputo, P. M. Pelagagge and P. Salini, "Manufacturing cost model for heat exchangers optimization", *Appl. Therm. Eng.*, vol. 94, pp. 513-533, 2016.
[12] J. Saari, S. Afanasyeva, E. K. Vakkilainen and J. Kaikko, "Heat transfer model and optimization of a shell□and□tube district heat condenser," in *Proceedings of International Conference on Efficiency, Cost, Optimization, Simulation and Environmental Impact of Energy Systems (ECOS) 2014*, Turku, 2014, pp. 1920-1933.
[13] J. Saari, J. Kaikko, E. Vakkilainen and S. Savolainen, "Comparison of power plant steam condenser heat transfer models for on-line condition monitoring," *Appl. Therm. Eng.*, vol. 62, pp. 37-47, 2014.
[14] A. L. Costa and E. M. Queiroz, "Design optimization of shell-and-tube heat exchangers", *Appl. Therm. Eng.*, vol. 28, pp. 1798-1805, 2008.
[15] P. D. Chaudhuri, U. M. Diwekar and J. S. Logsdon, "An automated approach for the optimal design of heat exchangers", *Ind Eng Chem Res*, vol. 36, pp. 3685-3693, 1997.
[16] B. Babu and S. Munawar, "Differential evolution strategies for optimal design of shell-and-tube heat exchangers", *Chemical Engineering Science*, vol. 62, pp. 3720-3739, 2007.
[17] S. Sanaye and M. Dehghandokht, "Modeling and multi-objective optimization of parallel flow condenser using evolutionary algorithm", *Appl. Energy*, vol. 88, pp. 1568-1577, 2011.
[18] X. Yang and S. Deb, "Cuckoo search: recent advances and applications," *Neural Computing and Applications*, vol. 24, pp. 169-174, 2014.
[19] X. Yang, "Cuckoo search and firefly algorithm: Overview and analysis," in *Cuckoo Search and Firefly Algorithm* Anonymous Springer, 2014, pp. 1-26.
[20] S. Komulainen, "Voimalaitoksen käytönaikaisen optimoinnin määrittely", (In Finnish; Eng. Definition of power plant on-line optimization) [master's thesis]. Lappeenranta, Finland: Lappeenranta University of Technology, 2012.
[21] W. Traupel, *Thermische Turbomaschinen: Thermodynamisch-Strömungstechnische Berechnung.* Springer-Verlag, 1966.
[22] T. Tveit, T. Savola and C. Fogelholm, "Modelling of steam turbines for mixed integer nonlinear programming (MINLP) in design and off-design conditions of CHP plants", in *Proceedings of the 46th Conference on Simulation and Modeling (SIMS 2005)*, 2005, pp. 13-14.
[23] M. Jüdes, S. Vigerske and G. Tsatsaronis, "Optimization of the design and partial-load operation of power plants using mixed-integer nonlinear programming," in *Optimization in the Energy Industry*, Springer, 2009, pp. 193-220.
[24] L. Koskelainen, R. Saarela, K. Sipilä. *Kaukolämmön käsikirja*. (In Finnish; eng. "Handbook of district heating"). Energiateollisuus ry (Association of Finnish Energy Industry), 2006.
[25] P. Pirinen, H. Simola, J. Aalto, J. P. Kaukoranta, P. Karlsson, R. Ruuhela. *Tilastoja Suomen ilmastosta 1981-2010*. (In Finnish; eng."Statistics about the climate of Finland 1981-2010"). Finnish Meteorological Institute, 2012.
[26] SFS-Käsikirja 13, "Paineastiat. Mitoitus" (In Finnish; Eng. Pressure vessels. Dimensioning), 1996.
[27] Tubular Exchanger Manufacturers Association, Inc., "Standards of the Tubular Exchanger Manufacturers Association, 9th Edition", 2007.
[28] T. Kuitunen, "Uusiutuvista energialähteistä tuotetun sähkön tukijärjestelmät Euroopan unionissa ja niiden vaikutus biomassavoimalaitosten kannattavuuteen" (In Finnish; Eng. Subsidy systems for electricity produced from renewable sources in the European Union and their effect on the profitability of biomass power plants) [master's thesis]. Lappeenranta, Finland: Lappeenranta University of Technology, 2011.
[29] R. Sinnott, *Coulson & Richardson's Chemical Engineering Design*. Oxford, UK: Butterworth-Heinemann, 2005.
[30] J. Taborek, "3.3 Shell-and-tube heat exchangers / 3.3.5 Input data and recommended practices", *Heat Exchanger Design Handbook 3: Thermal and Hydraulic Design of Heat Exchangers"*. Hemisphere Publishing Corporation, United States of America, 1983.
[31] SFS-EN 13445-3, "Lämmittämättömät painesäiliöt" (In Finnish; Eng. Unfired pressure vessels). 2002.
[32] R. K. Shah and D. P. Sekulic, *Fundamentals of Heat Exchanger Design.* John Wiley & Sons, 2003.
[33] W. Nusselt, Die Oberflachenkondensation des Wasserdampfes. (In German; Eng. Film condensation of water vapour). *Z. Vereines Deutsch. Ing.* Vol. 60, pp. 541-546,569-575, 1916.
[34] I.G. Shekriladze, V.I. Gomelauri, Theoretical study of laminar film condensation of flowing vapour, *International Journal of Heat and Mass Transfer*, Vol. 9, pp. 581–591, 1966.
[35] S. Kakac, *Boilers, Evaporators and Condensers*. Wiley & Sons, 1991.
[36] L. Råde, B. Westergren, *Mathematics Handbook for Science and Engineering*. Studentlitterature, Sweden, 1995.
[37] J.P. Holman, *Heat Transfer*. McGraw-Hill Book Company, Singapore, 1989.
[38] X.Yang, *Nature-inspired optimization algorithms*, Elsevier, 2014.
[39] S. Focardi, P. Montanaro, E. Pecchioli, "Adaptive Lévy Walks in Foraging Fallow Deer", *PLoS ONE* 4(8):e6587, 2009
[40] R. N. Mantegna, "Fast, accurate algorithm for numerical simulation of Levy stable stochastic processes," *Physical Review E*, vol. 49, pp. 4677, 1994.

Publication VII

Sermyagina, E., Saari, J., Vakkilainen, E., and Kaikko, J.
Integration of torrefaction and a CHP plant: Operational and economic analysis.

Reprinted with permission from
Applied Energy
Vol. 183, pp.88-99, 2016

Applied Energy 183 (2016) 88–99

Contents lists available at ScienceDirect

Applied Energy

journal homepage: www.elsevier.com/locate/apenergy

Integration of torrefaction and CHP plant: Operational and economic analysis

Ekaterina Sermyagina *, Jussi Saari, Juha Kaikko, Esa Vakkilainen

Lappeenranta University of Technology, Lappeenranta, Finland

HIGHLIGHTS

- Three scenarios of torrefaction integration into CHP plant are evaluated.
- Annual operation of integrated plants with part-load periods are considered.
- Economic performance is evaluated with NPV, IRR and PBP metrics.
- Sensitivity analysis of IRR is performed with several economic factors.

ARTICLE INFO

Article history:
Received 9 March 2016
Received in revised form 24 August 2016
Accepted 25 August 2016

Keywords:
Biomass torrefaction
Combined heat and power plant
Integration
Economic analysis

ABSTRACT

Biomass torrefaction is a pre-treatment technology with high potential to convert biomass into a valuable commodity. The heat integration of torrefaction and combined heat and power (CHP) plant was investigated in previous work (Sermyagina et al., 2015). The aim of the present study is to assess possible economic benefits from integration. Three most promising integration concepts from the previous work were studied in terms of seasonal operational changes of district heating demand and varying ambient conditions. The performance of two integration concepts were evaluated together with stand-alone and co-located plants. The integration leads to a higher utilization of the CHP boiler capacity during part-load operation, possible increase of the operation time and growth of electricity generation as a result. The total efficiencies of the integrated cases (around 72% in higher heating value terms) are slightly higher than the stand-alone CHP plant (69%) or the co-located option (71%). The integration requires 40% more capital investments than the stand-alone CHP. On the other hand, the total capital investments of the integration cases are 20% lower than in co-located plants, and a profitability evaluation shows that lower investment costs may make integration schemes advantageous over the non-integrated plants. Feedstock price and investment costs are the main economic drivers affecting the profitability of the integrated options. An integration case which uses back pressure steam to account for the torrefaction heat demand showed the highest profitability due to a longer annual operating time, resulting in a growth of electricity and DH production over the stand-alone CHP plant.

1. Introduction

Modern society depends on materials and products that have been historically produced from fossil fuels. At the same time, the concept of sustainability in various industrial spheres is attracting increasing attention, especially considering the growing environmental concerns associated with fossil fuel combustion. Under these circumstances, the demand for efficient utilization of renewable sources is increasing. Biomass can be efficiently used for the production of various commodities, such as vehicle fuels (e.g. bioethanol and biodiesel), chemicals and plastics, fertilizers and pharmaceuticals as well as for energy generation [1,2]. The complete recovery of different by-products and wastes from agriculture and industry along with the utilization of other biomass sources has a significant potential for substituting traditional fossil fuels.

Biomass-based combined heat and power (CHP) production or co-generation is a proven technology that can be effectively applied for local biomass feedstocks. Simultaneously, despite the positive environmental and potential economic benefits, the untreated woody biomass as a fuel is associated with certain problems: heterogeneous nature, poor grindability, relatively high

* Corresponding author.
E-mail address: ekaterina.sermyagina@lut.fi (E. Sermyagina).

http://dx.doi.org/10.1016/j.apenergy.2016.08.151
0306-2619/

Nomenclature

c	energy price [€/MW h]
E	energy [MJ]
HHV	higher heating value [MJ/kg]
i	interest rate [%]
LHV	lower heating value [MJ/kg]
MC	biomass moisture content [%]
n	plant economic lifetime [y]
Q	heat [MJ]
r	ratio of annual operation and maintenance cost to total capital investment [–]
t	time [h]

Greek letters

α	scaling factor [–]
η	efficiency [%]
Σ	sum

Abbreviations

CBM	bare module cost
CEPCI	Chemical Engineering Plant Cost Index
CHP	combined heat and power
DH	district heat
EU	European Union
EY	energy yield
FCI	fixed capital investment
GHG	greenhouse gas
IRR	internal rate of return
MY	mass yield
NPV	net present value
PBP	payback period
PEC	purchased equipment cost
TCI	total capital investment
USD	United States dollar

Subscripts

b	boiler
bc	biocoal
chips	total fuel input
dry	dry basis
el	electricity
f	boiler fuel
feed	torrefaction feedstock
net	net
O&M	operation and maintenance
p	purchased
s	sold
wet	wet basis

moisture content and low bulk density [3,4]. Torrefaction is a thermal pre-treatment process to convert raw biomass into more homogeneous and with subsequent pelletizing energy-dense product. In torrefaction, the feedstock is heated slowly (<50 °C/min) to the reaction temperature, typically 200–300 °C, under atmospheric pressure in the absence of oxygen [4–6].

The torrefied biomass (biocoal) with improved properties can be then co-fired with pulverized coal. Torrefaction thus makes it possible to increase the use of biomass in coal-fired boilers, reducing greenhouse gas (GHG) emissions and making the energy production more sustainable [7–9]. Even though there is still limited amount of available related data from industrial applications, the research in this area shows that co-firing of torrefied biomass with coal allows a significant reduction of CO_2 emissions without a major penalty in boiler efficiency [7,10]. Torrefied pellets also have certain advantages in comparison with traditional wood pellets considering not only their physical properties and energy content but also the gas emissions from combustion. McNamee et al. [11] evaluated the life-cycle GHG emissions of several supply chains for torrefied pine and reported that torrefaction could allow to produce lower GHG emissions per output energy content, compared to conventional wood pellets. In another study [12], the gas emissions from the combustion of a range of fuels (torrefied spruce, peat, biomass/coal blend and two coals) were investigated. The results indicated the lowest levels of NO_x and CO emissions for the torrefied wood briquettes among all the studied fuel samples and a significant reduction (approx. 40%) of particulate emissions from combustion of torrefied wood compared to the source material.

The integration of biomass pre-treatment processes with industrial systems can lead to benefits through more efficient utilization of the available mass and energy streams. Various integration possibilities of biomass conversion processes with CHP plants or other industrial processes have been evaluated recently. Technical, economic and environmental benefits of integration of the biomass gasification into CHP based district heating (DH) system have been reported in [13,14]. The combination of cellulosic bioethanol production and a CHP plant may help to increase the operating hours, resulting in an increased power generation and improved overall system efficiency [15]. Opportunities for integrating pellet production and a CHP plant have been also intensively studied in [16–18] with the main outcomes of annual power production growth, significant reduction of CO_2 emissions and additional economic benefits from pellets trade obtained. The integration of torrefaction within a CHP plant can potentially cover the energy requirements of the torrefaction process and simultaneously increase the power generation and annual operating hours of plant as well as generate the valuable product for sale. Starfelt et al. [19] investigated the advantages of a combined system of torrefaction and CHP that covers the energy demand of the torrefaction reactor and keeps the heat and power generation at required levels. Possibilities of co-location of torrefaction facilities with coal-fired power plants and corn ethanol plants were evaluated in [20]. Kohl et al. [21] compared the energetic and environmental performance of the retrofit-integration schemes of a CHP plant and three biomass pre-treatment processes (fast pyrolysis, torrefied pellets and wood pellets production).

Typically, the annual operation of a CHP plant follows the pattern of seasonally varying district heat demand [21]. In addition to quantitative changes in the DH demand, the required DH supply temperature, temperature of combustion air, and the moisture and temperature of the boiler fuel vary during the year. Despite the aforementioned issues, the CHP plant operating parameters are often calculated only at design point to evaluate the possibilities of integration [14,17,20,22]. Some researchers investigated the effect of part-load operation on the performance of integration schemes [16,21,23,24]. At the same time, the comprehensive evaluation of the integration scheme is only possible when all the seasonal changes of operational conditions along with the characteristic features of the CHP plant at part load are taken into account.

In a previous study [25], six integration concepts of torrefaction and a CHP plant were assessed within the typical range of torrefaction temperatures. The effect of the plant configuration and available boiler capacity on the thermodynamic performance of the integrated plants were evaluated by simulating the integration of torrefaction with two different CHP plants. The performance of both plants was evaluated only in one specific operation mode. In order to expand the evaluation to cover the seasonal operational changes, a multiperiod model was implemented to approximate the DH demand duration curve and to consider the annual variations of the fuel quality and ambient conditions in the present paper.

In Northern Europe co-generation plants are often backpressure steam plants for producing mainly district heat. Consequently, the plant annual operation time and corresponding power generation are limited by the DH network demand. The integration of this type of plant with torrefaction process allows utilizing the available plant capacity for a longer period to lower DH loads, thus increasing the annual production and thereby investment profitability. At the same time, fulfilling the heat demand of torrefaction without compromising the required thermal output can become problematic during the cold period of the year. Therefore, the changes of the plant operational parameters have to be taken into account for a proper and detailed evaluation of different integration schemes. On the basis of the results from the previous work, the current study evaluates the operability of the three most promising integration schemes in terms of varying the DH loads and ambient conditions.

In addition to the operational analysis, the present work evaluates the overall economic performance of the chosen alternatives of torrefaction integration into CHP plant. Considering a relatively high uncertainty of future energy prices, emission trading schemes and government support and taxes, the accurate prediction of profitability for new energy technologies can be challenging. At the same time, even preliminary assessment of these factors brings valuable information for determining technology potential. In the work, the integration cases together with stand-alone options are compared in terms of payback period (PBP), net present value (NPV) and internal rate of return (IRR) using three scenarios for electricity market prices and investment costs for the plants. The annual net cash flow for the considered cases is calculated at varying interest rate values. A sensitivity analysis for the internal rate of return is performed to determine the main economic factors influencing the profitability of each scenario.

2. Studied cases

CHP plants in district heating systems are typically base load plants; in Finland, as an example of a northern EU country, they are typically sized to cover approximately 40–60% of the peak DH load. The CHP plant can usually operate down to 40–50% part load [26]. The annual heat consumption and heat load duration curve of a DH demand strongly depends on the climate and can vary significantly from region to region. In addition, the types of heat consumers determine the DH load curve. The district heating systems in Northern Europe must be able to cover both winter peak load (usually a relatively short period), and minimum load (ca. 10% or less of the peak load) during the non-heating season [26]. Generally, the heat production of base load CHP plants accounts for at least 4000. . .5000 annual full-load operating hours and covers approximately 80% of the total heat demand. Auxiliary hot water boilers are usually operated to provide the heat to the DH network outside the limits of the CHP plant operation, i.e. at peak load and when the demand is less than the minimum load of the CHP plant.

Table 1 summarizes the main characteristics of the wood-fired CHP plant considered for the integration options. The small-scale co-generation backpressure plant has maximum and minimum district heating loads of 20 MW and 8 MW correspondingly, and a power generation of 8 MW_{el} at full load. In the following, the evaluated models are described briefly; more detailed description of the part-load modeling can be found from Ref. [27].

The torrefaction unit operational parameters are set to a temperature of 250 °C and 30 min of residence time. The resulting mass and energy yields are MY = 82.7% and EY = 92.5%, and the biocoal heating values of LHV_{dry} = 21.8 MJ/kg and HHV_{dry} = 23.0 MJ/kg. Modeling assumptions and further details on torrefaction unit simulation can be found in a previous study [25]. The electricity consumption of the biocoal pelletizing process (the pellet press is not presented in the process diagrams) is assumed to be 180 kJ/kg [28].

Three different integration concepts from the previous work [25] are considered: Case 1, Case 5 and Case 6. All cases are designed for torrefied pellet production at a rate of 5 t/h (1.39 kg/s). The process flow diagrams are presented in Fig. 1. The integrated cases are compared to the separate CHP plant and torrefaction unit co-located at the same site (Case 0). In this case, the heat demand of torrefaction is covered with a stoker boiler having an efficiency of η_b = 82%. Co-location of the considered processes will result in benefits for feedstock logistics, storage and handling even if the units themselves are not integrated.

For the integrated cases, the operating strategy is to fulfil completely the DH demand at any given load while maintaining also full-rate torrefaction, leaving electricity generation as a free variable. During part-load operation of the CHP plant certain operation parameters of the CHP cycle become limiting factors for the plant operation. The minimum boiler furnace temperature is set as 700 °C to maintain efficient combustion. Another boundary parameter is the stack temperature of flue gases, which is maintained higher or equal to 135 °C in order to avoid low temperature corrosion caused by flue gas condensation.

2.1. Multiperiod model

A multiperiod DH load model has been used in some earlier studies, such as Savola [29] and Kohl et al. [21,24]. In the current work, a typical Finnish DH demand curve of a small municipality is represented by 35 MW peak winter load with a linear approximation between a 20 MW heat load at 1800 h and 2.6 MW minimum load during the non-heating season. The annual district heating production amounts to 4740 full-load hours. The considered CHP plant operates 1800 h at full load with total annual operating time of 6000 h.

In order to consider the annual variation in heat load in the DH network and ambient conditions, a multiperiod approach is developed. The CHP plant DH load is modeled with two full-load periods (P1 and P2) which differ only in their DH temperatures and ambient conditions. These periods are then followed by a steady reduction of load by 4 MW intervals (from P3 to P6) until the summer low-load period P7 and minimum-load period P8.

Table 1
CHP plant main characteristics.

Parameter	Full load	Minimum load
Net power output	8.0 MW	2.0 MW
District heating output	20.0 MW	8.0 MW
Total (CHP) efficiency	85%	83%
Live steam parameters	90 bar/500 °C	90 bar/450 °C
Furnace temperature	900 °C	700 °C

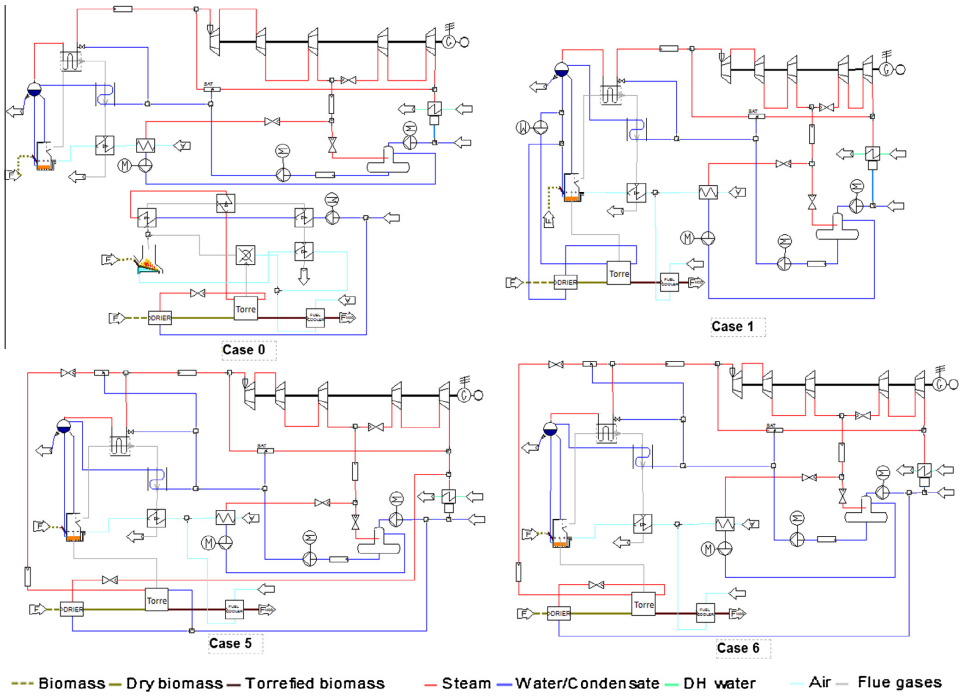

Fig. 1. Process flow diagrams of the co-located CHP and torrefaction units (Case 0) and three integrates (Case 1: saturated water from the drum for torrefier and drier; Case 5: live steam for torrefier and low pressure steam for drier; Case 6: live steam for torrefier and steam after torrefier to the drier).

The ambient temperature data is based on 30-year monthly average temperatures gathered by the Finnish Meteorological Institute [30] for city Jyväskylä (central Finland). The temperature of the boiler fuel and torrefaction feedstock is set equal to the average ambient temperature of each period. The combustion air temperature, taken from the boiler room, is assumed to be 20 °C higher than ambient temperature. The district heating water output and return temperatures are based on the temperature levels from [26]. The seasonal changes of wood chips quality is affected by their moisture levels that typically increase towards the winter. The main characteristics for each load point level within the multiperiod model are summarized in Table 2. The annual variation of district heat demand as well as the heat and electricity production is illustrated in Fig. 2.

3. Annual production and consumption

The integration schemes require heat and electricity from the CHP plant. At the same time, by increasing the operating hours it is possible to obtain revenues from higher power production by means of supplementary heat consumer – the torrefaction unit. The biocoal production capacity of the torrefaction unit is set at 30.3 MW_{LHV} throughout whole the operating period: 8000 h in Case 0, and equal to the CHP operating hours in the integrated cases. The torrefaction feedstock rate increases from 27.8 to 30.0 MW_{LHV} as the feedstock moisture reduces from 55% (in winter) to 40% (in summer).

Under the assumptions considered in the present work, Case 1 cannot be operated during winter months with the required torrefaction output. In this integration scenario, the heat of drum water for the torrefaction needs is taken straight from the boiler cycle, hampering remarkably the boiler performance, especially during high district heating demand. Because of this, the following analysis is concentrated on two other integration cases.

Fig. 3 presents the multiperiod model approximation of the obtained electricity and DH output levels produced within a year. The variation of boiler fuel input (including the stoker boiler in Case 0) together with the DH heat demand curve is also shown.

For the integrated cases, the heat demand of the dryer (ranging from 9.6 MW in winter to 3.7 MW in summer) presents a significant share in the overall balance of the considered CHP plant. At low loads, the flue gas temperatures decrease and start to approach the lower limit. The minimum operating point of 6.4 MW district heat output for Case 6 corresponding to the furnace temperature limit (700 °C) is reached at 7085 h operational time. When the heat requirement of the dryer is covered with low pressure steam before the DH condenser (Case 5), the steam flow through the turbine and consequently the boiler output are increased. Due to this further increase of the boiler load, the operating time of Case 5 integrated plant is prolonged to 7470 h corresponding to 4 MW district heat output.

The boiler fuel input for Case 6 differs clearly from Case 0 during full load and reduced-load periods (after 6000 h). At the same time, during a significant part of the year, the difference is very small

Table 2
Summary of the load points and their duration during the year in the multiperiod model.

Parameter	P0	P1	P2	P3	P4	P5	P6	P7	P8
Time									
Period duration [h]	0	240	1560	1400	1400	1400	1400	490	870
Cumulative at end [h]	0	240	1800	3200	4600	6000	7400	7890	8760
Load and production									
Mean heat load [MW]	35	30	22.5	18	14	10	6	4	2.6
CHP heat output [MW]	20	20	20	18	14	10	8	0	0
Temperatures									
Ambient [°C]	−20	−10	−5	0	5	10	12	15	15
Makeup water [°C]	5	5	5	5	10	10	10	10	10
DH water supply [°C]	105	90	85	80	75	75	75	75	75
DH water return [°C]	60	50	50	50	45	45	45	45	45
Fuel									
MC_{wet} [%]	55	55	55	50	50	45	45	40	40
Temperature [°C]	−20	−10	−5	0	5	10	12	15	15
LHV_{wet} [MJ/kg]	7.43	7.43	7.43	8.53	8.53	9.62	9.62	10.72	10.72

MC_{wet}: moisture content on wet basis; LHV_{wet}: lower heating value on wet basis

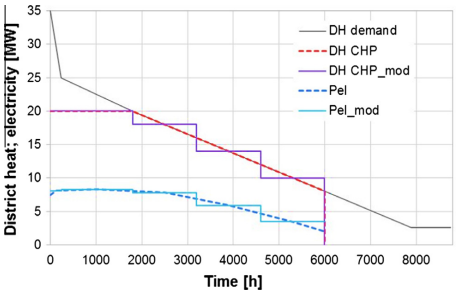

Fig. 2. DH load duration curve, DH production and electricity generation of the CHP plant with corresponding multiperiod approximations DH CHP_mod and Pel_mod.

(compare to the dashed lines Fig. 3). Case 5 shows a different pattern: covering the heat demand of the dryer with low pressure steam yields a clear increase of power generation from approximately 3000 h onwards, and thus also requires more boiler fuel input. At the full-load periods, however, the integration with torrefaction reduces the net power output of both integrated scenarios to approximately zero (in fact, slightly negative). This is due to the need to bypass most of the boiler steam production through the reduction valve to the torrefaction plant dryer and the district heat condenser to maintain both torrefaction and necessary DH output. The very small remaining power output is exceeded by the combined power consumption of the torrefaction plant and the auxiliary systems of the CHP plant.

Table 3 summarizes the overall figures of annual net production and consumption of various energy streams. The sold and purchased electricity is separated for the purposes of further economic analysis, since these have different prices. The trigeneration efficiencies of the plants are evaluated with Eqs. (1) and (2). The results are presented in Table 3. The values are calculated in both lower heating value (LHV) and higher heating value (HHV) terms from the net annual energy production of electricity $E_{el,net}$, district heating Q_{DH} and biocoal Q_{bc}, and the wood chips input as boiler fuel Q_f and torrefaction feedstock Q_{feed}:

$$\eta_{LHV} = \frac{E_{el,net} + Q_{DH} + Q_{bc,LHV}}{Q_{feed,LHV} + Q_{f,LHV}} \quad (1)$$

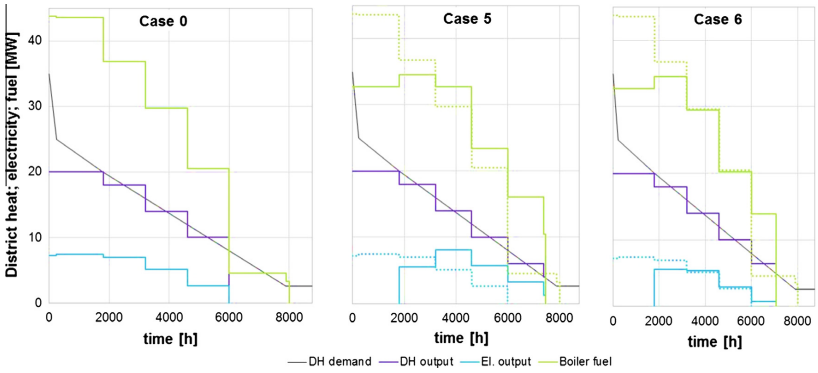

Fig. 3. DH load duration curve, annual district heat and power production of the CHP plant together with boiler fuel consumption (CHP and stoker boiler in Case 0) using the multiperiod model. Dashed lines in Cases 5 and 6 refer to Case 0 values.

Table 3
Annual energy inputs and outputs of separate CHP and torrefaction plants, co-located plants (Case 0), and two integration options.

Case	CHP	Torrefaction	Case 0	Case 5	Case 6
Fuel input					
CHP boiler fuel $Q_{f,BFB}$ [GW h_{LHV}]	157.27	–	157.27	209.01	191.85
Stoker boiler $Q_{f,S}$ [GW h_{LHV}]	–	51.39	51.39	–	–
Torre feedstock $Q_{feed,LHV}$ [GW h_{LHV}]	–	230.57	230.57	214.66	203.29
Total $Q_{chips,HHV}$ [GW h_{HHV}]	193.59	342.69	536.28	516.79	482.80
Total $Q_{chips,LHV}$ [GW h_{LHV}]	157.27	281.96	439.24	423.67	395.14
Energy products					
Net electricity $E_{el,net}$ [GW h]	38.96	−6.58	32.38	30.35	18.85
Sold electricity $E_{el,s}$ [GW h]	38.96	0	33.96	31.68	20.22
Purchased electricity $E_{el,p}$ [GW h]	0	6.58	1.59	1.33	1.37
District heat output Q_{DH} [GW h]	94.80	0	94.80	103.47	101.80
Biocoal output $Q_{bc,HHV}$[GW h_{HHV}]	0	255.79	255.79	238.71	226.53
Biocoal output $Q_{bc,LHV}$ [GW h_{LHV}]	0	242.35	242.35	226.30	214.63
Trigeneration efficiency					
η_{LHV} [%]	85.05	83.62	84.13	85.00	84.85
η_{HHV} [%]	69.09	72.72	71.41	72.09	71.91

$$\eta_{HHV} = \frac{E_{el,net} + Q_{DH} + Q_{bc,HHV}}{Q_{feed,HHV} + Q_{f,HHV}} \quad (2)$$

As can be expected, the total fuel input for the integrated cases is much higher than in the case of CHP plant. At the same time, the generation of an additional revenue stream through biocoal and the possible growth in power and heat production can make the integration schemes beneficial. The biocoal output along with the electricity and DH generation are the largest in Case 5 due to the longest plant operating time among all the other integrated cases. The stand-alone co-generation plant has higher efficiency in LHV terms than the stand-alone torrefaction case and any of the considered integrates. Nevertheless, since the feedstock for torrefaction is not burned except for the gaseous product from the torrefaction reactor, the loss with latent heat of biomass moisture decreases and the differences in trigeneration efficiencies in HHV terms of the integrated cases are relatively small. Even though the co-location of CHP and torrefaction plants (Case 0) is more advantageous in LHV terms than the stand-alone operation of torrefaction, the integration scenarios show better efficiencies in both LHV and HHV terms.

Fig. 4 illustrates the distribution of the relative fractions of the annual outgoing energy streams from the studied processes. The generated products are presented in blue-green tones, while the energy losses are coloured in orange-brown. The overall rating of the considered factors are quite similar for all the studied cases with the main differences in the products' share distribution between integrated and co-located cases. Biocoal takes the highest share among the outgoing streams, followed by district heating load and electricity production. DH production and power generation are gaining a slightly higher share in the case of integration. Among the losses, the heat demand of the dryer and the boiler losses are the largest. The heat consumption of torrefaction unit itself and electromechanical losses of the plant are relatively small within the balance. The main variations of the balance among the integrated options are connected to the plant operation time during the year, and the absolute amount of energy produced or lost will be determined by the annual performance. At the same time, the relative fractions of energy streams give an overall distribution between energy products and process losses for the integrated cases.

The variation of the trigeneration efficiencies in LHV and HHV terms within the operating time is shown in Fig. 5a. As it can be seen, the efficiencies of the considered integrated schemes are virtually the same. Certain alterations between stand-alone CHP, co-located plants and integration cases can be explained by varying levels of energy inputs and outputs which were mentioned earlier. The part-load operation with the higher electricity generation and the longer operating time make the differences between the integrated cases and CHP plant more pronounced. Closer to the minimum DH loads, efficiency of the CHP plant starts to reduce, while integration cases are still able to use more of the available boiler capacity, and maintain better efficiency. The operation of the co-located plants (Case 0) at the minimum load periods is determined only by the performance of the torrefaction unit with the stoker boiler. As a result, the HHV efficiency increases stepwise at 6000 h. This change proceeds more smoothly in the case of the LHV efficiency, since the difference between its value for the CHP plant at low loads and the torrefaction unit is quite small.

Fig. 5b represents the annual variations of boiler losses as one of the major loss components changing within a year. The lower efficiency of the stoker boiler results in slightly increased boiler loss in Case 0 compared to the integrated cases. The operating period between 6000 h and 8000 h for the co-located plants is associated solely with the loss from the stoker boiler as the CHP boiler is not

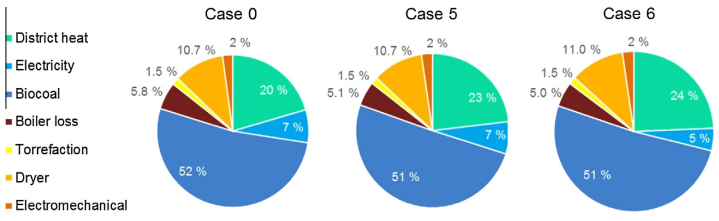

Fig. 4. Outgoing energy flows as fractions of plant annual operation.

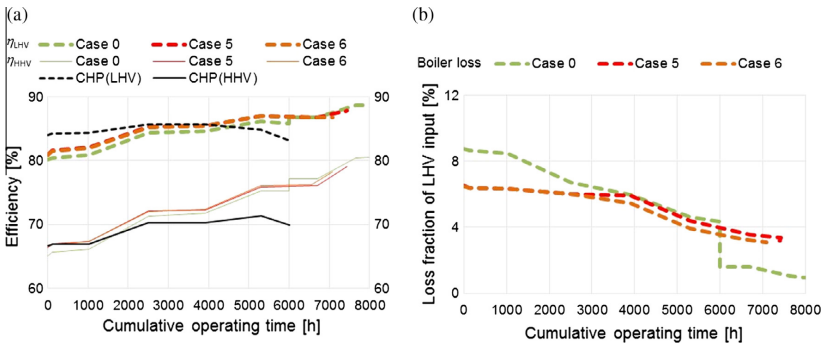

Fig. 5. Variation of efficiency and boiler losses as a function of cumulative operating time for the different cases.

used. The shutdown of the CHP boiler results in a step decrease of the boiler loss curve at 6000 h. Both graphs at Fig. 5 illustrate and underline the importance of considering the operational conditions throughout the year, since these result in significant seasonal variation of plant performance.

4. Economic analysis

4.1. Total capital investment

The equipment of the integration plants was sized on the basis of the maximum capacity obtained from the simulation results and increased by overdesign factors. Typical values of overdesign factors (1.1–1.2) allow to mitigate design uncertainties and possible alterations of the operating performance [31].

The cost of purchased equipment (PEC) was calculated by means of cost indexes and scaling factors. Cost indexes are used to predict the costs of materials and equipment based on historical cost data. The Chemical Engineering Plant Cost Index (CEPCI) was applied to make a general estimate of the processing equipment investment [31]. All prices were converted from year y to the base year 2014 Euro; the cost data given in US dollars (USD) was converted to Euro with the average annual exchange rate in the year of interest [32]:

$$Cost_{€,2014} = Cost_{USD,y} \frac{CEPCI_{2014}}{CEPCI_y} \frac{€_y}{USD_y} \quad (3)$$

If the cost for the particular operational capacity or size of the equipment is not available, it can be approximated on the basis of available cost data for the similar equipment of another capacity. The scaling factors allow to estimate the cost of an item a ($Cost_a$) of capacity X_a on the basis of the available data ($Cost_b$) for the equipment of the same type but different size or capacity (X_b) [28,33]:

$$Cost_a = Cost_b \left(\frac{X_a}{X_b}\right)^{\alpha} \quad (4)$$

where α is the equipment-specific scaling factor, and X is the capacity of the item.

Since torrefaction is a developing technology, the estimation of the equipment investment costs has some uncertainties due to the limited available information. In the present work, the equipment cost data for biomass processing (torrefaction reactor, pellet press, wood chips dryer and conveyor) was taken from a specific vendor information presented in [28]. The cost for standard equipment (e.g., heat exchangers) was taken from available literature [28,34]. The purchased cost of the CHP plant was evaluated from available data: [35] for the boiler; [36] for the turbine and generator; [31,33] for other equipment. The torrefaction stand-alone plant equipment assets along with the total module costs (CBM) are listed in Table 4.

The total module cost of equipment consists of the sum of the PEC and other cost factors directly related to the erection of the purchased equipment (i.e. instrumentation and controls, equipment erection and construction expenses, piping and electrical equipment and materials). If no item specific data is available, the ratio CBM/PEC was assumed to be 2.88 for the CHP plant components and 2.46 for the torrefaction plant as suggested in [37].

In order to calculate the total capital investments (TCI) of the studied integrated and stand-alone cases, the fixed capital investment (FCI) costs and working capital should be evaluated. The offsite costs (45% of PEC) summarize the cost for land, ancillary buildings, site development and utilities. The total module cost together with offsite costs are the direct costs. Start-up expenses (10% of PEC) cover the cost of possible start-up changes in materials and equipment and the loss of income before reaching the maximum design capacity. The expenses on engineering and construction design together with purchasing, procurement and construction supervision are addressed as the engineering and supervision cost component (12% of PEC). Start-up and engineering cost factors contribute to the indirect costs category. Contractor's fee is implemented as 5% of the indirect and direct costs. The contingencies (10% of indirect and direct costs) take into account the expenses on unpredictable circumstances (e.g. strikes, price changes, storms, floods, errors in estimations). The sum of the aforementioned cost factors represents the fixed capital investment category which covers all the capital required for the installed equipment together with all auxiliaries. The working capital for the industrial plant (15% of FCI) estimates the total amount of money needed above the fixed capital to start the plant up and to operate until the moment of receiving the first income. The final value of the total capital investments consists of the working and fixed capital. The aforementioned assumptions for the total capital investment component calculations were taken from the literature [31,33]. Table 5 summarizes the cost data for the considered plants.

The investment cost for torrefaction reactors published in the literature varies widely depending on the reactor type and other auxiliary equipment. Several selected facilities presented in [38] give a range of costs from 1.4 M€/(t/h) to 4.5 M€/(t/h) with annual

Table 4
Total module cost for torrefaction unit equipment.

Equipment	Specification	Capacity	CBM [M€]	Source
Torrefaction reactor	Moving bed reactor	6.4 t/h	2.2	[6,28]
Biomass dryer	Belt dryer	7075 kg_{H2Oev}/h	2.7	[28]
Biomass feeding and storage	Wood conveyor and storage	18.4 t/h	0.7	[28]
Stoker boiler	Biomass fired boiler	10 MWth	5.2	[40]
Biocoal cooler	Air-cooled heat exchanger	18 m^2	0.2	[28,31]
Pellet press and handling	Pellet press including conditioning	4.9 t/h	1.1	[28]
Biocoal storage/handling	Pellet storage	4.9 t/h	0.5	[28]

Table 5
Total capital investment calculation for studied cases. All numbers in millions of euros.

			CHP	Torrefaction	Case 0	Case 5	Case 6
Purchased equipment cost		Torrefaction unit	–	3.0	3.0	2.7	2.7
		Stoker boiler	–	1.8	1.8	–	–
		CHP	5.8	–	5.8	5.8	5.8
	Direct costs	Total module cost	16.6	12.5	29.1	23.2	23.2
		Offsite cost	2.6	2.1	4.7	3.8	3.8
		Σ	19.2	14.6	33.8	27.0	27.0
Fixed-capital investment	Indirect costs	Engineering	0.7	0.6	1.3	1.0	1.0
		Start-up	0.6	0.5	1.1	0.8	0.8
		Σ	1.27	1.05	2.3	1.9	1.9
	Contractor's fee		1.0	0.8	1.8	1.4	1.4
	Contingencies		2.0	1.6	3.6	2.9	2.9
	Σ		23.5	18.0	41.5	33.2	33.2
Working capital			3.5	2.7	6.2	5.0	5.0
Total capital investment			27.1	20.7	47.7	38.1	38.1

capacities of 10–70 kt/a of torrefied biomass. The specific TCI cost for the reactor considered in the current work is at the level of 4 M€/(t/h) within the mentioned limits. The differences between the equipment of the integrated cases are assumed to be negligible and their investment costs are thus identical. The integration of torrefaction and CHP requires 20% less capital investment than co-located plants. The torrefaction unit represents 32% of the total purchased equipment cost of the integrated plant and results in approximately 40% higher capital investments of the integrates over the stand-alone CHP plant.

4.2. Profitability evaluation

The most commonly used methods for profitability evaluation - net present value (NPV), internal rate of return (IRR) and payback period (PBP) - are used for the economical assessment of the considered integration schemes at three different price assumption scenarios. Among the methods, NPV and IRR are usually applied for project evaluation.

Different electricity price scenarios (high, medium and low) were set for the market price of sold electricity on the basis of a report ordered by the Finnish Ministry of Employment and Economy [39]. Table 6 summarizes the values of the parameters when they were not treated as variables for economical evaluation applied in current study.

Considered co-located and integrated scenarios have the incoming cash flows from the sold products: electricity, district heat and biochar. The outgoing cash flows are represented by the expenses on the boiler fuel and torrefaction feedstock, purchased electricity and the operation and maintenance cost. Assuming no residual value for the investment, the NPV of a project is determined as the total sum of the present worth of future cash flows during the project economic life time of n years discounted at an interest rate of i, subtracting the value of total capital investment TCI:

Table 6
Values of parameters (when not treated as variables in the economic analysis).

Parameter	Value	Energy product	Price
Maximum annual operating time t [h]	8000	Wood chips price c_f [€/MW h_{LHV}]	20
Interest rate i [%]	10	Sold electricity price (high) $c_{el,s}$ [€/MW h]	77
Plant economic life time n [y]	25	Sold electricity price (medium) $c_{el,s}$ [€/MW h]	44
Annual O&M cost ratio for CHP plant $r_{O\&M,CHP}$ [%]	4	Sold electricity price (low) $c_{el,s}$ [€/MW h]	21
		Purchased electricity price $c_{el,p}$ [€/MW h]	100
Annual O&M cost ratio for torrefaction unit $r_{O\&M,Torre}$ [%]	6	District heat price c_{DH} [€/MW h]	60
		Biocoal pellets price c_{bc} [€/MW h_{LHV}]	40

$$NPV = \frac{(1+i)^n - 1}{i \cdot (1+i)^n}\left[E_{el,s}c_{el,s} + Q_{DH}c_{DH} + Q_{bc,LHV}c_{bc} - Q_{chips,LHV}c_f - E_{el,p}c_{el,p} - C_{O\&M}\right] - TCI \quad (5)$$

where the annual energy streams E and Q are shown in Table 3 and the corresponding prices c.

The internal rate of return is calculated with Eq. (5) by solving it iteratively for such interest i that the NPV becomes zero. The PBP is found similarly by setting the NPV to zero in Eq. (5), and solving for the number of years n.

The annual operation and maintenance cost $C_{O\&M}$ is determined as a fraction $r_{O\&M}$ of the total capital investments. For a small-scale biomass-fired CHP plant the value for $r_{O\&M,CHP}$ = 4% was assumed based on another investigation [40]. Since the torrefaction is a developing technology, slightly higher O&M fraction of $r_{O\&M,Torre}$ = 6% was set in the current study. The overall cost for the operation and maintenance in all scenarios should include the

corresponding expenses of the CHP plant and torrefaction, thus the combined value of the cost for operation and maintenance $C_{O\&M}$ was applied. The value was calculated with the mean $r_{O\&M}$ weighted with the fractions of the purchased equipment cost of the CHP plant and torrefaction unit:

$$C_{O\&M} = \left(r_{O\&M,CHP} \frac{PEC_{CHP}}{PEC_{CHP+Torre}} + r_{O\&M,Torre} \frac{PEC_{Torre}}{PEC_{CHP+Torre}} \right) \cdot TCI \qquad (6)$$

Table 7 summarizes the annual cash flows for the considered cases in conditions of the investment amortization in equal annual payments within the project economic life time. Sold electricity is calculated with medium price of 44€/MW h. The relation between interest rate value (15%, 10% and 5%) and annual net cash flow was investigated. With the interest rates of 15% and 10%, the stand-alone torrefaction reactor is unprofitable. On the other hand, interest rate of 5% improves the performance of all studied cases, and even the stand-alone torrefaction unit becomes profitable. Among the integrated cases, the highest cash flow is observed in Case 5 yielding 62% increase of the net cash flow over the co-located plants. The integration Case 6 results in more moderate changes: cash flow is 39% higher than that of Case 0 (i = 5%). At the baseline interest rate of 10%, the integration options increase the annual cash flow by 8–11 times compared to the stand-alone CHP plant. With the higher level of interest rate (15%), only Case 5 results in positive annual cash flow value, thus making this integration option more beneficial than the stand-alone CHP plant or simple co-location.

Three different scenarios for the total capital investment of the studied cases are investigated: base level (TCI value from Table 5), optimistic (−25% from the base scenario) and pessimistic (+25% from the base scenario). The main results of IRR, NPV and PBP calculation in terms of concerned economic scenarios are illustrated in Fig. 6. In addition to the variation of the TCI (characterized by lines' colours), the effect of three different price levels of sold electricity is considered (indicated by the different line patterns).

As could be expected, the integration Case 5 shows the best results within all three investigated metrics for profitability evaluation due to its longer operating time and increased electricity and DH production. Compared to Case 0, both studied integration options improve the profitability in all considered schemes.

The main economic drivers which have an impact on the project performance can be identified from their effect on the internal rate of return. A sensitivity analysis of the project IRR to the range of parameters (with ±20% change) is presented in Fig. 7 with baseline investment costs and medium electricity cost assumptions.

The IRR of the stand-alone torrefaction unit is particularly sensitive to the price of wood chips. The investment cost is the second important factor which defines the profitability. The changes in other two parameters - purchased electricity price and O&M costs - result in variations of the IRR in a quite narrow range (2%). The profitability of CHP plant is mainly defined by the district heat price and the capital investment cost. While district heat constitutes the main product, the effect of sold electricity price appears to be limited. The electricity price is likely to be far more volatile than any of the other prices. The variation of 20% is a relatively large for most of the parameters, but the electricity price can in fact be subjected to uncertainties of even several times greater magnitude. The effect of the wood chips price is considerably smaller in comparison with the torrefaction plant due to the higher conversion efficiency of the generated products.

The integrated cases show practically identical results. The effect of the investment cost followed by the feedstock and district heat prices cause the highest impact on the project profitability. This dependence is relatively similar to the case of co-located plants (Case 0). The small effect of the purchased electricity price is a result of the need to augment the CHP plant's own production with purchased electricity to cover the total plant power demand during full-load periods. The IRR in Case 5 with the highest power generation among all the integration cases is slightly more sensible to the sold electricity price than in Cases 0 and 6 due to the increased power generation.

5. Summary and conclusions

This study has shown that the heat integration of a torrefaction process into a CHP cycle could be economically profitable over the co-located plants under certain circumstances. While the previous investigation revealed important benefits of the integration with CHP at reduced district heating load, the analysis of the integrated cases considering seasonal operational changes brings a more complete understanding of the annual operation for each scenario. The typical backpressure CHP plant that was analysed in the present work fulfils the district heating demand and, as a result, follows all the annual variations of the DH network (both qualitative and quantitative). The operational analysis of the current study takes into account all major changes that affect the plants performance in order to evaluate the potential of possible integration.

Three scenarios to cover the heat requirements of a torrefaction unit (30.3 MW_{LHV} production capacity) were initially evaluated: drum water (Case 1), live steam and low pressure steam (Case 5) and only live steam (Case 6). The analysis showed that integration options using live steam to cover the torrefaction demand have significant benefits. Within the frames of the considered capacity levels and the limitations for the plant operation, the integrated scenario of Case 1 cannot be operated during full-load periods. Reducing the capacity of the torrefaction unit may result into certain improvements, but for purpose of keeping the cases comparable, only Cases 5 and 6 were considered in the current work.

Table 7
Annual cash flows of different cases.

	CHP	Torrefaction	Case 0	Case 5	Case 6
Investment amortization (i = 15%) [M€]	−4.19	−3.20	−7.39	−5.90	−5.90
Investment amortization (i = 10%) [M€]	−2.98	−2.28	−5.26	−4.20	−4.20
Investment amortization (i = 5%) [M€]	−1.92	−1.47	−3.39	−2.71	−2.71
Operation and maintenance [M€]	−1.08	−1.65	−2.32	−1.75	−1.75
Boiler fuel [M€]	−3.15	−1.03	−4.17	−4.18	−3.84
Torrefaction feedstock [M€]	0	−4.61	−4.61	−4.29	−4.07
Purchased electricity [M€]	0	−0.66	−0.16	−0.13	−0.14
Sold electricity [M€]	1.71	0	1.49	1.39	0.89
Sold district heat [M€]	5.69	0	5.69	6.21	6.11
Sold biocoal [M€]	0	9.69	9.69	9.05	8.59
Annual net cash flow (i = 15%) [M€]	−1.01	−1.46	−1.78	0.40	−0.11
Annual net cash flow (i = 10%) [M€]	0.19	−0.54	0.35	2.10	1.59
Annual net cash flow (i = 5%) [M€]	1.25	0.27	2.22	3.59	3.09

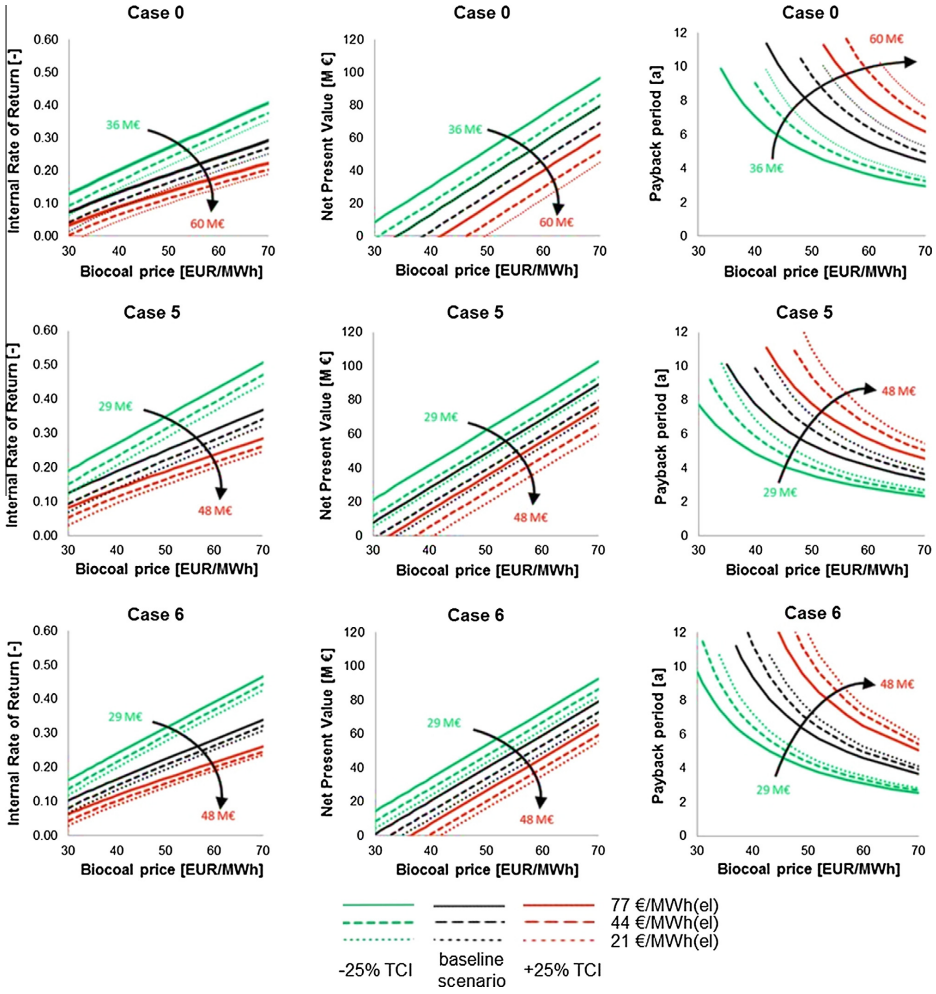

Fig. 6. Studied cases compared in terms of IRR, NPV and PBP. Line colour indicates the investment cost scenario (green – optimistic, black – base and red – pessimistic). Line pattern corresponds to the price level of sold electricity. (For interpretation of the references to colour in this figure legend, the reader is referred to the web version of this article.)

The energy efficiencies of the integrated cases are comparable with those of a stand-alone co-generation plant: in this respect, integration offers no clear benefits. The possibility to increase the annual operation of the CHP plant, on the other hand, makes integration advantageous over the stand-alone operation or the simple co-location of the plants. For both integrated cases studied in this work, the torrefaction unit acts as an additional and relatively constant heat consumer, thus enabling the CHP plant to operate at a lower DH load than would be possible otherwise. This allows the annual operation time and district heat output be increased. Fulfilling the significant heat demand of the dryer by low pressure steam provides the important benefits to the plant overall performance: with increased live steam mass flow through the turbine, the electrical power output is higher than in case of the stand-alone CHP plant at all load points except full load, when the turbine has to be mostly bypassed.

The economic assessment indicated that the share of the torrefaction equipment in the total purchased equipment cost of integrated plant accounts for approximately 30%. On the whole, the integration options require about a 40% more capital investment than a stand-alone CHP plant. The torrefaction products should thus bring a significant additional revenue from the sale to justify

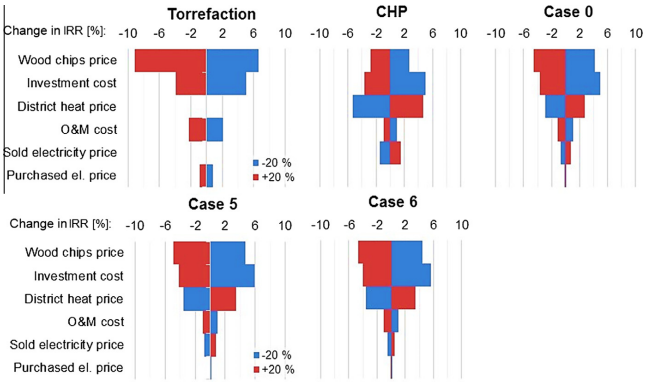

Fig. 7. Sensitivity analysis of IRR with ±20% change of parameters.

this investment. On the other hand, the integration options need ca. 20% less investments than co-located torrefaction and CHP plants. The relation between interest rate value and annual net cash flow for all studied cases was investigated. The integration options result into an annual cash flow increase by 8–11 times over the stand-alone CHP plant with the baseline interest rate of 10% and biocoal price of 40€/MW h. With a more realistic value of 5% interest rate, all integrated cases together with stand-alone torrefaction unit become profitable.

The profitability was evaluated with three commonly applied methods: net present value, internal rate of return and payback period. Different scenarios for sold electricity price and total investment cost helped to obtain a comprehensive assessment of the integrated options within different economic situations. The integration case with the longest operation time (Case 5) resulted into higher values of profitability in contrast to the other options: both integration and co-located. The investment cost and the wood chips price are the main economic factors influencing the profitability of the integrated options, while the IRR value of the stand-alone torrefaction unit is particularly sensitive to the price of wood chips.

The results confirm the importance of a detailed operational and economic analysis in order to evaluate the future potential of the torrefaction integration and to choose the most suitable configuration. Sustainable and economically efficient combination of the torrefaction process and co-generation plant has a lot of potential. Modeling and comprehensive analysis of available data from the pilot plants and other torrefaction facilities are necessary and important steps towards the development of torrefaction, and implementing it into real applications. The analysis of the present paper provides a basis for further more detailed evaluation that can be done for any existing co-generation plant of similar type. At the same time, the relatively high uncertainties over the future energy prices for electricity, district heat and biocoal make accurate evaluation of the economic perspectives difficult. The market price for electricity is subject to fluctuations due to a number of factors, such as renewable energy subsidies, and changes in the level of supply and demand. The investment costs for the torrefaction unit equipment are expected to decrease in the near future as this technology becomes more commercial. It was found from the operational analysis that the integration of torrefaction with a combined heat and power plant can be advantageous, particularly when using live steam for the high-temperature demand of torrefaction, and the lower-grade heat in the form of backpressure steam to fulfil the significant demand of the drier. The effect of torrefaction on a CHP plant is clearly determined by the torrefaction unit capacity, and more detailed investigation is necessary for the determination of the optimum size.

References

[1] Dahlquist E. An overview of thermal biomass conversion technologies. CRC Press; 2013. p. 1–3.
[2] McKendry P. Energy production from biomass (Part 2): conversion technologies. Bioresour Technol 2002;83(5):47–54. http://dx.doi.org/10.1016/S0960-8524(01)00119-5.
[3] Demirbas A. Combustion characteristics of different biomass fuels. Prog Energy Combust Sci 2004;30:219–30. http://dx.doi.org/10.1016/j.pecs.2003.10.004.
[4] Verhoeff F, Adell A, Boersma AR, Pels JR, Lensselink J, Kiel JHA, et al. TorTech: torrefaction technology for the production of solid bioenergy carriers from biomass and waste. ECN biomass, coal and environmental research, Petten, the Netherlands. Tech Rep ECN-E-11-039; July 2011.
[5] Yan W, Acharjee TC, Coronella CJ, Vásquez VR. Thermal pretreatment of lignocellulosic biomass. Environ Progr Sustain Energy 2009;28:435–40.
[6] Bergman PCA, Boersma AR, Zwart RWR, Kiel JHA. Torrefaction for biomass co-firing in existing coal-fired power stations "BIOCOAL". ECN, Petten, the Netherlands. Tech Rep ECN-C-05-013; July 2005.
[7] Li J, Brzdekiewicz A, Yang W, Blasiak W. Co-firing based on biomass torrefaction in a pulverized coal boiler with aim of 100% fuel switching. Appl Energy 2012;99(11):344–54. http://dx.doi.org/10.1016/j.apenergy.2012.05.046.
[8] Kihedu J. Torrefaction and combustion of ligno-cellulosic biomass. Energy Procedia 2015;75:162–7. http://dx.doi.org/10.1016/j.egypro.2015.07.273.
[9] Chen W, Huang M, Chang J, Chen C. Torrefaction operation and optimization of microalga residue for energy densification and utilization. Appl Energy 2015;154(9/15):622–30. http://dx.doi.org/10.1016/j.apenergy.2015.05.068.
[10] Koppejan J, Sokhansanj S, Melin S, Madrali S. Status overview of torrefaction technologies. Enschede (the Netherlands): IEA Bioenergy; 2012 [online].
[11] McNamee P, Adams PWR, McManus MC, Dooley B, Darvell LI, Williams A, et al. An assessment of the torrefaction of North American pine and life cycle greenhouse gas emissions. Energy Convers Manage 2016;113(4/1):177–88. http://dx.doi.org/10.1016/j.enconman.2016.01.006.
[12] Mitchell EJS, Lea-Langton AR, Jones JM, Williams A, Layden P, Johnson R, et al. The impact of fuel properties on the emissions from the combustion of biomass and other solid fuels in a fixed bed domestic stove. Fuel Process Technol 2016;142(2):115–23. http://dx.doi.org/10.1016/j.fuproc.2015.09.031.
[13] Difs K, Wetterlund E, Trygg L, Söderström M. Biomass gasification opportunities in a district heating system. Biomass Bioenergy 2010;34(5):637–51. http://dx.doi.org/10.1016/j.biombioe.2010.01.007.
[14] Fahlén E, Ahlgren EO. Assessment of integration of different biomass gasification alternatives in a district-heating system. Energy 2009;34(12):2184–95. http://dx.doi.org/10.1016/j.energy.2008.10.018.
[15] Starfelt F, Daianova L, Yan J, Thorin E, Dotzauer E. The impact of lignocellulosic ethanol yields in polygeneration with district heating – a case study. Appl Energy 2012;92(4):791–9. http://dx.doi.org/10.1016/j.apenergy.2011.08.031.

[16] Wahlund B, Yan J, Westermark M. A total energy system of fuel upgrading by drying biomass feedstock for cogeneration: a case study of Skellefteå bioenergy combine. Biomass Bioenergy 2002;23(10):271–81. http://dx.doi.org/10.1016/S0961-9534(02)00055-7.
[17] Song H, Starfelt F, Daianova L, Yan J. Influence of drying process on the biomass-based polygeneration system of bioethanol, power and heat. Appl Energy 2012;90(2):32–7. http://dx.doi.org/10.1016/j.apenergy.2011.02.019.
[18] Song H, Dotzauer E, Thorin E, Yan J. Annual performance analysis and comparison of pellet production integrated with an existing combined heat and power plant. Bioresour Technol 2011;102(5):6317–25. http://dx.doi.org/10.1016/j.biortech.2011.02.042.
[19] Starfelt F, Aparicio ET, Li H, Dotzauer E. Integration of torrefaction in CHP plants – a case study. Energy Convers Manage 2015;90(1/15):427–35. http://dx.doi.org/10.1016/j.enconman.2014.11.019.
[20] Tiffany DG, Lee WF, Morey V, Kaliyan N. Economic analysis of biomass torrefaction plants integrated with corn ethanol plants and coal-fired power plants. Adv Energy Res 2013;1:127–46. http://dx.doi.org/10.12989/eri.2013.1.2.127.
[21] Kohl T, Laukkanen T, Järvinen M, Fogelholm C. Energetic and environmental performance of three biomass upgrading processes integrated with a CHP plant. Appl Energy 2013;107(7):124–34. http://dx.doi.org/10.1016/j.apenergy.2013.02.021.
[22] Eriksson G, Kjellström B. Assessment of combined heat and power (CHP) integrated with wood-based ethanol production. Appl Energy 2010;87(12):3632–41. http://dx.doi.org/10.1016/j.apenergy.2010.06.012.
[23] Starfelt F, Thorin E, Dotzauer E, Yan J. Performance evaluation of adding ethanol production into an existing combined heat and power plant. Bioresour Technol 2010;101(1):613–8. http://dx.doi.org/10.1016/j.biortech.2009.07.087.
[24] Kohl T, Laukkanen TP, Järvinen MP. Integration of biomass fast pyrolysis and precedent feedstock steam drying with a municipal combined heat and power plant. Biomass Bioenergy 2014;71(12):413–30. http://dx.doi.org/10.1016/j.biombioe.2014.09.014.
[25] Sermyagina E, Saari J, Zakeri B, Kaikko J, Vakkilainen E. Effect of heat integration method and torrefaction temperature on the performance of an integrated CHP-torrefaction plant. Appl Energy 2015;149:24–34. http://dx.doi.org/10.1016/j.apenergy.2015.03.102.
[26] Koskelainen L, Saarela R, Sipilä K. Kaukolämmön käsikirja (in Finnish)/Handbook of district heating. Energiateollisuus ry (Assoc Finnish Energy Ind) 2006.
[27] Saari J, Sermyagina E, Kaikko J, Vakkilainen E, Sergeev V. Integration of hydrothermal carbonization and a CHP plant: effect of integration method and carbonization temperature on plant performance. Bioresour Technol [submitted for publication 29.08.2016].
[28] Erlach B. Biomass upgrading technologies for carbon-neutral and carbon-negative electricity generation: techno-economic analysis of hydrothermal carbonization and comparison with wood pelletizing, torrefaction and anaerobic digestion. Doctoral thesis. TU Berlin (Germany); 2014.
[29] Savola T, Tveit T, Fogelholm C. A MINLP model including the pressure levels and multiperiods for CHP process optimisation. Appl Therm Eng 2007;27(8):1857–67. http://dx.doi.org/10.1016/j.applthermaleng.2007.01.002.
[30] Finnish Meteorological Institute; 2016. Available: http://en.ilmatieteenlaitos.fi/.
[31] Peters MS, Timmerhaus KD, West RE. Plant design and economics for chemical engineers. New York: McGraw-Hill Publishing Company; 2003.
[32] PACIFIC Exchange Rate Service. Available: http://fx.sauder.ubc.ca/data.html.
[33] Sinnott RK. Chemical engineering design. 4th ed. Oxford: Elsevier Butterworth-Heinemann; 2005.
[34] Foster Wheeler. CFB engineering manual. Foster Wheeler; 2006.
[35] US Environmental Protection Agency (EPA). Biomass combined heat and power catalog of technologies; 2007.
[36] Darrow K, Tidball R, Wang J, Hampson A. Catalog of CHP technologies. US Environmental Protection Agency; 2015. Accessed online at: http://www.epa.gov/chp/technologies.html.
[37] Barišić V, Zabetta EC, Hotta A. Foster wheeler experience in combustion of low-grade high-ash fuels in CFBs. Varkaus (Finland): Foster Wheeler Energia Oy; 2008.
[38] Batidzirai B, Mignot APR, Schakel WB, Junginger HM, Faaij APC. Biomass torrefaction technology: techno-economic status and future prospects. Energy 2013;62(12/1):196–214. http://dx.doi.org/10.1016/j.energy.2013.09.035.
[39] Pöyry Management Consulting. Adequacy of power capacity in Finland and the development of capacity structure until 2030. Tech Rep 52X265022, 2.2.2015.
[40] Kuitunen T. Uusiutuvista energialähteistä tuotetun sähkön tukijärjestelmät Euroopan unionissa ja niiden vaikutus biomassavoimalaitosten kannattavuuteen (in Finnish)/Subsidy systems for renewable power generation in the European Union, and their effect on the profitability of biomass-fired power plants. M.Sc. thesis. Finland: Lappeenranta University of Technology; 2007.

ACTA UNIVERSITATIS LAPPEENRANTAENSIS

738. PATEL, GITESHKUMAR. Computational fluid dynamics analysis of steam condensation in nuclear power plant applications. 2017. Diss.

739. MATTHEWS, SAMI. Novel process development in post-forming of an extruded wood plastic composite sheet. 2017. Diss.

740. KÄHKÖNEN, TOMMI. Understanding and managing enterprise systems integration. 2017. Diss.

741. YLI-HUUMO, JESSE. The role of technical dept in software development. 2017. Diss.

742. LAYUS, PAVEL. Usability of the submerged arc welding (SAW) process for thick high strength steel plates for Arctic shipbuilding applications. 2017. Diss.

743. KHAN, RAKHSHANDA. The contribution of socially driven businesses and innovations to social sustainability. 2017. Diss.

744. BIBOV, ALEKSANDER. Low-memory filtering for large-scale data assimilation. 2017. Diss.

745. ROTICH, NICOLUS KIBET. Development and application of coupled discrete and continuum models in solid particles classification. 2017. Diss.

746. GAST, JOHANNA. The coopetition-innovation nexus: Investigating the role of coopetition for innovation in SMEs. 2017. Diss.

747. KAPOOR, RAHUL. Competition and disputes in the patent life cycle. 2017. Diss.

748. ALI-MARTTILA, MAAREN. Towards successful maintenance service networks – capturing different value creation strategies. 2017. Diss.

749. KASHANI, HAMED TASALLOTI. On dissimilar welding: a new approach for enhanced decision-making. 2017. Diss.

750. MVOLA BELINGA, ERIC MARTIAL. Effects of adaptive GMAW processes: performance and dissimilar weld quality. 2017. Diss.

751. KARTTUNEN, JUSSI. Current harmonic compensation in dual three-phase permanent magnet synchronous machines. 2017. Diss.

752. SHI, SHANSHUANG. Development of the EAST articulated maintenance arm and an algorithm study of deflection prediction and error compensation. 2017. Diss.

753. CHEN, JIE. Institutions, social entrepreneurship, and internationalization. 2017. Diss.

754. HUOTARI, PONTUS. Strategic interaction in platform-based markets: An agent-based simulation approach. 2017. Diss.

755. QU, BIN. Water chemistry and greenhouse gases emissions in the rivers of the "Third Pole" / Water Tower of Asia". 2017. Diss.

756. KARHU, PÄIVI. Cognitive ambidexterity: Examination of the cognitive dimension in decision-making dualities. 2017. Diss.

757. AGAFONOVA, OXANA. A numerical study of forest influences on the atmospheric boundary layer and wind turbines. 2017. Diss.

758. AZAM, RAHAMATHUNNISA MUHAMMAD. The study of chromium nitride coating by asymmetric bipolar pulsed DC reactive magnetron sputtering. 2017. Diss.

759. AHI, MOHAMADALI. Foreign market entry mode decision-making: Insights from real options reasoning. 2017. Diss.

760. AL HAMDI, ABDULLAH. Synthesis and comparison of the photocatalytic activities of antimony, iodide and rare earth metals on SnO2 for the photodegradation of phenol and its intermediates under UV, solar and visible light irradiations. 2017. Diss.

761. KAUTTO, JESSE. Evaluation of two pulping-based biorefinery concepts. 2017. Diss.

762. AFZALIFAR, ALI. Modelling nucleating flows of steam. 2017. Diss.

763. VANNINEN, HEINI. Micromultinationals - antecedents, processes and outcomes of the multinationalization of small- and medium-sized firms. 2017. Diss.

764. DEVIATKIN, IVAN. The role of waste pretreatment on the environmental sustainability of waste management. 2017. Diss.

765. TOGHYANI, AMIR. Effect of temperature on the shaping process of an extruded wood-plastic composite (WPC) profile in a novel post-production process. 2017. Diss.

766. LAAKKONEN, JUSSI. An approach for distinct information privacy risk assessment. 2017. Diss.

767. KASURINEN, HELI. Identifying the opportunities to develop holistically sustainable bioenergy business. 2017. Diss.

768. KESKISAARI, ANNA. The impact of recycled raw materials on the properties of wood-plastic composites. 2017. Diss.

769. JUKKA, MINNA. Perceptions of international buyer-supplier relational exchange. 2017. Diss.

770. BAYGILDINA, ELVIRA. Thermal load analysis and monitoring of doubly-fed wind power converters in low wind speed conditions. 2017. Diss.

771. STADE, SAM. Examination of the compaction of ultrafiltration membranes with ultrasonic time-domain reflectometry. 2017. Diss.

772. KOZLOVA, MARIIA. Analyzing the effects of a renewable energy support mechanism on investments under uncertainty: case of Russia. 2017. Diss.

773. KURAMA, ONESFOLE. Similarity based classification methods with different aggregation operators. 2017. Diss.

774. LYYTIKÄINEN, KATJA. Removal of xylan from birch kraft pulps and the effect of its removal on fiber properties, colloidal interactions and retention in papermaking. 2017. Diss.

775. GAFUROV, SALIMZHAN. Theoretical and experimental analysis of dynamic loading of a two-stage aircraft engine fuel pump and methods for its decreasing. 2017. Diss.

776. KULESHOV, DMITRII. Modelling the operation of short-term electricity market in Russia. 2017. Diss.